POLYTECHNIQUE MONTRÉAL
affiliée à l'Université de Montréal

Integration of Germanium-Tin Membranes for Mid-Infrared Silicon Photonics

CÉDRIC LEMIEUX-LEDUC
Département de génie physique

Thèse présentée en vue de l'obtention du diplôme de *Philosophiæ Doctor*
Génie physique

Avril 2025

© Cédric Lemieux-Leduc, 2025.

POLYTECHNIQUE MONTRÉAL
affiliée à l'Université de Montréal

Cette thèse intitulée :

Integration of Germanium-Tin Membranes for Mid-Infrared Silicon Photonics

présentée par **Cédric LEMIEUX-LEDUC**
en vue de l'obtention du diplôme de *Philosophiæ Doctor*
a été dûment acceptée par le jury d'examen constitué de :

David MÉNARD, président
Yves-Alain PETER, membre et directeur de recherche
Oussama MOUTANABBIR, membre et codirecteur de recherche
Ludvik MARTINU, membre
Lawrence R. CHEN, membre externe

DEDICATION

To my family, friends and Tracy.

À ma famille, mes amis et Tracy.

ACKNOWLEDGEMENTS

This Ph.D. journey has been filled with both challenges and rewarding moments. More than anything, it has been a deeply fulfilling experience, made possible by the support of many incredible people. This thesis would not have been possible without them.

I sincerely thank my research advisors, Yves-Alain Peter and Oussama Moutanabbir, for their invaluable guidance, patience, and support throughout my research. Their mentorship has been instrumental not only in shaping my scientific journey but also in teaching me perseverance and motivation. I had the privilege of working with outstanding colleagues from their respective research groups, the Microphotonics Laboratory and the Nano & Quantum Semiconductors Laboratory, who contributed directly or indirectly to helping me reach this milestone.

In the Microphotonics Lab, I was fortunate to work alongside Marc-Antoine Bianki and Régis Guertin, with whom I shared the office space, countless stimulating discussions, and many enjoyable coffee and lunch breaks since the beginning of our graduate studies. I'm also grateful to Antoine Leblanc-Hotte, with whom I had the pleasure of collaborating and from whom I learned a great deal. I would also like to acknowledge all of the current (Nicole Tebchrany, Salvador Poveda Hospital, Nicolas Malo, Thomas Grenon, Louis-Frédéric Racicot) and past (Ahmed Sami Bahgat Abdelaziz, Thomas Lapointe, Thomas Lacasse, Nathan Ferga, Rizki Arif Pradono, Laure Sène) members of the group for their valuable discussions and the great moments we shared. Our numerous badminton and wallyball games at CEPSUM, along with activities like mountain biking and canoe camping, made this experience even more enjoyable. Special thanks to Yves Drolet for his technical support in the lab.

In the Nano & Quantum Semiconductors Lab, I had the privilege of collaborating with many exceptional individuals, including Simone Assali and Mahmoud R. M. Atalla, from whom I learned a great deal through insightful discussions and experiments that contributed to the development of this project. I am also grateful to Gérard Daligou, Lu Luo, Patrick Daoust, Sebastian Kölling, Nicolas Rotaru, and Anis Attiaoui for their help through discussions and technical assistance in experiments. Beyond research, I also shared many memorable moments–from hiking and kayaking to lunches at Snowdon Deli–with colleagues who made this journey even more special. I extend my gratitude to all current members (Karim Moreno Omambac, Anthony Nomezine, Luc Montpetit, Sudarshan Singh, Eloïse Rahier, Guillaume Nadal, Jérémy Bélec, Simon Jean Michel, Ziqiang Cai) and past members (Jérôme Nicolas, Patrick Del Vecchio, Rayan Chane Kai Shing, Nathalie Rojas-Lobo, David Vaslov, Samik

Mukherjee, Duy-Thach Phan, Gabriel Fettu, Laurianne Borsoni, Coralie Bellemare) of the group. Special thanks to Joël Bouchard for his technical support and Catherine Caffiaux for her invaluable administrative assistance.

This research would not have been possible without access to multiple research facilities at Polytechnique Montréal and beyond. I extend my sincere appreciation to the staff at the Laboratoire de Microfabrication at Polytechnique Montréal (Marie-Hélène Bernier, Christophe Clément, André Hoang-Gaona, and Alexandre Perron Bacon) for their unwavering technical support. I am also deeply grateful to the Light-Matter Group at Polytechnique (Julien Brodeur and Prof. Stéphane Kéna-Cohen) for their assistance with transfer printing and for granting me access to their equipment. Additionally, I thank Mikaël Leduc from the Department of Engineering Physics for his assistance with various optical instruments and Bill Baloukas from the Functional Coatings and Surface Engineering Laboratory for his support with ellipsometry measurements. I am also appreciative of the team at the Laboratoire de Micro et Nanofabrication at INRS (Boris Le Drogoff and Amine Zitouni) for their technical support, as well as Dainelys Guadarrama Bello from the Laboratory of Calcified Tissues and Biomaterials at Université de Montréal for her assistance with scanning electron microscopy.

It would be impossible to acknowledge everyone I met during these years, but I would also like to express my gratitude to the friends with whom I shared many great experiences, including Jean-Sébastien Boisvert, Jennyfer Zapata Farfan, and several old-timers from the Department of Engineering Physics and other laboratories.

I also want to thank my Ph.D. committee members, Prof. David Ménard, Prof. Ludvik Martinu, and Prof. Lawrence R. Chen, for taking the time to review this thesis.

This research was made possible thanks to financial support from NSERC, FRQNT, and National Defence through the Innovation for Defence Excellence and Security (IDEaS) program, as well as scholarships and grants from SPIE, Hydro-Québec, and the Photonics Chapter of the IEEE Montreal Section.

Finally, I would like to thank my friends and family, who have always encouraged and believed in me, especially my parents, Richard and Karole, as well as my sister, Cynthia. A very special thank you to my partner, Tracy, and our cats–Catacombes, Alaska, and Jasper–for their unwavering love and support throughout this journey. You made this experience enjoyable, and I am truly grateful for your patience and encouragement.

RÉSUMÉ

L'essor de la photonique sur silicium (Si) a révolutionné les télécommunications, répondant à la demande croissante de transmission de données à haute vitesse et à faible consommation énergétique. Les circuits photoniques intégrés (PICs – *photonic integrated circuits*) exploitent la transparence du Si aux longueurs d'onde des télécommunications (1260–1625 nm) ainsi que la fabrication à grande échelle rendue possible par l'infrastructure CMOS (*complementary metal-oxide-semiconductor*). Cependant, l'intégration de dispositifs actifs, comme les lasers et les photodétecteurs, demeure un défi en raison du gap indirect du Si, limitant son efficacité en émission et en détection de lumière.

Parmi les solutions alternatives, les alliages de germanium-étain ($Ge_{1-x}Sn_x$ ou GeSn) suscitent un intérêt croissant, car l'incorporation d'atomes d'étain (Sn) dans le réseau cristallin du Ge permet une transition d'un gap indirect à un gap direct lorsque la concentration de Sn dépasse environ 8 at.%. Une augmentation de la teneur en Sn permet également de réduire l'énergie de gap, rendant possible l'opération dans l'infrarouge moyen (2–8 μm), une gamme d'intérêt pour des applications telles que la détection spectroscopique, la surveillance environnementale et les communications optiques. Contrairement aux matériaux III–V ou II–VI, le GeSn peut être intégré de manière compatible avec le Si via la déposition chimique en phase vapeur (CVD – *chemical vapor deposition*), permettant une fabrication extensible et rentable.

Cette thèse explore l'intégration des alliages GeSn comme matériau actif pour la photonique sur silicium. Malgré son potentiel, l'intégration du GeSn est entravée par des défis de croissance, notamment une faible solubilité du Sn dans le Ge (inférieure à 1%) et une différence significative des rayons atomiques entre le Ge et le Sn (14,7 %), qui induit des contraintes compressives générant des défauts de matériau et limitant la faisabilité de l'intégration monolithique avec la photonique sur silicium. Pour surmonter ces obstacles, des membranes en GeSn sont étudiées comme plateforme pour une intégration hétérogène du matériau. Ces membranes, fabriquées à partir de couches minces de GeSn déposées sur silicium avec une couche tampon de Ge, sont sélectivement sous-gravées et transférées sur des substrats alternatifs à l'aide d'une technique optimisée basée sur l'impression par transfert.

Les membranes contenant 11 at.% de Sn présentent une longueur d'onde de coupure étendue à 3,1 μm, offrant une large gamme d'opérations pour plusieurs applications, notamment en détection spectroscopique. Le potentiel d'intégration de ces membranes est évalué par des simulations numériques, analysant l'efficacité de couplage et les performances de pho-

todétection avec des guides d'ondes en silicium-sur-isolant (SOI – *silicon-on-insulator*) et en germanium-sur-silicium (GOS – *germanium-on-silicon*). Une preuve de concept démontre l'intégration de membranes en $Ge_{0.89}Sn_{0.11}$ avec des guides d'ondes SOI pour créer des photodétecteurs couplés à des guides d'ondes fonctionnant dans l'infrarouge moyen, atteignant une responsivité allant jusqu'à 361 mA/W à une longueur d'onde de 2,33 μm. Plusieurs dispositifs sont fabriqués en une seule étape d'impression par transfert, démontrant ainsi l'extensibilité de l'approche proposée.

Ce travail apporte plusieurs contributions novatrices, notamment l'optimisation de l'impression par transfert pour les membranes en GeSn relâchées en contrainte, une méthodologie pour l'étude systématique de l'efficacité de couplage dans différents scénarios d'intégration, et une solution extensible pour l'intégration du GeSn dans la photonique sur silicium pour les applications dans l'infrarouge moyen. Bien que cette approche ne repose pas sur une intégration monolithique, elle permet un prototypage rapide des dispositifs basés sur le GeSn tout en contribuant à l'adoption de l'alliage dans divers champs d'applications.

ABSTRACT

The rise of silicon (Si) photonics has revolutionized telecommunications, addressing the growing demand for high-speed and energy-efficient data transmission. Photonic integrated circuits (PICs) leverage Si's transparency at telecommunications wavelengths (1260–1625 nm) and the scalability of *complementary metal-oxide-semiconductor* (CMOS) fabrication processes. However, integrating active devices such as lasers and photodetectors remains challenging due to Si's indirect bandgap, which limits its light emission and detection efficiency.

To overcome these limitations, group-IV semiconductor alloys such as germanium-tin ($Ge_{1-x}Sn_x$ or GeSn) have garnered interest, as the incorporation of tin (Sn) into the Ge lattice leads to a transition from an indirect to a direct bandgap when the Sn content exceeds approximately 8 at.%. Increasing the Sn content also enables operation in the mid-infrared range (2–8 μm), relevant for applications such as spectroscopic sensing, environmental monitoring, and data communication. Unlike III–V or II–VI materials, GeSn alloys can be grown on Si using chemical vapor deposition (CVD), enabling scalable and cost-effective device fabrication.

This thesis has the primary goal to investigate the integration of GeSn alloys as an active material for silicon photonics. Despite its potential, GeSn integration faces significant challenges, including low Sn solubility in Ge (below 1%) and a 14.7% atomic radius mismatch, which induces compressive strain, leading to defects and hindering monolithic integration with Si photonics. To overcome these downsides, GeSn membranes are studied as a platform for heterogeneous integration of the material. These membranes, fabricated from GeSn layers grown on silicon with a Ge buffer layer, are selectively underetched and transferred to alternative substrates using an optimized approach based on transfer printing.

Membranes with 11 at.% Sn exhibit a cutoff wavelength extended to 3.1 μm. Their integration potential is evaluated through numerical simulations assessing coupling efficiency and photodetection performance on silicon-on-insulator (SOI) and germanium-on-silicon (GOS) waveguides. A proof-of-concept demonstration shows the integration of $Ge_{0.89}Sn_{0.11}$ membranes with SOI waveguides to fabricate waveguide-coupled mid-infrared detectors, achieving a responsivity of up to 361 mA/W at 2.33 μm. Multiple devices are fabricated in a single transfer-printing step, demonstrating the scalability of the approach.

This work offers several novel contributions, including the optimization of transfer printing for strain-relaxed GeSn membranes, a methodology for the systematic numerical investigation of the coupling efficiency in different integration scenarios, and a scalable solution for integrating GeSn into silicon photonics for mid-infrared applications. These advance-

ments are expected to accelerate the development and adoption of GeSn-based components in sensing, communications, and other fields. While not a monolithic integration scheme, this approach enables rapid prototyping of GeSn-based devices, offering valuable insights for future development and facilitating alloy adoption across various applications.

TABLE OF CONTENTS

DEDICATION iii

ACKNOWLEDGEMENTS iv

RÉSUMÉ vi

ABSTRACT viii

TABLE OF CONTENTS x

LIST OF TABLES xiii

LIST OF FIGURES xiv

LIST OF ACRONYMS xxiii

LIST OF APPENDICES xxvi

CHAPTER 1 INTRODUCTION 1
1.1 Motivation 3
1.2 Problematic 4
1.3 Objectives 6
1.4 Organisation of the thesis 7

CHAPTER 2 LITERATURE REVIEW 8
2.1 Current landscape of silicon photonics 8
2.2 Silicon-compatible optoelectronic devices based on germanium-tin alloys . . . 11
2.2.1 Material properties and band structure 12
2.2.2 Current state of the art in device demonstrations 18
2.2.3 Challenges 25
2.3 Mid-infrared optoelectronic applications 28
2.3.1 Applications 29
2.3.2 Current technologies 33
2.3.3 Mid-infrared integrated photonics 38

CHAPTER 3 METHODOLOGY 51

3.1 Chemical vapor deposition of GeSn 51
3.2 Microfabrication methods 52
3.2.1 Lithography 53
3.2.2 Etching 54
3.2.3 Thin film deposition 56
3.3 Transfer printing 56
3.4 Characterization methods 58
3.4.1 X-ray diffraction 58
3.4.2 Raman spectroscopy 59
3.4.3 Scanning electron microscopy and transmission electron microscopy . 60
3.4.4 Photoluminescence 61
3.4.5 Responsivity measurements 63
3.4.6 PIC characterization setup 64
3.5 $k \cdot p$ theory 65

CHAPTER 4 ARTICLE 1: TRANSFER-PRINTED MULTIPLE GESN MEMBRANE MID-INFRARED PHOTODETECTORS 67
4.1 Abstract 67
4.2 Introduction 68
4.3 Results and discussion 71
4.3.1 Growth and characterization of GeSn epilayers 71
4.3.2 GeSn membrane fabrication and transfer printing 72
4.3.3 Device characterization 76
4.4 Conclusion 80

CHAPTER 5 SIMULATION OF GERMANIUM-TIN MATERIAL INTEGRATION AND OPTICAL COUPLING 82
5.1 Introduction 82
5.2 Optical properties of GeSn and other materials 84
5.3 Waveguiding properties of the SOI and GOS platforms in the mid-infrared . 87
5.4 Modeling of the evanescent coupling in coupled waveguided structures 95
5.5 Discussion on the impact of additional design considerations 109
5.6 Conclusion 114

CHAPTER 6 TRANSFER-PRINTED GESN MEMBRANES FOR WAVEGUIDE-COUPLED MID-INFRARED DETECTORS 115
6.1 Introduction 115

6.2 Concept and modeling . . . 115
6.2.1 Layout design . . . 117
6.2.2 Grating coupler design . . . 118
6.2.3 Extraction of the optical constants of GeSn using ellipsometry . . . 121
6.2.4 Coupling mechanisms . . . 121
6.3 Device fabrication . . . 123
6.3.1 Chip fabrication . . . 124
6.3.2 Transfer printing . . . 127
6.4 Characterization results . . . 128
6.5 Estimation of the photoresponse bandwidth . . . 136
6.6 Conclusion . . . 138

CHAPTER 7 GENERAL DISCUSSION . . . 140
7.1 GeSn membranes as a transferable active platform . . . 140
7.2 Monolithic integration compared to heterogeneous integration . . . 143
7.3 GeSn for silicon photonics and mid-infrared applications . . . 145
7.4 GeSn material quality in its current state and limitations . . . 146

CHAPTER 8 CONCLUSIONS AND PERSPECTIVES . . . 148

REFERENCES . . . 151

APPENDICES . . . 180

LIST OF TABLES

Table 2.1 Parameters for Si, Ge, and α-Sn such as the bandgap energies E_i at 0 K, the cubic lattice constants a_0, and the elastic constants C_{ij}. 13

Table 2.2 Comparison of photonic platforms with transparency ranges where propagation loss remains below 2 dB/cm. 44

Table 4.1 Comparison of properties of different photodetectors based on $Ge_{1-x}Sn_x$ membranes. 69

Table 5.1 Thermal conductivity of GeSn and other materials. 113

Table 6.1 ICP-RIE parameters for the pseudo-Bosch etching of Si (Plasmalab 100 - Oxford Instruments at LMN). 125

Table 6.2 Comparison of waveguide-coupled photodetectors operating in the 2–3 μm range. 136

Table A.1 Dry etching recipes with reported etch rates and selectivities using chlorine- and fluorine-based chemistries. Various Sn contents were used for the GeSn samples (PL 100: Plasmalab 100 from Oxford Instruments). 182

Table A.2 Etch rates of wet etching recipes. The wet etching is carried out at room temperature. 189

Table A.3 Summary of the etch rate of the different materials using different compounds ('W': etch rate not measured, but expected to work. 'S': etch rate not measured, but expected to be slow or near zero). 194

LIST OF FIGURES

Figure 1.1 Illustration of an integrated GeSn photodetector coupled to an SOI waveguide. 5

Figure 2.1 Overview of the different components in a photonic integrated circuit (PIC) combined with an electronic integrated circuit using 3D integration, as developed by STMicroelectronics. 9

Figure 2.2 Electronic band structure of (a) Si, (b) Ge, and (c) α-Sn. The conduction (CB) and valence (VB) bands are identified in red and blue respectively. 13

Figure 2.3 Electronic band structure of GeSn alloys with Sn contents of (a) 5 at.%, (b) 15 at.%, and (c) 25 at.% to highlight the bandgap transition from indirect to direct along the Γ point. 14

Figure 2.4 Transition from an indirect to a direct bandgap in GeSn alloys as a function of Sn content, along with the bandgap directness. The energies were computed using an 8-band $k{\cdot}p$ model for unstrained material. The crossover from an indirect to a direct bandgap occurs at a content of approximately 7 at.% Sn. 15

Figure 2.5 Bandgap energy of GeSn (blue) with III–V (red) and II–VI (green) compounds as a function of lattice parameter with the respective Sn content. 16

Figure 2.6 Transition from an indirect to a direct bandgap in GeSn alloys as a function of Sn content and in-plane biaxial strain. Contour plots showing (a) the bandgap energy and (b) the energy difference between the conduction band minima at the L point (E_{C_L}) and the Γ point (E_{C_Γ}). 17

Figure 2.7 Overview of the different structures used in the demonstrations of GeSn (a) optically pumped lasers, (b) electrically pumped lasers, and (c) light-emitting diodes. 19

Figure 2.8 Overview of the different structures used in the demonstrations of GeSn photodetectors with (a) vertical photodetectors, (b) waveguide photodetectors (WGPDs), and (c) membrane photodetectors. 22

Figure 2.9 Illustration of a monolithically integrated GeSn photodetector (PD) onto an SOI photonic platform. 23

Figure 2.10 Ge–Sn phase diagram as a function of at.% Sn and temperature. a) Diagram from 0 to 100 at.% Sn. b) Diagram from 0 to 1.4 at.% Sn. . 27

Figure 2.11 Illustration of the electromagnetic spectrum with range definitions. The demonstrated range (cutoff wavelength in photodetectors) of GeSn is overlaid with the expected range that remains to be demonstrated, either using GeSn or SiGeSn compounds. 29
Figure 2.12 Examples of molecules of interest and key applications in mid-infrared sensing. 30
Figure 2.13 Absorption coefficient spectra of (a) water, (b) carbon monoxide, (c) carbon dioxide, and (d) methane from 1 to 5 μm. Data is taken from the HITRAN database. 31
Figure 2.14 Wavelength ranges of interest for communications. (a) Standard telecommunications band with the novel 2 μm band. (b) Transmittance of the atmosphere exhibiting the atmospheric windows from 3 to 5 μm and from 8 to 12 μm. 32
Figure 2.15 Solar irradiance and atmospheric absorption spectra up to 4 μm with the 2–2.5 μm window highlighted. 33
Figure 2.16 Wavelength coverage of mid-infrared light sources. Data taken from various references mentioned in this section including. 34
Figure 2.17 Comparison of the specific detectivity of various mid-infrared detectors. PC: Photoconductor. PV: Photovoltaic. 39
Figure 2.18 Overview of the different photonic platforms that can operate in the mid-infrared region. (a) Si-based platforms. (b) Ge-based platforms. . 41
Figure 2.19 Principal heterogeneous integration techniques. (a) Wafer bonding. (b) Single-die flip-chip transfer. (c) Transfer printing of multiple pre-processed devices. 46
Figure 2.20 Configurations of integrated mid-infrared sensing systems based on a mid-infrared (a) broadband source and (b) tunable laser source. . . . 50
Figure 3.1 CVD growth. (a) Schematic of the process chamber. Precursor gases are injected into the chamber through the showerhead above the wafer. (b) Sn content as a function of the growth temperature for pseudomorphic and relaxed layers. 52
Figure 3.2 Schematic of the principal microfabrication steps. 53
Figure 3.3 Comparison of etching profiles after anisotropic and isotropic etching. 54
Figure 3.4 Schematic of the plasma chamber of an ICP-RIE tool. 55
Figure 3.5 Overview of the transfer printing technique. (a) Illustration of the transfer printing steps. (b) Energy release rates as a function of the peeling rate for printing and picking up the ink with the stamp. . . . 58

Figure 3.6 Overview of XRD. (a) Working principle of XRD using Bragg's law. (b) Schematic of the main components of an XRD configured for RSM measurements. (c) Example of an RSM map of the sample stack displayed in the inset, where the different layers can be identified. 60
Figure 3.7 Scanning electron microscopy. (a) Schematic of an SEM. (b) Generation of secondary (SE) and backscattered electrons (BSE) with atoms. 61
Figure 3.8 Working principle of photoluminescence. (a) Generation of a photoluminescence photon after the material is excited by an excitation source. (b) Emission of a photon in direct bandgap material. (c) Emission in an indirect bandgap material, where a phonon is also required. 62
Figure 3.9 Photoluminescence setup showing the components and light path of the FTIR. 63
Figure 3.10 Responsivity setup using the FTIR. 64
Figure 3.11 PIC characterization setup. (a) CAD image of the different components used. (b) Picture of the actual setup with optical fibers and electrical probes aligned onto a PIC chip. 65
Figure 3.12 Responsivity setup using an optical fiber in the PIC setup. 66
Figure 4.1 Properties of the as-grown $Ge_{0.89}Sn_{0.11}$ alloy. (a) Cross-sectional TEM image of the layer stack. (b) EDX Ge and Sn profiles in the grown layer, starting from the top of the GeSn layer. (c) XRD-RSM around the asymmetrical (224) reflection peak, providing the composition and strain in the as-grown $Ge_{0.89}Sn_{0.11}$ layer. (d) 8-band $k{\cdot}p$ calculations of the room-temperature absorption of the $Ge_{0.89}Sn_{0.11}$ layer by varying the in-plane strain from compressive strain (-1%) to full relaxation (0%). 72
Figure 4.2 Membrane fabrication. (a) Illustration of the $Ge_{0.89}Sn_{0.11}$ membrane fabrication steps. (b) Optical microscope image and SEM micrograph of a released $Ge_{0.89}Sn_{0.11}$ membrane. (c) Raman spectroscopy measurements of the as-grown and the membrane samples with the position of the Ge−Ge longitudinal phonon Raman peak indicated. (d) Photoluminescence spectra of the as-grown and membrane samples acquired at room temperature. 73
Figure 4.3 Membrane photodetector fabrication via transfer printing. (a) Transfer printing steps. (b) Optical microscope image of multiple membrane devices (top) along with SEM images of selected devices (bottom). . . 75

Figure 4.4 Photoconductive device characterization. (a) Dark current of the contacted membrane and as-grown samples as a function of voltage. (b) Spectral responsivity of the membrane and as-grown devices under a bias of 1 V. (c) Time-dependent photocurrent response of a membrane device under a bias of 1 V and illuminated under different power densities using a 1.55 μm laser. (d) Photocurrent as a function of power density and of applied bias. 77

Figure 4.5 Device characterization after chemical treatment and annealing at different temperatures. (a) Dark current as a function of voltage. (b) Spectral responsivity normalized to the measurement made with the annealing at 200 °C. (c) Time-dependent photocurrent response under a bias of 1 V and illuminated by a 1.55 μm laser at a power density of 11.6 kW/cm^2. 79

Figure 5.1 Illustration of the evanescent coupling phenomenon. (a) 3D model of the structure with the 2D longitudinal cross-section under study identified. (b) Schematic of the different steps that the light undergoes in this structure, such as guiding through the waveguide (I) before undergoing coupling (II) with the GeSn layer and absorption (III). . . 83

Figure 5.2 Optical properties of Ge and GeSn films for various Sn contents up to a wavelength of 2.5 μm. (a) Refractive index. (b) Absorption coefficient. 84

Figure 5.3 Computed optical properties of $Ge_{0.89}Sn_{0.11}$ using the 8-band $k{\cdot}p$ model in its strained (-0.6%) and relaxed (0%) states. (a) Refractive index. (b) Extinction coefficient. 86

Figure 5.4 Material properties used in the modeling. (a) Refractive index and (b) extinction coefficient of Si, SiO_2, and Ge. 86

Figure 5.5 Dispersion of BCB and SU-8 measured using ellipsometry. 87

Figure 5.6 Overview of the SOI platform as a slab waveguide. (a) Layer stack composing the platform (left) and the refractive index profile of the materials (right). (b) Normalized E-field of different supported modes in an SOI slab waveguide at a wavelength of 1.55 μm. 88

Figure 5.7 Overview of the GOS platform as a slab waveguide. (a) Layer stack composing the platform (left) and the refractive index profile of the materials (right). (b) Normalized E-field of different supported modes in a GOS slab waveguide at a wavelength of 2.33 μm. 89

Figure 5.8 Effective refractive index of the different supported modes in the SOI platform as a function of slab thickness and wavelength. 90

Figure 5.9 Effective refractive index of the different supported modes in the GOS platform as a function of slab thickness and wavelength. 90
Figure 5.10 Properties of SOI waveguides. (a) Schematic of the cross-section. (b) n_{eff} as a function of width showing the first three TE modes. Inset: Electric field distribution of the modes. 91
Figure 5.11 Impact of the waveguide width on the wavelength-dependent behavior in the SOI platform. (a) Refractive index and (b) computed modal loss as a function of wavelength for different waveguide widths with a fixed height of 220 nm. 92
Figure 5.12 Impact of the waveguide height on the wavelength-dependent behavior in the SOI platform. (a) Refractive index and (b) computed modal loss as a function of wavelength for different waveguide heights with a fixed width of 2 μm. 93
Figure 5.13 Properties of GOS waveguides. (a) Schematic of the cross-section. (b) n_{eff} as a function of width showing multiple TE (solid lines) and TM (dashed lines) modes. Inset: Electric field distribution of the TE modes. 93
Figure 5.14 Impact of the waveguide width on the wavelength-dependent behavior in the GOS platform. (a) Refractive index and (b) computed modal loss as a function of wavelength for different waveguide widths with a fixed height of 1 μm. 94
Figure 5.15 Impact of the waveguide height on the wavelength-dependent behavior in the GOS platform. (a) Refractive index and (b) computed modal loss as a function of wavelength for different waveguide heights with a fixed width of 1 μm. 95
Figure 5.16 Illustration of the three integration scenarios. (a) Scenario 1. (b) Scenario 2. (c) Scenario 3. 98
Figure 5.17 The longitudinal cross-section of the three scenarios investigated (left) and the 2D electric field distribution of light propagating in the waveguide and interacting with the GeSn layer at a wavelength of 2 μm. (a) Scenario 1 with a 1 μm thick Ge buffer layer. (b) Scenario 2 using an adhesive (here SU-8). (c) Scenario 3. 99
Figure 5.18 Impact of the dimensions on the fraction of absorbed power. (a) Absorbed power fraction as a function of length. (b) Absorption as a function of GeSn thickness and Ge buffer height. 101
Figure 5.19 Wavelength dependence of P_{abs} in the GeSn and Ge layers separately (h_{Si} = 220 nm, h_{Ge} = 1 μm, and h_{GeSn} = 400 nm). 102

Figure 5.20 Wavelength dependence of coupling efficiency metrics in Scenario 1 by varying the waveguide height (h_{Si}) and the GeSn thickness (h_{GeSn}). (a) $1/\alpha_{Coupling}$. (b) $P_{abs,sat}$. 103
Figure 5.21 Impact of the properties of the gap on P_{abs}. (a) Dependence of the separation gap h_{Gap} using air, SU-8, and BCB as the medium for the gap. (b) Wavelength dependence for different separation gaps h_{Gap}. . 104
Figure 5.22 Influence of GeSn active region dimensions on the coupling efficiency. (a) Influence of the thickness of the GeSn layer for different gaps. (b) Influence of the thickness and the length of GeSn at a h_{Gap} of 200 nm. 105
Figure 5.23 Effective index of the first three TE slab modes of the GeSn active region as a function of GeSn thickness. A phase-matching condition is met with the SOI slab waveguide at GeSn thicknesses corresponding to the oscillations where P_{abs} is maximal. 106
Figure 5.24 Absorbed power fraction as a function of separation gap for different waveguide heights h_{Si} and polarizations. 106
Figure 5.25 Wavelength dependence of coupling efficiency metrics in Scenario 2 by varying the gap (h_{Gap}). (a) $1/\alpha_{Coupling}$. (b) $P_{abs,sat}$. 107
Figure 5.26 Impact of polarization on P_{abs}. (a) Absorbed power fraction as a function of length for TE and TM polarizations. (b) Wavelength dependence of the absorbed power fraction after propagating through 50 μm in the GOS waveguide. 108
Figure 5.27 Impact of geometry on P_{abs}. (a) Absorbed power fraction as a function of length and GeSn material thickness. (b) Absorbed power fraction as a function of length and Ge waveguide height. 108
Figure 5.28 Wavelength dependence of coupling efficiency metrics in Scenario 3 by varying the waveguide height (h_{Ge}) and the GeSn thickness (h_{GeSn}). (a) $1/\alpha_{Coupling}$. (b) $P_{abs,sat}$. 109
Figure 5.29 Absorbed power fraction as a function of separation gap for different waveguide widths w_{Si}. 111
Figure 6.1 Device schematic of a waveguide-integrated GeSn photodetector. (a) Illustration of the concept. (b) Cross-section of the designed device. A GeSn membrane is transfer-printed on top of a waveguide using a thin SU-8 layer to enhance adhesion and passivate the circuit. 116
Figure 6.2 Layout of the 2D array of waveguide-coupled GeSn membranes. Inset: Close-up view of a single device with the identification of the different components. 118

Figure 6.3 Concept of an SGC with the key design parameters. 119
Figure 6.4 2D FDTD calculation of the transmission through an SGC as a function of grating period and etch depth of the teeth on a 220 nm thick SOI. The grating angle is 10°, the operation wavelength is 2.33 μm, and the F ratio is 0.75. The transmission is normalized to the input power. . 120
Figure 6.5 Wavelength dependence of the transmission of the SGC using the optimized parameters computed using 3D FDTD. 120
Figure 6.6 Optical constants of $Ge_{0.89}Sn_{0.11}$ with a compressive strain of -0.6%. The extracted ellipsometry values are compared to 8-band *kp* calculations. 122
Figure 6.7 Modeling results of the evanescent and grating-assisted coupling between an SOI waveguide and a GeSn membrane. (a) Cross-section of the waveguide (top) with the normalized distribution of $|E|$ of TE_{00} at a wavelength of 2.33 μm (bottom). (b) Illustration of the principle of evanescent (top) and grating-assisted coupling (bottom) with the distribution of $|E|$ of the propagating mode in each case. 123
Figure 6.8 Evolution of the absorbed power fraction for the two coupling mechanisms as a function of (a) the separation gap and (b) the wavelength. 124
Figure 6.9 Overview of the fabrication steps for the GeSn membranes (donor chip) and the passive SOI chip (receiver chip). 124
Figure 6.10 Microscope images of the PIC (a) after EBL patterning and (b) after dry etching and PMMA removal. 125
Figure 6.11 SEM micrographs of the structures on the PIC. (a) Waveguide unit. (b) Close-up view of the grating coupler. 126
Figure 6.12 Stitching defects observed on the SOI chip caused by the EBL patterning step. 126
Figure 6.13 Transfer printing steps with the subsequent deposition of metal contacts on the transferred membranes. Insets: pictures taken from an optical microscope at different steps (The change in color is related to unintentional modifications in the camera settings of the microscope). 127
Figure 6.14 Images from optical microscopy and SEM for a device based on (a) Design EC and (b) Design ECGAC. 129
Figure 6.15 Characterization setup. (a) Schematic of the setup components to measure the responsivity while injecting light. (b) Microscope image of a coupled device with electrical probes. 130

Figure 6.16 Electrical and optical characterization of the devices. (a) Current-voltage measurements of a device from -1 V to 1 V under illumination. (b) Transient photoresponse of a device under illumination at different optical powers. 131
Figure 6.17 Current-voltage measurements of a device with evaporated contacts compared to exfoliated contacts. 131
Figure 6.18 Photocurrent as a function of optical power in the waveguide for a device based on (a) Design EC and (b) Design ECGAC. 132
Figure 6.19 Dark current as a function of bias for all fabricated devices based on (a) Design EC and (b) Design ECGAC. 133
Figure 6.20 Photocurrent as a function of optical power for all fabricated devices based on (a) Design EC and (b) Design ECGAC under a bias of 1 V. 133
Figure 6.21 Computation of the 2D and cumulative generation rates for designs EC and ECGAC using 3D FDTD. 135
Figure 7.1 Illustration of a transfer-printed GeSn p-i-n membrane onto an SOI waveguide. 142
Figure 7.2 Proposed processing flow for the fabrication of GeSn p-i-n membranes assisted by transfer printing. 143
Figure A.1 SEM micrographs of the cross-sections of etched structures using Cl_2-based chemistries at LMN, with recipes (a) **C4**, (b) **C6**, and (c) **C7**. Line defects in the facets were introduced during the cleaving of the samples. 184
Figure A.2 SEM micrographs of the etching profile of Ge using Recipe **C2** with (a) its initial parameters (RF = 100 W, ICP = 200 W) compared to (b) lower generator powers (RF = 75 W, ICP = 125 W). 185
Figure A.3 SEM micrographs showing the impact of the Cl_2/O_2 ratio on the sidewall profile of Ge structures for values of (a) 0.25, (b) 0.15, and (c) 0.05 using Recipe **C4**. Top: View of the cross-section. Bottom: Tilted view of the sidewall profile. 186
Figure A.4 Fabrication steps of partially underetched structures with a GeSn film sample composed of multiple layers with contents ranging from 6 to approximately 9 at.% Sn. (a) Resulting mesa after directional etching through the GeSn layers using a Cl_2/Ar plasma (recipe **C7**). (b) Resulting structure after selective and isotropic etching of Ge using a CF_4 plasma (recipe **F4**). (c) Disk structure from a different sample made of a single content around 11 at.% Sn. 191

Figure A.5 Overview of GeSn membrane structures. (a) Released GeSn microdisk patterned using wet etching. (b) Released membrane on Si. (c) Larger structures that exhibit structural bowing. (d) Released thin membranes, with some exhibiting significant structural bowing. 192

LIST OF ACRONYMS

APD	Avalanche photodiode
AWG	Arrayed waveguide grating
ART	Aspect ratio trapping
BCB	Benzocyclobutene
BEOL	Back-end-of-line
BOX	Buried oxide
BSE	Backscattered electrons
CAD	Computer-aided design
CCP	Capacitively coupled plasma
CMOS	Complementary metal-oxide-semiconductor
CVD	Chemical vapor deposition
CW	Continuous wave
DHS	Double heterostructure
DOS	Density of states
FDTD	Finite-difference time-domain
EBL	Electron beam lithography
EDX	Energy-dispersive X-ray spectroscopy
EIC	Electronic integrated circuit
FCA	Free carrier absorption
FEM	Finite element method
FET	Field-effect transistor
FIB	Focused ion beam
FPA	Focal plane array
FTIR	Fourier transform infrared spectroscopy
GAAFET	Gate-all-around field-effect transistor
GeSn	Germanium-tin
GOS	Germanium-on-insulator
HC-PBGF	Hollow-core photonic bandgap fiber
ICL	Interband cascade laser
ICP	Inductively coupled plasma
INRS	Institut National de la Recherche Scientifique
IoT	Internet of Things
MBE	Molecular beam epitaxy

MCT	Mercury cadmium telluride
MEMS	Micro-electromechanical systems
MOSFET	Metal-oxide-semiconductor field-effect transistor
MQW	Multi-quantum well
MSM	Metal-semiconductor-metal structure
MWIR	Mid-wave infrared
LED	Light-emitting diode
LiDAR	Laser detection And ranging
LMF	Laboratoire de microfabrication
LMN	Laboratoire de micro et nanostructure
LOD	Limit of detection
LWIR	Long-wave infrared
OPA	Optical phased array
OPO	Optical parametric oscillator
PAS	Positron annihilation lifetime spectroscopy
PAT	Photon-assisted tunneling
PCB	Printed circuit board
PDMS	Polydimethylsiloxane
PIC	Photonic integrated circuit
p-i-n	p-type/intrinsic/n-type semiconductor junction
PL	Photoluminescence
PMMA	Poly(methyl methacrylate)
PPLN	Periodically poled lithium niobate
QCL	Quantum cascade laser
QW	Quantum well
QWIP	Quantum well infrared photodetector
RC	Resistance-capacitance
RF	Radio frequency
RIE	Reactive ion etching
ROIC	Readout integrated circuit
SAE	Selective area epitaxy
SE	Secondary electrons
SEM	Scanning electron microscopy
SGC	Surface grating coupler
SiN	Silicon nitride
SiPSi	Silicon on porous silicon

SOI	Silicon on insulator
SON	Silicon on nitride
SOS	Silicon on sapphire
SPAD	Single-photon avalanche diode
SRH	Shockley-Read-Hall
SWIR	Short-wave infrared
TAT	Trap-assisted tunneling
T2SL	Type-II superlattice
TDD	Threading dislocation density
TDFA	Thulium-doped fiber amplifier
TDLAS	Tunable diode laser absorption spectroscopy
TE	Transverse electric
TEM	Transmission electron microscopy
TM	Transverse magnetic
TMAH	Tetramethylammonium hydroxide
TP	Transfer printing
TPA	Two-photon absorption
WGM	Whispering gallery mode
WGPD	Waveguide photodetector
XRD	X-ray diffraction

LIST OF APPENDICES

Appendix A Thin film processing techniques adapted for germanium-tin 180
Appendix B Uncertainty calculation on the optical power and photocurrent measurements 198

CHAPTER 1 INTRODUCTION

The digital infrastructure set in place over the past decades has led to numerous innovations in our everyday lives. It has resulted in vast amounts of data being generated and exchanged every second between multiple devices, particularly with the Internet of Things (IoT), cloud computing, and autonomous systems. In a report released a few years ago, Cisco projected significant growth in data traffic, estimating 5.7 billion Internet users and 29.3 billion connected devices by 2023, based on data from 2018 [1]. According to a recent forecast, it is expected that an additional 937 million users will join the global online population by 2028 to reach a total of 6.6 billion users in just 5 years [2]. As the growing interconnectivity between devices is increasingly essential to facilitate productivity, this rapid growth of data consumption and global data traffic comes with several bottlenecks. To meet this growing demand, novel solutions to enhance data processing must be implemented alongside the construction of new data centers. A major long-term challenge is the high energy consumption of electronic integrated circuits (EICs) that are densely packed in servers for signal processing. While these systems have enabled massive scalability, they now face fundamental physical limitations in speed, energy efficiency, and heat dissipation.

The considerable cumulative heat from copper interconnects in EICs and the increasingly packed processors in servers results in challenges in terms of thermal management, such as a higher energy consumption for cooling. Moreover, as the required bandwidth approaches the order of tens of Tb/s, the conventional electrical interconnects in printed circuit boards (PCBs) fall short in providing adequate line rates for inter-chip interconnects. Indeed, they are limited by a low bandwidth density coming from the relatively large input/output pads with a pitch typically around 100 μm, which leads to a required rate of 40 Gb/s per channel. However, this rate cannot be supported in this type of interconnect due to high transmission losses and reflections at connectors [3].

To tackle this bottleneck and achieve more sustainable growth in interconnectivity, optical chip-to-chip interconnects can be established. Optical links are supporting metro and long-haul networks and are gradually replacing electrical interconnects of increasingly shorter distances. This is motivated by the advantages of leveraging photons instead of electrons in data transmission, as they enable high-density and high-speed data processing with low power consumption, effectively addressing the aforementioned issues. To support this approach, optical components need to be monolithically integrated at the scale of EICs to establish functional optical circuits, ensuring that the incoming data in an optically modulated signal

is effectively converted to an electrical signal towards the processor and vice versa.

These compact optical systems are commonly known as photonic integrated circuits (PICs), where light propagates through optical waveguides with sub-micrometer cross-sectional dimensions that connect optoelectronic components designed at the chip scale. Since these circuits are typically fabricated on silicon (Si) substrates, the field dedicated to PIC development is known as *Si photonics* or *integrated photonics*. This field has gained momentum over the past few decades to address the increasing demands for energy efficiency, processing speed, and bandwidth in telecommunications and information technology [4]. PICs designed for communications can enable high-speed data transfers with a significantly lower energy consumption than electrical interconnects. Si benefits from advancements in microfabrication technologies developed for microelectronics over the last few decades, notably the *complementary metal-oxide-semiconductor* (CMOS) processes, which allow cost-effective PIC production at high throughput. This is paramount as the number of optoelectronic components, which can be costly at our scale, increases with the number of interconnects. Since only a handful of CMOS foundries dominate the global market, most companies working on PICs operate under a fabless model, relying on these foundries for manufacturing. Consequently, their designs must be CMOS-compatible to maintain a competitive cost advantage. While progress in the field has primarily focused on telecommunications, these scalable systems found use in multiple applications, ranging from environmental monitoring with on-chip gas sensors to integrated quantum optics.

While passive structures like low-loss waveguides and coupling interfaces for photonic chips are well-established, integrating efficient active optoelectronic devices remains a major challenge, with significant efforts devoted to developing them at telecom wavelengths, such as lasers and photodetectors. However, due to its indirect bandgap and energy gap of 1.12 eV, Si is inherently unsuitable for efficient active devices, particularly for optical signal detection above 1.1 μm and for light emission at telecommunication wavelengths. Although defect engineering has slightly extended Si's detection range, the improvement is insufficient for many applications [5]. Despite this, Si remains unsuitable for the development of light emitters that meet the standards of the telecommunications industry due to its indirect bandgap. To address this, multiple approaches have been explored for integrating light emitters. The integration of direct bandgap III–V compound semiconductors, which are based on gallium (Ga), arsenic (As), aluminum (Al), and phosphorus (P), is widely adopted but typically involves heterogeneous wafer bonding. The limited availability and high production costs of small-sized III–V wafers, along with their complex processing steps, significantly increase PIC costs.

1.1 Motivation

While the industry has mainly adopted the integration of III–V compounds, alternative approaches that leverage other Si-compatible compounds, such as germanium (Ge), have been explored to develop cost-effective active components suitable for monolithic integration. Ge also has an indirect bandgap with a gap energy of 0.67 eV, corresponding to a wavelength of about 1.6 μm. As a non-polar semiconductor compatible with Si, Ge has been widely adopted for monolithically integrated photodetectors covering telecommunication wavelengths from the O-band (1260–1360 nm) to the L-band (1565–1625 nm), and achieving bandwidths up to 265 GHz [6, 7]. Additionally, the energy difference in its band structure required for a direct bandgap transition is only 136 meV compared to 1.1 eV for Si, suggesting potential strategies to achieve a direct bandgap through the engineering of the band structure. To this end, high n-type doping and tensile strain in Ge have been investigated and demonstrated lasing via optical pumping, though they require large power thresholds [8, 9]. Another promising strategy is the incorporation of tin (Sn) into Ge to form germanium-tin ($Ge_{1-x}Sn_x$ or GeSn) alloys [10]. GeSn can be grown on Si, and its bandgap energy can be tuned based on Sn content and strain. Interestingly, it can achieve a direct bandgap when the alloy exceeds an Sn content ranging between 6 and 10 at.% (depending on the strain), generating considerable interest as a candidate for efficient light emission in Si photonics and a potential alternative to III–V compounds [11].

As the incorporation of Sn atoms leads to a decrease in the bandgap energy, this results in a redshift in the corresponding wavelength toward the mid-infrared region (2–8 μm). Recent prototypes of GeSn-based light emitters (lasers and light emitting diodes) and photodetectors demonstrated operation at wavelengths up to 4.6 μm using grown GeSn films [11–16]. This enables new opportunities in this wavelength range, where current technologies rely heavily on expensive III–V or II–VI (eg. mercury cadmium telluride) compound semiconductors and are associated with an important cost that restricts their broad use. GeSn's compatibility with Si wafers makes it a more scalable and cost-effective alternative for mid-infrared optoelectronics while supporting applications such as imaging and spectroscopic sensing.

Although lasing has been observed via optical [11] and electrical pumping [13], these demonstrations have typically been achieved below cryogenic temperatures to quench non-radiative mechanisms originating from numerous growth defects. Thus, GeSn alloys still require substantial improvements in their quality to enable electrically pumped lasing at room temperature. The progress in improving the alloy's quality is hindered by a few challenges, such as the low solubility of Sn in Ge at equilibrium which is below 1 at.%, meaning that higher Sn contents are not thermodynamically stable and can lead to phase separation. Growth

under metastable conditions is therefore employed, generally at low temperatures (<350 °C), which in turn limits the thermal stability and crystalline quality of the film. Moreover, there is a significant mismatch in the atomic radii between Sn and Ge (14.7%), resulting in the build-up of a compressive strain in the film when grown on a Si or Ge substrate. This accumulation of compressive strain not only inhibits the incorporation of Sn atoms [17], but also generates the nucleation of lattice defects, such as misfit and threading dislocations. The bandgap energy also undergoes a blueshift when the film is under compressive strain, thereby impacting device performance, including increasing the Sn content required to achieve a direct bandgap [18]. A Ge buffer layer is usually grown on Si before GeSn growth to reduce the impact of compressive strain, without completely suppressing it.

1.2 Problematic

Current efforts on GeSn generally focus on achieving room-temperature lasing, enhancing mid-infrared detection toward the formation of GeSn cameras, and improving the growth quality. These efforts also aim to better understand defect formation mechanisms and to develop strategies to overcome the material's inherent challenges. However, its integration with silicon photonics has remained limited, primarily due to challenges in growth compatibility and limited experimental validation beyond a few modeling results and prototypes. GeSn has strong potential as an active material for PICs operating in the mid-infrared, with applications in communications, spectroscopic sensing, and mid-infrared diagnostics for environmental and biomedical systems. A key application of GeSn alloys is the development of photodetectors for telecommunication bands with enhanced absorption, especially to enable complete L-band coverage. The bandgap tunability towards longer photodetection cutoff wavelengths also opens access to the emerging 2 μm band (1900–2100 nm), which is under consideration for future spectral channel expansion in optical communications [19]. Figure 1.1 illustrates the concept of an integrated GeSn photodetector coupled to a silicon-on-insulator (SOI) optical waveguide.

Practical implementation of GeSn coupled to low-loss waveguides in a PIC is limited by the lack of demonstrated selective area epitaxy (SAE) of GeSn on Si, which is the current method employed for monolithically integrating Ge detectors onto predefined photonic structures [6]. The few integration demonstrations of GeSn on a PIC involve flip-chip bonding with SOI structures [20] and top-down etching of GeSn/Ge multi-quantum wells (MQWs) grown on a Si substrate to form monolithically integrated devices coupled to germanium-on-silicon waveguides (GOS) [21]. While these approaches sound promising, they suffer from either high coupling loss between the passive structures and the die containing the photodetector

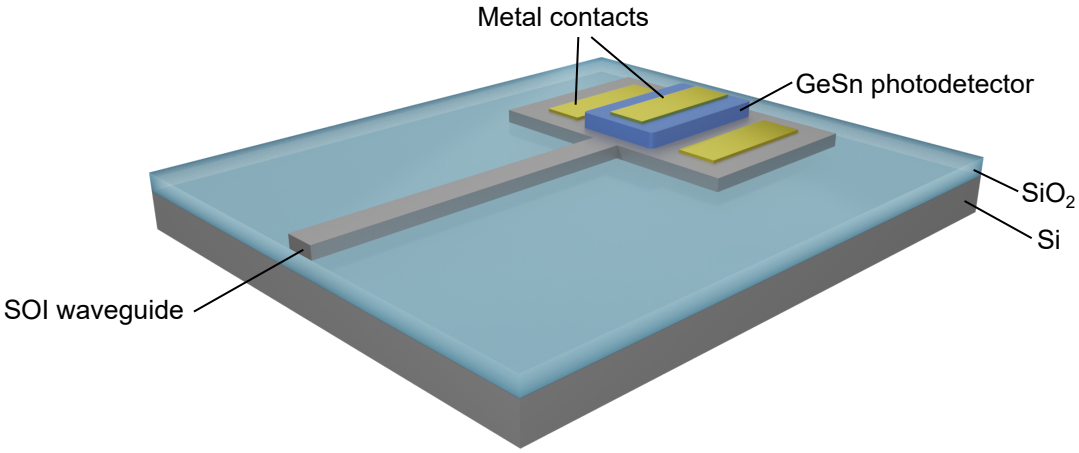


Figure 1.1 Illustration of an integrated GeSn photodetector coupled to an SOI waveguide.

for the former or high propagation loss in waveguides combined with defective interfaces for the latter. Like Ge, monolithic integration of GeSn is expected to lead to a defective interface, which can affect the performance in both light emitters and detectors.

Given these limitations, alternative integration strategies that circumvent growth-related constraints, such as strain engineering and layer transfer, are being investigated. This opens an opportunity for exploring heterogeneous integration using GeSn, particularly using approaches that are scalable and compatible with CMOS fabrication environments. This could involve techniques based on strain engineering and layer transfer of GeSn on more adequate substrates, such as GeSn-on-insulator (GeSnOI) [22,23]. In the work led by Dr. Mahmoud R. M. Atalla, the release of the GeSn layer, achieved by selectively underetching an underlying Ge buffer layer, has been explored for the formation of what we call GeSn membranes [14]. These consist of detached GeSn layers that can be transferred onto alternative substrates using transfer printing, providing a pathway for integrating GeSn onto non-epitaxial platforms where direct growth is challenging. These structures undergo a relaxation of the compressive strain that built up during growth, which has an impact on the band structure and the electrical and optical properties of the material. This resulted in a drastic increase in the photodetection cutoff wavelength from 3.5 to $\sim$4.6 μm in photodetectors based on $Ge_{0.83}Sn_{0.17}$ membranes compared to detectors made using the unreleased film. The strain relaxation in GeSn membranes combined with their ability to be transferred onto various substrates make them an interesting option for the heterogeneous integration of the material for silicon photonics, especially for substrates on which epitaxy is challenging. However, although GeSn membranes show promising properties, initial devices have shown that they suffer from mechanical challenges such as a large structural bowing that hinders their adhesion after transfer

printing and ultimately restricts the fabrication yield of devices based on them. These issues need to be addressed to establish these structures as a viable option for their scalable integration.

Moreover, as the reported modeling studies are essentially based on a monolithic integration scheme [24–26], the efficiency of a potential integration scheme involving these membranes would need to be assessed and compared to other methods through an in-depth numerical analysis before performing a proof of concept. The successful development and implementation of a solution for efficiently integrating GeSn into silicon photonics could enable the rapid prototyping of GeSn-based active devices and demonstrate their practicality in real-world applications, which could potentially serve as a robust alternative to III–V components as the alloy is Si-compatible. The successful integration of GeSn into silicon photonics could establish a scalable, CMOS-compatible platform for mid-infrared photonics, accelerating advancements in spectroscopy, sensing, and high-speed optical communication.

1.3 Objectives

This thesis is motivated by the need to unlock the full potential of GeSn alloys for Si photonics, which could enable new functionalities in mid-infrared photonic integrated circuits. It aims to overcome the limitations of monolithic integration by investigating innovative approaches such as heterogeneous integration of the material through GeSn membranes. Within the scope of this thesis, we primarily aim to explore strategies for integrating GeSn onto silicon photonics while considering GeSn membranes as a candidate material for this integration. The specific challenges related to the integration of membranes are first addressed to reliably employ them in the heterogeneous integration of the material into a PIC. This is followed by an investigation of possible integration scenarios that consider different photonic platforms and integration approaches, which is carried out through numerical simulations. We then aim to provide an experimental demonstration of the integration of GeSn membranes as an active material in a PIC and that can operate in the mid-infrared region. To systematically address these challenges, this research is structured around the following specific objectives:

- **Objective 1:** Optimize the fabrication of GeSn membranes to enhance their scalability, reliability, and integration efficiency.
- **Objective 2:** Perform an in-depth analysis of the different integration techniques for incorporating GeSn into Si photonics to evaluate the potential of heterogeneously integrated GeSn membranes.

- **Objective 3:** Provide a proof-of-concept demonstration of the integration of GeSn membranes with Si photonics.

1.4 Organisation of the thesis

This chapter serves as the introduction to the thesis. The structure of the remaining chapters is outlined below:

Chapter 2 provides a literature review of key topics relevant to the objectives of this thesis. It begins with a brief review of the state-of-the-art in silicon photonics, followed by a description of the GeSn material system, highlighting its development, properties, current challenges, and demonstrated applications. This includes an overview of the current effort made in integrating GeSn with silicon photonics. A survey of applications and technologies related to the mid-infrared region is also presented.

Chapter 3 describes the methodology employed in this research, encompassing techniques used for the growth of GeSn alloys and the characterization of devices. Fabrication techniques are briefly described, with additional information provided in the appendices.

Chapter 4 details the work carried out to improve the fabrication and integration of GeSn membranes to fulfill the first objective. A method to transfer-print multiple $Ge_{0.89}Sn_{0.11}$ membranes at once is presented, including the use of exfoliated contacts. The work in this chapter has been published as a paper in the *IEEE Journal of Selected Topics in Quantum Electronics*.

Chapter 5 explores the different options for integrating GeSn as an active material onto a photonic platform through numerical simulations. An in-depth investigation of the coupling efficiency of different integration scenarios is conducted to meet the second objective.

Chapter 6 presents a proof-of-concept demonstration of GeSn integration with Si photonics using transfer-printed $Ge_{0.89}Sn_{0.11}$ membranes atop SOI waveguides to complete the third objective. Multiple devices are fabricated in a single transfer printing step, and characterization is performed at a wavelength of 2.33 μm.

Chapter 7 presents a general discussion on various aspects of the work presented in this thesis, including its limitations.

Chapter 8 concludes the thesis with a brief summary of the work and future research directions.

CHAPTER 2 LITERATURE REVIEW

This chapter provides an overview of the three main topics covered in this thesis. We first summarize the state-of-the-art in silicon photonics, including its current challenges and potential solutions. Next follows a detailed review of germanium-tin ($Ge_{1-x}Sn_x$ or GeSn), focusing on its properties, progress in device demonstrations, and challenges. This includes a brief overview of the efforts to study GeSn alloys for integrated photonics. Finally, since GeSn's bandgap energy corresponds to wavelengths in the mid-infrared region, we examine key applications and current technologies related to this region to evaluate the potential and utility of GeSn devices.

2.1 Current landscape of silicon photonics

Si photonics has garnered significant interest for enabling photonic integrated circuits (PICs) in diverse applications, ranging from optical data communication to chemical and biomedical sensing [4,27]. The origins of the field can be traced back to 1969, when S. E. Miller from Bell Labs introduced the concept of integrated optics with a vision of fabricating optical circuits in a manner similar to microelectronics [28]. The field gained compelling attention in 1985 after R. A. Soref and J. P. Lorenzo proposed using silicon as a medium for integrated optics in the 1.3–1.6 μm range by patterning channel waveguides [29]. The adoption of *complementary metal-oxide-semiconductor* (CMOS) processing techniques, along with the use of the existing microelectronics infrastructure, enabled high-volume, low-cost production of PICs on silicon-on-insulator (SOI) wafers. This platform offers several advantages, including the high transparency of Si and SiO_2 in the near-infrared at telecom wavelengths and a large refractive index contrast ($\Delta n \sim 2$). These properties allow for high light confinement and low propagation losses, which are crucial for processing sensitive optical signals.

The vision of co-integrating optical and electronic components on a single chip holds the promise of substantial improvements in size, cost, and power efficiency, while simultaneously increasing processing speeds, particularly for high-bandwidth telecommunications. Research advancements in this field have largely been driven by the needs of telecommunications, especially around the 1.3 μm and 1.5 μm wavelength bands. Figure 2.1 illustrates various components of a PIC integrated with an electronic circuit through 3D integration.

Light is coupled into silicon photonic chips using edge couplers or surface grating couplers, with specialized fiber components often required for simultaneous multi-port operation. To

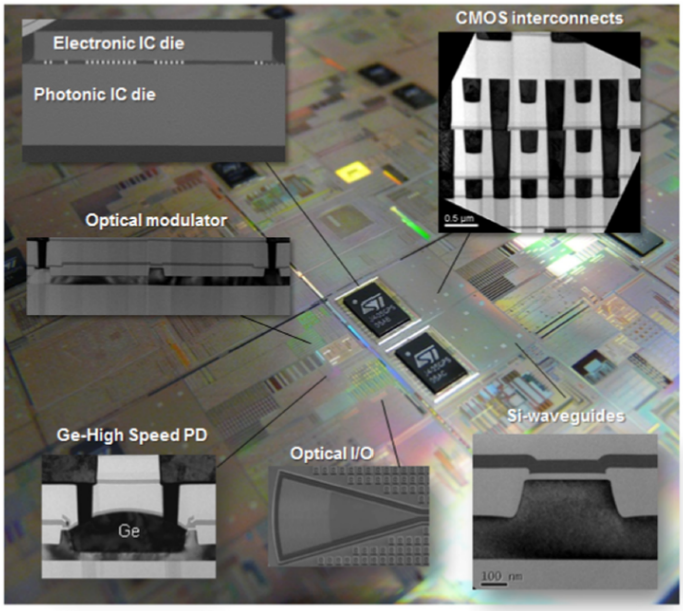


Figure 2.1 Overview of the different components in a photonic integrated circuit (PIC) combined with an electronic integrated circuit using 3D integration, as developed by STMicroelectronics. Reproduced with permission from [4].

convert light into an electric signal and vice versa, or to process the encoded information, active components such as detectors, modulators, and lasers are essential. These active components must meet specific performance criteria, including sufficient output power for light emitters and high responsivity combined with a broad spectral range for photodetectors. Silicon detectors cannot cover telecom wavelengths due to Si's bandgap energy of 1.12 eV, which corresponds to a photodetection cutoff wavelength of approximately 1.1 μm. Additionally, silicon has an indirect bandgap, making it a highly inefficient light emitter because it relies on a phonon-assisted process. Therefore, other active materials must be considered to achieve high performance.

To enable seamless co-integration of photonics and electronics, integration must be achieved using CMOS-compatible processes. Germanium (Ge), another group-IV element, has been gradually adopted by the industry due to its compatibility with Si. Ge can be used to form integrated photodetectors due to its bandgap of 0.67 eV at room temperature, which provides good responsivity at an operational wavelength of 1.55 μm [6]. Germanium-based photodetectors can achieve 3-dB bandwidths up to 265 GHz, significantly outperforming state-of-the-art indium phosphide (InP)-based photodetectors [7]. While the heteroepitaxial growth of Ge is a promising approach for detection at telecom wavelengths, it introduces challenges such as defective interfaces, which generate high dark currents, and non-uniform growth across

the wafer. These issues, combined with the limited capability of some foundries to achieve this growth and the associated costs, restrict the widespread adoption of this technology. To address these limitations, all-silicon devices are being developed to further reduce chip fabrication costs by exploiting sub-bandgap absorption mechanisms such as defect-based absorption [30] and photon-assisted tunneling (PAT) [31]. Recently, Peng *et al.* demonstrated an all-silicon eight-channel receiver based on PAT, achieving a data transmission rate of 160 Gb/s per channel, culminating in a total aggregated data rate of 1.28 Tb/s [32].

Since Ge, like Si, has an indirect bandgap that limits its efficiency as a light emitter, alternative materials with direct bandgap properties are required. While efforts have been made to develop lasers based on germanium [9, 33], their efficiency remains insufficient for practical applications. Consequently, the focus has shifted towards materials already known for their efficient light-emitting properties within this range, such as III–V compounds or other gain media that are either optically or electrically pumped [34]. The integration of III–V materials into Si photonics has been extensively investigated, as these materials were already used in the fabrication of laser diodes and photodetectors operating in the near-infrared.

III–V compound semiconductors, which are typically grown on gallium arsenide (GaAs) and indium phosphide (InP) wafers, are more suitable candidates for the formation of light emitters as their alloys provide a direct bandgap emission with tunable emission or photodetection wavelengths. While these materials benefit from decades of material engineering leading to efficient light emission in lasers and high detectivities in detectors, their manufacturing cost is high, and the available wafer sizes are small. This high cost is due to complex fabrication steps, expensive raw materials, and the limited scalability of III–V wafer production. A complete monolithic integration of photonic components is achievable on a III–V platform with GaAs or InP substrates [35]. However, the component density is lower than what can be achieved on an SOI platform due to the reduced refractive index contrast between the core and cladding layers ($\Delta n \sim 0.3$). Additionally, the yield is limited by multiple regrowth steps and small wafer sizes [36].

Epitaxy of III–V materials on Si faces several challenges, including significant lattice mismatch, large differences in thermal expansion coefficients, and the formation of anti-phase domains due to polarity mismatches [37]. These factors lead to high defect densities at the interfaces, reducing laser efficiency through non-radiative recombination. Alternatively, III–V lasers cut into dies can be coupled externally to the silicon chip using flip-chip integration [38], or the III–V material can be heterogeneously bonded onto the SOI chip before a subsequent patterning of the material to define the active components locally [39]. Both approaches are labeled as heterogeneous integration and can vary in terms of fabrication complexity and

integration costs. Fang *et al.* demonstrated the first III–V/SOI laser, where a waveguide couples evanescently into a bonded III–V quantum well used as the gain medium [40]. Heterogeneously integrated III–V lasers using a back-end-of-line (BEOL) integration approach are now commercially available and have become widely adopted by various companies.

For optical communication links, integrated optical modulators are required. High-speed modulation in integrated photonics is typically achieved by exploiting the electro-optic effect in designs based on p-n Si junctions [41] or hybrid Si/lithium niobate ($LiNbO_3$) systems [42], where modulation rates exceeding 100 Gb/s can be achieved. With this broad library of components, complex optical systems can be designed to meet the requirements of various applications while maintaining a high degree of compactness [43]. Netherton *et al.* recently developed a transceiver architecture for short-reach interconnects that enables a data transmission rate of 1 Tb/s per PIC while achieving low power consumption below 0.4 pJ/bit [44]. In addition to telecommunications, Si photonics has applications in diverse fields [45], such as sensing, where photonic components detect environmental changes and provide expanded functionality in biosensing and environmental monitoring. The interaction between waveguides and the medium under investigation enables the detection of variations in light intensity or shifts in optical resonance, allowing for precise measurements. For example, absorption spectroscopy in the infrared near telecom wavelengths can achieve detection limits below 100 ppm [46].

The integration of various materials onto silicon photonic chips is being explored to enhance the properties of these systems [47]. Other materials such silicon nitride (SiN) are also investigated for forming ultra-low-loss passive waveguides as a propagation loss below 0.06 dB/cm can be achieved compared to SOI waveguides yielding a loss typically around 2 and 3 dB/cm. The current fabrication ecosystem for Si photonics comprises various foundries, ranging from large industrial fabs like GlobalFoundries, AMF, and TSMC to prototyping services like Cornerstone and Applied Nanotools Inc [48]. To reduce fabrication costs, designs from multiple clients, including academic labs and startups, are aggregated and processed on multi-project wafers (MPWs) at these foundries.

2.2 Silicon-compatible optoelectronic devices based on germanium-tin alloys

The quest for a direct-bandgap and Si-compatible material for light emitters led to the investigation of non-conventional alloys, such as the $Ge_{1-x}Sn_x$ alloy whose growth is challenging due to thermodynamic constraints. The interest in the $Ge_{1-x}Sn_x$ binary system emerged when C. H. L. Goodman first proposed that a solid Sn–Ge alloy could exhibit desirable properties, such as a direct bandgap, high mobilities, and the absence of polar scattering

typically present in III–V and II–VI compounds [49]. This potential motivated decades of research into stabilizing GeSn solid solutions and growing high-quality layers, initially pursued through magnetron sputtering (MS) and molecular beam epitaxy (MBE) [50].

Despite this progress, the transition to a direct bandgap remained speculative for many years. The low solubility of Sn in Ge led to various strategies to prevent phase separation, such as low-temperature growth to incorporate higher Sn concentrations. Decades passed before films could be successfully grown using chemical vapor deposition (CVD) with commercially available gases as precursors [51]. Advances in CVD and MBE epitaxy led to the fabrication of metastable GeSn compositions [10], accompanied by several device demonstrations. To date, research continues to enhance device performance, alongside continued investigations into the material properties to further improve quality.

This section provides an overview of the properties of GeSn alloys and progress in device fabrication, followed by a discussion of the challenges limiting further progress.

2.2.1 Material properties and band structure

To better understand the origin of this interest, we examine the properties of the materials involved and analyze their electronic band structures, including Si, Ge, and Sn. Sn possesses a cubic diamond lattice in its α phase (α-Sn), also referred to as *grey tin*, which behaves as a semi-metal whose its conduction band minimum lies below its valence band maximum. While this phase is compatible with the crystalline structures of Si and Ge, it becomes unstable above 13.2 °C. At higher temperatures, phase separation into its β phase (β-Sn or *white tin*) occurs. The β phase behaves as a metal and exhibits a body-centered tetragonal lattice. We will focus on the properties of α-Sn as its diamond cubic crystal structure is compatible with that of Ge and Si. Table 2.1 summarizes key properties of Si, Ge, and α-Sn, such as the bandgap energies at different points in the Brillouin zone (E_i), cubic lattice constants (a_0), and elastic constants (C_{ij}). Figure 2.2 illustrates their band structures along specific points in the Brillouin zone.

To understand how Sn incorporation modifies Ge's electronic properties, we predict the band structure of GeSn alloys based on the known properties of Ge and Sn. Alloying Sn with Ge results in a change in the bandgap, which can be expressed as [54]:

$$E_i^{GeSn}(x) = E_i^{Ge}(1-x) + E_i^{Sn}x + b_{E,i}^{GeSn}x(1-x) \tag{2.1}$$

where E is the bandgap energy at a given crystal orientation, and $b_{E,i}$ is the bowing parameter used to correct the linear interpolation along the crystalline orientation i, such as Γ, X, and L.

Table 2.1 Parameters for Si, Ge, and α-Sn such as the bandgap energies E_i at 0 K, the cubic lattice constants a_0, and the elastic constants C_{ij}. Values taken from [52].

Parameter	Si	Ge	α-Sn
E_Γ (eV)	3.3	0.892	-0.408
E_L (eV)	2	0.744	0.12
E_X (eV)	1.2	0.901	0.910
a_0 (Å)	5.43	5.65	6.49
C_{11} (GPa)	166	129	69
C_{12} (GPa)	64	48	29
C_{44} (GPa)	80	68	36

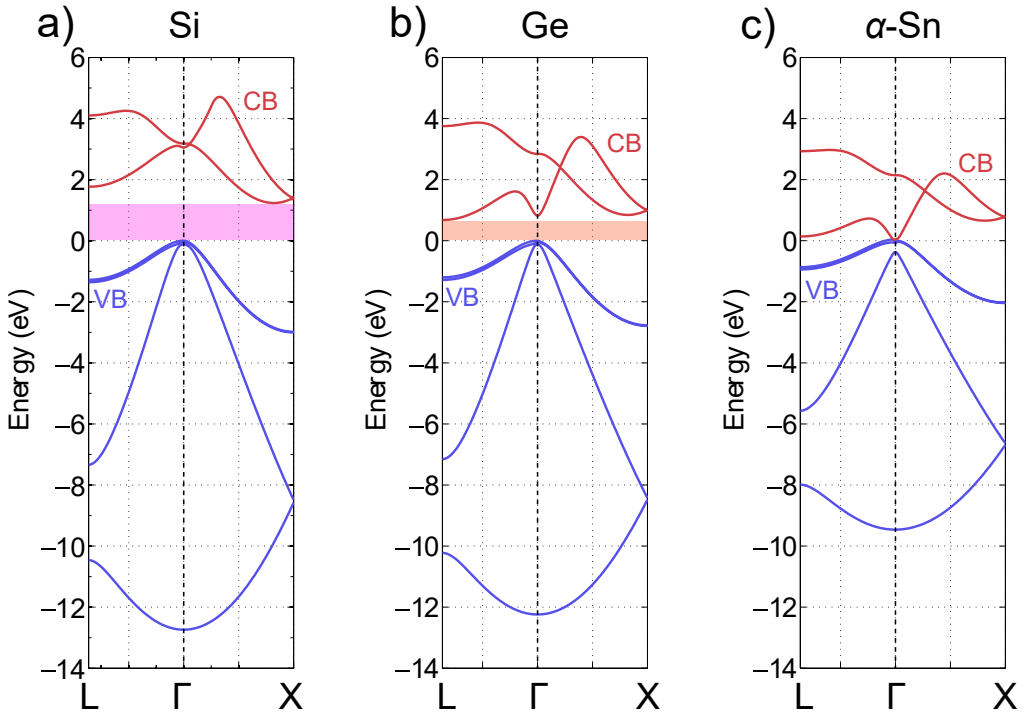


Figure 2.2 Electronic band structure of (a) Si, (b) Ge, and (c) α-Sn (adapted from [53]). The conduction (CB) and valence (VB) bands are identified in red and blue respectively.

We focus on the Γ and L points, as the indirect bandgap in Ge is determined by these two points, where the interband energy difference is the lowest. Since the bandgap of α-Sn is negative at the Γ point, the incorporation of Sn leads to a faster bandgap reduction at the Γ point than at the L point. Figure 2.3 illustrates the band structure of GeSn for selected Sn contents, highlighting the more pronounced decrease in the bandgap energy at the Γ point compared to the L point, which leads to a transition from an indirect to a direct bandgap.

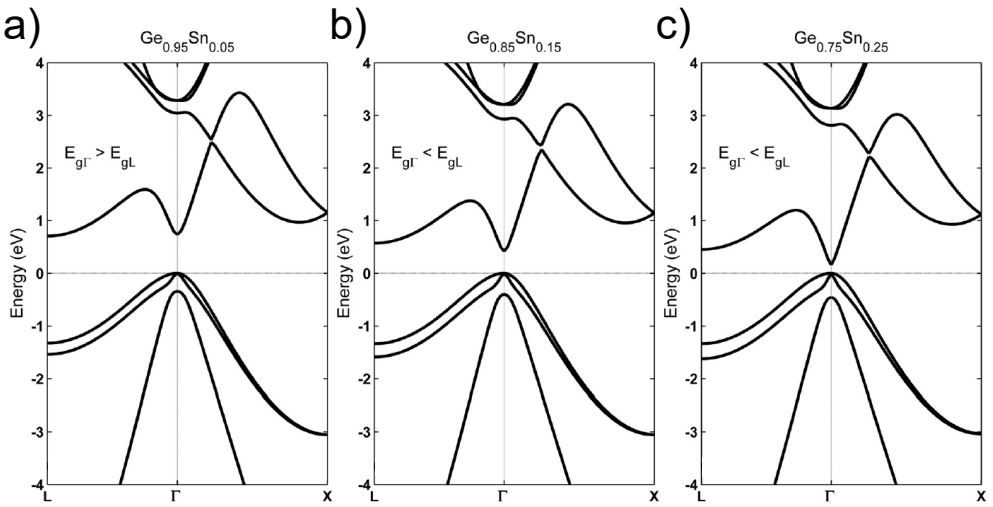


Figure 2.3 Electronic band structure of GeSn alloys with Sn contents of (a) 5 at.%, (b) 15 at.%, and (c) 25 at.% to highlight the bandgap transition from indirect to direct along the Γ point. Adapted from [55].

This progressive transition toward a direct bandgap indicates a threshold Sn content for the transition from an indirect to a direct bandgap. The bandgap energies at different points can be computed to determine the crossover concentration when the energy at the Γ point becomes smaller than that at the L point. Using an 8-band $k{\cdot}p$ model (details can be found in Section 3.5), these energies were computed and are plotted in Fig. 2.4. According to these calculations, the crossover occurs at a content of 7 at.% Sn. This value varies between 6–10 at.% Sn in literature as different values for the bowing parameters are used [56]. By systematically investigating optically pumped emission from Fabry-Perot cavities, Wirths *et al.* observed this transition to occur at a content of ∼9 at.% Sn [11]. Bandgap directness, defined as the energy difference between the L and Γ points, determines whether a material favors radiative recombination, which is essential for efficient light emission. A positive directness value indicates that electrons preferentially occupy the Γ-valley, enhancing optical transitions. A higher directness, achieved here by increasing the Sn content, enhances the probability of radiative recombination. Temperature must also be considered in these

calculations, as it can affect the density of states (DOS).

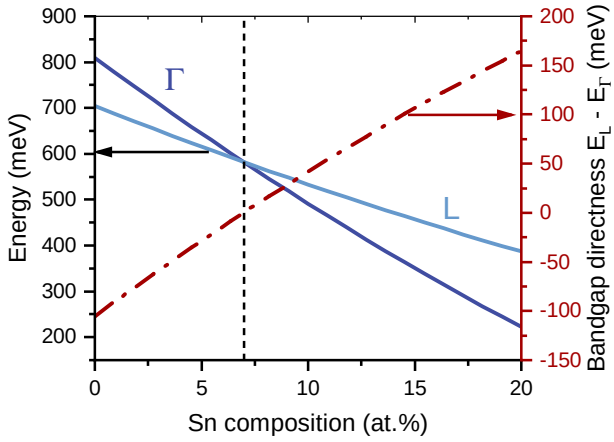


Figure 2.4 Transition from an indirect to a direct bandgap in GeSn alloys as a function of Sn content, along with the bandgap directness. The energies were computed using an 8-band $k{\cdot}p$ model for unstrained material. The crossover from an indirect to a direct bandgap occurs at a content of approximately 7 at.% Sn.

The lattice constant a^{GeSn} of the alloy can be expressed using a bowing parameter b_a^{GeSn} for correction:

$$a_0^{\mathrm{GeSn}} = a_0^{\mathrm{Ge}}(1-x) + a_0^{\mathrm{Sn}}x + b_a^{\mathrm{GeSn}}x(1-x) \tag{2.2}$$

Figure 2.5 shows the bandgap energy of GeSn as a function of the lattice parameter, compared to III–V and II–VI compounds. Relatively low bandgap energies can be achieved by alloying Ge with Sn. For instance, a value below 0.2 eV can be obtained when the Sn content exceeds 20 at.%, making it comparable to indium antimonide (InSb), which is the III–V material with the lowest bandgap energy. II–VI materials can also achieve low bandgap values, but their synthesis and processing are challenging, even though they have been the workhorse of mid-infrared detectors for decades. The wide tunability of GeSn is particularly attractive for the development of novel mid-infrared detectors based on group-IV materials, as it enables cost-effective growth on Si wafers. An overview of different technologies for mid-infrared detection is provided in Section 2.3.2.

While this wide bandgap tunability is promising, α-Sn has a lattice parameter of about 6.493 Å, approximately 19% larger than Ge's lattice constant of 5.658 Å. As Sn atoms are incorporated into the Ge lattice, the mismatch in the atomic radii generates strain, impacting the band structure by modifying the electronic properties, such as shifting the energy levels

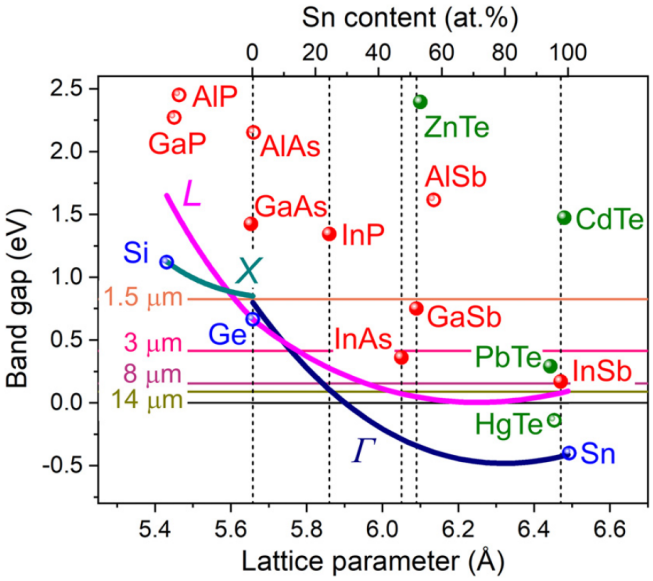


Figure 2.5 Bandgap energy of GeSn (blue) with III–V (red) and II–VI (green) compounds as a function of lattice parameter with the respective Sn content. The calculated curves were computed using an 8-band $k \cdot p$ model. Reproduced from [10].

and altering the bandgap type. Gupta *et al.* used a theoretical model based on the nonlocal empirical pseudopotential method to investigate the impact of biaxial strain on the bandgap energy [55]. Figure 2.6 shows contour plots of the bandgap energy (Fig. 2.6(a)) and the energy difference between the minima of the conduction bands at the L (E_{C_L}) and Γ (E_{C_Γ}) points (Fig. 2.6(b)) as a function of in-plane biaxial strain and Sn content. For a relaxed layer (0% in-plane strain), the transition from indirect to direct occurs at a content of roughly 6.5 at.% Sn. However, typical growth methods, such as chemical vapor deposition (CVD), generally lead to a compressively strained layer due to differences in thermal expansion and lattice mismatch, requiring a higher Sn content to achieve a direct bandgap. Conversely, applying tensile strain to the layer reduces the need for high Sn contents to obtain a direct bandgap. This suggests that strain engineering could be key to enhancing light emission efficiency in GeSn-based optoelectronic devices. A direct bandgap correlates with higher radiative recombination efficiency, which is crucial for improving the efficiency of light-emitting devices such as light emitting diodes (LEDs) and lasers. By increasing bandgap directness, the material can emit light more efficiently, improving device performance.

The lattice constant of GeSn can be determined using the following equation:

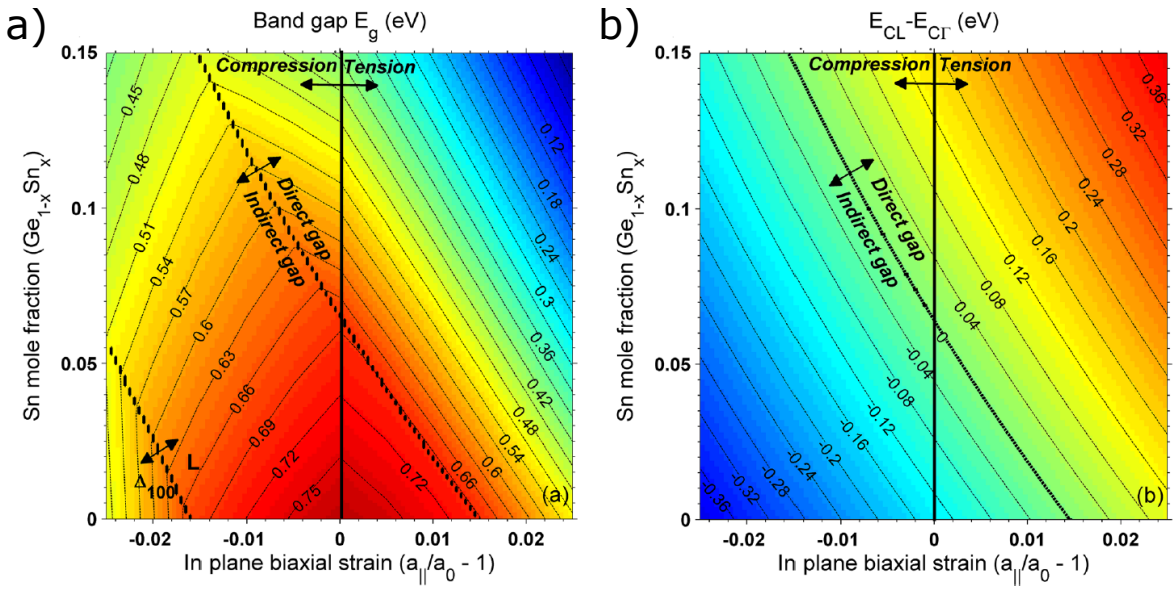


Figure 2.6 Transition from an indirect to a direct bandgap in GeSn alloys as a function of Sn content and in-plane biaxial strain. Contour plots showing (a) the bandgap energy and (b) the energy difference between the conduction band minima at the L point (E_{C_L}) and the Γ point (E_{C_Γ}). Adapted from [55].

$$a_0^{\mathrm{GeSn}} = \frac{a_\perp^{\mathrm{GeSn}} + 2a_\parallel^{\mathrm{GeSn}} C_{12}/C_{11}}{1 + 2C_{12}/C_{11}} \tag{2.3}$$

where $a_\perp$ and $a_\parallel$ are the lattice constants in the perpendicular and parallel directions, respectively. The biaxial strain, $\epsilon_\parallel$, can be estimated using:

$$\epsilon_\parallel = \frac{a_\parallel^{\mathrm{GeSn}} - a_0^{\mathrm{GeSn}}}{a_0^{\mathrm{GeSn}}} \tag{2.4}$$

which is negative when $a_\parallel^{\mathrm{GeSn}}$ is smaller than a_0^{GeSn}, resulting in compressive strain.

While this thesis focuses on the binary GeSn system, ternary silicon-germanium-tin (SiGeSn) alloys are also being investigated, as they could allow independent control of strain and bandgap energy, offering greater flexibility in the material's properties [57]. However, the growth kinetics remain challenging, and their properties are still speculative due to missing parameters, such as the bowing parameter between Si and Sn. The incorporation of Si is expected to increase the bandgap at the Γ-point more significantly than at the L-point, implying that the transition to a direct bandgap would occur at a higher Sn content. Challenges related to this ternary will be briefly addressed in Section 2.2.3.

2.2.2 Current state of the art in device demonstrations

Following breakthroughs in alloy growth, device demonstrations rapidly emerged, particularly in optoelectronic applications to highlight its potential [10, 58]. Various types of devices have been developed for specific applications, including LEDs, lasers, photodetectors, and modulators. Due to the reduction in bandgap energy as Sn is incorporated into the Ge lattice, the wavelengths corresponding to these energies lie in the mid-infrared region. While this is less convenient for telecom applications, it enables new opportunities through Si-compatible growth, which will be discussed in Section 2.3. This section provides an overview of the current performance of these devices. The development of GeSn optoelectronic devices has been inspired by their III–V counterparts, which serve as benchmarks due to their high efficiency, material stability, and long-standing commercial adoption in optoelectronics.

Light emitters and lasers

The interest in GeSn alloys first arose with the development of LEDs and lasers as potential Si-compatible light sources. After the first observation of photoluminescence in GeSn [59], prototypes of LEDs were demonstrated [12, 60, 61], and lasing has been observed through optical [11, 62–65] and electrical pumping [13, 16, 66, 67]. Figure 2.7 shows an overview of the different structures developed in these categories of light emitters. The first demonstration of lasing through optical pumping was reported by Wirths *et al.* in 2015 using GeSn waveguides forming Fabry-Perot cavities, where emission at 2.3 μm could be observed in a sample with 12.6 at.% Sn up to a temperature of 90 K and a lasing threshold of 325 kW cm^{-2} (at 20 K) [11]. However, a low external quantum efficiency (estimated at 1.5%) and a reduced carrier lifetime (350 ps at 300 K) were observed and most likely originated from trap-assisted recombination centers along other mechanisms. Since then, significant efforts have been made to improve the lasing performance, primarily by lowering lasing thresholds, reducing cavity losses, and increasing operating temperatures.

Lower lasing thresholds have mainly been obtained by investigating partially underetched microdisk resonators to form the laser cavity, where Stange *et al.* managed to observe lasing at 125 kW cm^{-2} and 220 kW cm^{-2} (at 50 K) in GeSn microdisks with contents of 8.5 and 12.5 at.% Sn respectively [62]. As these structures are partially underetched to confine whispering gallery modes (WGMs), they also benefit from a localized relaxation of compressive strain. To enhance carrier confinement in the active region, a design based on multi-quantum wells (MQWs) can be employed. However, these suffer from reduced band offsets, limiting their effectiveness at elevated temperatures [69]. For proper carrier confinement at room temperature within the active layer, the band offset needs to be greater

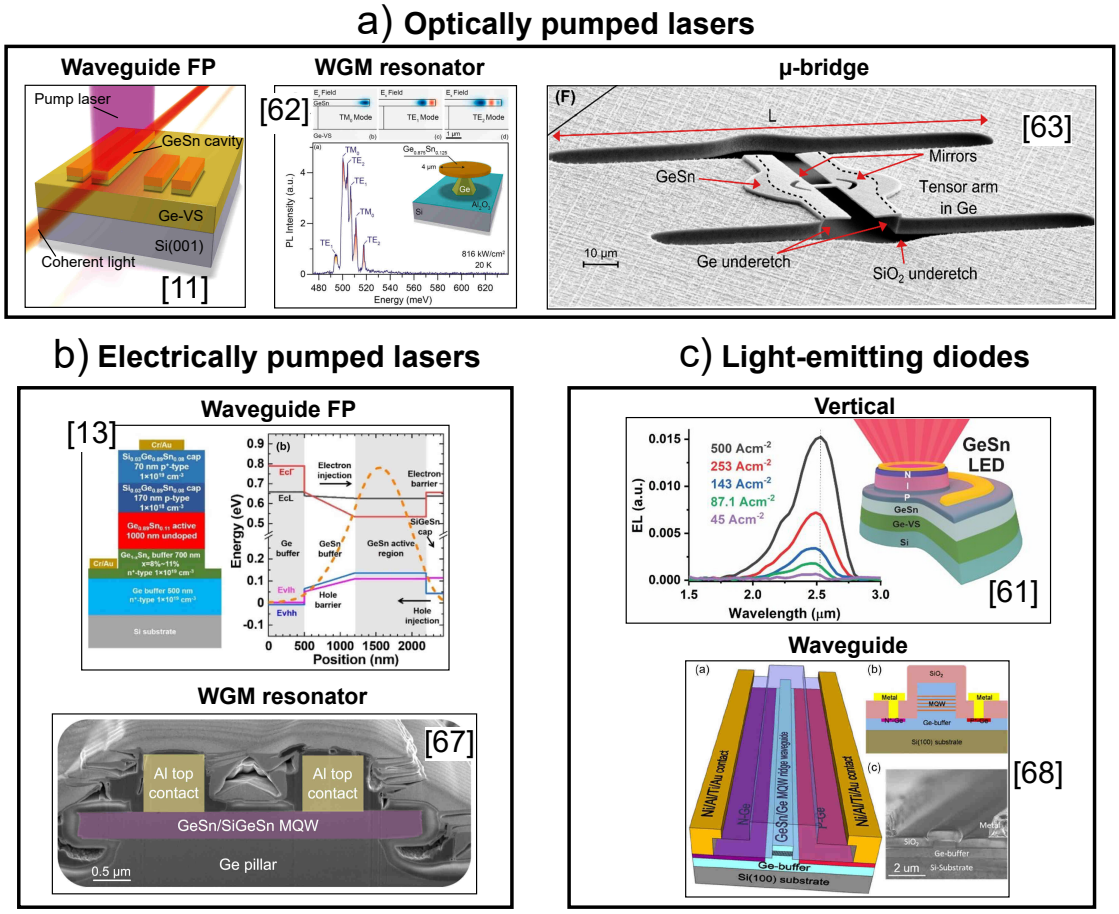


Figure 2.7 Overview of the different structures used in the demonstrations of GeSn (a) optically pumped lasers [11, 62, 63], (b) electrically pumped lasers [13, 67], and (c) light-emitting diodes [61, 68].

than $2k_BT$, which translates to roughly 52 meV at 300 K. SiGeSn alloys are also studied as the Si concentration adds another parameter to tune both the bandgap and the strain, which can produce barriers with a large band offset. SiGeSn barriers were introduced in MQWs in microdisk resonators by Stange *et al.*, where a lasing threshold of 40 kW cm^{-2} was obtained at $T = 20$ K [70], with lasing being observed up to 120 K.

With Sn contents close to the transition from an indirect to a direct bandgap, carriers occupy states in both the Γ and L valleys. Transitions involving the latter lead to inefficient emission as a phonon is required, thus limiting lasing to low temperatures when fewer carriers occupy states in the L valley. Higher Sn contents generally lead to higher operating temperatures as the bandgap directness increases, but this comes at the cost of an increased lasing threshold due to lower-quality layers and a higher concentration of point defects in the film, as growth must be carried out at lower temperatures [71]. This motivated the use of strain and defect engineering. Elbaz *et al.* demonstrated lasing in $Ge_{0.946}Sn_{0.054}$ microdisks with record-low lasing thresholds of 0.8–1.1 kW cm^{-2} [64]. This threshold range is at least one order of magnitude lower than the other reported thresholds in other GeSn structures and is similar to that of heterogeneously integrated III–V lasers on Si operating at room temperature. To achieve this, a tensile strain of 1.4% was applied to the microdisks by encapsulating them with a silicon nitride (SiN) stressor layer, enabling a transition to a direct bandgap at lower Sn contents. They also demonstrated continuous-wave lasing in the same microdisk cavities, whereas previous demonstrations were carried out under pulsed operation. Tensile strain can also be applied uniaxially in suspended GeSn microbridges, where Chrétien *et al.* showed wide tunability in the lasing emission wavelength up to 4.6 μm and operation temperature up to 273 K [63]. A few demonstrations of room-temperature lasing using optical pumping were achieved in 2022 through a combination of high Sn content (17 at.%) and GeSn layer transfer via wafer bonding to metallic interlayers to improve heat dissipation [65, 72]. A similar approach using tensile strain with an "all-around" SiN stressor layer was also employed on $Ge_{0.86}Sn_{0.14}$ microdisks with 14 at.% Sn to demonstrate lasing at room temperature [73]. While this approach is not monolithic, the GeSn layer transfer technique offers a direct method to mitigate the defective GeSn/Ge interface by simply removing it, as it can be a major source of non-radiative recombination centers.

In parallel, efforts to achieve electrically pumped lasing have been pursued, as this scheme is essential for practical integration into Si photonics. However, achieving lasing through electrical pumping is more challenging due to numerous factors, such as non-radiative channels enabled by defects that contribute to leakage current and the presence of metals that can contribute to optical losses. Zhou *et al.* demonstrated electrical pumping in 2020 with emission at 2.3 μm and lasing observed up to 100 K in Fabry-Perot waveguide cavities [13].

In these structures, an optical peak power of 2.7 mW/facet and an external quantum efficiency of 0.3% was achieved, with a recorded threshold of 598 $\mathrm{A\,cm^{-2}}$ at 10 K. Since then, only a few iterations have been carried out to improve the performance, with recently a laser operating up to 140 K at a wavelength of 2.7 μm [66]. Measurements were carried out at high hydrostatic pressure on electrically pumped SiGeSn/GeSn lasers by Ellis *et al.* to further understand the limiting mechanisms in these devices [74]. They determined that defect-related recombination is responsible for roughly 93% of the threshold current in their devices at a temperature of 85 K. They also observed that carrier leakage due to occupation of L-valley states contributed increasingly to the threshold current as the bandgap directness decreased. While the performance is still not on par with III–V lasers, progress is ongoing to achieve lower lasing thresholds and room-temperature lasing. Other geometries of electrically pumped lasers have recently been investigated, such as microring [75, 76] and microdisk resonators [67], with the latter showing continuous-wave emission.

LEDs are typically less efficient with a broad emission range compared to lasers, but can operate at room temperature as they are essentially based on the electroluminescence of the material. A few demonstrations have been carried out with peak wavelengths up to 3.3 μm [12, 60, 61, 77–79]. They have been used in applications such as gas sensing [78]. While their performance appears promising, they suffer from similar limitations as lasers, such as trap defects, which impact their quantum efficiency. An LED with a ridge waveguide and a horizontal p-i-n (p-type/intrinsic/n-type semiconductor junction) architecture have been investigated by Peng *et al.*, but showed a low output power of 2 μW for a high injection current density of 200 $\mathrm{kA\,cm^{-2}}$ [68].

Photodetectors

While the initial attention was focused on light emission, the first demonstration of an optoelectronic device based on GeSn was a p-i-n photodetector reported by Mathews *et al.* in 2009, which exhibited a photodetection cutoff of 1.75 μm [80]. As the Sn content increases, the bandgap shrinks, leading to an extension in the cutoff wavelength of these detectors. The incorporation of Sn is a promising strategy for the design of avalanche photodiodes (APDs), as the absorption edge is shifted toward longer wavelengths [81, 82]. This shift also leads to an increase in responsivity at 1550 nm, which is the operational wavelength used in key applications such as light detection and ranging (LiDAR) and quantum communication, where single-photon detection is required. However, GeSn single-photon avalanche detectors (SPADs) have not yet been demonstrated. Low Sn contents are sufficient to cover the optical communication bands from 1260 to 1625 nm, combined with enhanced absorption [80]. On

the other hand, higher Sn contents in p-i-n detectors provide an extended detection range above 2 μm, reaching up to 3.5 μm in cutoff wavelength [83]. Multiple demonstrations have been carried out with the aim of either operating at a longer wavelength, achieving higher bandwidth, reducing dark current, or increasing detectivity [15, 84–94]. Figure 2.8 shows an overview of the different structures developed for photodetector demonstrations.

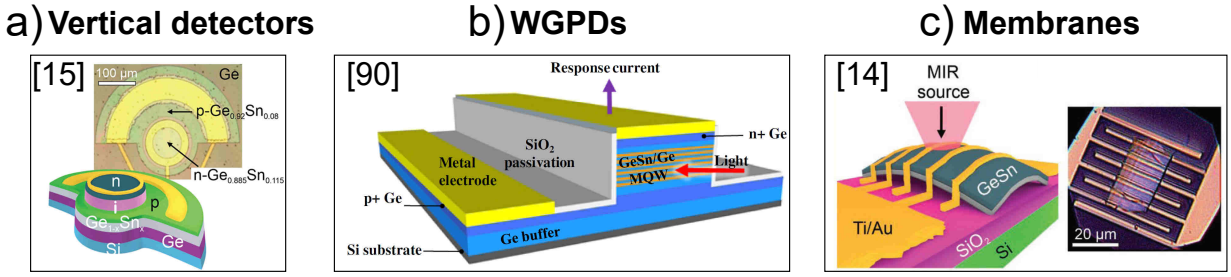


Figure 2.8 Overview of the different structures used in the demonstrations of GeSn photodetectors with (a) vertical photodetectors [15], (b) waveguide photodetectors (WGPDs) [90], and (c) membrane photodetectors [14].

The performance of GeSn photodetectors is not yet on par with state-of-the art mid-infrared detectors as the specific detectivity, a figure of merit that accounts for spectral responsivity, dark current noise, and device area, currently ranges between 10^8 and 10^{10} cm $\mathrm{Hz}^{1/2}$ W^{-1}, which is about two orders of magnitude lower than the commercially available III–V detectors. This lower performance is notably attributed to the large dark current density found in these devices, which originates from current leakage such as trap-assisted tunneling (TAT) and Shockley-Read-Hall (SRH) leakage due to the numerous defects in the GeSn layers [95]. This issue will be discussed in detail in the following section. While the performance of GeSn photodetectors remains in early development and is not yet comparable to III–V photodetectors, they operate at room temperature and have demonstrated the highest bandwidths for wavelengths above 2.3 μm to date [96], with bandwidths exceeding 7.5 GHz [15, 89, 92–94]. Strategies such as the integration of metasurfaces are being explored to enhance the properties of GeSn photodetectors [97].

As with lasers, strain engineering can play a role in improving the performance of GeSn photodetectors. One notable example is the complete underetching of GeSn suspended structures to form GeSn membranes, which undergo relaxation of compressive strain. Atalla *et al.* demonstrated photoconductive detectors based on strain-relaxed GeSn membranes with a maximum Sn content of 17 at.%, which exhibited an increase in the cutoff wavelength to approximately 4.6 μm compared to their as-grown counterparts, which showed a cutoff of 3.5 μm, as the compressive strain was around -1.3% [14]. One interesting advantage of these

structures is their ability to transfer onto various substrate using a transfer printing technique. This type of structure will be discussed in detail in Chapter 4, as it will be used in the scope of this thesis. Comparable structures, called *ribbons*, have been recently demonstrated by Zhao *et al.* using a similar release process [98].

The ability to detect longer wavelengths makes GeSn alloys an attractive alternative to III–V semiconductors and other compounds for the development of mid-infrared detectors and cameras, with the promise of lower fabrication costs due to Si-compatible growth. Efforts are ongoing in imaging demonstrations [91] and in the development of arrays of detectors [99]. Prototypes of focal plane arrays (FPAs) are gradually being presented [100, 101].

Compatible designs for integrated photonics

GeSn, though still in its early stages, could play a key role in the monolithic integration of optoelectronic components with PICs, with selective growth following approaches used for Ge detectors. Despite the current limitations in light-emitting performance and material quality, recent advancements in GeSn photodetectors have demonstrated impressive high-speed capabilities for the development of optical receivers in the mid-infrared region, with reported bandwidths of up to 50 GHz and cutoff wavelengths above 2.3 μm [92–94]. Figure 2.9 shows the schematic of a GeSn photodetector monolithically integrated onto an SOI PIC.

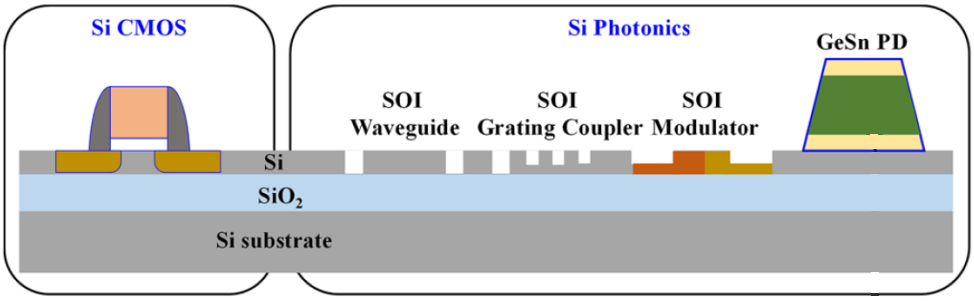


Figure 2.9 Illustration of a monolithically integrated GeSn photodetector (PD) onto an SOI photonic platform. Adapted from [10].

To date, both modeling and experimental reports have examined designs for light-emitting and photodetecting devices with a lateral configuration that are compatible with in-plane propagation of light. Modeling efforts include evaluating the performance of integrated GeSn photodetectors [26], modulators [24, 102], and lasers [103–105]. However, the lack of data on some properties of GeSn alloys complicates the accurate modeling of optoelectronic devices. Modeling results can still provide valuable insights into expected performance metrics, such

as optical net gain and pumping threshold [106]. Improvements in material quality, coupled with further investigations into the properties of GeSn, are expected to enhance the accuracy of performance predictions for optoelectronic devices.

While a few GeSn devices have been fabricated and demonstrated using an in-plane configuration as stand-alone devices, only a handful of experimental studies have attempted tackling the coupling of GeSn-based active components with passive structures or waveguides, which is essential for their integration into PICs. Wang *et al.* carried out coupling demonstrations with GeSn devices consisting of a Ge/GeSn MQW in the active region, grown using MBE [20, 21]. They initially tested the flip-chip integration of a single photodetector on a die coupled vertically to an SOI surface grating coupler, but this resulted in a weak coupling between the two structures and thus in a low responsivity [20]. Subsequently, they investigated an approach based on monolithic integration, where photodetectors and modulators coupled to Ge-on-Si waveguides were defined via consecutive etching steps [21]. While this demonstrated the integration of GeSn-based components, the waveguides suffered from high propagation losses (47 dB/cm at a wavelength of 2 μm), possibly due to the significant overlap of the propagating optical mode with the defective Si/Ge interface. Monolithic integration of GeSn thin films as an active medium for waveguide-coupled GeSn lasers was also investigated by M. Adams in his master thesis, although lasing in these structures has yet to be observed [107].

Despite significant progress in monolithic device demonstrations, the integration of GeSn with Si photonics is still in its infancy. Addressing current challenges in material quality and fabrication will be critical to unlocking its full potential in optoelectronic applications. This progress makes GeSn an attractive candidate for mid-infrared optoelectronics, despite the ongoing challenges in achieving high-quality growth. A general overview of the effort carried out in the investigation of integrated photonics in the mid-infrared will be provided in Section 2.3.3.

Other devices and structures

In addition to light emitters and photodetectors, other types of devices based on GeSn have also been demonstrated. Notably, electro-absorption modulation has been investigated using the Franz-Keldysh effect in GeSn to achieve a practical modulation scheme [108]. Devices based on GeSn nanowires, which are often used to study the intrinsic properties of the alloy [109–111], include photodetectors [112, 113] and lasers [114]. GeSn has also attracted significant attention due to its predicted high electron and hole mobilities, which are crucial for improving the performance of transistors as the industry explores CMOS alternatives

beyond Si [115]. Han *et al.* observed a superior mobility in metal-oxide-semiconductor field-effect transistors (MOSFETs) based on p-type GeSn compared to their Ge counterparts [116]. Moreover, gate-all-around nanowire (GAA NW) transistors with an Sn content of 11 at.% demonstrated an overall superior performance over those based on Ge [117, 118].

2.2.3 Challenges

While GeSn alloys hold promise for various applications in optoelectronics as an alternative for III–V compounds, their primary challenges stem from growth-related material defects and low thermal stability, which directly impact device performance and hinder their competitiveness for commercial viability. Two key factors contribute to these challenges: the significant lattice mismatch between GeSn and its Ge or Si substrates and the low solubility of Sn in Ge at equilibrium. Extensive efforts have been made to uncover the origin and impact of various defects found in GeSn alloys, with the current knowledge being still limited. This section will briefly summarize the origin of these challenges and the current solutions that are employed to tackle them. A. Giunto and A. Fontcuberta i Morral recently published an extensive review on the current understanding of defects found in GeSn, highlighting their impact on optoelectronic properties and the current challenges in material quality and device performance [119].

GeSn is ideally grown on a group-IV material such as Si or Ge, which share a diamond cubic lattice. However, as shown in Fig. 2.5, the lattice parameter of GeSn becomes significantly higher than Ge (5.658 Å) and Si (5.431 Å) as the Sn content increases, which leads to an inevitable lattice-mismatched growth. The heteroepitaxy of GeSn alloys on Si will therefore be initially pseudomorphic, where the lattice parameter of the epitaxial film will match that of the underlying substrate to maintain coherent growth, but with an increasing compressive strain as the thickness increases. Compressive strain not only increases the minimum Sn content required to achieve a direct bandgap in the alloy [18], but it also restricts the incorporation of Sn into the lattice when using CVD [17]. Once the epitaxial film reaches a specific thickness, called the critical thickness, dislocation defects such as misfit and threading dislocations form, relieving some of the accumulated compressive strain but degrading film quality. As the thickness increases beyond the critical thickness, a compositional gradient starts to form in the layer along the growth direction as the Sn incorporation becomes progressively less restricted.

To minimize the lattice mismatch with the GeSn film and thus reduce the compressive strain, a Ge interlayer, commonly referred to as a Ge virtual substrate (Ge-VS), is first grown on Si to be used as a buffer [120]. Although the critical thickness varies with the Sn content in

the GeSn epitaxial film, this Ge buffer layer helps increase this value within tens or hundreds of nanometers compared to just a few nanometers when grown directly on Si [119]. The growth of high-quality, thick GeSn layers with high Sn content is particularly challenging due to these limitations. To improve the quality of GeSn layers with a high Sn content, a promising strategy involves growing several GeSn buffer layers of progressively increasing Sn content [121]. Using this approach, defects are largely confined to the underlying GeSn layers, resulting in defect-free top layers. This approach has enabled the demonstration of GeSn layers with a uniform content of up to 18 at.% [122]. Minimizing the aforementioned growth defects is essential for improving the performance of GeSn-based optoelectronic devices as they are the primary contributors to the observed high dark current. These defects can be electrically active and create localized energy states within the bandgap, referred to as traps, where they enable current leakage mechanisms such as SRH and TAT [95]. Dislocation defects generally generate shallow acceptor traps [123]. Interfaces of layers grown on lattice-mismatched substrates generally possess a large density of misfit dislocations that undermines device performance. Defect management of the interface can be achieved through etching, especially with GeSn microdisk lasers by selectively etching Ge over GeSn. Elbaz *et al.* observed a reduction of the lasing threshold in these optically pumped structures by etching away the large array of misfit dislocations in GeSn near the former Ge/GeSn interface [124]. This was achieved by changing the chemistry for the plasma underetching step from CF_4 to SF_6, where the latter appears slightly less selective to GeSn.

In addition to the mismatched-growth, the large difference in the lattice constants between α-Sn (6.493 Å) and Ge (5.658 Å), which is approximately 14.7%, leads to a Sn solubility in Ge below 1%. Figure 2.10 shows the phase diagram of the Ge–Sn binary system, where the maximal solubility of α-Sn is $\sim$1.1 at.% in Ge at 380 °C [125]. This concentration is about an order of magnitude lower than what is required to achieve a direct bandgap. Sn atoms tend to segregate, forming a β-Sn phase at equilibrium. Thus, non-equilibrium techniques have been developed to avoid its formation, primarily by growing at low temperatures to limit atomic diffusion.

The low temperature growth sets the material's thermal budget before Sn segregation occurs when it is exposed to high temperatures in post-growth processes. These processes are therefore typically avoided to preserve the stability of the material, but they are essential in key steps for device fabrication, such as post-growth annealing, which aids defect management and dopant activation post-ion implantation. By investigating the thermal stability of GeSn layers ranging from 5 to 12 at.%, Zaumseil *et al.* found that segregation of Sn occurs within the range from 350 to 600 °C, with segregation occurring at lower temperatures as the Sn content in the layer increases [126]. They also found that annealing can induce

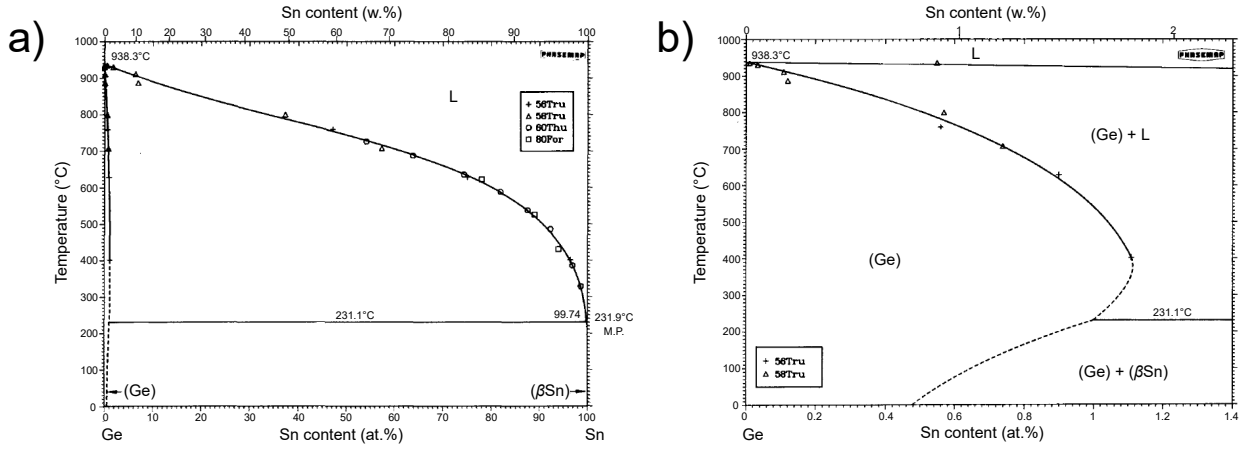


Figure 2.10 Ge-Sn phase diagram as a function of at.% Sn and temperature. a) Diagram from 0 to 100 at.% Sn. b) Diagram from 0 to 1.4 at.% Sn. Adapted from [125].

further strain relaxation in partially relaxed GeSn layers before resulting in a sudden phase separation, while the Sn segregation appears to be slower in pseudomorphic samples. The sudden segregation is attributed to a mechanism called pipe diffusion, in which threading dislocations facilitate Sn diffusion towards the surface and the Sn diffusion coefficient increases by a factor of 10^4 [127, 128]. Microstructuring GeSn into isolated shapes such as microdisks enhances thermal stability during annealing and delays Sn clustering, as defects at the Ge/GeSn interface are removed [129].

The growth under out-of-equilibrium conditions is also the source of additional defects that form in the layer, such as point defects like impurities and Sn-vacancy complexes [119]. Like dislocations, these defects can introduce electrically active trap levels. Sn-vacancy complexes are often attributed to the unintentional p-type doping observed in GeSn thin films, with a carrier concentration within the range of 10^{16} to $10^{17}\,\mathrm{cm}^{-3}$. However, their origin and properties are still under investigation and they can be characterized using positron annihilation lifetime spectroscopy (PAS). Their formation mechanisms remain under investigation, including Sn-vacancy pairing to explain the reduction of vacancy clusters and increase in divacancy formation as the Sn content increases [130].

Defects in GeSn occur at interfaces, in the bulk, and on the surface, which, along with dangling bonds, generate surface traps that increase the dark current. These can be mitigated through passivation using SiO_2 [87], Al_2O_3 [131], or Si [132]. While there is no simple solution to address all the intricate challenges in growing high-quality GeSn layers, advances in thin film engineering combined with the mastery of growth kinetics and defect management are crucial for improving device performance. Moreover, the thermal conductivity has been

observed to drop by Spirito *et al.* as the Sn content increases, from $58\,\mathrm{W/(m \cdot K)}$ for pure Ge down to $4\,\mathrm{W/(m \cdot K)}$ for $Ge_{0.86}Sn_{0.14}$ [133]. Heat transport in GeSn-based devices is then expected to be hindered compared with their pure Ge counterparts.

Regarding SiGeSn ternary alloys, their synthesis is complicated by the very low solubility of Sn in the presence of Si, which can drop to roughly 0.1 at.% in the case of pure Si [52]. These alloys, just like GeSn, are namely Ge-rich and have been used in a few device demonstrations as mentioned in the previous section. Progress in the growth of thick SiGeSn layers have been made, which would help improve the performance in electrically pumped GeSn lasers [134].

2.3 Mid-infrared optoelectronic applications

The mid-infrared region, which is often defined as spanning from 2 to 20 μm, is a part of the electromagnetic spectrum that offers unique advantages for several applications, notably due to the presence of multiple molecular absorption peaks, blackbody radiation for thermal imaging, and atmospheric windows for free-space communications. While the exact range of the mid-infrared varies depending on the field or application, it is generally divided into smaller subranges: the short-wave infrared (SWIR) from 1.4 to 3 μm, the mid-wave infrared (MWIR) from 3 to 8 μm, and the long-wave infrared (LWIR) from 8 to 14 μm. The widespread adoption of these applications is limited by the high cost of light-emission and detection technologies in these wavelength ranges compared to conventional telecom wavelengths. This thesis refers to the range between 2 and 8 μm when referring to the mid-infrared region.

As the resulting bandgap energies of GeSn primarily lie in the mid-infrared region, this alloy is being explored as a cost-effective material for mid-infrared systems. Figure 2.11 illustrates the specific subranges and the demonstrated versus expected GeSn operating range. The bandgap energy as a function of Sn content shown in Fig. 2.5, computed using 8-band $k \cdot p$, predicts that a strain-free GeSn material with Sn contents just above 12 and 20 at.% is adequate to cover the SWIR and MWIR regions respectively. Sn contents above 20 at.% have been achieved, but with lower quality and limited thicknesses within a few tens of nanometers, remaining one to two orders of magnitude thinner than needed in optoelectronic applications [119]. Progress in the growth of alloys with even higher Sn contents exceeding 30 at.% Sn has been achieved using advanced growth techniques. While misfit dislocations are generated, the direct growth on Si(100) can facilitate strain relaxation and thus enhance the Sn incorporation [135]. By using this strategy and choosing the appropriate Sn precursor gas, Mircovich*et al.* demonstrated a GeSn layer with 35.4 at.% Sn, sufficient for LWIR operation, despite the layer being only 49 nm thick [136]. Although their growth is more

complex, SiGeSn compounds could be used to access this spectral range while enabling strain decoupling from the composition.

While these compositions could enable coverage of the mid-infrared and the LWIR region, this thesis focuses on the demonstrated operating range of GeSn-based optoelectronic devices, which is currently set to a wavelength 4.6 μm based on strain-relaxed GeSn membrane photodetectors with a Sn content of about 17 at.% [14, 63]. This section will cover key mid-infrared applications and existing technologies. Additionally, we will briefly discuss efforts in integrating these technologies into photonic platforms and chip-scale systems.

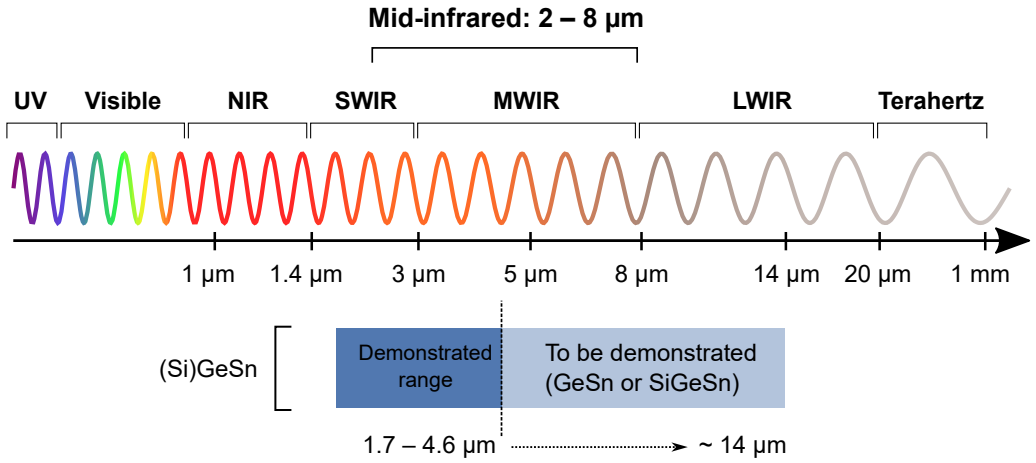


Figure 2.11 Illustration of the electromagnetic spectrum with range definitions. The demonstrated range (cutoff wavelength in photodetectors) of GeSn is overlaid with the expected range that remains to be demonstrated, either using GeSn or SiGeSn compounds.

2.3.1 Applications

The mid-infrared region provides a wealth of information. The primary applications of the mid-infrared range are thermal imaging, spectroscopic sensing, and data communications. The shift towards the mid-infrared is also driven by the potential for developing new systems, especially for environmental monitoring and industrial process control, due to the strong molecular absorption features in this range [137–139].

Absorption spectroscopy for biological and chemical sensing

A key application of the mid-infrared region is absorption spectroscopy for chemical and biological analysis, including the detection of gases such as carbon monoxide (CO), carbon dioxide (CO_2), methane (CH_4), and water vapor (H_2O), as well as biological compounds

like proteins and glucose. Molecules possess vibrational and rotational modes with energies that correspond to mid-infrared photons, allowing them to be identified by a unique pattern of absorption lines [140]. Mid-infrared absorption spectroscopy identifies molecules through their unique vibrational and rotational modes. The fingerprint region (8–14 μm) offers minimal spectral overlap, enhancing detection accuracy. Overtones enable detection at shorter wavelengths but with lower sensitivity and higher spectral interference [141]. Figure 2.12 shows examples of key molecules detectable in the mid-infrared region between 3 and 14 μm, with strategic applications in environmental monitoring, defense, and medical diagnostics.

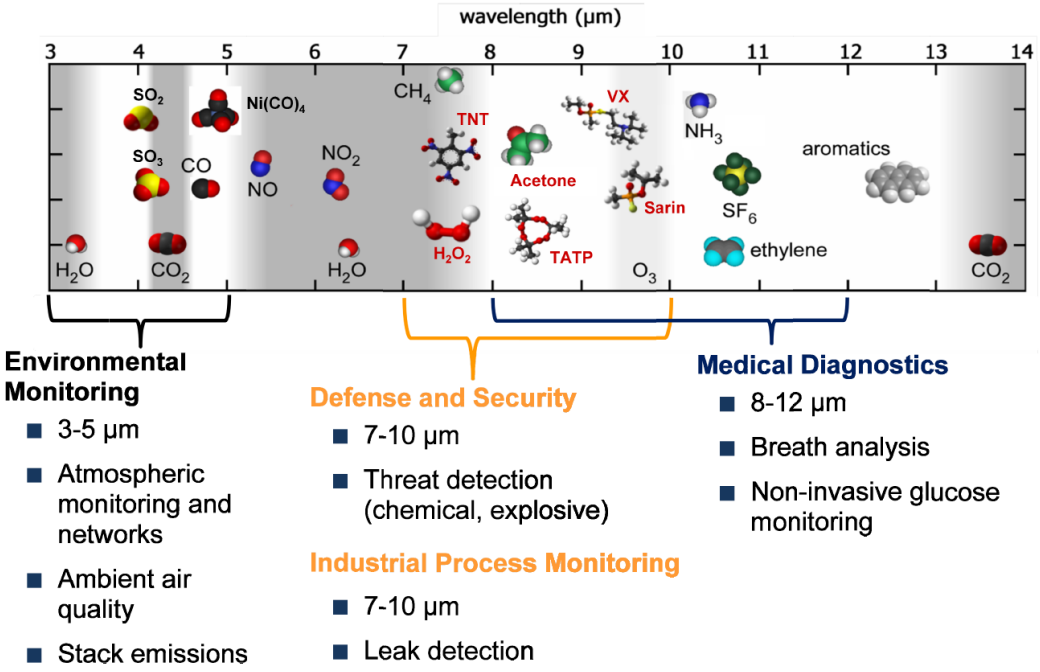


Figure 2.12 Examples of molecules of interest and key applications in mid-infrared sensing. Reproduced with permission from [141].

Figure 2.13 shows spectra of absorption coefficients for water (Fig. 2.13(a)), CO (Fig. 2.13(b)), CO_2 (Fig. 2.13(c)), and CH_4 (Fig. 2.13(d)) from 1 to 5 μm [142]. Generally, the strength of absorption lines increases toward longer wavelengths, where a greater sensitivity in analyte detection would then be expected to be provided. The 2–2.5 μm range is well-suited for detecting critical compounds such as greenhouse gases. CO_2 and CH_4 have absorption bands at approximately 2 and 2.3 μm, respectively. While this range is currently covered by extended-InGaAs and gallium antimonide (GaSb) detectors, GeSn offers a cost-effective alternative for this detection range. Some optical sensors rely on techniques such as tunable diode laser absorption spectroscopy (TDLAS) or Fourier transform infrared (FTIR) spectroscopy [143]. Free-space optical systems widely employ these techniques in remote sensing, but the current

challenge lies in miniaturizing them for chip-scale integration. Sensing in the near-infrared remains attractive for applications requiring portable systems due to the availability of materials and the relatively low manufacturing costs of devices. Several demonstrations of sensing using GeSn optoelectronic devices have shown their potential in this field [78, 83].

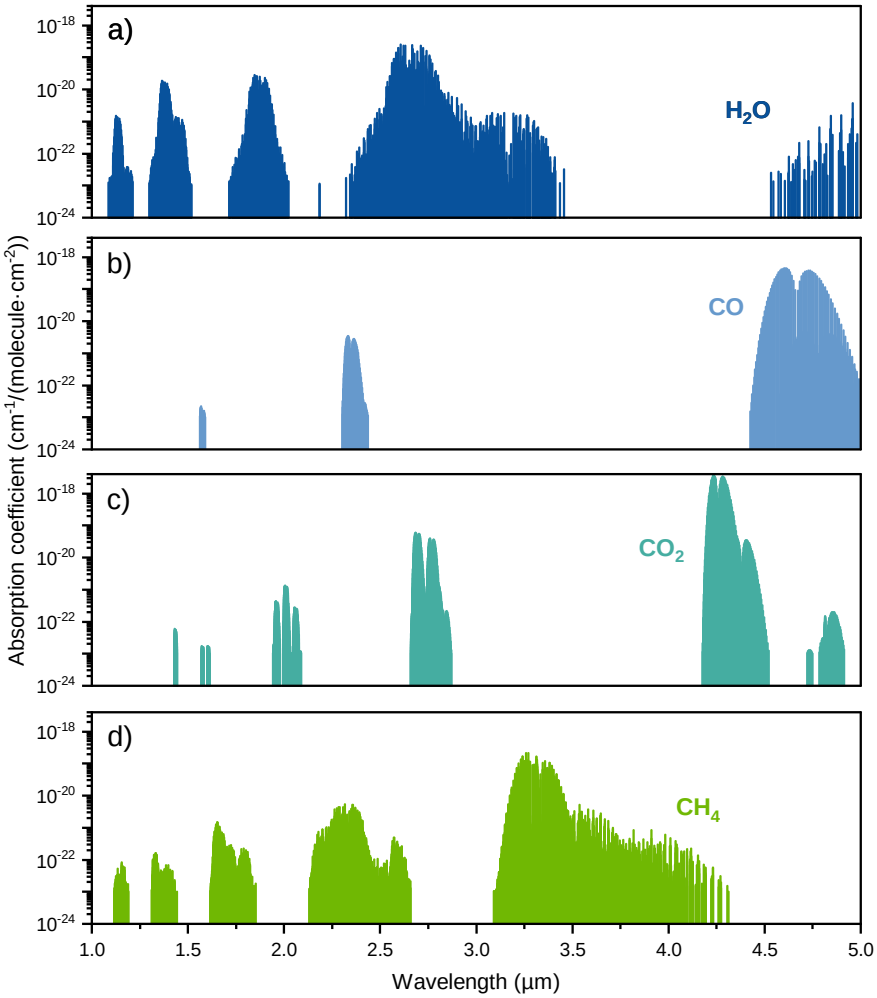


Figure 2.13 Absorption coefficient spectra of (a) water, (b) carbon monoxide, (c) carbon dioxide, and (d) methane from 1 to 5 μm. Data is taken from the HITRAN database [142].

Data communication

There is growing interest in exploiting other wavelength ranges as the current bands (1260–1650 nm) are facing limitations such as congestion, increased nonlinearity, and high attenuation at higher data rates amid rising bandwidth demands. The industry is primarily focusing on the 2 μm band (1.9–2.1 μm) due to the availability of low-loss hollow-core pho-

tonic bandgap fibers (HC-PBGFs), which exhibit low nonlinearity and low latency, as well as thulium-doped fiber amplifiers (TDFAs) for signal amplification. Transceivers for intra-chip or chip-to-chip communications operating at 2 μm could be fabricated at a lower cost than receivers at 1.55 μm [19].

Beyond expanding current telecommunication bands, certain wavelength ranges offer inherent advantages, particularly for free-space optical communications within atmospheric transmission windows from 3 to 5 μm and 8 to 12 μm [144]. Compared to radar-based links, these links support land-air and satellite communications with minimal interference from environmental perturbations, making them suitable for both civilian and military applications. However, developing reliable and fast links requires powerful lasers, sensitive detectors, and high-speed modulators. Figure 2.14 illustrates the communication bands of interest in the mid-infrared, such as the 2 μm band (Fig. 2.14(a)) and the atmospheric windows (Fig. 2.14(b)).

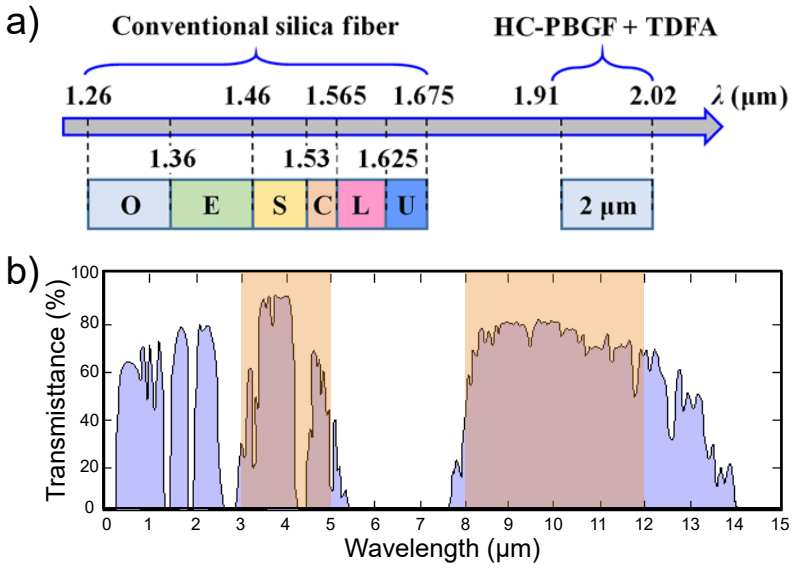


Figure 2.14 Wavelength ranges of interest for communications. (a) Standard telecommunications band with the novel 2 μm band (Adapted from [10]). (b) Transmittance of the atmosphere exhibiting the atmospheric windows from 3 to 5 μm and from 8 to 12 μm (Adapted from [145]).

Imaging

The mid-infrared region offers significant opportunities for enhanced imaging techniques [146]. Imaging in the 2–2.5 μm range benefits from superior atmospheric transmission, reduced solar irradiance (three times lower than at 1.55 μm, and minimal atmospheric absorption, as shown in Fig. 2.15. These advantages enhance contrast for imaging applications such as Li-

DAR [147]. Blackbody radiation detection in this range enables tracking of high-temperature objects like aerospace vehicles [148].

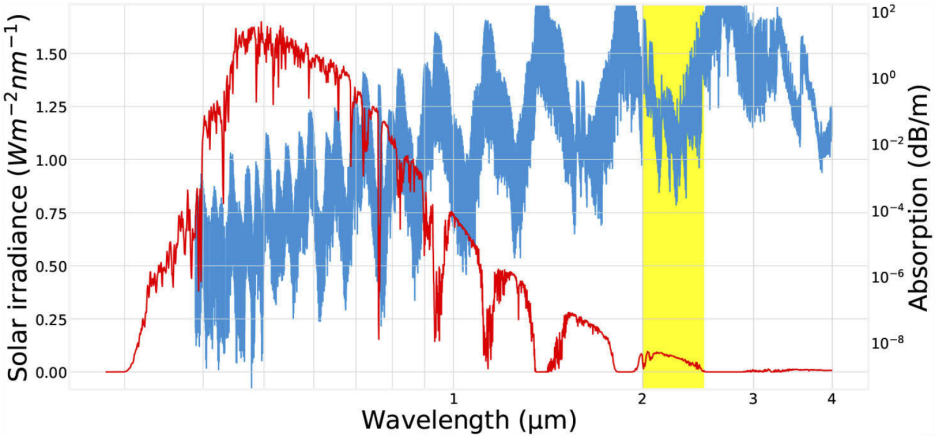


Figure 2.15 Solar irradiance and atmospheric absorption spectra up to 4 μm with the 2–2.5 μm window highlighted. Reproduced with permission from [147].

Mid-infrared cameras, which are primarily based on III–V materials and II–VI compounds like mercury cadmium telluride (MCT), are associated with very high costs due to challenges related to film processing, such as maintaining uniformity and stoichiometry, small wafer sizes that limit production scalability, and compatibility issues with readout integrated circuits (ROICs), which often require complex hybrid integration due to differences in thermal expansion and material properties. Recent demonstrations have shown the potential of GeSn for imaging applications [87, 91].

2.3.2 Current technologies

Specific optoelectronic components capable of operating in this wavelength range, such as light sources and detectors, are required for the aforementioned applications. Unlike near-infrared technologies, mid-infrared light sources and detectors are often bulky, require cooling, and rely on materials like MCT and InSb, which are difficult to process. These factors contribute to systematically high costs for mid-infrared equipment, including manufacturing challenges, material scarcity, and the need for specialized fabrication techniques. In the following section, we will briefly review the different technologies employed for light emission and detection throughout the mid-infrared region.

Light sources

There are numerous solutions for generating light in the mid-infrared, from cost-effective incoherent sources such as thermal emitters to coherent and narrow-linewidth sources such as optical parametric oscillators (OPOs). The operating ranges of these sources is illustrated in Fig. 2.16, and they are summarized as follows:

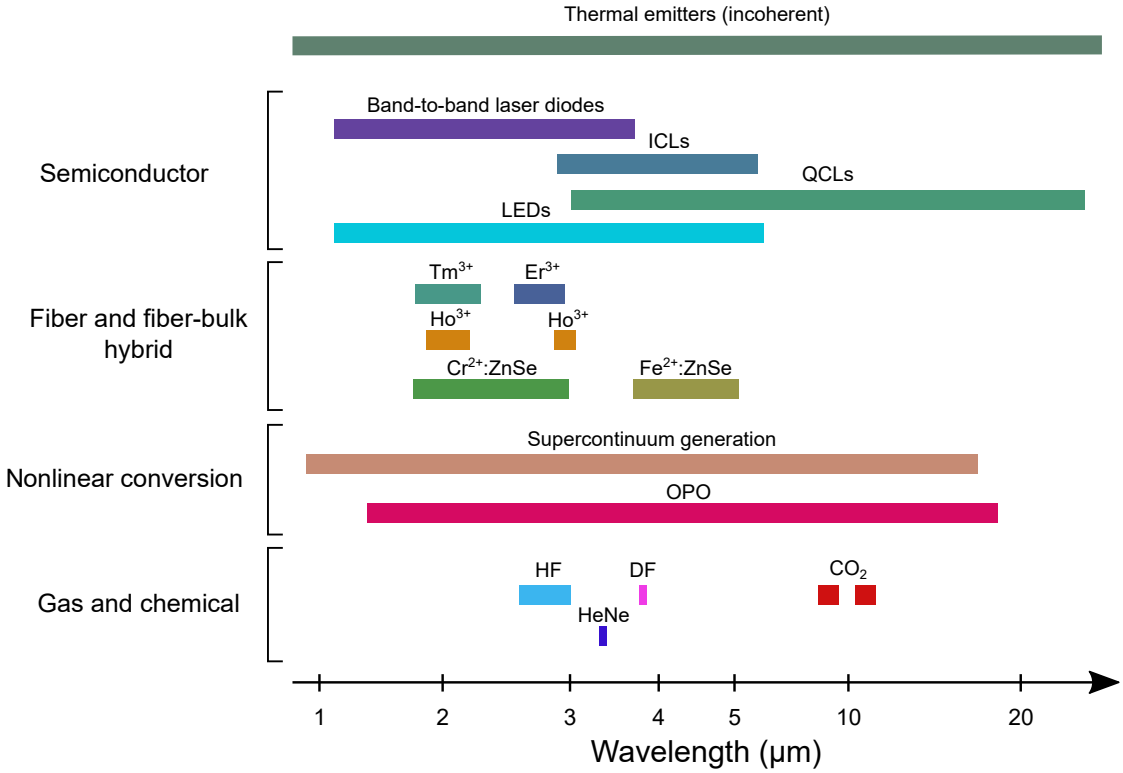


Figure 2.16 Wavelength coverage of mid-infrared light sources. Data taken from various references mentioned in this section including [149, 150].

- **Thermal emitters:**

  Thermal emitters, such as tungsten-halogen lamps and *Globar* sources, emit broadband mid-infrared radiation via blackbody emission. While widely used in Fourier Transform Infrared (FTIR) spectroscopy, their incoherence limits precision applications [151].

- **Semiconductor lasers and LEDs:**

  Significant progress has been made in developing III–V semiconductors for active devices operating in the mid-infrared range [152,153], particularly with materials like InP and GaSb, which have demonstrated cutoff wavelengths exceeding 2.3 μm [154, 155].

Electrical pumping in a double heterostructure (DHS) can provide lasing at the bandgap energy, while the active region can be designed with quantum wells (QWs) to engineer emission properties for lower energies. GaSb-based type-I QW laser diodes, which confine both electrons and holes in the QW, emit up to 3.7 μm at room temperature [156]. A major challenge in interband mid-infrared lasers is the Auger effect, which contributes to carrier losses and increases exponentially as the bandgap decreases [157].

To address this issue, alternative semiconductor laser designs, such as quantum cascade lasers (QCLs) and interband cascade lasers (ICLs), have been developed. The lasing mechanism of QCLs relies on intersubband transitions of electrons within the conduction band, involving multiple quantum wells, instead of interband transitions. QCLs can emit light from approximately 3 μm [158] to terahertz (THz) wavelengths (> 30 μm) [159]. The emission wavelength is mainly tuned through the design of the different layers in the quantum well stack. They are usually grown on InP and GaAs substrates. Faist *et al.* demonstrated the first QCL in 1994 [160]. Today, QCLs are widely used, although they are significantly more expensive than typical laser diodes. ICLs, in contrast, are based on interband transitions between electron states in the conduction band and hole states in the valence band of type-II quantum wells. They emit between 2.9 and 5.7 μm at room temperature [161] and require less power than QCLs to reach the lasing threshold.

Mid-infrared LEDs provide a cost-effective alternative to lasers, with coverage up to 5.8 μm [162]. However, their output power is significantly lower and decreases at longer wavelengths, with optical power being less than 1 mW for wavelengths above 2 μm. The layered architecture used in ICLs can be adapted in LEDs to achieve higher optical power in the mid-infrared range [163].

- **Fiber and fiber-bulk hybrid lasers:**

  Optical fibers can be doped with rare earth elements such as thulium (Tm^{3+}), holmium (Ho^{3+}), and erbium (Er^{3+}), which possess transitions that emit photons in the mid-infrared, creating a gain medium that can be excited by a standard laser diode [149, 164, 165]. These devices typically operate at wavelengths below 3 μm. Fiber lasers based on erbium-doped fluoride fibers (or other doped mid-infrared fibers) can emit at wavelengths around 2.8–2.9 μm. However, the use of optical fibers based on silica limits their operation range, as silica starts absorbing light in the early mid-infrared. Chalcogenide glass fibers can be used to extend the operating range into the mid-infrared.

  For longer wavelengths, fiber-bulk hybrid lasers are used, incorporating chalcogenide

glass such as zinc selenide (ZnSe) doped with chromium or iron. These materials offer wide wavelength tunability and high power. Chromium-doped zinc selenide (Cr^{2+}:ZnSe) emits between 1.8 and 3 μm, while iron-doped zinc selenide (Fe^{2+}:ZnSe) emits between 3.7 and 5.1 μm [149, 166].

- **Sources based on nonlinear conversion:**

  Light from lasers operating at shorter wavelengths can be converted to mid-infrared wavelengths, which are challenging to access at high power, using nonlinear processes, particularly with optical parametric sources like optical parametric oscillators (OPOs). Nonlinear mixing occurs in highly nonlinear materials, such as periodically poled lithium niobate (PPLN) and other ferroelectric materials, providing emission up to 4.5 μm. Emission up to 19 μm is achievable with materials like gallium selenide (GaSe) [167]. Although these systems offer wide wavelength tunability, narrow linewidths, and high optical powers, they are bulky and require precise alignment of optical components and beam paths, resulting in high costs. Nonlinear mixing can also be used for supercontinuum sources, which generate a supercontinuum spectrum through the spectral broadening of intense pulses in dispersion-engineered fibers. Broad spectra of light up to 18 μm can be produced using chalcogenide glass fibers [168]. A similar process is used for generating optical frequency combs, where a stabilized pulsed laser generates sharply defined lines in the frequency spectrum, with a spectral spacing defined by the repetition rate. This comb of spectral lines can be generated using an infrared laser and extended into the mid-infrared [169].

- **Gas- and chemical-based lasers:**

  There are also lasers that rely on light emission from an excited gas or from a chemical reaction, known as gas lasers and chemical lasers, respectively [170]. In gas lasers, gas molecules emit light when an electric current passes through them. The most well-known example is the carbon dioxide (CO_2) laser, which emits at approximately 9.6 μm and 10.6 μm. These lasers are widely used in industrial applications due to their high power output. Helium-neon lasers, typically known for emission at 0.633 μm, also have a transition that enables emission at 3.39 μm. Chemical lasers, on the other hand, achieve lasing through a chemical reaction, with the product molecules emitting light through stimulated emission that becomes coherent lasing when placed in an optical cavity. Hydrogen fluoride (HF) can lase between 2.7 and 2.9 μm, while deuterium fluoride (DF) lases at 3.8 μm. Although these lasers are bulky and difficult to tune, they can emit significant power, making them suitable for industrial and medical applications.

Detectors

Detecting light in the mid-infrared range poses unique challenges, despite the development of various materials leading to the development of devices broadly categorized as photodetectors and thermal detectors [171]. A comprehensive review with an in-depth historical perspective on the evolution of infrared detectors is provided by A. Rogalski, highlighting key advancements and technological milestones [172].

- **Photodetectors:**

  Photodetectors, as previously mentioned, rely on the absorption of photons to create electron-hole pairs, which contribute to the generation of an electrical current. For detectors based on bulk materials, narrow-bandgap materials are required, with the bandgap energy matching that of mid-infrared photons. Photodetectors can operate in either photoconductive or photovoltaic mode, where the key difference is whether the response results in an increase in electrical conductivity or voltage generation across a p-n junction.

  Lead salt materials such as lead sulfide (PbS) and lead selenide (PbSe) have been developed for this purpose. Several narrow-bandgap materials have been discovered, including III–V semiconductors such as InSb, which provides photodetection up to 8 μm, and indium arsenide (InAs), which can detect up to 3.1 μm. II–VI compounds, especially alloys based on MCT, offer wide bandgap tunability, covering wavelengths up to approximately 20 μm. However, the presence of mercury and cadmium makes MCT a highly hazardous material, and its synthesis is challenging due to solid-liquid phase separation during growth. Additionally, processing MCT into devices is difficult, and the small wafer sizes available significantly increase manufacturing costs. Despite these challenges, these technologies are considered mature after decades of development, with cameras and focal plane arrays (FPAs) commercially available for both civilian and military applications [171].

  The layered architecture of semiconductors can also be engineered to enable the detection of lower energies, particularly using quantum wells, which can be designed to form quantum well infrared photodetectors (QWIPs) and Type-II superlattices (T2SLs) [173]. In QWIPs, the quantum well, similarly to laser diodes, defines states as a function of its dimensions to engineer the energy of the transitions. More common compounds like GaAs can be used to form the quantum well. Detectors based on T2SLs, which rely on a type-II alignment and typically use 6.1 Å materials (InAs, GaSb), can be designed to detect longer wavelengths beyond that of their bandgap

energy [174].

- **Thermal detectors:**

  Thermal detectors are the earliest type of infrared detectors, relying on an increase in temperature caused by the absorption of infrared radiation. These include various devices where the actuation mechanism depends on a small change in temperature, such as thermocouples, thermopiles, and bolometers [171]. While these detectors are widely used due to their lower cost, they typically exhibit lower sensitivity and slower response compared to photodetectors.

  In bolometers, a change in temperature generates an electrical current. Arrays of microbolometers can be fabricated using *microelectromechanical systems* (MEMS) technology to suspended pixels made of an absorbing material, such as amorphous silicon (a-Si) or vanadium oxide (VO_x). Upon absorbing mid-infrared light, the electrical resistance of the pixel changes. However, they are sensitive to thermal noise and are relatively wavelength-insensitive. Microbolometers are cheaper compared to semiconductor-based detectors and can operate without cooling, although their sensitivity is lower.

Figure 2.17 shows a comparison of the specific detectivity D^* for various detectors. Values above $10^{11}\,\mathrm{cm\,Hz^{1/2}\,W^{-1}}$ can be achieved up to a wavelength of 5 μm with the current technologies.

2.3.3 Mid-infrared integrated photonics

There is growing interest in extending the operational capacity of PICs to longer wavelengths in the mid-infrared range, with particular attention to the 2 μm band to surpass conventional infrared wavelengths for intra-chip communications, as mentionned earlier [19, 175–177]. Scaling mid-infrared components for integration with Si photonics is key for cost-effective mass production. While OPO-based lasers and MCT detectors offer superior performance, semiconductor-based solutions strike a better balance between efficiency and scalability. The integration of mid-infrared light sources and detectors faces similar challenges as those encountered in active materials for the near-infrared. The active materials are typically integrated onto passive circuits via hybrid or heterogeneous integration methods, as direct growth of these compounds on silicon presents significant obstacles.

This section presents an overview of the different integrated photonic platforms that have been investigated for mid-infrared operation and the integration methods employed to com-

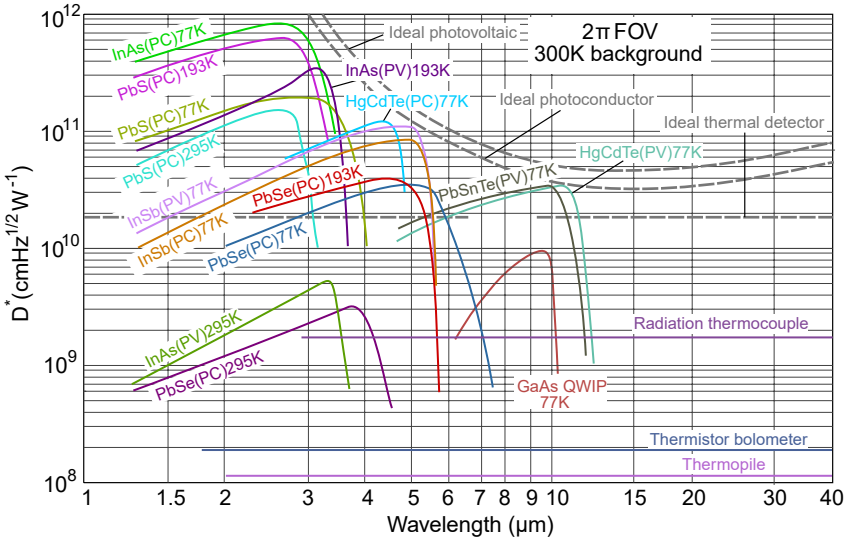


Figure 2.17 Comparison of the specific detectivity of various mid-infrared detectors. PC: Photoconductor. PV: Photovoltaic. Adapted from [171].

bine active materials, including GeSn, to these platforms before briefly discussing how these chip-scale systems can serve key applications.

Mid-infrared photonic platforms

The conventional SOI platform, commonly used in the near-infrared, has properties that restrict its use in the mid-infrared: SiO_2, used as both the bottom cladding and sometimes the top cladding, exhibits significant material absorption between 2.6 and 2.9 μm and above 3.8 μm. New platforms incorporating materials with wider transparency in the mid-infrared must be considered for operation at longer wavelengths, such as Ge, which provides good material transparency from 2 to 14 μm.

Waveguide material selection depends on dispersion properties, transparency, cost, and fabrication compatibility. For waveguides to function effectively, they must exhibit low propagation losses, typically defined as less than 3 dB/cm. This level of loss ensures efficient signal transmission over practical distances, which is essential for many photonic applications [178]. Optical loss mechanisms in waveguides include material absorption, modal radiation, scattering from defects, free carrier absorption (FCA), and other non-radiative processes. In the mid-infrared range, low-loss waveguides are vital to maximize and transmitted signal strength.

Si- and Ge-based platforms are ideal for GeSn integration due to their robustness, high

refractive indices, and broad transparency. Additionally, their compatibility with CMOS fabrication processes makes them practical for large-scale deployment. Ideally, the platform should support operation ideally from the telecom wavelengths up to 4 μm or beyond, as GeSn has demonstrated functionality up to 4.6 μm. Illustrations and micrographs of waveguides from literature on these platforms are shown in Fig. 2.18 with their properties summarized in Table 2.2.

Silicon has long been a preferred material for waveguides in integrated photonics due to its abundance, transparency in the near-infrared region, and compatibility with CMOS processes. With excellent transparency up to 8 μm, silicon is well-suited for mid-infrared applications [189]. Below, we highlight some key silicon-based platforms that have demonstrated successful mid-infrared operation:

- **Silicon-on-insulator (SOI):**

  The silicon-on-insulator (SOI) platform is widely used due to silicon's transparency, CMOS compatibility, and cost-effective large-scale fabrication [190]. SOI uses a silicon layer atop a buried silicon dioxide (BOX) layer, ensuring strong optical confinement and low-loss waveguiding ($\sim$0.6 dB/cm) at telecom wavelengths (1.31–1.55 μm). Its large refractive index contrast ($\Delta n \approx 2$) supports compact device layouts. To prevent optical mode leakage into the silicon handle underneath the BOX, the BOX typically needs to be 2–3 μm thick. However, silicon dioxide exhibits significant absorption between 2.6 and 2.9 μm, and beyond 3.5 μm, the platform's mid-infrared performance [189]. Thicker Si layers (up to 2 μm) can extend operation up to 6 μm [179, 183], though alternative platforms are required for longer wavelengths.

- **Silicon-on-sapphire (SOS):**

  In the silicon-on-sapphire (SOS) platform, silicon is epitaxially grown on sapphire (Al_2O_3), a low-index substrate that prevents substrate leakage. This platform provides a wide transparency range up to approximately 6.2 μm. Propagation losses between 0.7 and 4.3 dB/cm have been reported in SOS waveguides at wavelengths of 4.5 and 5.2 μm [180, 191]. Although promising, the wafer fabrication cost is higher and the hardness of sapphire complicates the polishing of waveguide facets.

- **Silicon on silicon nitride (SON):**

  Silicon can be bonded onto silicon nitride (SiN) to form silicon-on-silicon-nitride (SON) waveguides, where SiN is transparent up to approximately 6.7 μm. A propagation loss of around 5.1–5.2 dB/cm at 3.39 μm has been measured in SON waveguides [181].

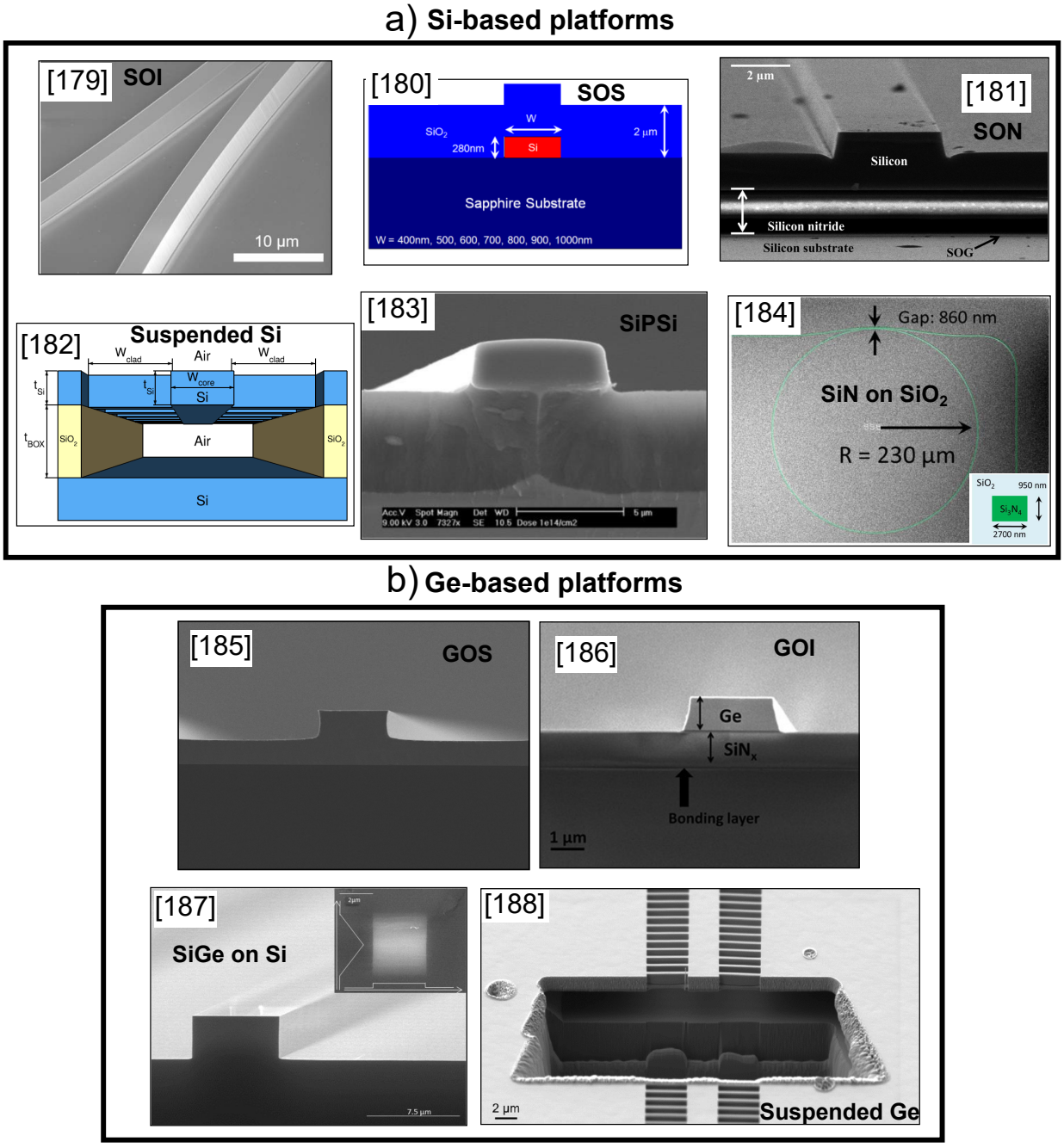


Figure 2.18 Overview of the different photonic platforms that can operate in the mid-infrared region. (a) Si-based platforms [179–184]. (b) Ge-based platforms [185–188].

- **Suspended Si:**

  The underlying BOX in the SOI platform can be selectively removed underneath silicon waveguides using wet etching to eliminate material absorption from the cladding and take advantage of silicon's full transparency range. These waveguides require the addition of mechanical supports in the circuit design, which compromise their mechanical stability and generate optical loss. As air-clad designs improve optical confinement, they suffer from poor heat dissipation and more complex fabrication processes. Propagation losses of 0.8 dB/cm at 3.8 μm [182] and 3.1 dB/cm at 7.67 μm [192] have been reported, demonstrating the potential for mid-infrared applications.

- **Silicon on porous silicon (SiPSi):**

  Porous silicon can be created as a low-index medium through proton irradiation of silicon after electrochemical etching with a mixture of hydrofluoric acid (HF), water, and ethanol. The resulting refractive index can reach 1.4, offering an alternative to silicon dioxide as a cladding material. However, the resulting surface roughness causes moderate propagation losses due to scattering. Using this method, Mashanovich *et al.* achieved a propagation loss of 3.9 dB/cm at 3.39 μm [183].

- **Silicon nitride on silicon dioxide (SiN on SiO_2):**

  Silicon nitride (SiN) on SiO_2 offers record-low propagation losses but faces limitations due to silicon dioxide absorption in the mid-infrared. It has also gained attention for its high nonlinearity, making it ideal for intra-chip communications, quantum photonics, and optical frequency comb generation. It has demonstrated promising results, including a propagation loss of 0.16 dB/cm at 2.6 μm with high Q-factors in microresonator-based frequency comb spanning from 2.3 to 3.5 μm [184].

While silicon provides relatively wide transparency in the mid-infrared, it cannot cover the fingerprint region, which lies roughly between 6 and 14 μm. Ge has a broad transparency window from 1.9 to 15 μm [190], effectively covering this region while maintaining compatibility with CMOS processes and can be grown epitaxially on Si. Consequently, Ge-based platforms are promising candidates for mid-infrared photonic systems.

- **Germanium on silicon (GOS):**

  GOS waveguides have been explored for mid-infrared photonics across a broad wavelength range [185, 193–196]. Ge acts as the core material, with a refractive index ($n_{\mathrm{Ge}} \sim 4$) slightly higher than that of Si. Chang *et al.* first demonstrated GOS waveguides with a propagation loss of 2.5 dB/cm at a wavelength of 5.8 μm [193]. While

GOS waveguides offer an effective light confinement, dislocation defects are concentrated near the Ge/Si interface can lead to high propagation losses [197]. The TDD at this interface, which can be measured via defect-sensitive wet etching, ranges within 2–5 $\times$ $10^7\,\mathrm{cm}^{-2}$ [185]. Low propagation losses can be achieved by minimizing mode overlap with the defective interface, which requires the use of larger waveguide geometries. This approach was employed by Nedeljkovic *et al.* to achieve a propagation loss of 0.6 dB/cm at a wavelength of 3.8 μm [185]. Operation in the 8–14 μm window has been investigated by Gallacher *et al.*, who reported propagation losses between 1 and 5 dB/cm for transverse electric (TE) and transverse magnetic (TM) polarizations [198].

- **Germanium on insulator (GOI):**

  Challenges associated with the Ge/Si interface can be mitigated by creating a germanium-on-insulator (GeOI) platform using the *Smart-cut* technology. The insulating layer, typically SiO_2 or SiN, provides a higher refractive index contrast, thereby improving optical confinement. Kang *et al.* demonstrated GeOI waveguides using SiO_2 as the cladding layer, with a propagation loss of 14 dB/cm at 1.95 μm [199]. Using SiN instead, Li *et al.* reported a propagation loss of 3.4 dB/cm at 3.8 μm [186]. Bonding Ge to SiO_2 offers a better refractive index contrast while reducing defects during chemical mechanical polishing (CMP) steps. However, SiO_2 and SiN limit the platform's transparency range. Alternative materials, such as calcium fluoride (CaF_2) or yttrium oxide (Y_2O_3) with transparency up to 13 μm and superior thermal conductivity, could extend the operational range and performance of Ge waveguides [200].

- **Silicon-germanium on silicon (SiGe on Si):**

  SiGe alloys form an attractive platform due to its tunable refractive index and lower TDD, especially with the ability to create a buffer layer with graded content. The graded content buffer layer helps to gradually reduce lattice mismatch, thereby minimizing defects. The tunability of the Ge content in Si allows for the engineering of the refractive index and dispersion profile of waveguides, which is particularly beneficial for designing waveguides for supercontinuum generation [201, 202] and frequency combs in the mid-infrared. Brun *et al.* demonstrated graded SiGe waveguides on Si with a maximum Ge content of 40 at.%, exhibiting propagation losses of approximately 1 dB/cm at 4.5 μm and 2 dB/cm at 7.4 μm [187].

- **Suspended Ge:**

  Germanium can also be suspended, similarly to the suspended Si platform, to take advantage of its full transparency range up to 15 μm. A germanium film can be grown

on an SOI wafer and then processed in a similar process, with the underlying Si layer removed using tetramethylammonium hydroxide (TMAH). Osman *et al.* reported a propagation loss of 2.6 dB/cm at 7.67 μm [203]. Sanchez-Postigo *et al.* reported a simplified design in which a subwavelength grating to minimize leakage losses, reducing the required number of etch steps from two to one and leading to a propagation loss of 5.3 dB/cm at 7.7 μm [188]. While providing a wide transparency, this platform suffers from similar technical limitations as the suspended Si waveguides.

While the use of Si and Ge is highly desirable due to established processing methods, they are limited by relatively high absorption losses in certain mid-infrared wavelengths, making other less common materials necessary for mid-infrared operation. III–V materials, for example, are transparent across a wide range in the mid-infrared and can facilitate the monolithic integration of light sources and photodetectors. Karnik *et al.* demonstrated an arrayed waveguide grating (AWG) based on InGaAs waveguides on InP, with a propagation loss of 1.2 dB/cm in the 5.15–5.24 μm range [204]. Chalcogenide glasses also exhibit wide transparency ranges in the mid-infrared with low propagation losses [205–207].

Table 2.2 Comparison of photonic platforms with transparency ranges where propagation loss remains below 2 dB/cm. The values are adapted from [177, 189, 208].

	Platform	**Transparency range (μm)**	**Propagation loss (dB/cm)**
Si-based	SOI	1.2–2.6 and 2.9–4.3[a]	0.6 @ 3.4 μm [183], 0.2 @ 3.8 μm [179]
	SOS	1.2–5.2	4.3 @ 4.5 [191], 1.9 @ 5.18 μm [180]
	SON	1.2–6.2	5.2 @ 3.39 μm [181]
	Suspended Si	1.2–6.7	0.8 @ 3.8 μm [182], 3.1 @ 7.67 [192]
	Si on porous Si	1.2–6.7	3.9 @ 3.39 μm [183]
	SiN on SiO_2	0.4–4.3	0.16 @ 2.6 μm [184]
Ge-based	GOS	1.9–8.7	2.5 @ 5.8 μm [193], 0.6 @ 3.8 μm [185], 1–4.5 @ 7.5–11 μm [198]
	GOI (SiO_2)	1.9–4.3	14 @ 1.95 μm [199]
	GOI (SiN)	1.9–5.5	3.4 @ 3.8 μm [186]
	Suspended Ge	1.9–14.6	2.6 @ 7.7 μm [203], 5.3 @ 7.7 μm [188]
	SiGe	1.9–6.7	1 @ 4.5 μm and 2 @ 7.4 μm [187]
Others	III–V	∼2–20	1.2 @ 5.2 μm [204]
	Chalcogenides	∼2–20	0.75 @ 3.6 μm [206], 0.3 @ 5 μm [205], 1.4 @ 2 μm [207]

[a] This range can be extended by using a thicker silicon (Si) layer to minimize mode overlap with silicon dioxide (SiO_2).

Integration methods

Integrating active materials into mid-infrared photonic platforms requires fabrication-compatible methods, similar to those used for near-infrared components. These techniques are typically categorized as monolithic and heterogeneous integration as discussed in Section 2.1.

Monolithic integration involves growing active materials like GeSn via heteroepitaxy. However, lattice mismatch leads to defect networks at the interface, with dislocations propagating and causing non-radiative recombination. In contrast, InP-based platforms allow for the monolithic integration of III–V materials with minimal defects due to lattice matching [209], but they are incompatible with CMOS processing and are more costly. III–V mid-infrared lasers epitaxially grown on on-axis (100) Si substrates are achievable, but can require the blanket epitaxy (uniform deposition) of a buffer layer to reduce the formation of defects originating from a mismatch in the lattice constants, thermal coefficients, and the polarity [153]. They can be coupled to waveguides based on thin films that were deposited prior to the growth of the active material in a recessed area, though regrowth on a patterned PIC can be challenging [210].

Selective area epitaxy (SAE) with aspect ratio trapping (ART) confines defects to localized regions, reducing their spread and allowing for larger defect-free active areas [37]. This can eliminate the need for a thick buffer layer. While the growth of GeSn through SAE is still in development [211], the current scheme for monolithic integration with GeSn involves the initial growth of the active layers on a bare wafer before etching the components into their final dimensions. Wang *et al.* investigated monolithically integrated GeSn/Ge photodetectors and modulators using the Ge buffer layer to form waveguides [21]. The Ge buffer layer, which was 1 μm thick, was etched down to 500 nm to form the waveguide and achieve single-mode dimensions. However, this led to propagation losses of 47 dB/cm in the waveguides, which is unsuitable for layouts with large-scale lengths. These high losses are most likely related to the increased overlap with the defective Ge/Si interface, which might possibly be avoided by considering larger waveguide geometries.

Heterogeneous integration avoids heteroepitaxy-related defects by growing active materials on native substrates before transferring them to passive chips via bonding, flip-chip, or transfer printing. ICLs, QCLs, and photodetectors have been successfully integrated with silicon-based waveguides using these techniques [212–216], which are illustrated in Fig. 2.19.

Wafer bonding (Fig. 2.19(a)) is a common approach for III-V/Si integration, using either direct [215] or adhesive [217] bonding to enable mid-infrared devices. Adhesive bonding allows integration at lower temperatures compared to direct bonding [218]. While adhesive

bonding provides better tolerance to surface roughness, direct bonding offers superior thermal management, as polymers used as adhesives typically have poor thermal conductivity. Wafer bonding usually occurs after passive waveguides are processed on the target wafers. Following bonding, the active material is processed to form the final active devices, often resulting in material waste and potential incompatibilities with other layers. III-V/Si lasers have been demonstrated, with coupling performance largely dependent on the separation gap between the waveguide and active layers [40, 219]. Direct bonding of GeSn on various substrates has also been proposed by several groups to form novel platforms [22, 23].

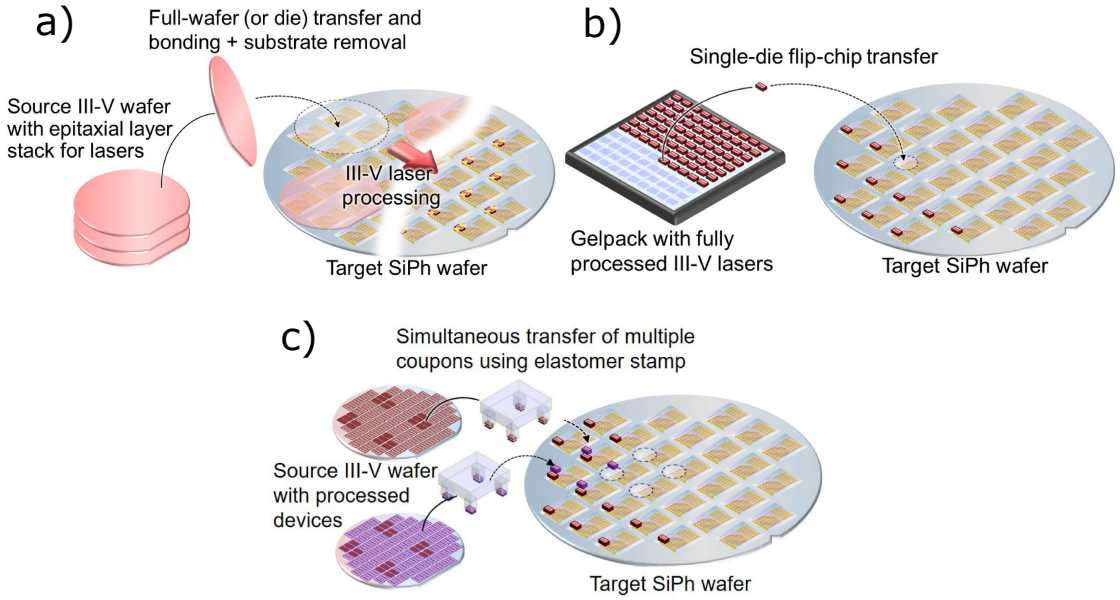


Figure 2.19 Principal heterogeneous integration techniques. (a) Wafer bonding. (b) Single-die flip-chip transfer. (c) Transfer printing of multiple preprocessed devices. Adapted from [220].

Flip-chip bonding (Fig. 2.19(b)) mounts preprocessed active dies to a passive platform using solder bumps. Although straightforward, this method suffers from larger footprints and critical alignment challenges that affect proper coupling. This integration scheme is also referred to as hybrid integration, where different dies are bonded onto a common platform. However, their dense co-integration is limited by wafer die sizes.

Transfer printing (Fig. 2.19(c)) enables high-throughput placement of micron-scale active devices onto passive PICs via an elastomeric PDMS stamp. This technique has recently emerged as an effective method for heterogeneously integrating active materials into passive photonic platforms where direct growth is challenging, which combines the advantages of wafer bonding and flip-chip integration [221–224]. It has also garnered significant interest due to its ability to co-integrate various active components and print dense arrays of devices

while minimizing active material waste, unlike traditional wafer bonding. This significantly reduces manufacturing costs.

A demonstration of a flip-chip integrated Ge/GeSn PD with an SOI grating coupler has been carried out by Wang *et al.*, but exhibited low responsivity [20]. The low performance is attributed to coupling losses from the waveguide and the grating coupler to the photodetector, likely due to misalignment during the flip-chip bonding step. Moreover, this approach significantly increases the footprint. Heterogeneous integration avoids lattice mismatch, improves material quality, and enables flexible co-integration, leading to better device performance. Xu *et al.* suggested using GeOI to integrate GeSn components at the 2 μm band instead of using wafer bonding [225]. Overall, heterogeneous integration remains the preferred approach for combining high-quality active materials with passive platforms, especially for photonic circuits. It avoids many of the challenges of monolithic integration, such as lattice mismatch and defects.

Monolithic integration of QCLs to low-loss passive InGaAs waveguides has also been demonstrated [209], although platforms based on III–V semiconductors can lead to a substantial chip cost [36]. While the most viable short-term solution for integrating light sources, monolithic integration remains a long-term goal if SAE can achieve high yields at lower costs than bonding. While GeSn light sources do not yet exhibit good performance, other materials, such as III–V compounds, should still be considered for light source integration. Transfer printing is particularly suitable for the co-integration of III–V compounds and GeSn to create light sources and detectors, respectively. Furthermore, heterogeneous integration enables rapid prototyping of integrated systems with GeSn, which could provide valuable feedback for advancing its monolithic integration on Si or Ge.

Chip-scale mid-infrared applications

GeSn alloys in this study exhibit a cutoff up to 4.6 μm, enabling the SOI platform to be adapted with various geometries to cover this range. SOI ensures compatibility with existing near-infrared systems. Alternatively, the GOS platform offers mid-infrared operation but suffers from significant absorption losses below 2 μm, limiting its use in telecommunications. SOI is preferable for the 2 μm band and early mid-infrared applications, performing well up to the 2.6–2.9 μm absorption peak and extending to 3.8 μm. The 2–2.5 μm range is particularly valuable for extended communication wavelength bands and sensing applications involving analytes such as glucose, carbon monoxide (CO), and methane (CH_4). For wavelengths above 3 μm, the SOI platform can still be engineered to extend its operational range. Since a Ge buffer layer is often used to grow GeSn alloys on Si, it can also serve as the core

material for waveguides, forming the GOS platform. While several platforms support mid-infrared operation, selecting the appropriate one requires careful consideration of compatible integration methods.

Photonic components are optimized for specific requirements, including power efficiency, compactness, sensitivity, and high-speed operation, to form complete circuits. It is worth noting that these schemes are broadly studied at telecom wavelengths in the near-infrared, and the components are simply adapted for operation within the mid-infrared range. The primary applications targeted for mid-infrared PICs include sensors for spectroscopic sensing and transceivers for fiber-based or free-space communications at extended wavelengths.

The envisioned compact mid-infrared sensors typically include a laser, one or more photodetectors, and an exposed waveguide for analyte interaction [226]. Figure 2.20 shows schematics of integrated absorption spectroscopy sensors, relying on either a broadband mid-infrared light source (Fig. 2.20(a)) or a tunable laser (Fig. 2.20(b)). In these configurations, waveguides serve as the medium for light-analyte interaction, where the evanescent field of the propagating mode overlaps with the surrounding air cladding. Absorption of light occurs as this evanescent field interacts with the analyte present in the air cladding. Chang *et al.* demonstrated liquid-phase cocaine detection using a GOS waveguide at 5.8 μm via evanescent field interaction [227]. Analyte presence is detected via transmission (T) changes following the Beer-Lambert law, where absorption depends on the coefficient α_a and concentration C:

$$T = e^{-\alpha_w L} e^{-\Gamma C \alpha_a L} \tag{2.5}$$

where L and α_w are the waveguide length and loss respectively and Γ is the confinement factor of the waveguide mode that overlaps with the clad where analyte can be present. To maximize detection sensitivity, the sensing unit should exhibit low propagation loss in the absence of analyte while maximizing the overlap of the guided mode in air. Spiral waveguides are typically employed as transducers to increase the interaction length in sensing demonstrations, but the performance can be limited by the waveguide loss and the performance of the light source [228]. Waveguide dimensions are optimized to enhance analyte interaction while minimizing losses. Novel designs, such as slot waveguides, are being explored for mid-infrared applications [229, 230].

Although the integration of these waveguides into a complete photonic chip that includes a light source has yet to be demonstrated, prototypes with integrated detectors have been realized. Photonic sensors offer high sensitivity, fast response, and low limits of detection (LOD), crucial for defense-related molecular detection. These figures of merit will be impacted by the

combined performance of the different components employed, such as the noise level in the light source and the detectivity of the detector. Integrated spectrometers, such as arrayed waveguide gratings (AWGs), have also been demonstrated on SOI [214, 231, 232] and GOS platforms [233], which can be used to recover spectral information. Practically, these sensors could either have the light source integrated to the chip in the case where it would be part of a deployed system like a drone, or mid-infrared light could be coupled from an external source in the case where it would be disposable, like in a clinical setting [234].

Optical communication systems require transceivers, light emitters, modulators, photodetectors, and (de)multiplexers like AWGs. Components from different platforms have shown operation at wavelengths within the 2 μm band [19]. A high operation speed in these components is however desirable to enable high data rates, depending on the target application. Si avalanche photodetectors relying on sub-bandgap transitions from lattice defects showed extended operation up at 1.96 μm with a responsivity of 0.3 A/W and a bit rate of 20 Gb/s, though the applied voltage bias above 15 V for avalanche mode is relatively high [5]. Modulators intended for this application generally rely on electro-optic effects and can operate with bit rates over 20 Gb/s [235]. While heterogeneous integration offers flexibility in using optimal materials for each component, monolithic integration remains a promising approach for high-volume production using group-IV materials. Another type of system for chip-to-free-space interconnects are optical phased arrays (OPAs) [236]. These are used to control the direction of emitted light beams, enabling beam steering without mechanical movement, which is particularly advantageous for free-space communication systems. Though demonstrations in the mid-infrared are limited, the required optical power level depends on the range and monolithically integrated QCLs on an InP-based platform could provide a suitable performance for the mid-infrared due to a more efficient heat dissipation [236].

In this section, we reviewed the development history and key properties of GeSn. We first introduced the challenges in silicon photonics and the context of the mid-infrared region, highlighting potential applications where the alloy is expected to play a significant role. As efforts focus on miniaturizing mid-infrared components to the chip scale, III–V semiconductors have shown significant progress in demonstrating active devices, such as lasers and photodetectors. However, the growth of these III–V compounds remains costly, and their photodetectors exhibit limited bandwidths below 10 GHz for cutoff wavelengths above 2.3 μm [96]. GeSn alloys offer a tunable bandgap, making them promising for mid-infrared photodetection [10, 58].

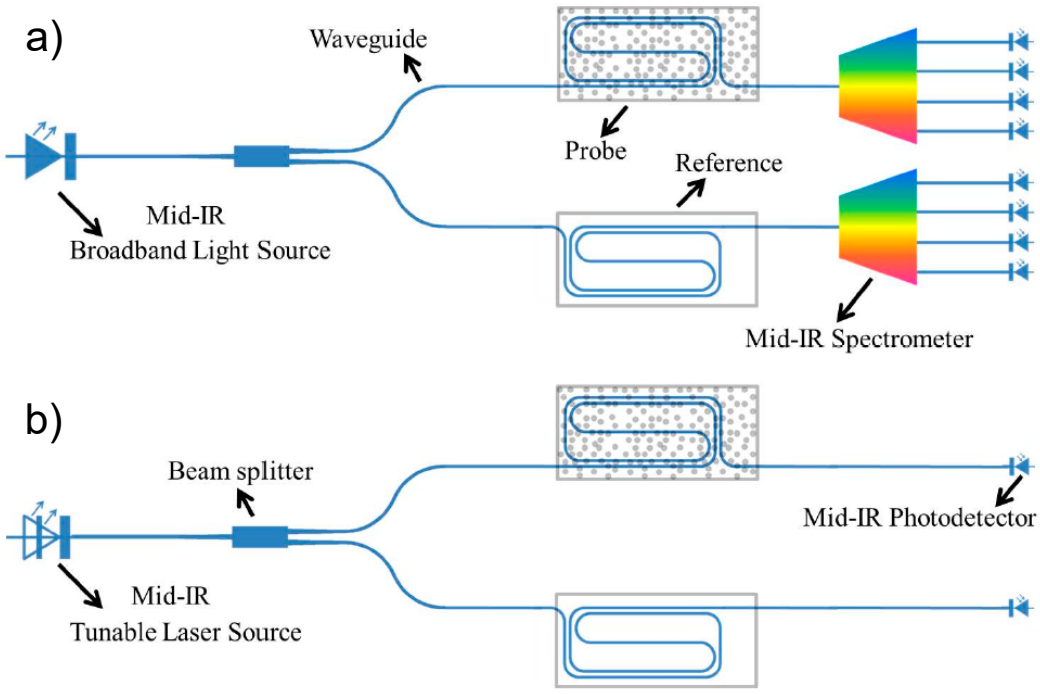


Figure 2.20 Configurations of integrated mid-infrared sensing systems based on a mid-infrared (a) broadband source and (b) tunable laser source. Reproduced with permission from [226].

CHAPTER 3 METHODOLOGY

This chapter outlines the methods used for material growth, device fabrication, and characterization, detailing their principles and limitations. This chapter provides an overview of these methods and their limitations. Due to the diverse techniques involved, this project was a collaborative effort, with various group members contributing their expertise. While I conducted most experiments, colleagues performed some specialized techniques, and their contributions are acknowledged in the relevant sections.

3.1 Chemical vapor deposition of GeSn

The GeSn layers were grown using a chemical vapor deposition (CVD) reactor on 4-inch (100)-oriented Si wafers, typically boron-doped (p-type) with resistivity between 1 and 10 Ω·cm. Figure 3.1(a) shows a schematic of the CVD chamber, where precursor gases enter via a showerhead and decompose on the substrate. The growth process utilizes monogermane (GeH_4) and tin tetrachloride ($SnCl_4$) as precursor gases for the deposition of Ge and GeSn layers, with hydrogen (H_2) serving as the carrier gas to dilute and transport the precursors into the chamber. As the gases decompose, a thin film forms on the substrate, aligning with its crystalline structure and resulting in pseudomorphic growth.

However, differences in lattice constants between the substrate and the deposited layer lead to strain accumulation in the growing film. The layer remains pseudomorphic as long as its lattice constant matches that of the substrate, despite the accumulation of strain. When the layer surpasses its critical thickness, strain is relieved through the nucleation of misfit and threading dislocations, leading to relaxation. A germanium (Ge) interlayer, or Ge virtual substrate (Ge-VS), is deposited before GeSn growth to minimize lattice mismatch, as the difference in atomic radii is smaller between Ge and Sn compared to Si and Sn. This buffer layer is typically grown at 450 °C, followed by thermal cyclic annealing at temperatures exceeding 800 °C. Due to the high Sn content desired, the growth is carried out under metastable conditions to avoid Sn-rich zones, which are thermodynamically favored. Therefore, the growth temperature is maintained between 280 and 350 °C. The Sn content in the GeSn alloy can be controlled by adjusting the temperature and pressure [237], but here only the temperature is tuned while keeping all the other parameters constant for reproducibility. Figure 3.1(b) shows the temperature dependence of the Sn content for pseudomorphic and relaxed layers. Although lower temperatures increase Sn content, they also reduce the growth rate and may lead to more defective layers. After growth, two types of defects were commonly observed

in GeSn films: Sn-rich spots where Sn atoms agglomerated (segregation spots) and pit-like defects likely related to particles present on the Si wafer surface prior to growth.

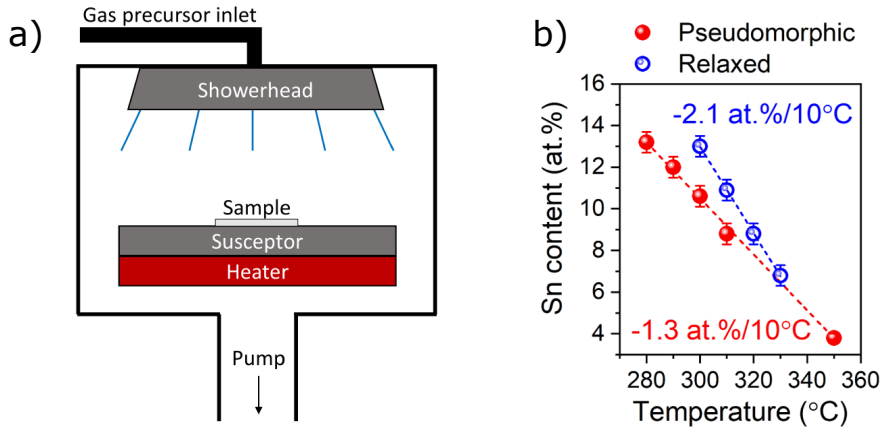


Figure 3.1 CVD growth. (a) Schematic of the process chamber. Precursor gases are injected into the chamber through the showerhead above the wafer (adapted from [238]). (b) Sn content as a function of the growth temperature for pseudomorphic and relaxed layers (adapted from [239]).

The *in situ* doping of GeSn layers during growth is possible by introducing doping precursor gases like arsine (AsH_3) for n-type doping and diborane (B_2H_6) for p-type doping, enabling the formation of p-i-n heterostructures. The Sn content and strain within the layers were estimated using X-ray diffraction reciprocal space mapping (XRD-RSM), which will be discussed in subsequent sections. Additional techniques, such as atom probe tomography (APT), provide further insights into the atomic ordering of Ge and Sn atoms. The growth of the samples used in this thesis was carried out by Dr. Simone Assali.

3.2 Microfabrication methods

The fabrication of devices involves a series of intricate microfabrication steps illustrated in Fig. 3.2, including lithography (Fig. 3.2(a)), etching (Fig. 3.2(b)), and thin-film deposition (Fig. 3.2(c)). This section provides an overview of the working principles and key aspects of each of these processes. The microfabrication steps presented in this work were carried out by myself.

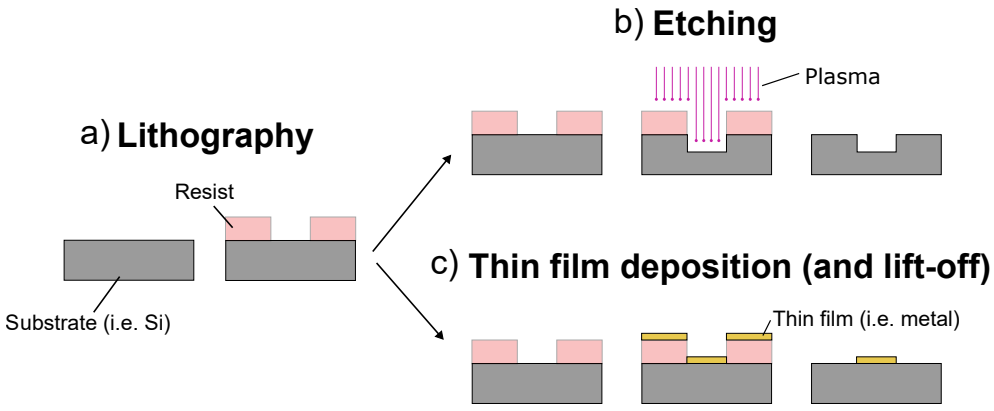


Figure 3.2 Schematic of the principal microfabrication steps.

3.2.1 Lithography

Lithography (Fig. 3.2(a)) transfers patterns onto a substrate for subsequent fabrication steps. Both photolithography and electron beam lithography (EBL) are used in this thesis to meet specific requirements. Each method involves coating the substrate with a polymer film that is sensitive either to UV light (photoresist) or to electrons (EBL resist). Upon exposure, the resist undergoes a chemical transformation, creating a patterned polymer mask after development. For positive resists, UV light or electron exposure breaks down the polymer cross-links, producing smaller chains that are easily dissolved by a developer solution. In contrast, negative resists create additional cross-links when exposed, making the exposed regions insoluble while the unexposed areas are removed during development. The resulting patterned resist can then be used in various processes, such as defining contacts in a lift-off procedure or acting as a hard mask during etching. Photolithography transfers patterns onto the substrate by exposing the photoresist to UV light through a photomask, which consists of a glass substrate with patterns etched onto a chromium layer. While highly efficient for covering large substrate areas in a short period, photolithography is limited in resolution due to factors such as the numerical aperture and UV light wavelength. In this work, photolithography is performed using a mask aligner (MA-6, Karl Suss) at the *Laboratoire de Microfabrication* (LMF) at Polytechnique Montréal, with a minimum resolution of approximately 1 μm. Although effective for larger structures, this resolution is insufficient for nanoscale features like grating grooves.

For applications requiring higher resolution, EBL is employed. Unlike photolithography, EBL does not require a physical photomask as the pattern is directly written onto the resist. The design is divided into writefields, typically 100 μm $\times$ 100 μm or 200 μm $\times$ 200μm, which are

written sequentially as the stage moves. While EBL enables the fabrication of sub-micron patterns, it is considerably slower than photolithography and introduces challenges such as precise alignment between writefields to avoid stitching defects. The EBL system used at LMF (e-line, Raith) operates with a maximum electron acceleration voltage of 30 kV.

3.2.2 Etching

The etching process (Fig. 3.2(b)) involves the removal of material, either uniformly or according to a defined pattern. This can be accomplished through selective or non-selective methods, using either wet etching, which uses chemical solutions, or dry etching, also known as plasma etching, where ions generated in a plasma interact with the material. The desired pattern is typically defined in a masking layer, often a resist from lithography, which must offer good etching selectivity.

Wet etching offers a generally fast and cost-effective alternative to plasma etching, though it typically produces isotropic etch profiles. The isotropic nature of wet etching can lead to undercutting, where the material beneath the resist is also removed. This can result in lower aspect ratios and reduced dimensions compared to the initial design of the mask, which can degrade the intended performance unless these dimension changes are taken into account in the mask design. Figure 3.3 shows a comparison of the etching profiles of an SiO_2 layer using either anisotropic or isotropic etching.

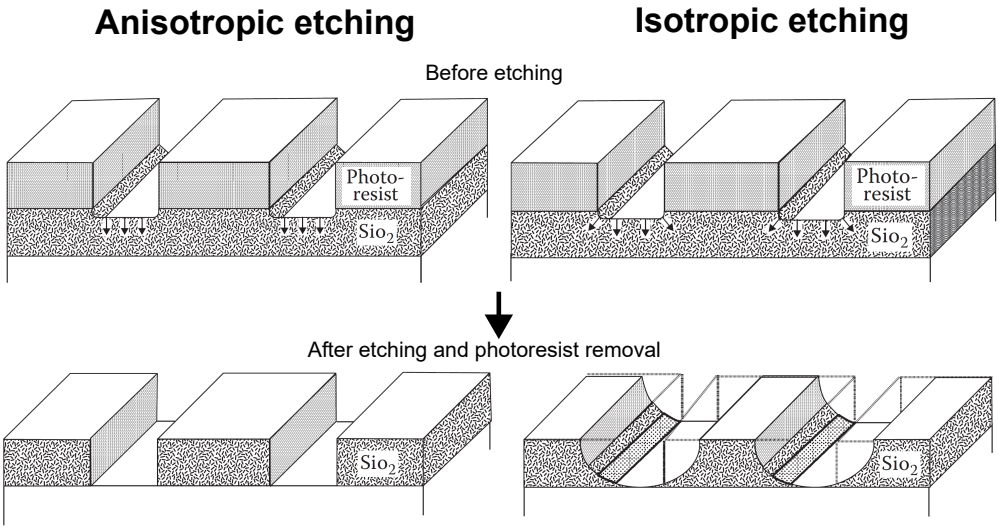


Figure 3.3 Comparison of etching profiles after anisotropic and isotropic etching. Adapted from [240].

On the other hand, plasma etching offers a more anisotropic etching profile. A plasma etching technique commonly used in both academic and industrial settings is reactive ion etching (RIE). In RIE, gases are introduced into a low-pressure chamber, where a capacitively coupled plasma (CCP) is generated between an anode and a cathode plate, the latter holding the sample. A radio-frequency (RF) generator applies a bias that accelerates the reactive ions toward the sample, where they chemically and physically interact with the material, leading to its removal. While RIE can produce high aspect ratio etch profiles, its plasma density is directly linked to the applied bias, making it difficult to finely adjust sidewall profiles. To address this, inductively coupled plasma reactive ion etching (ICP-RIE) offers greater control. In ICP-RIE, a second RF generator, typically a coil surrounding the chamber, controls the plasma density independently of ion acceleration, allowing for more precise tuning of the etching process. Figure 3.4 shows the schematic of an ICP-RIE chamber [241], illustrating the glow discharge (in purple) being generated inside the coil of the ICP generator with the reactive species being accelerated toward the wafer (in green) with the help of the CCP generator.

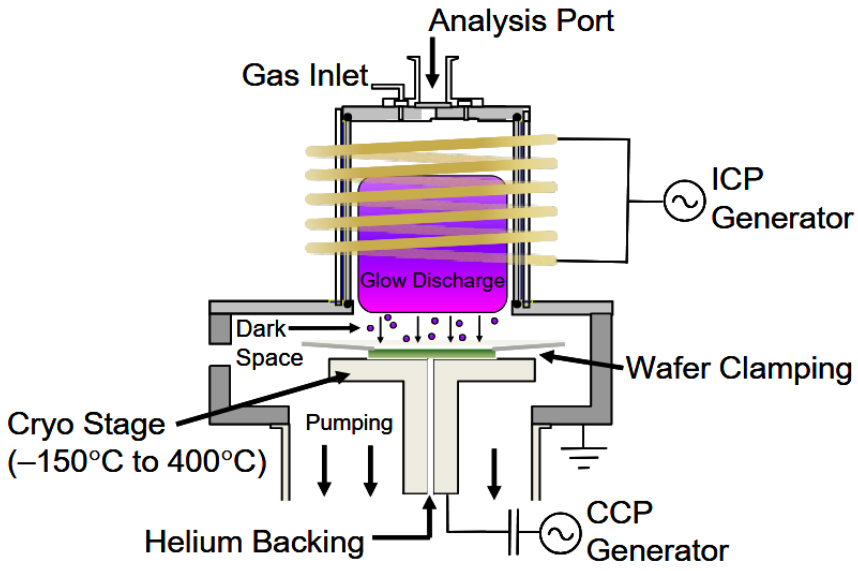


Figure 3.4 Schematic of the plasma chamber of an ICP-RIE tool. Adapted from [241].

The plasma etching process generates reactive species that interact with the material surface, forming volatile compounds that subsequently desorb. This process can involve chemical reactions, physical bombardment, or a combination of both, depending on the gases used and the level of ion bombardment. For example, chlorine ions react chemically with Si and Ge to create volatile compounds like $SiCl_4$ and $GeCl_4$, while inert gases like argon (Ar)

facilitate physical etching by removing material through momentum transfer. Free radicals produced in the plasma, due to their incomplete bonds, react with the material to form volatile byproducts that are vented away. The physical etching aspect, driven by accelerated ions, assists in surface damage and the removal of less volatile byproducts. Together, these chemical and physical processes ensure high selectivity and anisotropy, which are crucial for creating well-defined sidewalls, with various parameters optimized to achieve the desired etching profile.

Efforts in the investigation and optimization of the etching of GeSn thin films have been carried out during this thesis. An overview of the different etchants employed for both dry and wet etching of GeSn that enable the fabrication of microstructures is presented in Appendix A, with a description of etching mechanisms and results regarding the optimization of the etching recipes.

3.2.3 Thin film deposition

Thin-film deposition techniques add material layers to samples. In this study, electron-beam evaporation is utilized to deposit metal layers onto a sample that has been pre-patterned and coated with photoresist. Following the deposition, the photoresist is removed through a process known as lift-off (Fig. 3.2(c)), leaving only the metal layers that were deposited directly onto the substrate. This technique is widely used for the formation of metal contacts on patterned devices.

3.3 Transfer printing

Transfer printing (TP) is a technique that enables the transfer of releasable structures, such as membranes or pre-processed devices, from their original substrate to a different one using a stamp made of an elastomeric material [242–246]. Figure 3.5(a) illustrates the main steps of transfer printing. An elastomeric stamp, typically made of polydimethylsiloxane (PDMS), is used to pick up the released structures (referred to as the ink or donor wafer/chip) and then deposit them onto a target substrate. The pick-up and release process depends on the peeling rate of the PDMS from each substrate as the adhesion strength of the PDMS stamp varies across different regimes, thanks to its viscoelastic properties. These regimes are depicted in Fig. 3.5(b). The separation energy of the PDMS stamp with the released object being peeled vertically can be described by the energy release rate between the two objects ($G_{crit}^{stamp/ink}(v)$) using the following equation [247]:

$$G_{crit}^{stamp/ink}(v) = G_0 \left(1 + \left(\frac{v}{v_0}\right)^n\right) \tag{3.1}$$

where v is the peeling rate, G_0 is the separation energy rate at the slowest peeling rate, v_0 is the reference peeling rate at which the rate is equal to G_0, and n is a parameter that is determined experimentally. The peeling rate is thus adjusted to either print or pick-up the released objects as the release energy is either lower or higher than the separation energy of the ink with the donor substrate ($G_{crit}^{ink/substrate}$). These two regimes are separated by the critical peeling rate v_c, which can be expressed as:

$$v_c = v_0 \left(\frac{G_{crit}^{ink/substrate} - G_0}{G_0}\right)^{1/n} \tag{3.2}$$

In practice, distortions at the interfaces of either the ink or the donor/receiver substrate may affect the adhesion strength. An adhesive layer can be spin coated onto the receiver substrate to provide a superior adhesion of the transferred objects with minimal delamination [221].

TP has been successfully applied to the fabrication of pre-processed active devices [248] and their integration onto silicon photonic dies at the wafer scale [222, 223]. The TP setup used in this thesis (from HQ Graphene), belonging to the Light-Matter Group at Polytechnique Montréal, is placed inside a glovebox under a nitrogen environment and consists of mechanical stages: one holds the sample by vacuum, while the other holds a microscope slide with the PDMS stamp. A microscope enables the user to see through the PDMS stamp to enable the manual alignment of the transferred structures.

To assist in the transfer of larger structures or onto substrates with lower adhesion, a polycarbonate (PC) film can be attached to the PDMS to increase adhesion. This film can also be used for the exfoliation of metal contacts that can then be attached to the stamp, a technique used in Chapter 4. After transfer, the PC film can be dissolved in dichloromethane (DCM), although this solvent also dissolves other organic materials, making it unsuitable for certain processes. In this thesis, relatively large PDMS stamps, typically over 1 mm × 1 mm, are manually cut with a scalpel, which often leads to the simultaneous pick-up of multiple structures and residual dirt particles. To enable more selective pick-up, the stamp can be molded to define posts that correspond to the size of the objects to be picked-up to enable a smaller contact area. The TP manipulations in this work were carried out by myself, with assistance and training provided by Julien Brodeur from the Light-Matter Group at Polytechnique Montréal.

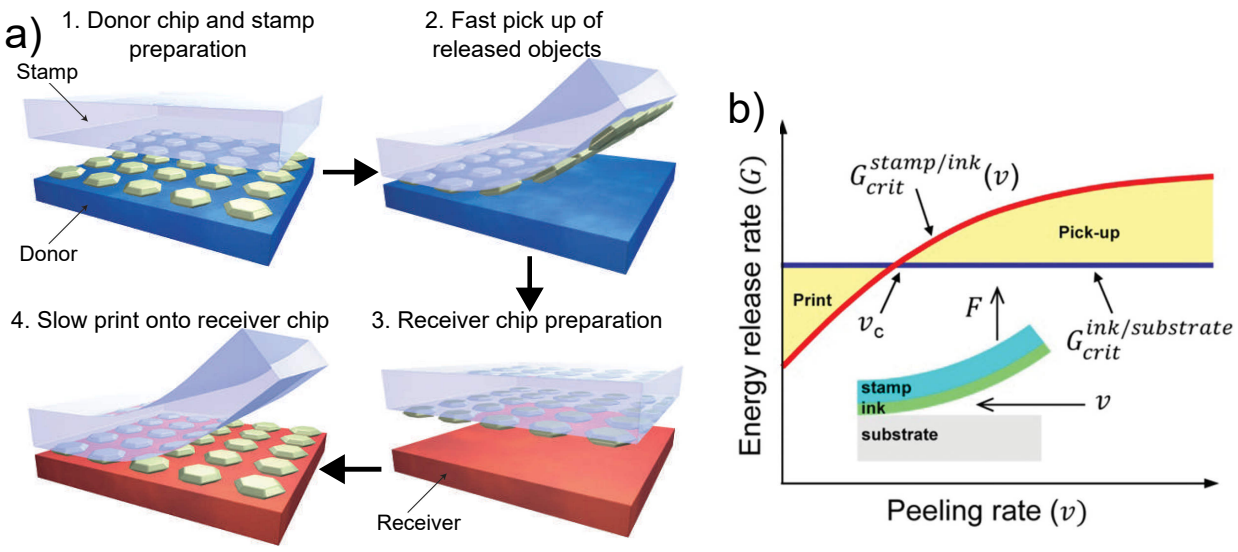


Figure 3.5 Overview of the transfer printing technique. (a) Illustration of the transfer printing steps (adapted from [242]). (b) Energy release rates as a function of the peeling rate for printing and picking up the ink with the stamp (adapted from [245]).

3.4 Characterization methods

This section presents the different characterization methods used in this project to assess either the properties of the grown thin films or the performance of fabricated structures and devices.

3.4.1 X-ray diffraction

X-ray diffraction (XRD) is employed to assess the crystallinity of thin film materials by measuring the interplane distance and extracting the lattice parameter. An X-ray source (typically the K-α1 line from copper with a wavelength of 1.5406 Å) is used to illuminate a sample at a given angle θ, with the reflected rays being collected. While the incident rays are mostly scattered by the material, constructive interference occurs when Bragg's law is satisfied:

$$n\lambda = 2d\sin\theta \tag{3.3}$$

where λ is the wavelength of the X-ray source, d is the distance between the atomic planes observed, and n is the diffraction order. The interference scheme is depicted in Fig. 3.6(a), and Fig. 3.6(b) shows a schematic of an X-ray diffractometer. When analyzing epitaxial

film samples, the layers may be oriented along a preferential orientation. Thus, the sample's orientation is adjusted to an angle ω to align the diffraction condition with respect to the source and the detector. In reciprocal space mapping (RSM), changing both θ and ω can be used to map the reciprocal space of the sample with their respective coordinates [249]:

$$q_x = \frac{1}{\lambda}[\cos(2\theta - \omega) - \cos\omega] \tag{3.4}$$

$$q_z = \frac{1}{\lambda}[\sin(2\theta - \omega) + \sin\omega] \tag{3.5}$$

where q_x and q_z are related to the parallel and perpendicular lattice parameters $a_{\parallel}$ and $a_{\perp}$, as described in Section 2.2.1, and the Miller plane indices (h, k, and l) using the following equations:

$$a_{\parallel} = \frac{\sqrt{h^2 + k^2}}{q_x} \tag{3.6}$$

$$a_{\perp} = \frac{l}{q_z} \tag{3.7}$$

Part of the reciprocal space map of the material is used to extract the lattice constants of each layer present. An asymmetrical plane like (224) is typically chosen for RSM-XRD mapping, as it provides good contrast, as depicted in Fig. 3.6(c). An XRD-RSM measurement presented in Chapter 4 was performed by Dr. Patrick Daoust.

3.4.2 Raman spectroscopy

Raman spectroscopy is a technique based on the analysis of inelastic light scattering and is widely used to identify chemical bonds in materials and compounds. While most photons from the excitation source undergo elastic scattering, a fraction is scattered inelastically, either losing or gaining energy via Stokes and anti-Stokes processes, respectively. This energy shift corresponds to the excitation of specific vibrational or rotational modes in the molecules. In this work, Raman spectroscopy is employed to study the longitudinal optical (LO) Ge–Ge bond, whose spectral position is influenced by strain and the Sn content of the material [239, 250]. The lasers used were either 532 or 633 nm, with penetration depths typically on the order of tens of nanometers. Therefore the properties of the material are mainly probed near the surface. This method is used in Chapter 4 to evaluate the strain variation of membranes that were selectively released. Measurements (inVia, Renishaw) were carried out using the

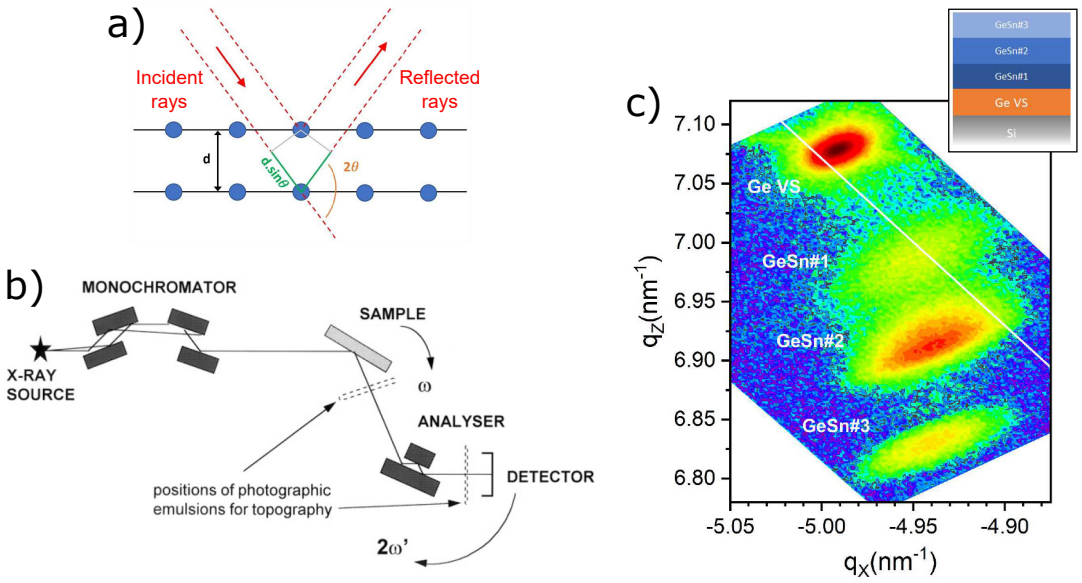


Figure 3.6 Overview of XRD. (a) Working principle of XRD using Bragg's law. (b) Schematic of the main components of an XRD configured for RSM measurements. (c) Example of an RSM map of the sample stack displayed in the inset, where the different layers can be identified. Images adapted from [249].

Raman spectroscopy system at the Materials Characterization Laboratory at Université de Montréal and were performed by Dr. Lu Luo.

3.4.3 Scanning electron microscopy and transmission electron microscopy

The fabrication of microstructures requires qualitative evaluation through visual inspection. Given that the features are smaller than the diffraction limit of optical microscopy, scanning electron microscopy (SEM) is employed to observe nanoscale features. In SEM, an electron beam interacts with the sample, producing secondary electrons (SE), which reveal topographical information with a near-3D effect, and backscattered electrons (BSE), which indicate compositional differences. Figure 3.7(a) shows the schematic of an SEM tool and the interaction at the origin of SE and BSE. The electrons used for probing are typically accelerated to energies ranging between 1 and 30 keV before interacting with the sample.

Transmission electron microscopy (TEM) operates differently by transmitting electrons through an ultrathin sample, usually less than 100 nm thick, prepared via a focused ion beam (FIB). This method allows for the observation of defects and, in some cases, crystalline structures. Although its schematic resembles that of SEM as depicted in Fig. 3.7(a), TEM places the

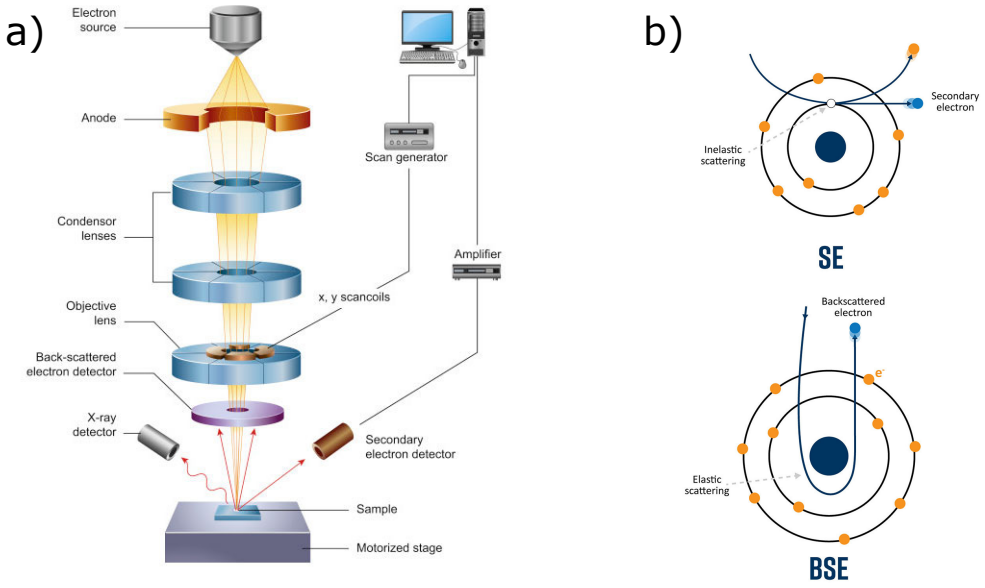


Figure 3.7 Scanning electron microscopy. (a) Schematic of an SEM. (b) Generation of secondary (SE) and backscattered electrons (BSE) with atoms. Adapted from [251].

sample between the condenser and objective lenses, and transmitted electrons are detected by a fluorescent screen. The electrons are accelerated to energies ranging from 100 to 300 keV, which is significantly higher than in SEM. Both SEM and TEM can generate characteristic X-rays that are specific to certain elements. These can be analyzed via energy-dispersive X-ray (EDX) spectroscopy to identify the elemental composition and perform elemental mapping. However, the sensitivity of the measurements decreases with lighter atoms, making the detection of low atomic number elements like carbon and oxygen more challenging.

In this thesis, SEM micrographs were acquired by myself using a system at the *Laboratory for the Study of Calcified Tissues and Biomaterials* at Université de Montréal (Regulus 8220, Hitachi) to assess structural morphology after fabrication steps. TEM and EDX, performed by Dr. Sebastian Koelling, were used to characterize the $Ge_{0.89}Sn_{0.11}$ material discussed in Chapter 4, with the results shown in Fig. 4.1.

3.4.4 Photoluminescence

Photoluminescence (PL) evaluates light emission and extracts bandgap information by analyzing light emitted after excitation with above-bandgap photons. Figure 3.8 summarizes the basic mechanisms of PL, showing photon emission after excitation. Figure 3.9 presents the PL setup used in the work of this thesis. An 808 nm laser diode used for excitation

is modulated by a mechanical chopper for lock-in detection before passing through a beam splitter to then be focused onto the sample via a microscope objective. The emitted light from the sample is collected through the same microscope objective and is redirected by the beam splitter toward the Fourier-transform infrared (FTIR) spectrometer (Vertex 70, Bruker). FTIR generates an interference pattern by splitting the incident light into two paths: one to a fixed mirror and the other to a motorized mirror that creates an optical path difference. These beams recombine at the beam splitter, producing an interferogram as the mirror sweeps across path differences. A Fourier transform converts the interferogram into a spectrum. Before reaching the liquid-nitrogen-cooled InSb detector, the light passes through a 1350 nm long-pass filter to block light from the excitation laser. The photocurrent from the detector is amplified and synchronized with the chopper frequency using a lock-in amplifier, isolating the signal from noise. The resulting spectrum typically shows a broad peak near the bandgap energy of the sample. In this thesis, PL measurements, performed at room temperature, are detailed in Chapter 4. For micro-photoluminescence (μ-PL), a CMOS camera is integrated into the setup to position the objective over specific microstructures, such as GeSn membranes. The PL measurements were carried out by myself with assistance and training provided by Dr. Mahmoud R. M. Atalla.

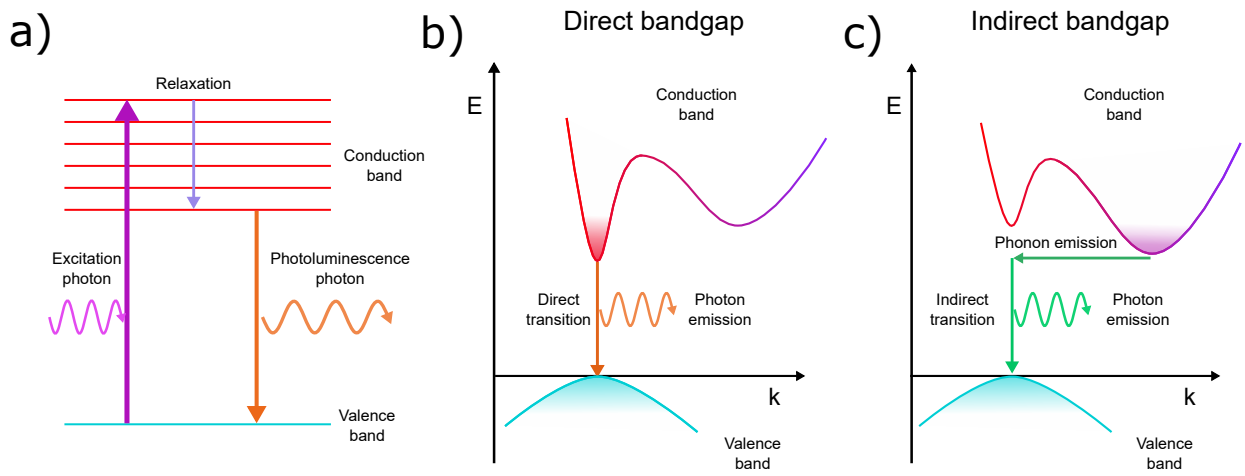


Figure 3.8 Working principle of photoluminescence. (a) Generation of a photoluminescence photon after the material is excited by an excitation source. (b) Emission of a photon in direct bandgap material. (c) Emission in an indirect bandgap material, where a phonon is also required.

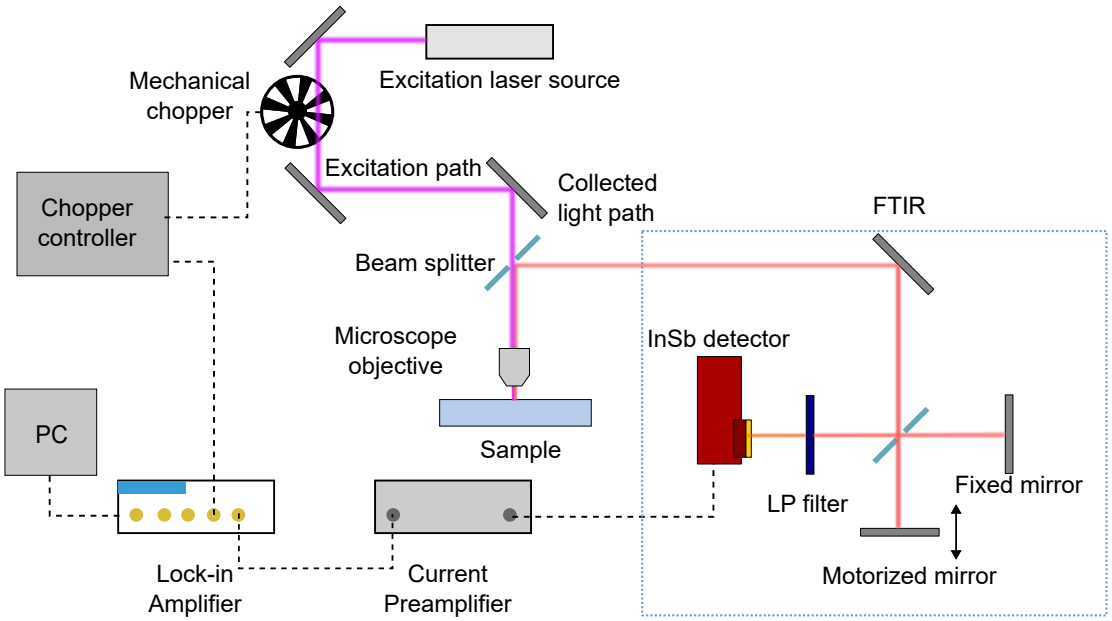


Figure 3.9 Photoluminescence setup showing the components and light path of the FTIR.

3.4.5 Responsivity measurements

As the fabricated devices mainly involve photodetectors, we are interested in evaluating their key performance metrics, specifically responsivity and dark current. Dark current (I_{dark}) is the current in a device without illumination and originates from thermal noise and electrically active defects in addition to other leakage mechanisms. Initial electrical performance is assessed at room temperature using a semiconductor parameter analyzer (4200-SCS, Keithley) to measure current-voltage (I–V) characteristics and observe dark current behavior. The responsivity (R) is the amount of photocurrent (I_{ph}) generated per unit power of incident light at a given wavelength, defined as:

$$R = \frac{I_{ph}}{PA} \tag{3.8}$$

where P is the incident light power density and A is the active area exposed to light. The photocurrent is calculated by subtracting the dark current from the total current under illumination at a given wavelength and power. Spectral responsivity is measured using an FTIR spectrometer (Fig. 3.10). Mid-infrared light from an internal tungsten lamp passes through the interferometer, illuminates the device, and the resulting photocurrent is collected via electrical probes. A current preamplifier supplies the bias voltage while measuring the photocurrent. A 40× microscope objective is employed to focus light to a ∼7 μm diam-

eter spot. However, the current values are relative to the lock-in amplifier and the current amplifier, resulting in a relative responsivity spectrum $R_{rel}(\lambda)$, which can be used to identify the detection cutoff wavelength. The responsivity spectrum is calibrated by measuring the photocurrent with a 1550 nm laser using the Keithley 4200-SCS. The absolute spectral responsivity $R_{abs}(\lambda)$ is then obtained from the relative responsivity $R_{rel}(\lambda)$ using:

$$R_{abs}(\lambda) = R_{rel}(\lambda)\frac{R_{abs}(1550\text{ nm})}{R_{rel}(1550\text{ nm})} \tag{3.9}$$

I performed the responsivity measurements with assistance and training from Dr. Mahmoud R. M. Atalla.

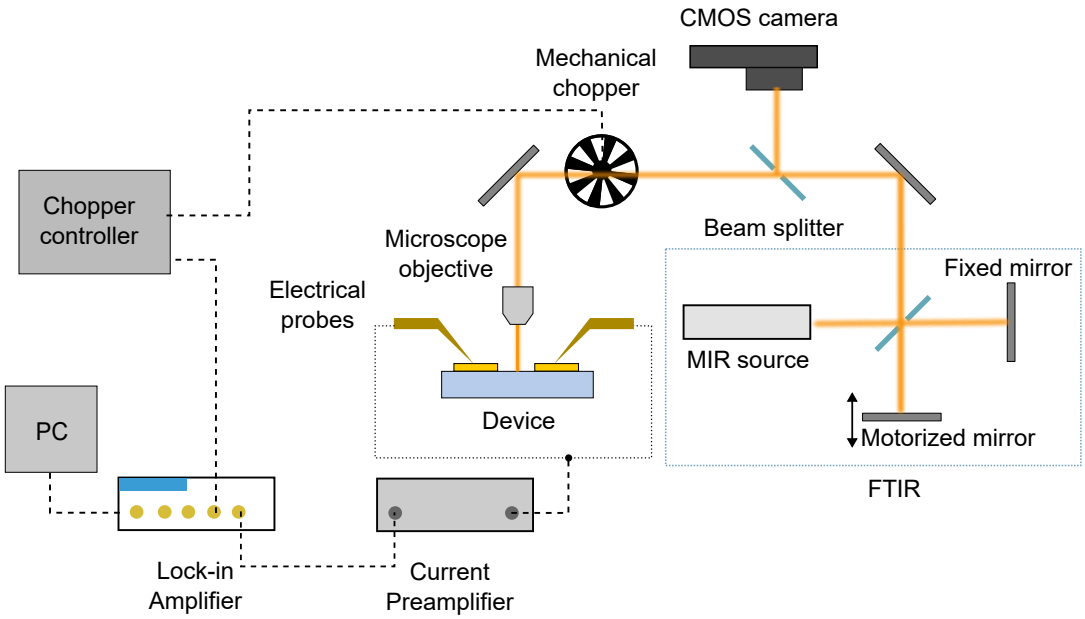


Figure 3.10 Responsivity setup using the FTIR.

3.4.6 PIC characterization setup

Waveguide-based PIC devices require angled light injection into surface grating couplers (SGCs), making the previous setup unsuitable. To address this, a dedicated setup was built for measuring the responsivity of PIC photodetectors, using a 5-axis stage to position optical fibers at the required angle, which will be used in Chapter 6. Figure 3.11 shows a CAD image and a picture of the PIC characterization setup and Fig. 3.12 shows a schematic of the configuration used for responsivity measurements. The optical fibers are placed into fiber chucks and mounted into 3D-printed fiber chuck mounts fixed at a 10° angle. Two fibers

enable transmission measurements through waveguides, while two electrical probes collect current from the integrated devices. For responsivity measurements, only a single fiber is necessary to inject light into the waveguide. A 2330 nm laser (custom DBR laser from Nanoplus) is collimated into one optical fiber via a fiberport collimator (PAF2P-11E, Thorlabs) and a mechanical chopper modulates the incident light for lock-in detection. Although standard SMF-28 fibers provide sufficient transmission at 2330 nm, fluoride fibers such as fluorozirconate (ZrF_4) or fluoroindate (InF_3) glass fibers are more suitable for mid-infrared wavelengths but are mechanically fragile and require careful handling. Currently, the setup is limited to single-wavelength lasers due to the wavelength-dependent properties of both the fiber collimation and the surface grating couplers. The design of the PIC setup and the measurements using it were carried out by myself.

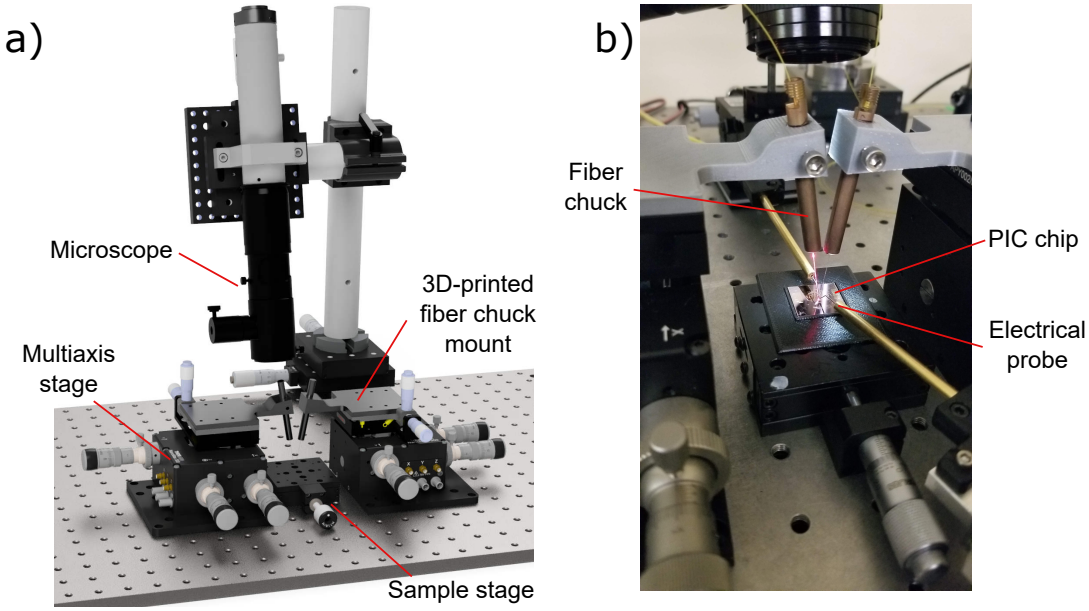


Figure 3.11 PIC characterization setup. (a) CAD image of the different components used. (b) Picture of the actual setup with optical fibers and electrical probes aligned onto a PIC chip.

3.5 $k \cdot p$ theory

Calculations of the electrical and optical properties of GeSn alloys were performed using a model developed in the group based on $k \cdot p$ perturbation theory, which is a semi-empirical method for computing the band structure of a material. The code employs an 8-band model, which considers the conduction band, the light-hole band, the heavy-hole band, and the

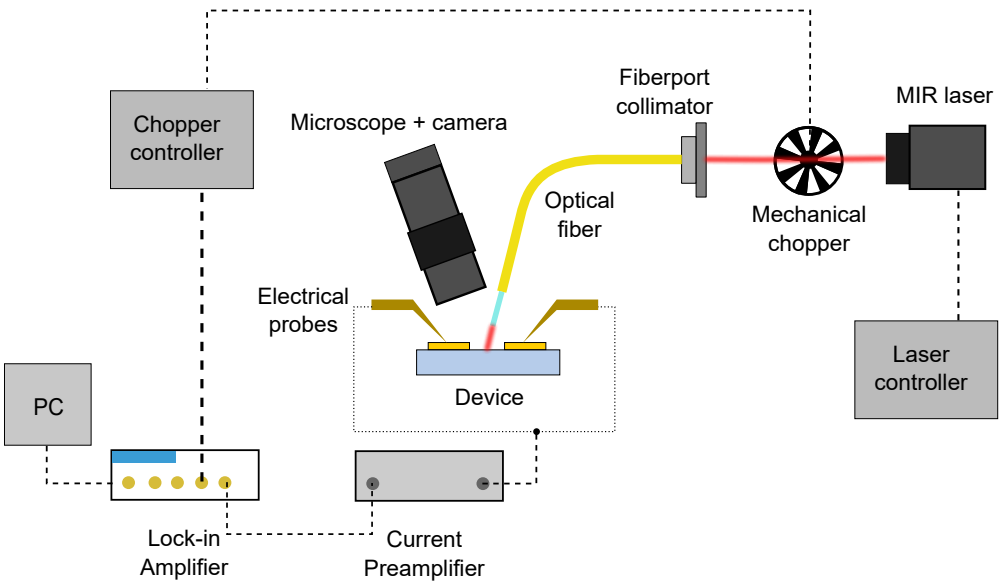


Figure 3.12 Responsivity setup using an optical fiber in the PIC setup.

spin-orbit split-off valence bands [252]. More details on the formalism employed in this code can be found in [253] and [254]. The absorption coefficient as a function of photon energy is derived by considering interband transitions between the conduction and valence bands. These results are used in Chapters 4 and 5 for the calculation of the optical properties of GeSn alloys. The calculation of the bandgap energy, and consequently several extracted results, relies on the bowing parameter for GeSn. The literature reports different values ranging from 2.4 to 2.8 eV. It is expected that finding a universal expression for b_{GeSn} may be nearly impossible, as it appears to vary as a function of composition and strain [255]. In Chapter 4, a value of 2.85 eV was used to fit the respective absorption cutoff wavelengths observed in the spectral responsivities of the membrane (0% compressive strain) and as-grown (-0.6% compressive strain) samples. All calculations were carried out at 300 K and included a p-type carrier concentration of $1 \times 10^{17}\,\mathrm{cm}^{-3}$. More accurate results can be obtained by considering more bands in the model, with a significant increase in the computation time required. The 8-band model is suitable for calculations around the Γ point for small momentum (k) values. The framework has been developed by several former members of the Nano & Quantum Semiconductors Laboratory at Polytechnique Montréal, such as Dr. Anis Attiaoui and Dr. Patrick Del Vecchio. Calculations using this framework were performed by myself with assistance from Gérard Daligou.

CHAPTER 4 ARTICLE 1: TRANSFER-PRINTED MULTIPLE GESN MEMBRANE MID-INFRARED PHOTODETECTORS

This article was submitted to the *IEEE Journal of Selected Topics in Quantum Electronics* on June 2nd, 2024, accepted on July 22nd, 2024, and published on August 26th, 2024. (JSTQE, 31(1), 2024: 3800410; doi:10.1109/JSTQE.2024.3450302). This paper presents a method for transfer printing multiple GeSn membrane detectors, building on prior work carried out in the group [14]. The method employs relaxed $Ge_{0.89}Sn_{0.11}$ layers to minimize structural bowing, an adhesive layer to improve transfer yield, and exfoliated contacts to enable single-step transfer of photoconductive devices. The $Ge_{0.89}Sn_{0.11}$ membranes are characterized as mid-infrared photodetectors and exhibit an extended cutoff wavelength of up to 3.1 μm. This approach could enable low-cost, transferable mid-infrared photodetectors compatible with diverse substrates. The ultimate goal was to establish a reliable membrane transfer method for patterned substrates, facilitating PIC integration, as demonstrated in Chapter 6 with slight methodological variations.

Authors

Cédric Lemieux-Leduc, Mahmoud R. M. Atalla, Simone Assali, Sebastian Koelling, Patrick Daoust, Lu Luo, Gérard Daligou, Julien Brodeur, Stéphane Kéna-Cohen, Yves-Alain Peter, Oussama Moutanabbir

Department of Engineering Physics, École Polytechnique de Montréal, Montréal, C.P. 6079, Succ. Centre-Ville, Montréal, Québec, Canada H3C 3A7

4.1 Abstract

Due to their narrow band gap and compatibility with silicon processing, germanium-tin ($Ge_{1-x}Sn_x$) alloys are a versatile platform for scalable integrated mid-infrared photonics. These semiconductors are typically grown on silicon wafers using Ge as an interlayer. However, the large lattice mismatch in this heteroepitaxy protocol leads to the build-up of compressive strain in the grown layers. This compressive strain limits the material quality and its thermal stability besides expanding the band gap, thereby increasing the Sn content needed to cover a broader range in the mid-infrared. Released $Ge_{1-x}Sn_x$ membranes provide an effective way to mitigate these harmful effects of the epitaxial strain and control the band gap energy while enabling the hybrid integration onto different substrates. Nevertheless, the epitaxial

strain is also known to affect the fabrication of membrane devices due to a significant bowing upon release from the growth substrate, especially in high Sn content structures. With this perspective, herein these limitations are discussed and addressed by introducing bow-free, strain-relaxed $Ge_{1-x}Sn_x$ membranes in the fabrication of mid-infrared devices. These devices are transfer-printed with metal contacts to create multiple photodetectors in a single transfer step. The resulting photodetectors exhibit an extended photodetection cutoff reaching a wavelength of 3.1 μm for a Sn content of $x = 0.11$ compared to as-grown photoconductive devices. The latter yields a reduced cutoff of 2.8 μm due to the inherent compressive strain. Additionally, a significant reduction in the dark current of two orders of magnitude is observed, which could be related to the formation of a Schottky barrier or to a change in the contact resistivity during the processing steps of the membranes. Furthermore, the impact of chemical treatment and annealing on the device performance was also investigated showing a further reduction in the dark current. The demonstrated transfer printing, along with the use of an adhesive layer, allows the transfer of multiple $Ge_{1-x}Sn_x$ membranes onto virtually any substrate. This approach paves the way for scalable fabrication of hybrid optoelectronic devices leveraging the tunable band gap of $Ge_{1-x}Sn_x$ in the mid-infrared range.

4.2 Introduction

The mid-wave infrared (MWIR, $2-8$ μm) range is a highly strategic portion of the electromagnetic spectrum relevant to numerous applications in sensing, imaging, and free-space communication [137, 174, 177, 256]. Current commercial platforms for MWIR detectors predominantly rely on III-V semiconductors such as InSb [257] and type-II superlattices (T2SL) [258, 259] and II-VI compounds including HgCdTe (MCT) [260, 261]. InSb and MCT detectors cover wavelengths up to 7 μm and 12 μm respectively, which enabled the development of MWIR imaging systems based on focal plane arrays (FPAs) [262, 263]. While these technologies are mature, they remain costly, suffer from limited integration with silicon-based electronics, and are associated with a low bandwidth that is usually below 10 GHz for photodetectors with a cutoff wavelength above 2.3 μm [96]. Recently, germanium-tin ($Ge_{1-x}Sn_x$) alloys have emerged as alternate narrow-band gap materials for silicon-compatible MWIR optoelectronics [10]. Indeed, this class of semiconductors covers a broad range of band gap energies by controlling the lattice strain and Sn content. $Ge_{1-x}Sn_x$ materials have been used in photodetectors operating at room temperature in the near-infrared (NIR) and MWIR [15, 87, 89, 91, 264], as well as for modulation based on the Franz-Keldysh effect [108]. Additionally, $Ge_{1-x}Sn_x$ alloys also pave the way towards silicon-compatible light sources. Indeed, as the atomic content of Sn increases, the band gap at the Γ-valley diminishes faster than the one at the

L-valley, leading to a transition to a direct band gap when the Sn content exceeds 10 at.% Sn in a relaxed layer [10]. This band gap directness has been exploited to implement silicon-integrated light emitting diodes [77, 79, 265] and lasers [16, 63, 65, 73, 266]. However, due to the low solubility of Sn in Ge (< 1 at.%) the growth of high-quality $Ge_{1-x}Sn_x$ layers with the minimal Sn composition required for MWIR applications is challenging. Furthermore, the alloy suffers from a substantial lattice mismatch induced by the 14.7% difference between Ge and Sn atomic radii, resulting in compressively strained layers. This strain build-up leads to an increase in the band gap energy at the Γ-valley and impedes the Sn incorporation during growth, thus shrinking the wavelength range covered by the compressively strained devices [267].

Table 4.1 Comparison of properties of different photodetectors based on $Ge_{1-x}Sn_x$ membranes.

Substrate	Sacrificial layer	Sn content (%)	Responsivity (mA/W)	Cutoff wavelength (μm)
PET/SU-8[a]	SiO_2[b]	8	1.03 @ 2 μm[c]	2.08 [268]
SiO_2/Si	Ge-VS	17	0.4 @ 1.55 μm	4.6 [14]
PET/SU-8	SiO_2	8	148.5 @ 1.55 μm[d, e]	> 2[f] [269]
SiO_2/Si[g]	SiO_2	10	510 @ 2 μm	– [270]

[a] PET: Polyethylene terephthalate.
[b] The GeSn sample is wafer bonded to an oxidized Si substrate before the release.
[c] Responsivity increases to 3.68 mA/W with a 0.42% tensile strain.
[d] TiN/GeSn junction.
[e] Responsivity increases to 218 mA/W with a 0.3% tensile strain.
[f] Extension of ∼ 180 nm in the optical absorption wavelength.
[g] Membrane transferred on a distributed Bragg reflector (DBR).

Several approaches were investigated to alleviate these drawbacks [271], including the growth of graded $Ge_{1-x}Sn_x$ buffers where the composition of Sn is gradually increased by controlling the temperature and precursors flow during growth [121, 122, 272]. This method was found to be effective in partially relaxing the compressive strain in the top layer by allowing the misfit dislocations to glide in the initially grown $Ge_{1-x}Sn_x$ buffer layers. $Ge_{1-x}Sn_x$ nanowires offer an alternative method to relax strain at the facets without compromising the crystalline quality, enabling nanoscale optoelectronic devices with promising performance [109–114]. For applications requiring larger active material areas, strain-relaxed membranes emerge as a promising solution to mitigate the harmful effects of compressive strain [244, 273]. Material properties that are practically unattainable by conventional growth or wafer bonding tech-

niques can be achieved through the transfer of membranes onto a wide variety of substrates using transfer printing [245, 246]. While group-IV [274, 275] and III-V [276] semiconductor membranes have been introduced for broadband photodetection and light emission, their operational range does not cover the MWIR. Although progress has been made in membranes based on InAs/InAsSb T2SLs [277] and ultrathin MCT layers [278], $Ge_{1-x}Sn_x$ alloys provide a solution to implement transferable group-IV MWIR membrane-based photodetectors [14, 268–270, 279]. Table 4.1 summarizes the reported properties of photodetectors based on $Ge_{1-x}Sn_x$ membranes developed by different groups. One approach is based on wafer bonding of a GeSn on an oxidized Si wafer to form a GeSn-on-insulator (GeSnOI) substrate. Membranes were subsequently released by etching the SiO_2 layer using hydrofluoric acid (HF) and transferred onto a flexible substrate [268, 269]. However, this involves several processing steps as the surfaces of the two wafers must be sufficiently flat to obtain a high yield during the bonding step. Alternatively, the germanium virtual substrate (Ge-VS), usually grown before $Ge_{1-x}Sn_x$, can be selectively removed using dry etching using a CF_4 plasma [14]. Using this approach results in free-standing membranes in fewer processing steps, but the etching selectivity decreases for low Sn compositions, and the $Ge_{1-x}Sn_x$ surface can be damaged or over-etched when attempting to fabricate large membranes (more than 20 μm $\times$ 20 μm) [273]. The fabrication of $Ge_{0.83}Sn_{0.17}$ membrane photodetectors using the latter approach resulted in an impressive increase in the detection cutoff from 3.5 μm to 4.6 μm while maintaining operation at room-temperature [14]. Moreover, $Ge_{1-x}Sn_x$ membranes provide a reduced dark current as the conductive Ge and Si layers underneath are removed, which helps in improving the power dissipation and allows the use of a higher bias voltage. However, these membranes suffered from a structural bowing that reduces their adherence to the host substrate after using transfer printing. Alleviating these limitations requires revisiting the growth process to minimize the compressive strain in addition to introducing an adhesive layer [243] and reducing the number of post-processing steps by adding transferable contacts [280].

Herein, to demonstrate the mass-transfer of GeSn membranes, we fabricated $Ge_{0.89}Sn_{0.11}$ membrane metal-semiconductor-metal (MSM) photodetectors that operate at room temperature with a cutoff of 3.1 μm and a reduced dark current. The growth of a single $Ge_{0.89}Sn_{0.11}$ layer led to membranes with a reduced bowing and an initial compressive strain of -0.6% before the membrane release. The reduced bowing helps in transferring membranes efficiently as an array at a high yield while the relaxation of the residual compressive strain aids extend the photodetection cutoff. To streamline the processing steps, transferable contacts are initially exfoliated and affixed to an elastomeric stamp before the transfer printing step, ensuring their attachment to the membranes. This results in an array of contacted devices upon completion of the transfer process. SU-8, which is used as an adhesive and an

insulating layer, is spin-coated on the host substrate before transfer printing. Subsequently, the performance of the membrane devices is systematically analyzed and compared to their as-grown counterparts, followed by the discussion of the influence of chemical treatment and annealing on device characteristics.

4.3 Results and discussion

4.3.1 Growth and characterization of GeSn epilayers

The $Ge_{0.89}Sn_{0.11}$ alloy growth was carried out in a low-pressure chemical vapor deposition (CVD) reactor on a 4-inch Si (100) wafer. First, a 1.02 μm-thick Ge-VS was grown using 10% monogermane (GeH_4) and a continuous flow of pure hydrogen following a two-temperature growth protocol at 460 °C and 600 °C. In addition to reducing the lattice mismatch between the Si substrate and GeSn, Ge-VS also acts as a sacrificial layer, facilitating the GeSn membranes underetching and release.

Subsequently, a $Ge_{0.89}Sn_{0.11}$ film was grown on Ge-VS at 320 °C using GeH_4 and $SnCl_4$ precursors. The microstructure of the as-grown material was assessed using cross-sectional transmission electron microscopy (TEM), as displayed in Fig. 4.1(a). Notably, a high density of threading dislocations and defects is localized at the Ge-VS/Si and $Ge_{0.89}Sn_{0.11}$/Ge-VS interfaces, indicative of misfit dislocation gliding [121, 267] while the top of the $Ge_{0.89}Sn_{0.11}$ layer is relatively defect-free. To obtain a more detailed understanding of the alloy's elemental composition, energy-dispersive X-ray spectroscopy (EDX) is employed. Fig. 4.1(b) exhibits the measured Sn and Ge composition profiles, revealing the approximate atomic fraction of Ge and Sn across the $Ge_{1-x}Sn_x$ layer. The layer thickness is estimated to be approximately 520 nm and the Sn composition starts at 9% as it increases towards 12% from the bottom to the top of the $Ge_{1-x}Sn_x$ layer respectively. The background noise coming from the surrounding elements during the EDX measurements was subtracted to avoid an overestimation of the Sn content.

For a comprehensive analysis of the composition and strain in the sample, X-ray diffraction reciprocal space mapping (XRD-RSM) is performed around the asymmetrical (-2-24) reflection peak, as depicted in Fig. 4.1(c). The map reveals peaks related to the Ge-VS and the GeSn layers. Using the GeSn peak, a composition of 11.1% Sn and an in-plane biaxial compressive strain $\varepsilon_{\parallel}$ of -0.6% are extracted. This composition value is within the range observed in the Sn profile from EDX in Fig. 4.1(b) and will be used throughout this study.

Fig. 4.1(d) depicts calculations of the absorption spectrum based on the semi-empirical 8-band $k \cdot p$ theory [253] as the compressive strain is varied from -1% to 0% at 300 K. Bowing

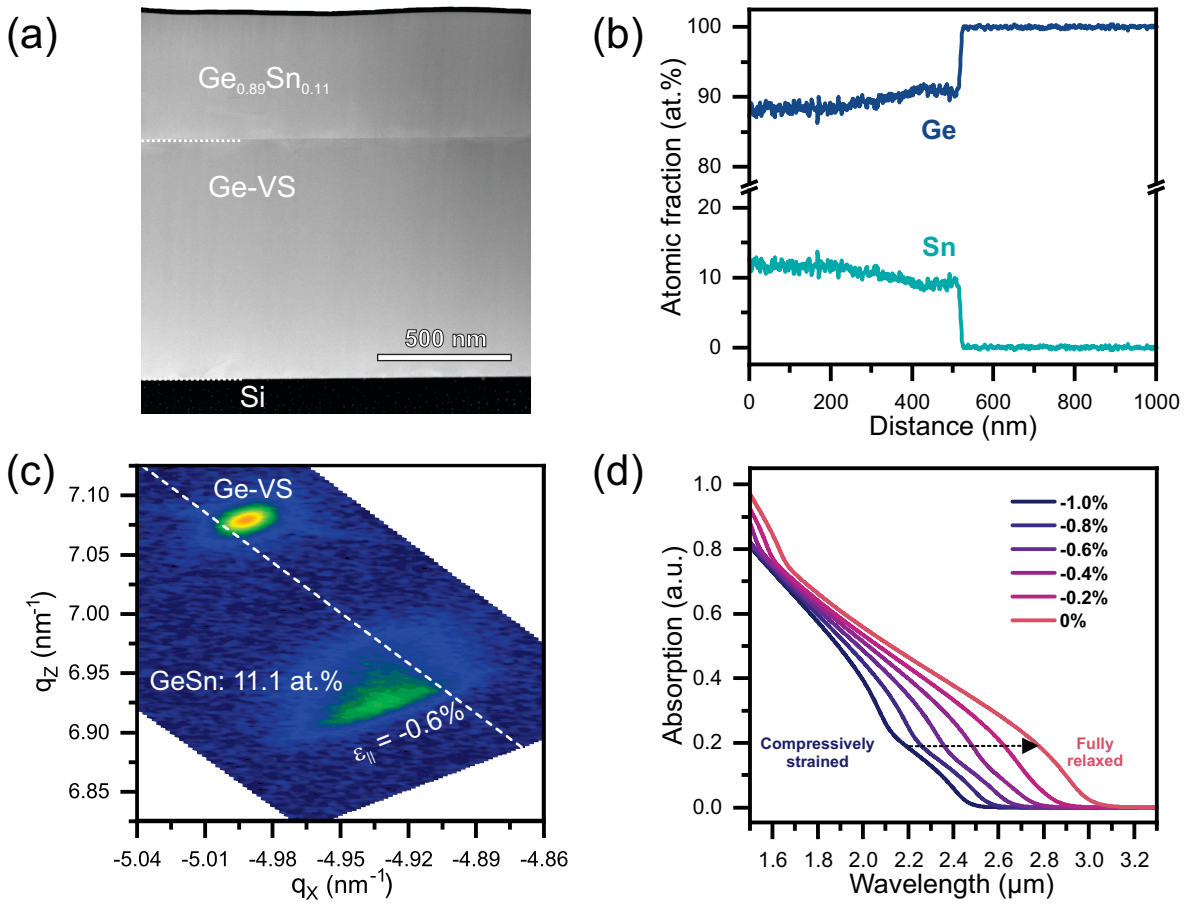


Figure 4.1 Properties of the as-grown $Ge_{0.89}Sn_{0.11}$ alloy. (a) Cross-sectional TEM image of the layer stack. (b) EDX Ge and Sn profiles in the grown layer, starting from the top of the GeSn layer. (c) XRD-RSM around the asymmetrical (224) reflection peak, providing the composition and strain in the as-grown $Ge_{0.89}Sn_{0.11}$ layer. (d) 8-band $k{\cdot}p$ calculations of the room-temperature absorption of the $Ge_{0.89}Sn_{0.11}$ layer by varying the in-plane strain from compressive strain (-1%) to full relaxation (0%).

parameters are implemented in the model to reduce the relative error in the estimation of the band gap at the Γ and L symmetry points using Vegard's law. Strain-independent values of 2.85 eV at the Γ point and 1.23 eV at the L point were used for the bowing parameters in these calculations. Expectedly, a remarkable increase in the absorption wavelength cutoff is observed as the band energy shrinks due to strain relaxation.

4.3.2 GeSn membrane fabrication and transfer printing

The fabrication of $Ge_{0.89}Sn_{0.11}$ membranes starts with a standard photolithography of the as-grown sample to pattern an array of 20 μm × 20 μm squares with a pitch of 200 μm × 400 μm,

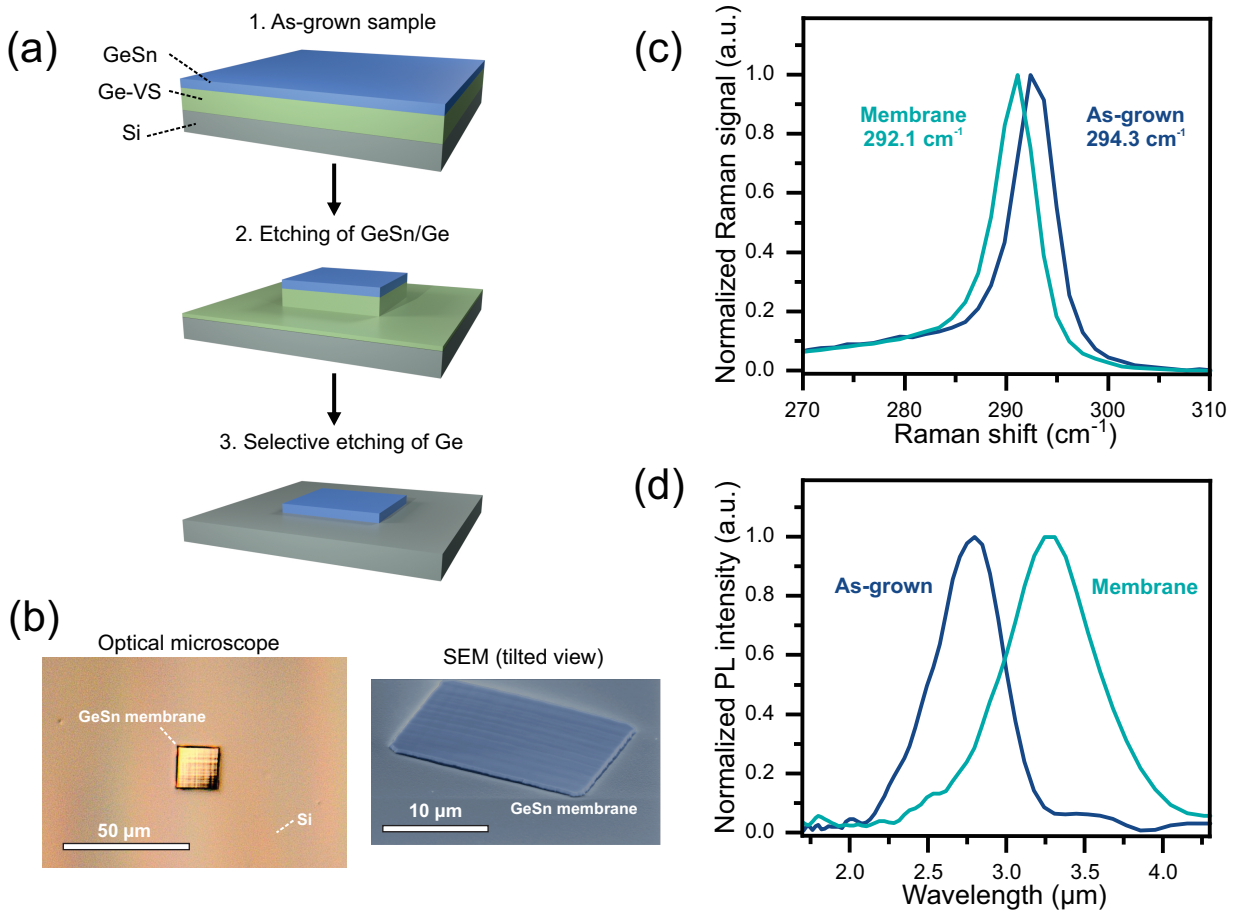


Figure 4.2 Membrane fabrication. (a) Illustration of the $Ge_{0.89}Sn_{0.11}$ membrane fabrication steps. (b) Optical microscope image and SEM micrograph of a released $Ge_{0.89}Sn_{0.11}$ membrane. (c) Raman spectroscopy measurements of the as-grown and the membrane samples with the position of the Ge−Ge longitudinal phonon Raman peak indicated. (d) Photoluminescence spectra of the as-grown and membrane samples acquired at room temperature.

as shown in Fig. 4.2(a). These patterns are subsequently transferred onto the $Ge_{0.89}Sn_{0.11}$ sample by wet etching of GeSn and Ge-VS layers using a mixture of ceric ammonium nitrate and nitric acid. The wet etching process induces an undercut of approximately 1 μm with tapered sidewalls, reaching a depth of 1.4 μm. By selectively etching the Ge-VS, membranes are formed and fully released from the Si substrate using a CF_4-based plasma dry etch. The selectivity in etching Ge-VS rather than $Ge_{1-x}Sn_x$ arises from the reaction of fluoride-based radicals with Sn at the exposed surface of $Ge_{1-x}Sn_x$. This reaction produces a thin, non-volatile SnF_y layer, effectively shielding the layer from further etching and ensuring a high selectivity [281]. Images of a single released $Ge_{0.89}Sn_{0.11}$ membrane are shown in Fig. 4.2(b) using optical microscopy (left) and scanning electron microscope (SEM) (right). A slight

downward bowing can be observed in the SEM image, indicating either remaining traces of the Ge-VS layer at the center of the membrane or a partial etching of the edge compared to the outer contour of the membrane.

To assess the impact of the underetching process on strain relaxation, room-temperature Raman spectroscopy measurements were conducted on both as-grown and membrane samples. The acquisition of the Raman spectra shown in Fig. 4.2(c) was carried out using a 633 nm excitation laser and a 100× microscope objective lens. The Ge−Ge longitudinal (LO) phonon Raman peak is located around 300 cm^{-1} in pure Ge and it can either red-shift as the Sn concentration increases or blue-shift as the compressive strain increases [239]. The peak position shifts from 294.3 cm^{-1} in the as-grown alloy to 292.1 cm^{-1} in the membrane, which indicates a relaxation of the compressive strain. Here, a fit with an exponentially modified Gaussian function was performed to extract the central frequency of the asymmetrical Raman peak [239]. It is important to note that the released membranes may be subject to local strain fluctuations [14], which should impact the optical properties as the band structure is locally modified. Room-temperature photoluminescence (PL) analysis was carried out on the investigated samples using an 808 nm excitation laser. The PL peak serves as an approximate indicator of the band gap energy and the absorption range. A 40× microscope reflective objective lens with a 7 μm spot size was used to focus the light on a single $Ge_{0.89}Sn_{0.11}$ membrane. The spectrum of the as-grown sample depicts a single peak centered at 2.8 μm while the membrane shows a single peak at 3.3 μm. This redshift of the PL peak indicates a reduction of the band gap energy in the released membrane compared to the as-grown sample, which is in qualitative agreement with the $k \cdot p$ calculations (Fig. 4.1(d)), showing that the band gap is expected to shrink as the compressive strain is relaxed. Systematic temperature-dependent PL studies of released GeSn layers compared to as-grown layers at Sn content of 13 and 17 at.% Sn can be found in a previous study [255]. The same study also showed that the underetching step did not affect the material quality in microdisks with 17 at.% Sn.

The fabrication of $Ge_{0.89}Sn_{0.11}$ membrane photodetectors was carried out using a transfer printing technique [245, 246], as illustrated in Fig. 4.3(a). This technique utilizes a setup equipped with a microscope and mechanical stages within a glovebox with a nitrogen environment. An elastomeric PDMS stamp, sized roughly 2 mm × 2 mm, enables the simultaneous pick up of multiple membranes. To create photoconductive detectors, metal contacts are first detached from a separate substrate using mechanical exfoliation. These contacts are then affixed to a PDMS stamp before picking up the membranes. In this approach, pre-processed exfoliated contacts are utilized since the adhesive layer (SU-8) can be easily removed during a metal lift-off process. This technique is versatile and can be employed

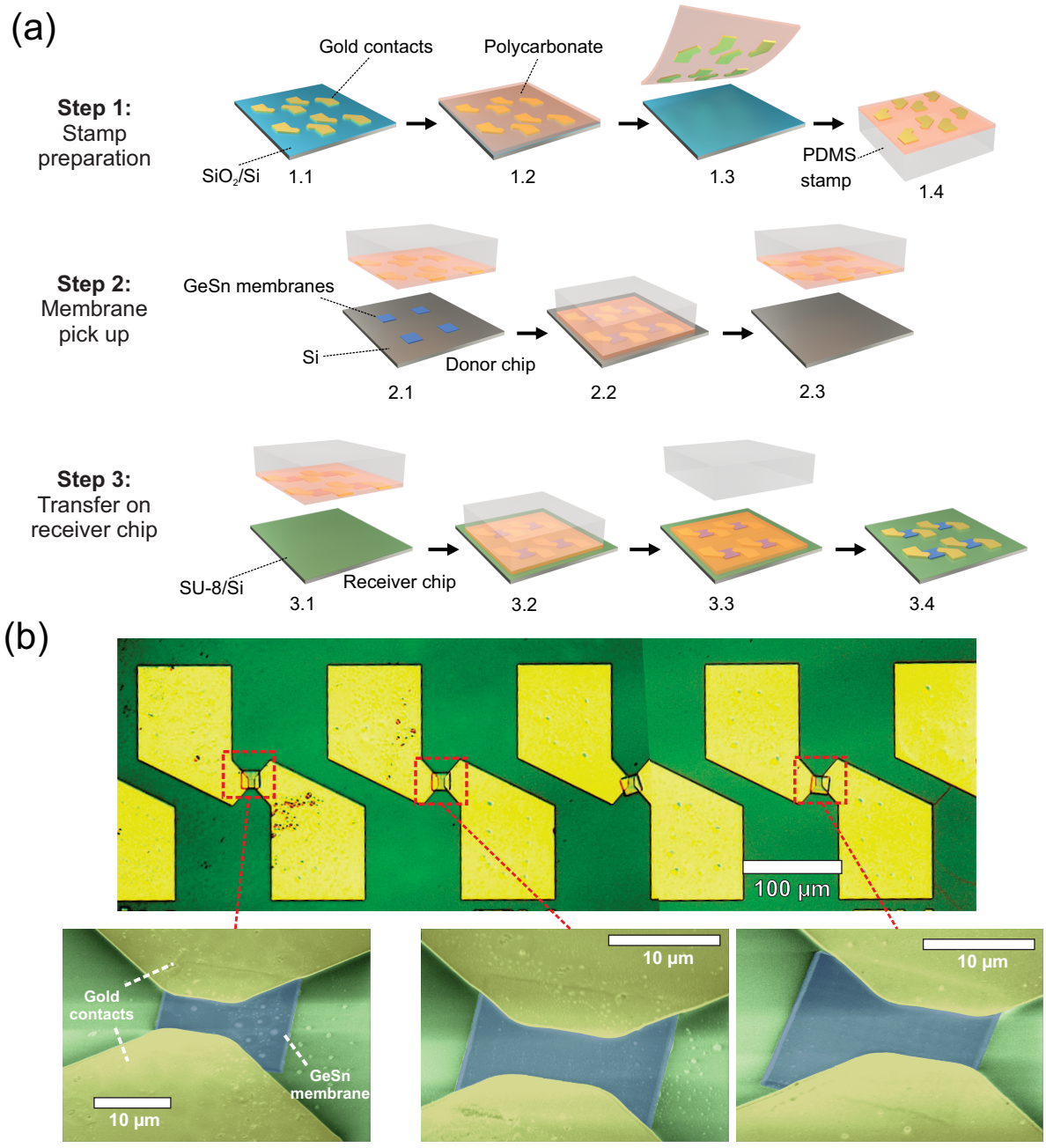


Figure 4.3 Membrane photodetector fabrication via transfer printing. (a) Transfer printing steps. (b) Optical microscope image of multiple membrane devices (top) along with SEM images of selected devices (bottom).

with various substrates without subjecting them to potentially damaging process conditions. A transferable array of metal contacts with a 5 μm contact separation gap is patterned in a photoresist layer coated on a separate SiO_2/Si substrate using photolithography. Subsequently, a 200 nm-thick Au layer is deposited via electron beam evaporation followed by a

lift-off process (Fig. 4.3(a), step 1.1). The substrate with the Au contacts is then coated with a polycarbonate layer (Fig. 4.3(a), step 1.2) to facilitate the mechanical exfoliation of the contacts (Fig. 4.3(a), step 1.3) and enhance their adherence to the PDMS stamp (Fig. 4.3(a), step 1.4). The donor substrate, which has the released $Ge_{0.89}Sn_{0.11}$ membranes, is positioned beneath the PDMS stamp with alignment marks aiding in aligning the membranes between the contact pads (Fig. 4.3(a), step 2.1). The membranes are then picked up by applying pressure on the sample using the PDMS stamp with the exfoliated contacts (Fig. 4.3(a), step 2.2). Subsequently, the PDMS stamp is lifted back to its original position to complete the membrane pick up (Fig. 4.3(a), step 2.3). Afterward, the Si receiver substrate coated with an SU-8 layer is placed beneath the PDMS stamp containing the contacted devices (Fig. 4.3(a), step 3.1). To transfer the contacted devices, pressure is applied using the PDMS stamp onto the receiver substrate (Fig. 4.3(a), step 3.2) and the temperature is increased to 200 °C to melt the polycarbonate film, facilitating the separation of devices from the PDMS stamp (Fig. 4.3(a), step 3.3). The transfer process is finalized by dissolving the polycarbonate film in dichloromethane for 30 s (Fig. 4.3(a), step 3.4). To enhance the quality of the Au contacts, the devices undergo annealing at 280 °C for 30 min.

Fig. 4.3(b) presents a microscope image of transferred devices with close-up views from SEM micrographs of representative devices. A noticeable misalignment of contacts with membranes is observed, attributable to both the limited alignment accuracy of the setup and the displacement of the released GeSn membranes from their initial array position during underetch release. The latter can potentially be resolved by an improved design of the membranes or by adding mechanical anchors, which can hold membranes after their complete underetching and can be easily broken during the pick up step [223].

4.3.3 Device characterization

Electrical characterization of the $Ge_{0.89}Sn_{0.11}$ photoconductive (PC) devices was conducted using a Keithley 4200A semiconductor parameter analyzer to assess their performance. The transferred membrane devices are compared to as-grown $Ge_{0.89}Sn_{0.11}$ PC devices to highlight the advantages of strain relaxation and transfer onto a dielectric-caped substrate. Dark current as a function of voltage, as shown in Fig. 4.4(a), is systematically measured from -4 V to 4 V for both the as-grown and the membrane samples. A pronounced reduction by two orders of magnitude in the dark current is observed in the membrane device compared to its as-grown counterpart. The Schottky behavior observed in the dark current curve of the membrane device is most likely due to the passivation resulting from the underetching of Ge using a CF_4 plasma, leading to a suppression of the number of surface states through the

formation of Ge–F covalent bonds and subsequent alleviation of Fermi level pinning [282]. The residual passivation from the underetching step may also have induced a change in the contact resistivity, which could be at the origin of the significant reduction in the dark current.

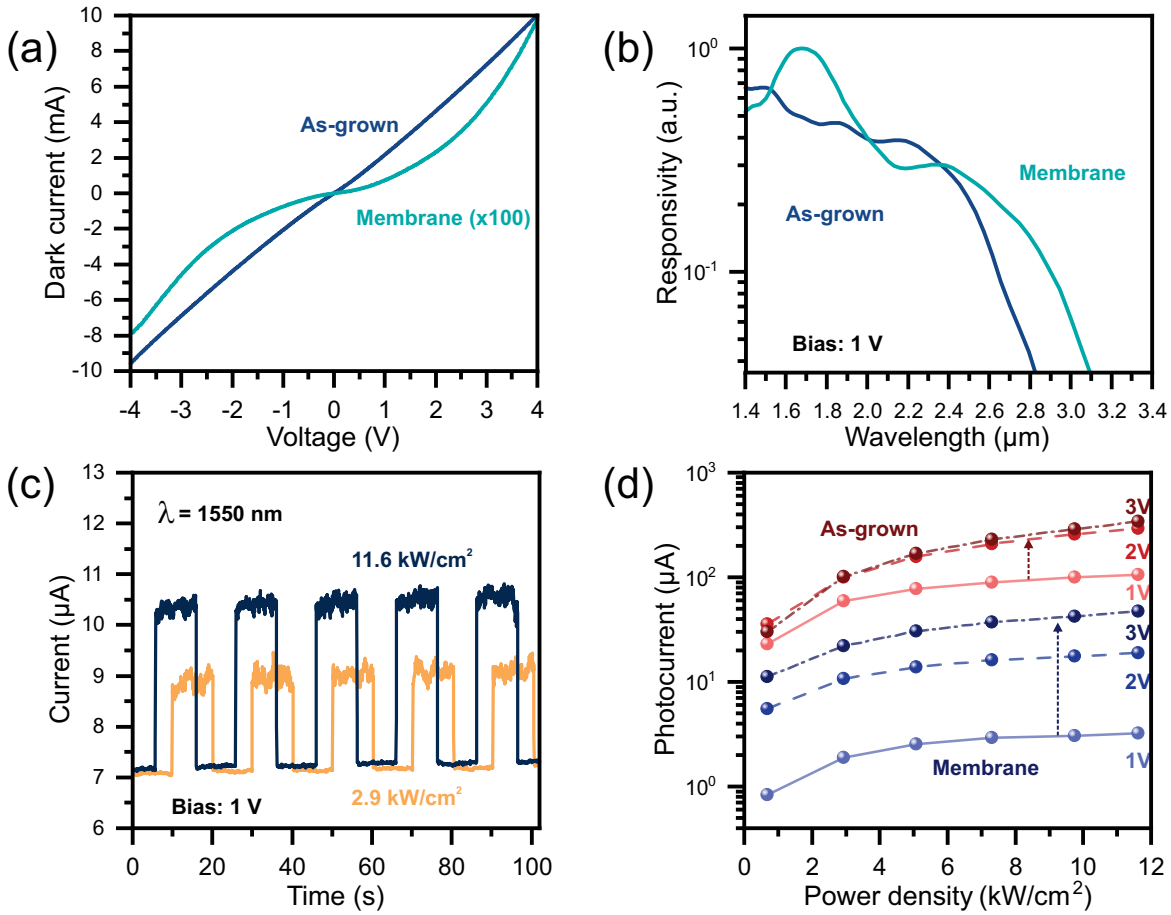


Figure 4.4 Photoconductive device characterization. (a) Dark current of the contacted membrane and as-grown samples as a function of voltage. (b) Spectral responsivity of the membrane and as-grown devices under a bias of 1 V. (c) Time-dependent photocurrent response of a membrane device under a bias of 1 V and illuminated under different power densities using a 1.55 μm laser. (d) Photocurrent as a function of power density and of applied bias.

The spectral responsivity for both as-grown and membrane devices is presented in Fig. 4.4(b). The acquisition of the responsivity spectra was carried out using a Fourier-transform infrared (FTIR) spectrometer (Bruker Vertex 70), with a calibrated tungsten lamp serving as a MWIR source. The MWIR light is focused onto the device using a 40× microscope reflective objective lens. The photocurrent was measured under a bias of 1 V and using a lock-in technique synchronized to an FTIR step scan to acquire the spectral intensity response of the measured

PC devices. The spectral responsivity can then be determined from the measured intensity spectra using a calibrated InSb photodetector. A responsivity of 0.3 mA/W is measured at 1.55 μm for the membrane device, and the cutoff wavelength is increased from 2.8 μm to 3.1 μm relative to the as-grown device. The measured wavelength cutoff values are similar to the absorption cutoff values computed using 8-band $k \cdot p$ (Fig. 4.1(d)) at their respective strain values within less than $\sim$ 4% uncertainty. The latter is strongly dependent on the bowing parameters used in the model [253].

The transient response of the membrane photodetector is investigated under a bias of 1 V using a 1550 nm laser, as shown in Fig. 4.4(c). A distinctive increase in the total current is observed as the illumination is varied over several cycles at a fixed power density. As the power density increases from 2.9 kW/cm^2 to 11.6 kW/cm^2, the collected photocurrent increases from 1.9 μA to 3.2 μA. Fig. 4.4(d) presents the photocurrent measured as a function of power density for both as-grown and membrane samples at biases ranging from 1 V to 3 V. A notable increase in the photocurrent is noted with rising incident light power density and applied bias. Specifically, the $Ge_{0.89}Sn_{0.11}$ membrane photodetector exhibits an increase in responsivity at 1550 nm from 0.3 mA/W to 8.8 mA/W as the bias is increased from 1 V to 3 V. In contrast, the as-grown sample shows an increase from 13.8 mA/W to 89 mA/W over the same bias range.

The responsivity of the membrane devices can potentially be improved by removing the residual non-volatile species from the release step using cleaning solutions [281] and by annealing the contacts [283]. It is expected that Sn should start segregating in $Ge_{0.89}Sn_{0.11}$ at an annealing temperature close to the growth temperature [128], which is an additional constraint in post-growth processing. In this regard, new devices were fabricated to investigate the influence of surface treatments on the membranes and the annealing of the contacts. To isolate these effects, the process flow is modified to first transfer the membranes to the host chip without transferable contacts. Subsequently, the chip undergoes immersion in a mixture of water and hydrochloric acid (4 H_2O : 1 HCl) for 10 s, followed by rinsing in water. The exfoliated contacts are then transferred in a second transfer printing step thereafter. As the polycarbonate film is melted at 200 °C, membranes and contacts are initially annealed at this temperature for 10 min within a nitrogen environment. The dark current and the responsivity are measured before and after the device annealing at 320 °C and 335 °C close to the growth temperature, which were also 10 min long steps each. Note that the annealing at 280 °C for 30 min was not performed for this device to study the effect of annealing independently.

The obtained device exhibits a responsivity of 3.1 mA/W at 1.55 μm, representing a tenfold increase in comparison to untreated devices. This enhancement may be attributed to the

partial removal of residual by-products that could have created a barrier for the carriers. As the annealing temperature increases, the magnitude of the dark current decreases as depicted in Fig. 4.5(a). The dark current decreases by a factor of 10 after annealing at 320 °C and by an additional factor of 2 after annealing at 335 °C while gradually leaning towards an Ohmic behavior. Although the spectral responsivity maintains a consistent wavelength range at different annealing temperatures, a reduction in the responsivity is observed when compared to the initial annealing carried out at 200 °C, as shown in Fig. 4.5(b). Specifically, it diminishes to 2.6 mA/W and 0.9 mA/W after annealing at 320 °C and 335 °C, respectively.

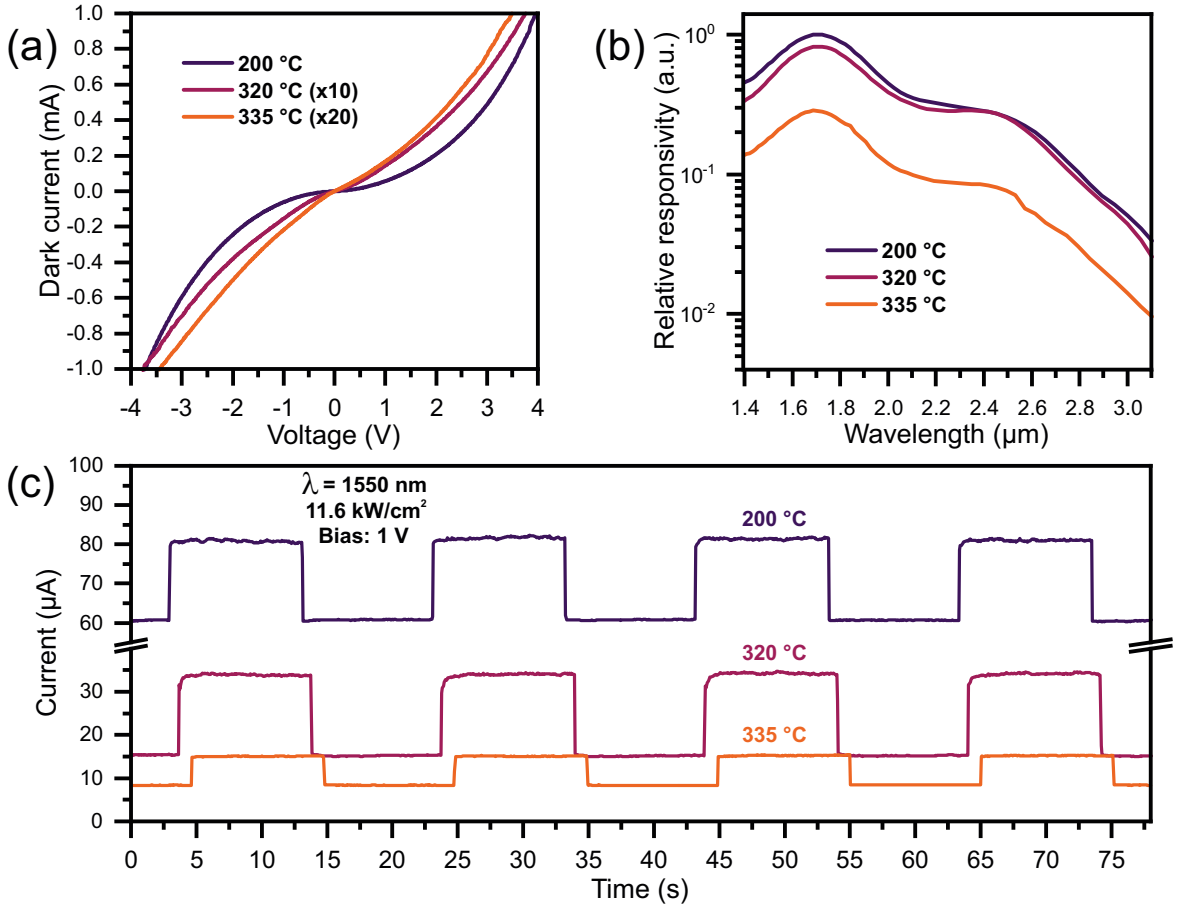


Figure 4.5 Device characterization after chemical treatment and annealing at different temperatures. (a) Dark current as a function of voltage. (b) Spectral responsivity normalized to the measurement made with the annealing at 200 °C. (c) Time-dependent photocurrent response under a bias of 1 V and illuminated by a 1.55 μm laser at a power density of 11.6 kW/cm^2.

The time-dependent response of the device under a 1 V bias and illumination by a 1.55 μm laser at a power density of 11.6 kW/cm^2 is presented in Fig. 4.5(c) for different annealing

temperatures. Remarkably, a reduction in both dark current and photocurrent is observed with increasing annealing temperatures. This reduction in dark current is mainly attributed to an enhancement in the crystalline quality of $Ge_{0.89}Sn_{0.11}$ through annealing, likely reducing vacancy-like defects capable of trapping charge carriers [130]. However, an increase in contact resistivity may also contribute to the reduction with rising annealing temperatures as less photocurrent is being collected. These factors appear to be competing, highlighting the need for defect removal in the microstructure with a minimal impact on contact resistivity.

4.4 Conclusion

In summary, the current progress in mid-infrared group IV membrane detectors was briefly reviewed. The major difficulty related to strain relaxation-induced bowing, preventing a controlled processing of membrane devices, was addressed through an enhanced lattice relaxation during the epitaxial growth while keeping the Sn content sufficiently high to extend the detector cutoff in the mid-infrared range. As a proof-of-concept, $Ge_{0.89}Sn_{0.11}$ membrane photodetectors were developed and characterized showing room-temperature operation in the mid-infrared range. The control of Sn content and lattice strain throughout the epitaxial growth yields highly relaxed alloys leading to released membranes without any significant structural bowing, thus facilitating the large-scale transfer of membrane detector arrays. Indeed, the fabrication process based on transfer printing was improved by using an SU-8 adhesive layer and transferable gold contacts. These improvements enabled the transfer of multiple membrane-based photoconductive devices in a single transfer printing step. Furthermore, the effects of annealing and chemical treatment on the photodetectors were explored to identify avenues to improve the device's performance. During the release, the membranes were subjected to an additional relaxation of the residual strain inducing an extension of the cutoff wavelength from 2.8 μm to 3.1 μm. Moreover, the transferred detectors were found to exhibit two orders of magnitude reduction in the dark current as compared to detectors made of as-grown layers, which could be the result of a change in the surface properties of the membrane during the fabrication steps that had an impact on the contact resistivity or helped form a Schottky barrier. These findings not only underscore the potential of $Ge_{1-x}Sn_x$ membranes as a robust group IV platform for mid-infrared photodetection and sensing but also emphasize the ongoing progress in their practical implementation. A platform based on group IV semiconductors benefits from compatibility with silicon, which is vital for the development of large-scale mid-infrared components.

Author contributions

Cédric Lemieux-Leduc conducted sample fabrication, including its various constituents, as well as transfer printing, 8-band $k \cdot p$ calculations, photoluminescence measurements, chemical treatment and annealing, basic electrical characterization, and responsivity measurements. Mahmoud R. M. Atalla assisted with the setup of electrical characterization and responsivity measurements. Simone Assali carried out the growth of the $Ge_{0.89}Sn_{0.11}$ sample. Sebastian Koelling conducted the TEM and EDX measurements. Patrick Daoust performed the XRD-RSM measurement. Lu Luo conducted the Raman measurements. Gérard Daligou assisted with the 8-band $k \cdot p$ calculations. Julien Brodeur and Stéphane Kéna-Cohen assisted with transfer printing. Yves-Alain Peter and Oussama Moutanabbir supervised the project.

CHAPTER 5 SIMULATION OF GERMANIUM-TIN MATERIAL INTEGRATION AND OPTICAL COUPLING

5.1 Introduction

The successful transfer of GeSn membranes, as demonstrated in the previous chapter, paves the way for their heterogeneous integration with photonic integrated circuits (PICs). This approach mitigates challenges associated with defective interfaces during GeSn growth while enabling mid-infrared functionalities essential for applications such as chemical sensing, environmental monitoring, and free-space communication. A key question that arises from this advancement is: how does heterogeneous integration of GeSn alloys compare to monolithic integration on an integrated photonic platform?

To address this, this chapter presents numerical simulations focusing on the 2–4 μm wavelength range. A central aspect of this investigation is the coupling efficiency between a photonic platform's waveguide or passive component and the transferred GeSn layer, which serves as the active medium. Efficient light coupling is crucial, as it directly affects device performance metrics such as signal strength, power loss, and functionality, ultimately determining the feasibility of integrating GeSn alloys with photonic platforms. While numerical studies [24,26,102] and limited experiments [20,21] have explored Si photonics-compatible designs, a comprehensive investigation into this specific challenge remains unexplored. Through finite-difference time-domain (FDTD) simulations, we model integration concepts for practical photonic structures to identify promising strategies and assess their advantages and limitations.

As discussed in Section 2.3.3, mid-infrared photonic platforms and integration strategies highlight the need to evaluate light coupling efficiency from waveguides into GeSn layers. This is particularly important for photodetectors, where maximizing light absorption directly enhances performance. Among various coupling mechanisms, evanescent coupling is a practical and versatile approach [284]. In this scheme, light couples vertically from a waveguide to the GeSn material deposited or transferred on top, facilitating energy transfer between supported optical modes as the propagating light interacts with the GeSn structure. Figure 5.1 illustrates this concept, depicting guided light undergoing evanescent coupling before absorption in the GeSn layer.

The broad wavelength range of GeSn complicates the selection of an optimal integration method and platform. This requires careful consideration of both technical limitations and

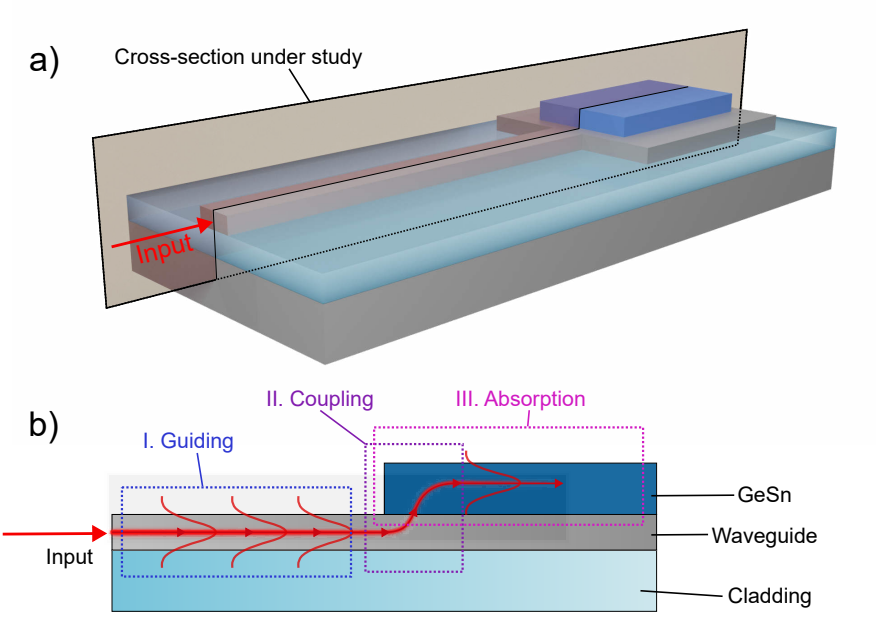


Figure 5.1 Illustration of the evanescent coupling phenomenon. (a) 3D model of the structure with the 2D longitudinal cross-section under study identified. (b) Schematic of the different steps that the light undergoes in this structure, such as guiding through the waveguide (I) before undergoing coupling (II) with the GeSn layer and absorption (III).

experimental observations. The silicon-on-insulator (SOI) platform provides an operational range (from 1.2 to 4.3 μm) that overlaps most of the demonstrated photodetection range of GeSn alloys, which ranges roughly from 1.5 to 4.6 μm [14]. The range of the germanium-on-silicon (GOS) platform extends further into the mid-infrared, at the cost of compatibility with telecom wavelengths. However, this platform would still be suitable if the demonstrated photodetection range of GeSn alloys exceeds 4.6 μm. As mentioned earlier, GeSn or SiGeSn compounds are expected to potentially cover a broader range within the mid-infrared region. Epitaxial growth of GeSn is achievable onto these platforms, with the current requirement of a Ge buffer layer for the SOI platform.

Although other mid-infrared platforms could be considered, this investigation focuses on SOI and GOS platforms, which are the most promising candidates for GeSn integration. This chapter examines SOI and GOS waveguides across the GeSn operational range and evaluates coupling efficiency in different integration scenarios. Integration of GeSn onto these platforms can be achieved through direct growth using a Ge buffer layer (monolithic integration) or through bonding and transfer printing (heterogeneous integration). In the case of heterogeneous integration, the impact of a gap between the waveguide and active layer will be studied, which is typically present in adhesive bonding. While the influence of selected key

design parameters will be evaluated in each modeling scenarios, a general discussion regarding the impact of additional design considerations that were not systematically included in the modeling scenarios is provided.

5.2 Optical properties of GeSn and other materials

To effectively design integrated GeSn photonic components, their critical optical properties, such as refractive index and absorption, must be known or accurately modeled. These properties are represented by the complex refractive index $\tilde{n} = n + i\kappa$, where n and κ are the refractive index and the extinction coefficient respectively. Accurate optical property data are essential for optimizing light coupling efficiency, minimizing propagation losses. Ellipsometry is a precise and non-destructive method for extracting the optical properties of GeSn. The low Sn incorporation results in minimal refractive index contrast with the Ge buffer layer, complicating the extraction of optical properties. Tran *et al.* used ellipsometry to systematically report the optical properties of GeSn as a function of Sn content [285]. Fig 5.2 shows extracted optical properties of GeSn thin films from this study, with Fig. 5.2(a) and Fig. 5.2(b) showing the refractive index and the absorption of GeSn respectively for different Sn contents. However, the properties can be influenced by the growth conditions, resulting strain, and doping concentration among other parameters.

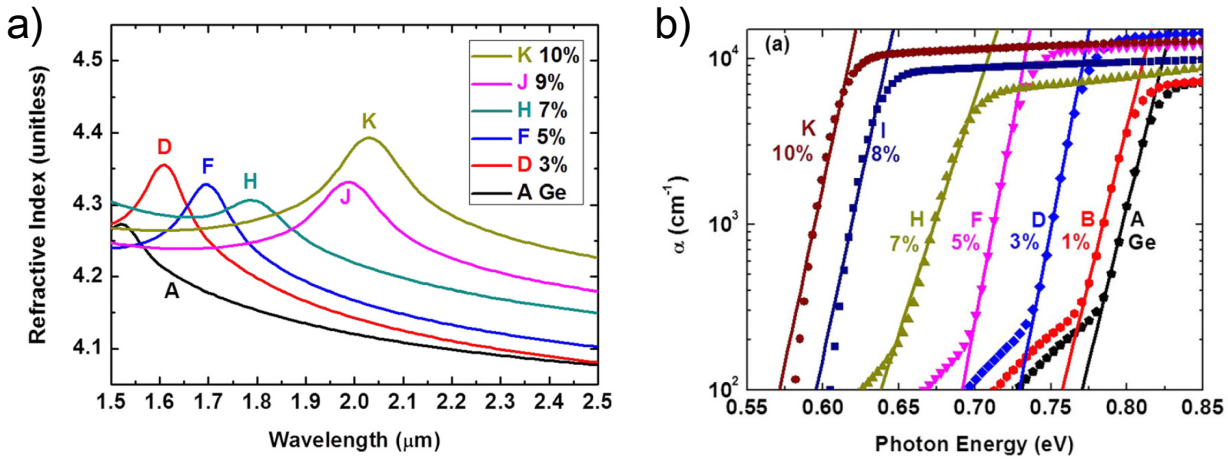


Figure 5.2 Optical properties of Ge and GeSn films for various Sn contents up to a wavelength of 2.5 μm. (a) Refractive index. (b) Absorption coefficient. Reproduced with permission from [285].

Since ellipsometry measurements are restricted to 2.5 μm with the available instrument (see Section 6.2.3), alternative approaches such as the $k{\cdot}p$ model employed in Chapter 4 are neces-

sary to extend the analysis to longer wavelengths, particularly for mid-infrared applications. The model described in Section 3.5 enables the computation of optical properties as a function of different parameters that define the alloy. The Kramers-Kronig relation is used to derive the wavelength-dependent refractive index $n(\lambda)$ from the computed absorption $\alpha(\lambda)$:

$$n(\lambda) = 1 + \frac{1}{2\pi^2} \wp \int_0^{+\infty} \frac{\alpha(\lambda')}{1 - (\lambda'/\lambda)^2} \mathrm{d}\lambda' \tag{5.1}$$

where $\wp$ is the Cauchy principal value. This integral can be solved numerically. Several parameters in the $k!\cdot!p$ model are interpolated between Ge and Sn in its α phase. One of the critical parameters is the bandgap bowing parameter, for which there is no general expression and which is typically extracted from temperature-dependent PL measurements [255]. This parameter likely depends on the Sn content and strain. In this chapter, the 8-band $k{\cdot}p$ model is used to estimate the optical properties of GeSn films and access longer wavelengths. Optical properties from GeSn extracted using ellipsometry will be employed in Chapter 6 as we will consider an operation wavelength below 2.5 μm. An Sn content of 11 at.% was selected for simulations, aligning with the material composition used in Chapter 4. This choice ensures consistency in modeling while supporting experimental validation for heterogeneous integration with SOI waveguides in Chapter 6. The kp model has been found to provide values that are within the same order of magnitude when compared to ellipsometry measurements around 2 μm (see Section 6.2.3).

Monolithic integration assumes a compressively strained layer (-0.6%), whereas heterogeneous integration assumes a relaxed layer (0%). The change in strain essentially offsets the cutoff wavelength in the extinction coefficient, as observed in Fig. 5.3, where it shifts from roughly 2.8 to 3.1 μm when going from compressively strained to fully relaxed. Figure 5.3(a) and Fig. 5.3(b) shows the computed refractive index and absorption coefficient respectively for a strained and relaxed $Ge_{0.89}Sn_{0.11}$ layer.

Beyond GeSn, the integration of photonic components requires an understanding of the optical behavior of adjacent materials, including waveguide layers (Si, SiO_2, Ge) and adhesive bonding layers. Figure 5.4 presents the optical properties of Si, Ge, and SiO_2 used in the modeling of SOI and GOS waveguides. The optical properties of Si [286] and SiO_2 were taken from literature. The noticeable peak in the extinction coefficient around $\lambda = 2.8$ μm is related to the presence OH groups in silica in the reported measurements, where its magnitude may vary depending on the presence of water vapor during the formation of the oxide layer [287]. Since we have a Ge film, defects and the doping concentration can impact the absorption spectrum and its cutoff. The coefficients are extracted from a Ge buffer layer film grown on

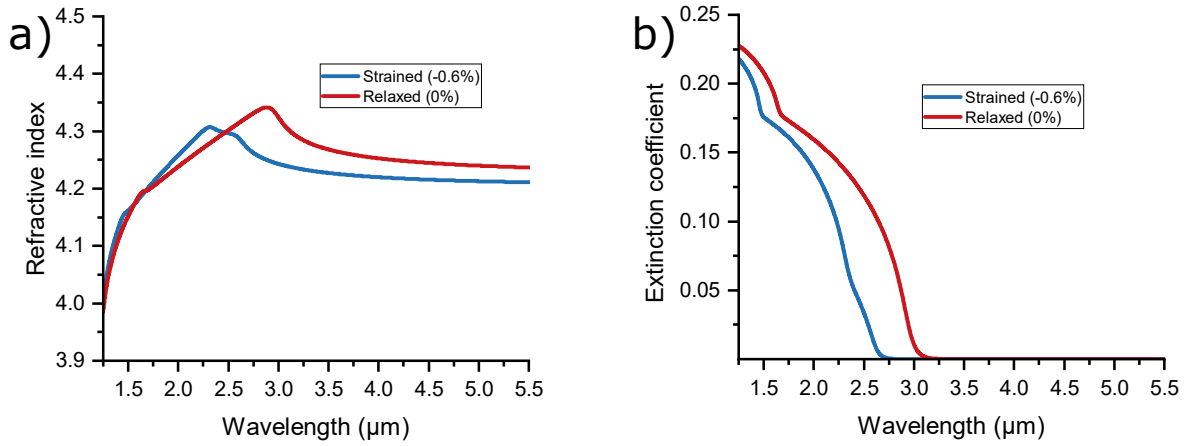


Figure 5.3 Computed optical properties of $Ge_{0.89}Sn_{0.11}$ using the 8-band $k \cdot p$ model in its strained (-0.6%) and relaxed (0%) states. (a) Refractive index. (b) Extinction coefficient.

a Si wafer up to 2.5 μm using ellipsometry. For wavelengths above 2.5 μm, values from the literature are used [286]. The refractive indices and absorption coefficients of Si, Ge, and SiO_2 are plotted in Fig. 5.4(a) and Fig. 5.4(b) respectively.

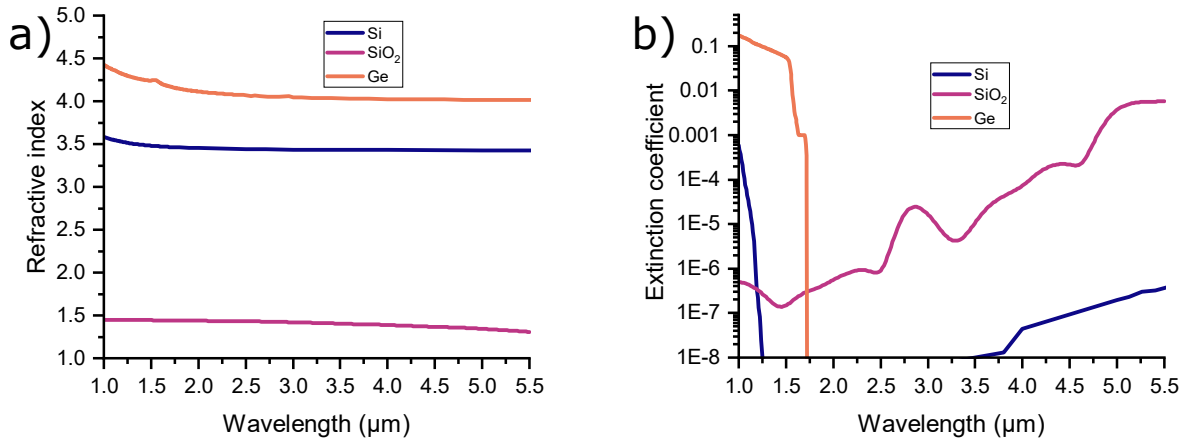


Figure 5.4 Material properties used in the modeling. (a) Refractive index and (b) extinction coefficient of Si [286], SiO_2 [287], and Ge [286].

Benzocyclobutene (BCB) and SU-8 polymer films are used as adhesive layers for heterogeneous integration. They exhibit good dielectric properties after curing, similar to that of SiO_2, which are extracted using ellipsometry with a model based on Cauchy coefficients (see Section 6.2.3). The absorption is negligible in the measurement range. Figure 5.5 shows the refractive index dispersion of BCB and SU-8 up to 2.5 μm using ellipsometry.

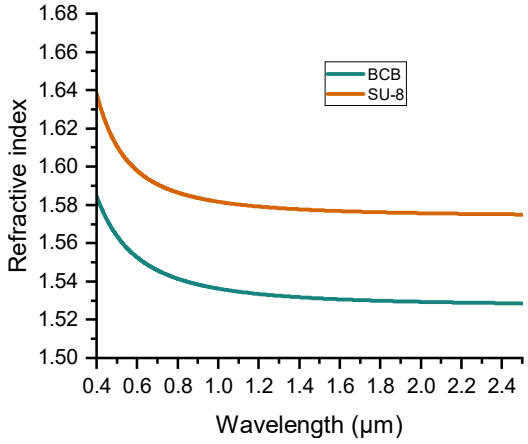


Figure 5.5 Dispersion of BCB and SU-8 measured using ellipsometry.

5.3 Waveguiding properties of the SOI and GOS platforms in the mid-infrared

Optimizing light coupling requires a thorough understanding of waveguide behavior across the relevant wavelength range. This evaluation ensures efficient mode confinement and minimizes propagation losses, both of which are critical for practical photonic device integration. Before introducing coupling with GeSn, we evaluate the waveguiding properties of the SOI and GOS platforms over the relevant wavelength range. Waveguides are typically designed for single-mode operation, supporting only the fundamental TE and TM modes. Single-mode operation is crucial for minimizing modal dispersion, ensuring high signal integrity, and improving the efficiency of integrated photonic circuits. The number of supported propagating modes is dimension-dependent, and the cutoff dimensions can be identified using modeling based on the finite element method (FEM)[1]. Designing a single-mode waveguide [178] begins with determining the supported modes in a slab waveguide (1D waveguide) along the vertical axis. This analysis establishes the minimum thickness required to support higher-order modes along the vertical axis. Since the problem is in one dimension, the modes can be computed either analytically or numerically. Once the thickness is fixed, we vary the width of a 2D waveguide. Next, we determine the minimum width at which higher-order modes emerge along the horizontal axis.

Figure 5.6 and Fig. 5.7 show an overview of the properties of slab waveguides based on the SOI and GOS platforms respectively. A slab waveguide is the simplest structure, consisting of a high-refractive-index core layer sandwiched between lower-refractive-index cladding layers. The light is confined in the high-index layer. Maxwell's equations can be used to determine

[1]The maximum mesh step was set to 20 nm. Perfectly matched layers are set at the boundaries of the simulation domain.

the possible distributions of the electric (E) and magnetic (H) fields representing the different supported modes inside the waveguide. With light traveling in-plane along the z-axis, these fields are perpendicular along the x- and y-axes, depending on the polarization. In TE polarization, E is aligned along the x-axis ($E_x = E$, $E_y = 0$), while in TM polarization, H is aligned along the x-axis ($H_x = H$, $H_y = 0$). The resulting wave equations are:

$$\frac{\partial^2 E_x}{\partial y^2} + (k^2 - \beta^2)E_x = 0 \tag{5.2}$$

$$\frac{\partial^2 H_x}{\partial y^2} + (k^2 - \beta^2)H_x = 0 \tag{5.3}$$

where k is the wavenumber and β is the propagation constant. When the slab thickness is sufficiently large, it can support additional modes beyond the fundamental TE and TM modes. The fundamental modes are identified as TE_0 and TM_0, while the other supported modes are noted as TE_m and TM_m (where $m = 1, 2, ...$).

Figure 5.6(a) and Fig. 5.7(a) depict the materials involved and the refractive index profile along the vertical axis for both platforms. The E-field distribution of some of the first modes is plotted in Fig. 5.6(b) and Fig. 5.7(b) for each platform, using a slab thickness of 500 nm at a wavelength of 1.55 μm for the SOI platform and a slab thickness of 1 μm at a wavelength of 2.33 μm for the GOS platform.

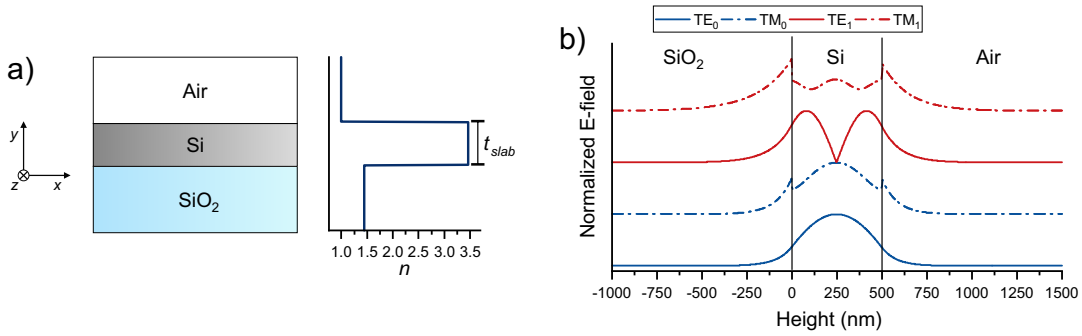


Figure 5.6 Overview of the SOI platform as a slab waveguide. (a) Layer stack composing the platform (left) and the refractive index profile of the materials (right). (b) Normalized E-field of different supported modes in an SOI slab waveguide at a wavelength of 1.55 μm.

In each mode, we observe that part of the field distribution lies outside the core layer, referred to as the evanescent field. This field interacts with other structures, enabling evanescent coupling. In evanescent coupling, energy is transferred between optical modes, allowing for efficient energy transfer between the supported optical modes in each structure.

For single-mode operation, the waveguide height must be small enough to support only

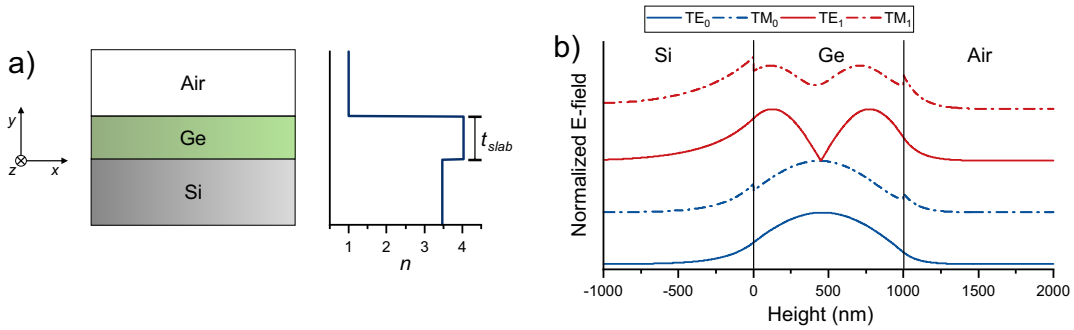


Figure 5.7 Overview of the GOS platform as a slab waveguide. (a) Layer stack composing the platform (left) and the refractive index profile of the materials (right). (b) Normalized E-field of different supported modes in a GOS slab waveguide at a wavelength of 2.33 μm.

the TE_0 and TM_0 modes. As the wavelength increases, the mode expands, necessitating larger waveguide dimensions. It then becomes challenging to find waveguide dimensions that ensure single-mode operation over a broad wavelength range. To illustrate this challenge, the effective refractive index n_{eff} as a function of slab waveguide thickness t_{slab} is plotted for different wavelengths in Fig. 5.8 and Fig. 5.9 for the SOI and GOS platforms, respectively. The vertical dashed lines define the minimum thicknesses that can support modes at each wavelength.

For the SOI platform, the usual thickness to support only the fundamental mode is typically below 250 nm for a wavelength of 1.55 μm. However, this thickness cannot support any mode at a wavelength of 3.5 μm, while a thickness of 500 nm seems to be adequate. A thickness of 220 nm is generally used to provide single-mode operation around 1550 nm. However, as the wavelength increases, the mode expands until it can no longer be supported or high radiation losses occur. A thickness of 500 nm is typically used for single-mode operation in the mid-infrared, but this thickness is multimode at 1.55 μm, as the TE_1 and TM_1 modes are also supported. For the GOS slab waveguide, the cutoff thickness is near 750 nm at a wavelength of 2.33 μm. While a mode would still be supported, the effective refractive index is much lower, indicating a much leakier mode that could lead to increased overlap with defects at the Si/Ge interface. GOS waveguides are typically 1-2 μm thick, with larger thicknesses reducing propagation losses by minimizing overlap with the Si/Ge interface. While SOI wafers are mostly defect-free compared to GOS wafers, they sustain a shorter operational range.

The next step involves lateral mode confinement by defining the waveguide width, typically achieved by etching the core material down to the bottom cladding layer to form strip waveguides. The width affects the confinement of light and the number of modes that can

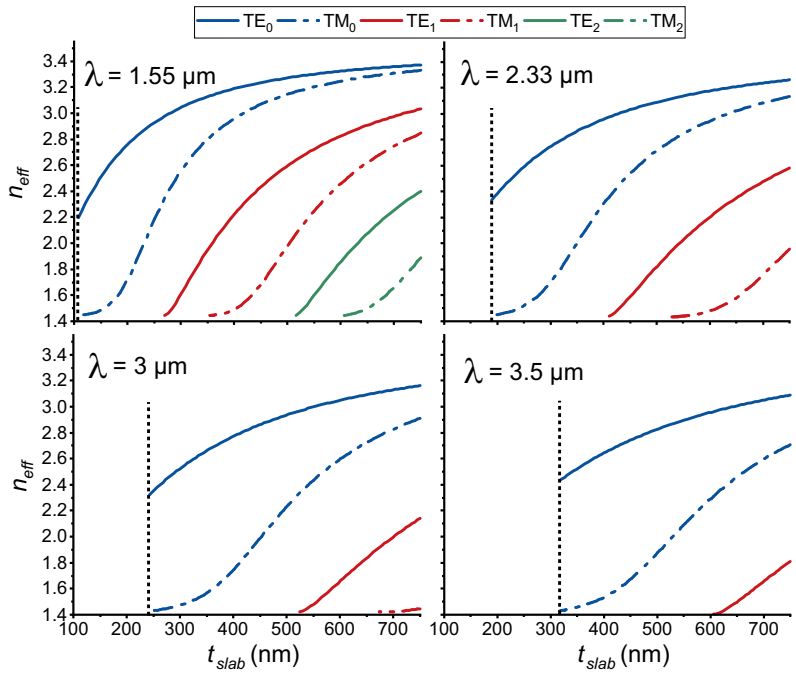


Figure 5.8 Effective refractive index of the different supported modes in the SOI platform as a function of slab thickness and wavelength.

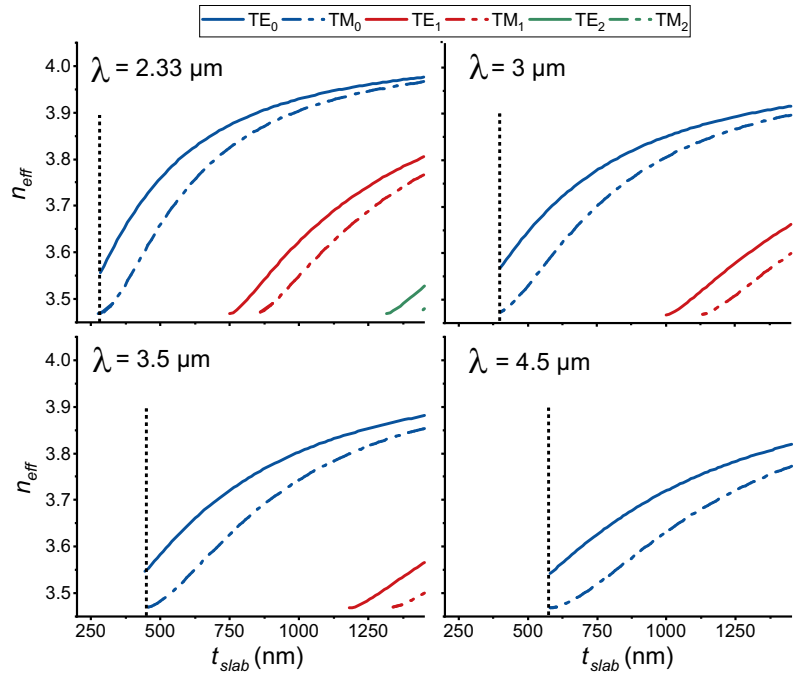


Figure 5.9 Effective refractive index of the different supported modes in the GOS platform as a function of slab thickness and wavelength.

propagate. Minimizing the waveguide width can ensure that only the fundamental modes can propagate and reduces the chances of higher-order modes being supported. It is important to note that polarization modes in 2D are not purely TE or TM and are rather called quasi-TE or quasi-TM, as the field distribution is more complex. They can however still be labeled as such depending on the fraction of the E-field residing in a specific axis. The modes are labeled with an additional subscript number, like TE_{00} and TM_{00} for the fundamental modes, with the first subscript determining the mode order in the vertical orientation and the second along the horizontal orientation.

For the SOI platform, Fig. 5.10(a) shows the cross-section of the waveguide, where we can define a width. In Fig. 5.10(b), the effective index as a function of the waveguide width is shown for the first three supported modes at a wavelength of 2 μm, using a thickness of 220 nm. Only TE modes are supported for this width range up to TE_{02}, where they are distinguished by the number of maxima in the E-field distributions shown as insets. Similarly to the slab thickness, the width determines the number of supported modes that can exist along the horizontal axis, but the condition varies as a function of wavelength. As the wavelength increases, the mode becomes increasingly evanescent until it can no longer be supported by the waveguide, resulting in significant modal loss. The imaginary part of the computed effective refractive index can be used to estimate propagation losses in waveguides at different wavelengths, accounting for a combination of material absorption and mode radiation losses. However, it does not account for free-carrier absorption (FCA) and scattering-induced loss, although models have been developed to estimate this using information on sidewall roughness [288].

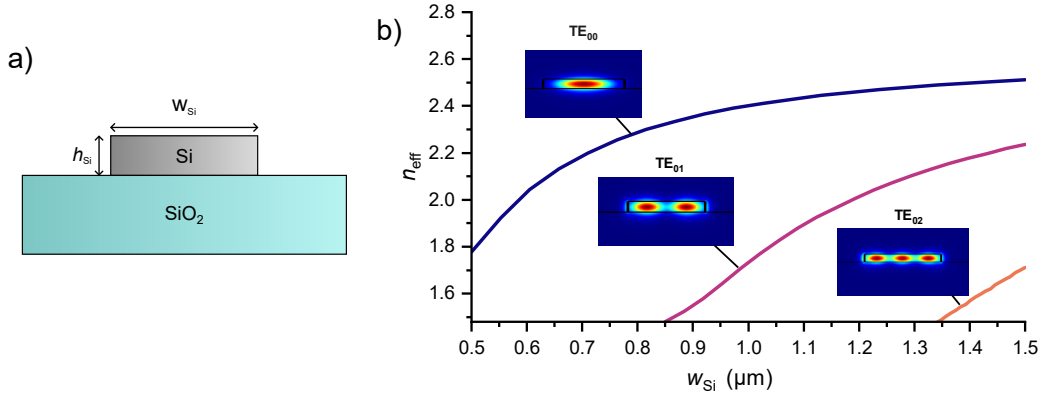


Figure 5.10 Properties of SOI waveguides. (a) Schematic of the cross-section. (b) n_{eff} as a function of width showing the first three TE modes. Inset: Electric field distribution of the modes.

Figure 5.11(a) and Fig. 5.11(b) show the refractive index and the computed loss as a function

of waveguide width for a fixed height of 220 nm. Varying the width impacts the range at which an optical mode can be supported. The typical dimensions for single-mode operation at telecom wavelengths involve a width of 500 nm, which supports only the fundamental mode up to a wavelength of roughly 2.25 μm. Light confinement in the waveguide core decreases with increasing wavelength, leading to enhanced radiation loss and material absorption in SiO_2. Increasing the width to 1 μm increases this cutoff up to 3.4 μm. Even with a width of 5 μm, a significant loss is observed between 2.6 and 3 μm and above 3.5 μm. As mentioned earlier in Section 5.2, this peak is related to the potential presence of OH groups in SiO_2, which is highly dependent on the growth or deposition conditions when the oxide is formed [287]. Larger waveguide widths enable smaller variations in n_{eff} as a function of wavelength.

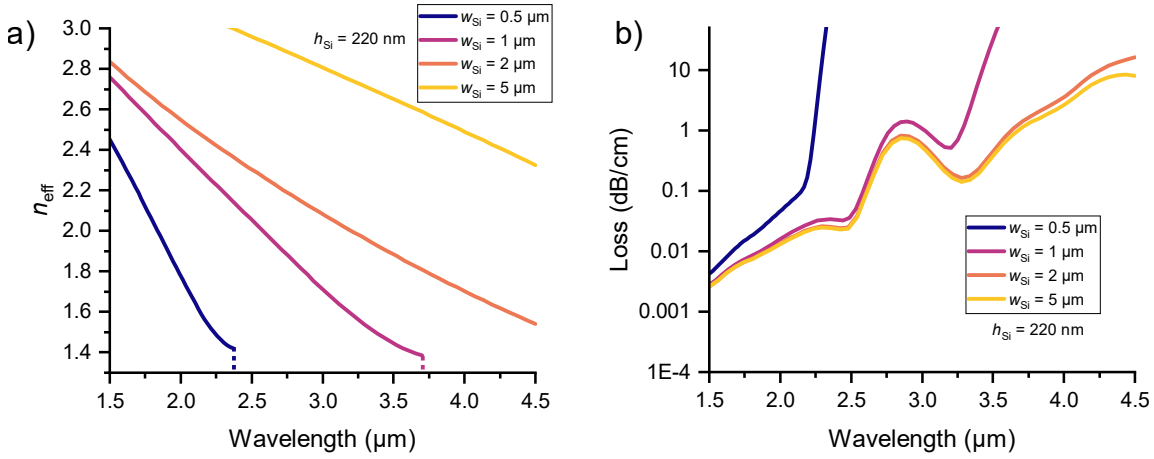


Figure 5.11 Impact of the waveguide width on the wavelength-dependent behavior in the SOI platform. (a) Refractive index and (b) computed modal loss as a function of wavelength for different waveguide widths with a fixed height of 220 nm.

Figure 5.12(a) and Fig. 5.12(b) show the refractive index and the computed loss as a function of waveguide height for a width of 2 μm. Increasing the thickness to 500 nm significantly decreases the loss at longer wavelengths, resulting in almost an order of magnitude improvement. However, considerable SiO_2 absorption still occurs above 4 μm. While a thickness of 220 nm provides single-mode operation at telecom wavelengths, slightly larger thicknesses could extend the operational range of the SOI platform into the mid-infrared.

Different observations can be made for the GOS platform. Figure 5.13(a) shows the cross-section of the waveguide, while Fig. 5.13(b) shows the different modes supported in a 1 μm thick waveguide for different widths at a wavelength of 2 μm. TE (TM) higher-order modes are present along the vertical axis as TE_{10} (TM_{10}) and along the horizontal axis as TE_{01} (TM_{01}).

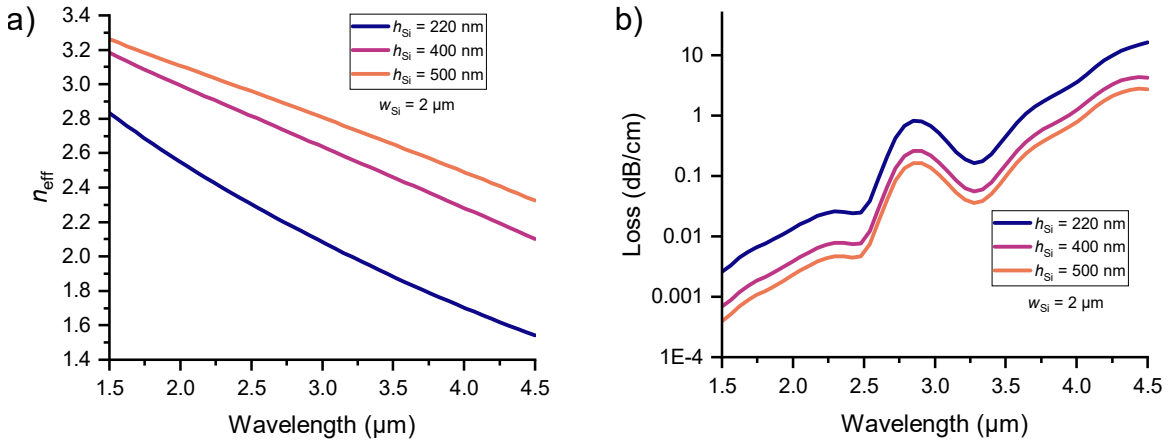


Figure 5.12 Impact of the waveguide height on the wavelength-dependent behavior in the SOI platform. (a) Refractive index and (b) computed modal loss as a function of wavelength for different waveguide heights with a fixed width of 2 μm.

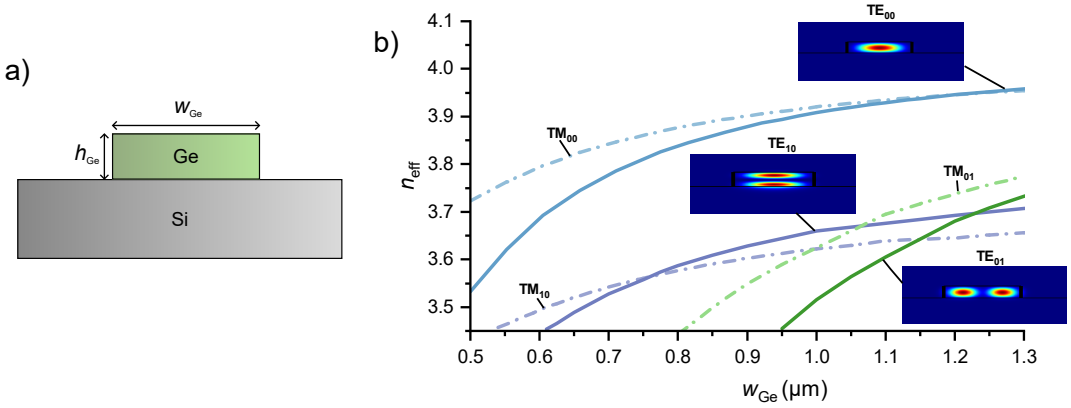


Figure 5.13 Properties of GOS waveguides. (a) Schematic of the cross-section. (b) n_{eff} as a function of width showing multiple TE (solid lines) and TM (dashed lines) modes. Inset: Electric field distribution of the TE modes.

Figure 5.14 and Fig. 5.15 show the impact of the waveguide width and height, respectively, on the wavelength-dependent properties of GOS waveguides. As observed in Fig. 5.14(b), wavelengths below 1.75 μm are not supported due to the high absorption in Ge. The waveguide is relatively transparent between 1.75 to 2.5 μm, where material absorption is negligible. Some absorption beyond 2.5 μm is observed, which may partly be due to radiation losses, as material absorption in both Si and Ge is negligible up to at least 3.5 μm, according to the data presented in Fig. 5.4(b). For a width of 1 μm with a thickness of 1 μm, the waveguide becomes significantly lossy for wavelengths above approximately 3.7 μm, possibly due to leakage in Si. Figure 5.15(b) shows that increasing the thickness of the waveguide reduces loss.

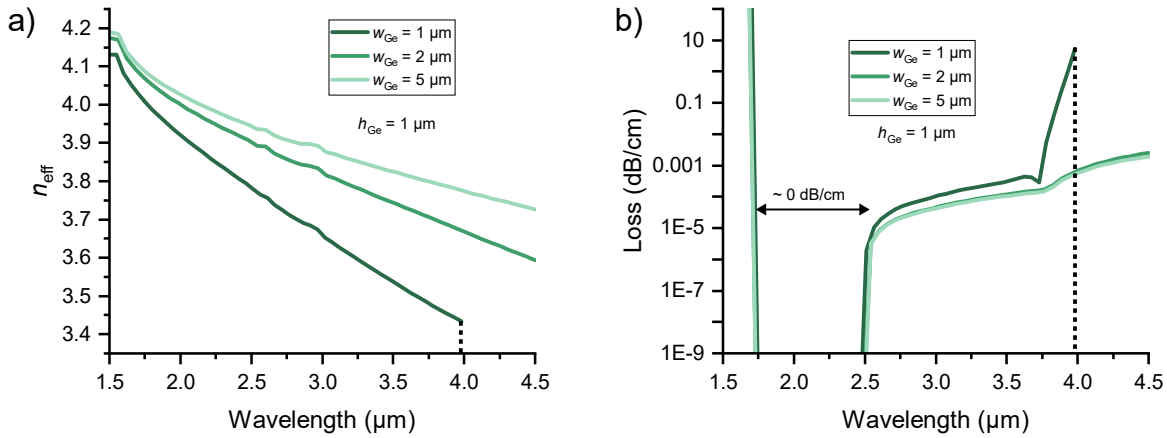


Figure 5.14 Impact of the waveguide width on the wavelength-dependent behavior in the GOS platform. (a) Refractive index and (b) computed modal loss as a function of wavelength for different waveguide widths with a fixed height of 1 μm.

The results from FEM modeling provide critical design guidelines for fabricating waveguides that ensure stable, low-loss light propagation across a broad wavelength range, making them suitable for mid-infrared sensing and communication applications. Single-mode operation can be maintained in waveguides with large dimensions by introducing a slab thickness to form ridge waveguides. In this design, the etch depth is less than the core layer thickness, allowing higher-order modes to leak into the slab while the fundamental mode remains confined in the core [289]. This approach ensures single-mode operation without requiring excessively small waveguide dimensions. Another critical factor to consider is the loss induced by waveguide bends. Small bend radii are essential for achieving compact and dense photonic circuits, which are typically possible when the refractive index contrast between the core and cladding is high. This advantage is more pronounced in the SOI platform compared to the GOS platform, where the lower refractive index contrast limits the achievable bend radii.

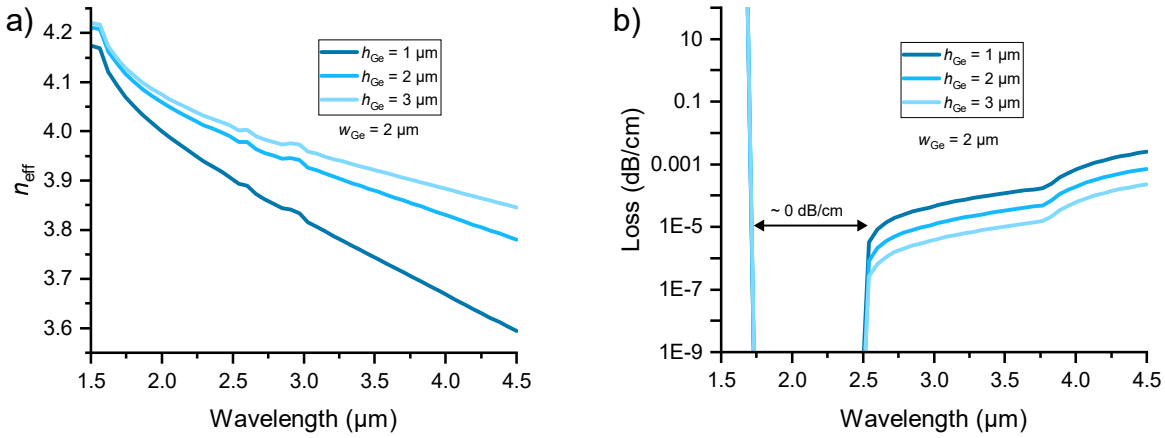


Figure 5.15 Impact of the waveguide height on the wavelength-dependent behavior in the GOS platform. (a) Refractive index and (b) computed modal loss as a function of wavelength for different waveguide heights with a fixed width of 1 μm.

5.4 Modeling of the evanescent coupling in coupled waveguided structures

After examining the SOI and GOS platforms, we now focus on the interaction of light with monolithically or heterogeneously integrated GeSn. The efficiency of this interaction depends on several design parameters, particularly in waveguide-coupled photodetectors. Maximizing absorption efficiency is crucial for developing highly sensitive photodetectors for mid-infrared applications, such as chemical sensing and free-space communication. Efficient light coupling ensures stronger signal detection and lower power losses, enhancing overall device reliability. Ghosh *et al.* conducted a detailed study on the optimal design parameters for a p-i-n GeSn waveguide photodetector (WGPD) monolithically integrated on an SOI platform, focusing on operation around the 2 μm band [26]. Their analysis, based on FEM simulations of supported modes in the GeSn structure and by looking at the confinement factors, provides valuable insights into design optimization. While FEM provides insights into waveguide mode distributions, FDTD better captures transient and multi-modal effects in photodetectors, enabling more accurate absorption and coupling analysis.

The performance of a photodetector is primarily determined by its responsivity (R), which is defined as the amount of photocurrent (I_{ph}) generated by a given amount of absorbed optical power (P_{in}). It can also be determined by the following equation:

$$R = \frac{I_{ph}}{P_{in}} = \eta \frac{q\lambda}{hc} \tag{5.4}$$

where η is the quantum efficiency, q is the elementary charge, h is Planck's constant, and c is

the speed of light. The quantum efficiency in a planar photodetector can be defined as [290]:

$$\eta = (1 - \mathcal{R})\zeta P_{abs} \tag{5.5}$$

where $\mathcal{R}$ is the reflectance at the interface with the active medium, ζ is the fraction of electron-hole pairs generated per photon absorbed, and P_{abs} is the fraction of the total optical power absorbed by the active medium. Assuming there is no reflection ($\mathcal{R} = 0$) and every photon generates one electron-hole pair ($\zeta = 1$), the quantum efficiency primarily depends on P_{abs}. In a planar photodetector, which is either bottom or top illuminated, this fraction can be expressed as the normalized difference between the input and output powers (P_{in} and P_{out}) using [178]:

$$P_{abs} = \frac{P_{in} - P_{out}}{P_{in}} = 1 - e^{-\alpha L} \tag{5.6}$$

where α is the absorption coefficient and L is the length or thickness of the active region along the propagation path of the collected light. In a waveguide coupled to an active medium, calculating the absorbed power fraction is less straightforward due to the field distribution spanning multiple materials, including the GeSn layer, the waveguide core, and the cladding. The absorption varies depending on the portion of the optical mode that interacts with GeSn, mainly defined by the confinement factor within this layer.

The introduction of an active medium gives rise to new optical modes that intricately couple with the original waveguide mode. This coupling can be analyzed using coupled-mode theory, where the coupling coefficient $\tilde{C}_{1,2}(x)$ between two modes (labeled as 1 and 2) along the propagation direction is given by:

$$\tilde{C}_{1,2}(x) = \tilde{C}^*_{2,1}(x) = \frac{k^2}{2\sqrt{|\beta_1 \beta_2|}} \int_A (n_r^2 - \bar{n}_r^2) E_1^* E_2 dA \tag{5.7}$$

where k is the wavenumber ($k = 2\pi/\lambda$), β_m is the propagation constant of the mode m ($\beta_m = n_{eff,m}k$), n_r is the real part of the refractive index, $\bar{n}_r$ is the non-perturbed refractive index profile, and E_m is the distribution of the electric field of the mode m. This theory, further detailed in [291], provides a framework for understanding how light interacts with the GeSn medium from a waveguide. However, the coupling introduces complex interactions among the supported optical modes, resulting in energy exchange between them. This dynamic influences coupling efficiency, as some light remains confined in the waveguide, leading to mode interference and coupling variations.

FDTD simulations offer a powerful tool for analyzing such interactions. Extracting field distributions from simulations allows calculating absorbed power (P_{abs}) in complex structures using [292]:

$$P_{abs} = -\frac{kc\epsilon_0}{P_{in}} \int_V n_r n_i |E|^2 dV \tag{5.8}$$

where c is the speed of light, ϵ_0 is the vacuum permittivity, $|E|$ is the magnitude of the electric field, and n_i is the imaginary part of the refractive index. The integration is carried out over the volume (or area in 2D simulations) of the active region and normalized by the input power (P_{in}).

In the context of integrated photodetectors, achieving optimal performance involves balancing multiple factors, including responsivity, bandwidth, and dark current. To optimize these metrics, it is important to identify the minimal active region length that provides a satisfactory trade-off. Shorter detector lengths are advantageous because they reduce the device's resistance and capacitance, minimizing dark current and maximizing bandwidth. This optimization will be examined under three integration scenarios:

- **Scenario 1:** Monolithic integration on an SOI waveguide with a Ge buffer layer.
- **Scenario 2:** Heterogeneous integration on an SOI waveguide using transfer printing.
- **Scenario 3:** Monolithic integration on a GOS waveguide, where the Ge buffer layer serves as the waveguide core material.

These scenarios are illustrated in Fig. 5.16. Although practical PICs typically employ a top cladding layer such as SiO_2 or SiN, air was used in the simulations to simplify the problem, acknowledging that this approximation affects the effective refractive indices. In scenario 2, light is launched into an SOI waveguide with an SU-8 top cladding to specifically model the transient coupling with the GeSn active region, decoupling it from other potential sources of coupling losses. Figure 5.17 presents schematics of the longitudinal cross-section (left) and 2D field distributions of light coupling into the GeSn layer before absorption (right) for each case. The field distribution illustrations reveal distinct coupling behaviors across the scenarios. In scenarios 1 and 2, relatively efficient absorption is observed over short coupling distances. In contrast, scenario 3 exhibits slower absorption, with some light remaining in the waveguide even after an absorption length of 20 μm.

To compare the performance of these coupling scenarios effectively, the absorption efficiency can be modeled using a method similar to that described in Equation 5.6, following the

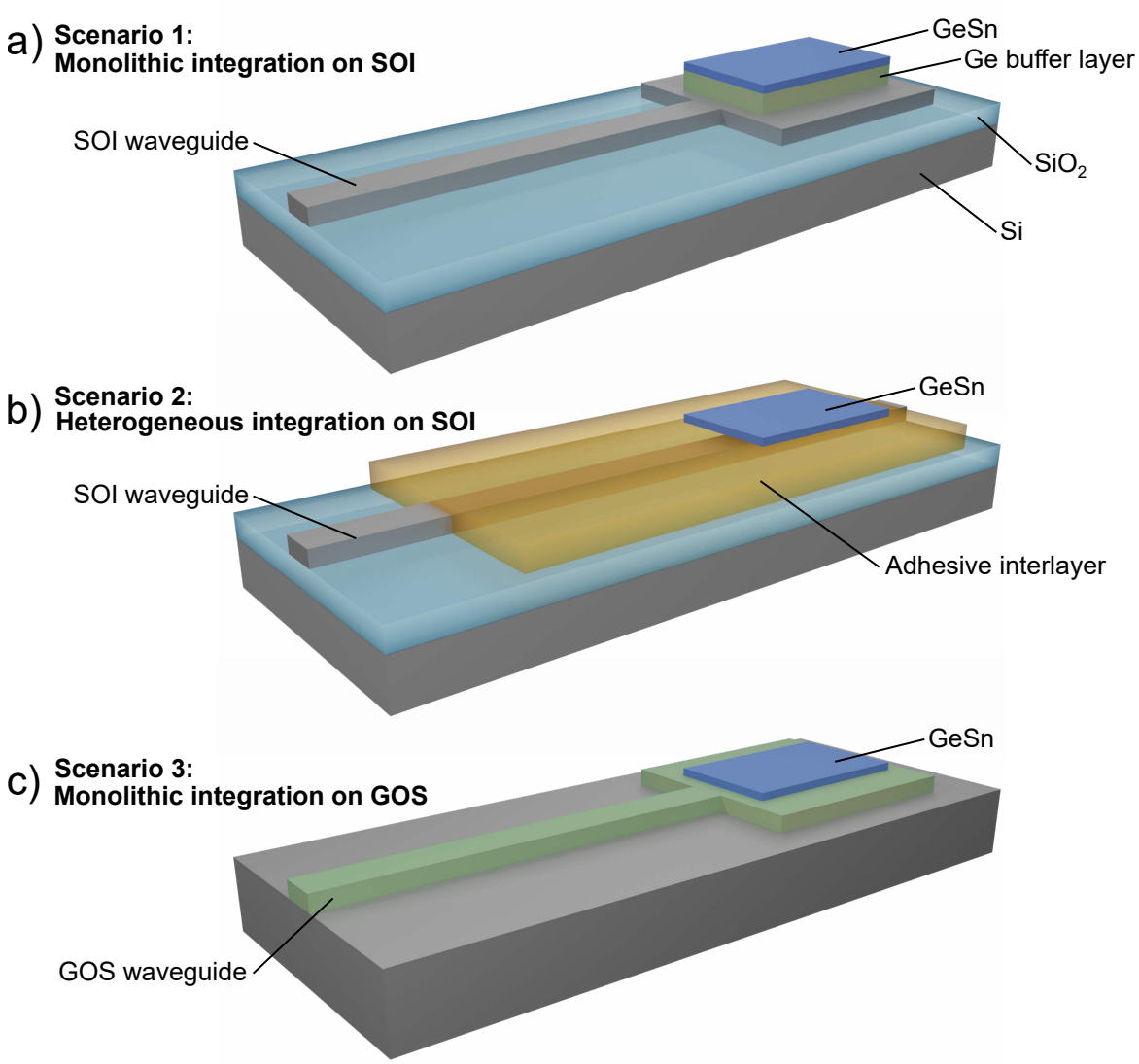


Figure 5.16 Illustration of the three integration scenarios. (a) Scenario 1. (b) Scenario 2. (c) Scenario 3.

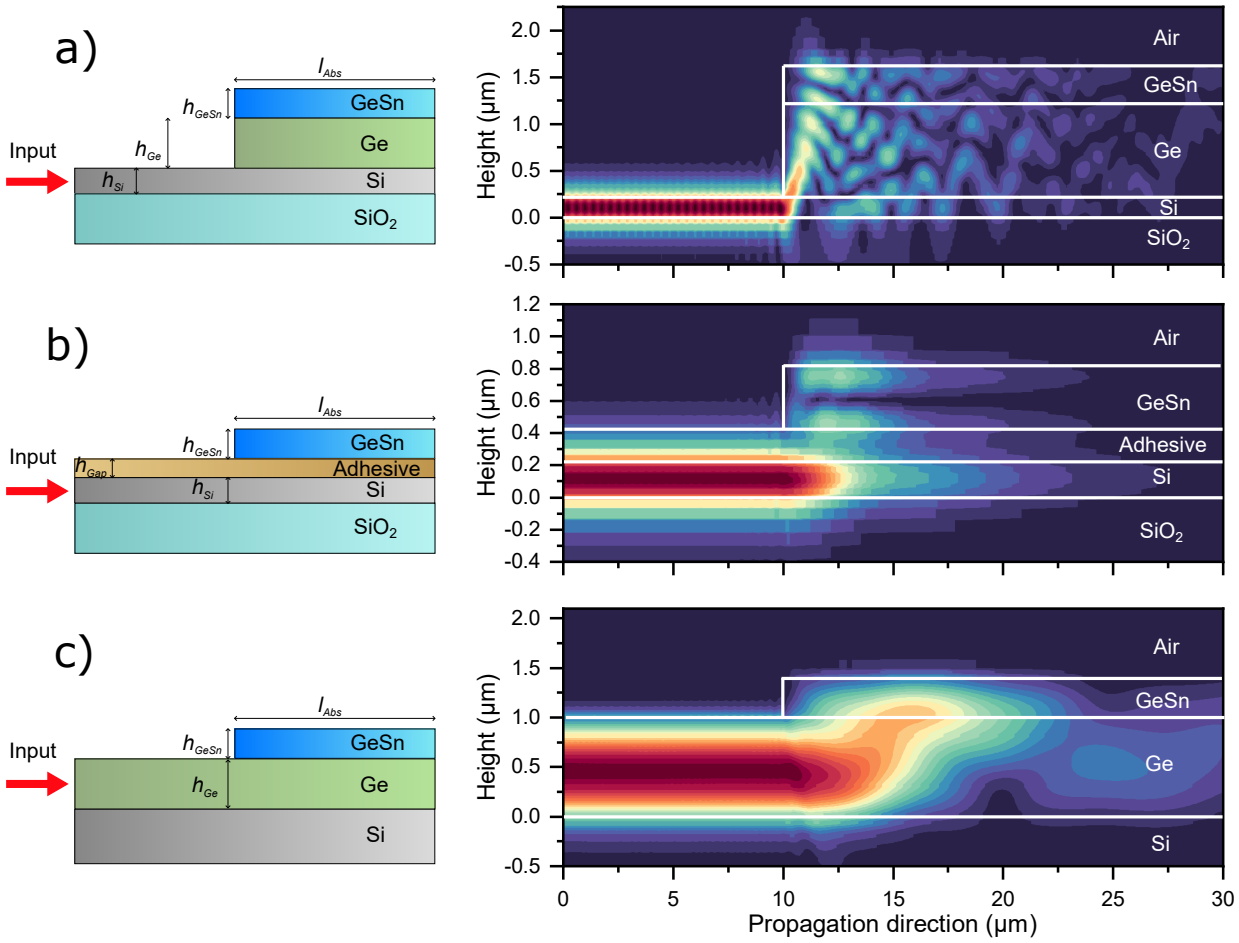


Figure 5.17 The longitudinal cross-section of the three scenarios investigated (left) and the 2D electric field distribution of light propagating in the waveguide and interacting with the GeSn layer at a wavelength of 2 μm. (a) Scenario 1 with a 1 μm thick Ge buffer layer. (b) Scenario 2 using an adhesive (here SU-8). (c) Scenario 3.

approach outlined by Ahn *et al.* [293]:

$$P_{abs} = P_{abs,sat}\left(1 - e^{-\alpha_{Coupling}L}\right) \tag{5.9}$$

where $\alpha_{Coupling}$ is the coupling rate for a given configuration and $P_{abs,sat}$ the value of P_{abs} at saturation. These parameters are extracted by fitting the equation to simulation data, allowing for a direct comparison of different configurations. The value of $1/\alpha_{Coupling}$ provides the absorption length at which 63% of the maximal value is achieved (here $P_{abs,sat}$). Therefore, we wish to find configurations for which we can maximize both $\alpha_{Coupling}$ and $P_{abs,sat}$.

2D FDTD simulations are conducted along the longitudinal cross-section to analyze light propagation through the structure, with a maximum absorption length l_{GeSn} of 100 μm[2]. Slab waveguides are used without metal contacts, and simplifying assumptions are made, such as homogeneous materials and the absence of defects or roughness, which could otherwise introduce additional losses. While these assumptions may affect simulation accuracy, their impact will be addressed later.

The active material used in the calculations is a single $Ge_{0.89}Sn_{0.11}$ layer, whose release as a transferable membrane has been demonstrated and thoroughly characterized in Chapter 4. Most simulations are carried out with a GeSn layer thickness (h_{GeSn}) of 400 nm and at a wavelength of 2 μm, where Ge is essentially transparent.

Scenario 1: Monolithic integration using the SOI platform

In scenario 1, light couples from the SOI waveguide into the Ge/GeSn stack, as shown in the electric field distribution in Fig. 5.17(a). Initially, the light leaks into the Ge buffer layer due to its significantly higher refractive index, which provides stronger optical confinement. This interaction excites multiple modes, allowing the light to be absorbed by the GeSn layer. The tendency of light to propagate in materials with higher refractive indices increases the overlap with the Ge buffer layer, enhancing coupling efficiency. The Ge buffer layer is set to 1 μm, as most GeSn samples are grown with a similar or greater thickness. To mitigate overlap with this defective region and minimize propagation losses, a thicker buffer layer is preferable. This positions the optical mode further from the defect-rich interface, reducing scattering and absorption caused by defects. The GeSn layer could potentially be grown without the need of a Ge buffer layer using selective area epitaxy (SAE).

Figure 5.18(a) shows the absorbed power fraction as a function of length, with light injected

[2]Using Lumerical FDTD. The mesh type is *auto non-uniform* with a mesh accuracy setting of 6 and a minimum mesh size of 20 nm. Perfectly matched layers are set at the boundaries of the simulation domain.

in TE polarization and at an operating wavelength of 2 μm. Different waveguide height values ranging from 220 to 500 nm are simulated while keeping the height of the Ge buffer layer fixed at 1 μm and the GeSn thickness at 400 nm. The waveguide height does not appear to significantly impact P_{abs} for these values because the optical mode is already well confined within the GeSn layer, resulting in efficient absorption regardless of the waveguide height. A fraction of 0.9 is reached relatively quickly after an interaction length of approximately 10 μm. It should be noted that only TE-polarized modes were considered in the simulations. Although TM polarization was initially evaluated, the TM mode exhibits significantly higher propagation losses for the SOI waveguide thickness of 220 nm used in this study as only TE modes are supported for this thickness. However, the TM mode field distribution could in principle offer a enhanced evanescent coupling for larger thicknesses. Figure 5.18(b) shows P_{abs} as a function of the GeSn and Ge buffer layer thicknesses over a 20 μm long active region, also using a TE polarization. The Ge buffer layer thickness ranges from 0 to 3 μm, the former corresponding to a case where SAE is employed. The results suggest that a GeSn thickness of at least 200 nm is sufficient to achieve significant absorption, with little improvement observed for thicker layers. Conversely, while a Ge buffer layer thickness ranging from 0 to 1 μm seems to provide a similar absorption efficiency, it tends to decrease as the thickness increases. The oscillations observed in P_{abs} at given thicknesses are attributed to a scattering loss that occur at the moment when the propagating light interacts with the Ge/GeSn stack and undergoes an abrupt change in effective refractive index. The total scattered light that exits the simulation domain (T_{loss}) is plotted as the dashed lines for each value of Ge buffer thickness along the second y-axis.

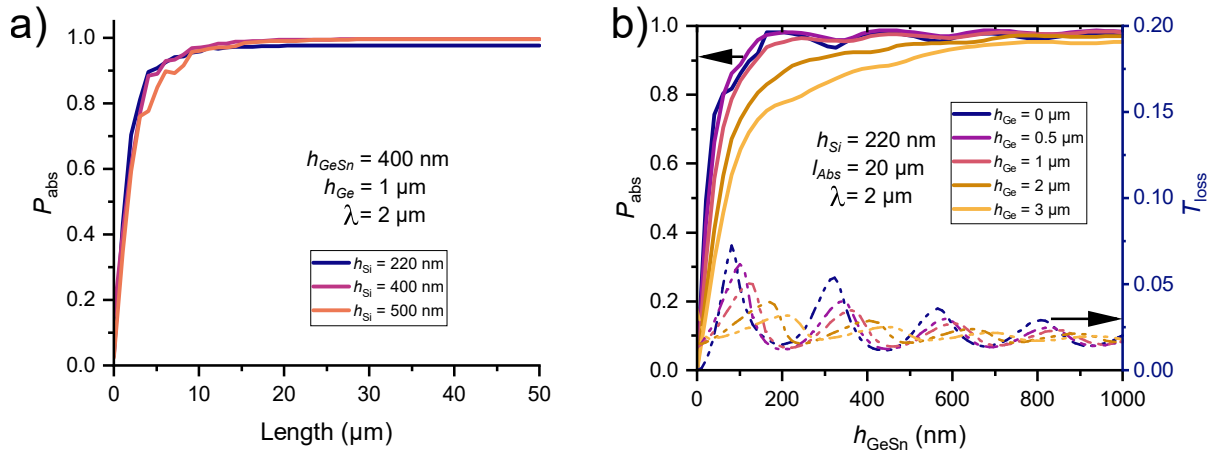


Figure 5.18 Impact of the dimensions on the fraction of absorbed power. (a) Absorbed power fraction as a function of length. (b) Absorption as a function of GeSn thickness and Ge buffer height.

Figure 5.19 shows the wavelength dependence of P_{abs} over a 20 μm long active region in the GeSn and Ge layers. The absorption dip below 1.75 μm is attributed to absorption in the Ge buffer layer. The absorption fraction decreases up to the cutoff wavelength of the GeSn. Longer detector lengths would be required to enhance absorption efficiency for operation near the cutoff wavelength. The negligible absorption observed in the curve associated to the Ge layer above a wavelength of 1.75 μm could be attributed to an overlap of the absorption monitor over the Ge/GeSn interface, when it actually occurs in the GeSn material.

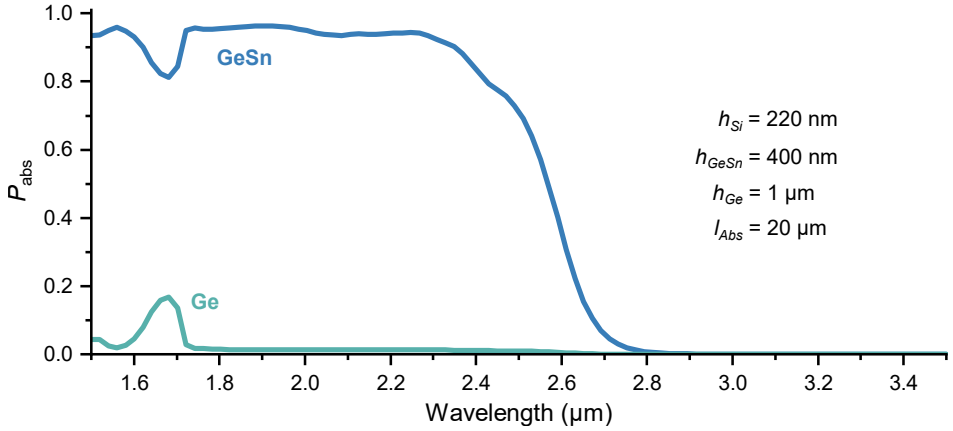


Figure 5.19 Wavelength dependence of P_{abs} in the GeSn and Ge layers separately (h_{Si} = 220 nm, h_{Ge} = 1 μm, and h_{GeSn} = 400 nm).

Using Equation 5.9, we can extract $\alpha_{Coupling}$ and $P_{abs,sat}$ by varying a few parameters. Figure 5.20 shows the wavelength dependence of $1/\alpha_{Coupling}$ (Fig. 5.20(a)) and $P_{abs,sat}$ (Fig. 5.20(b)). The coupling rate tends to decrease at longer wavelength toward the cutoff value near 2.75 μm as seen in Fig. 5.3(b). While the coupling rate also varies with the waveguide height h_{Si}, no clear trend emerges, which may be attributed to wavelength-dependent phase matching conditions. Both the coupling rate and $P_{abs,sat}$ show slight improvement with an increase in GeSn thickness h_{GeSn} from 0.4 to 1 μm, resulting in more efficient absorption.

Although this scenario demonstrates a relatively high absorbed power fraction, which can contribute to a high quantum efficiency, the value of ζ in Equation 5.5 that sets the proportion of photons contributing to the generation of photocarriers may decrease significantly due to defects at the Si/Ge and Ge/GeSn interfaces. The Ge buffer layer could potentially be removed in an integration scheme involving SAE, which could potentially lead to a more efficient absorption if it helps minimize the density of dislocations.

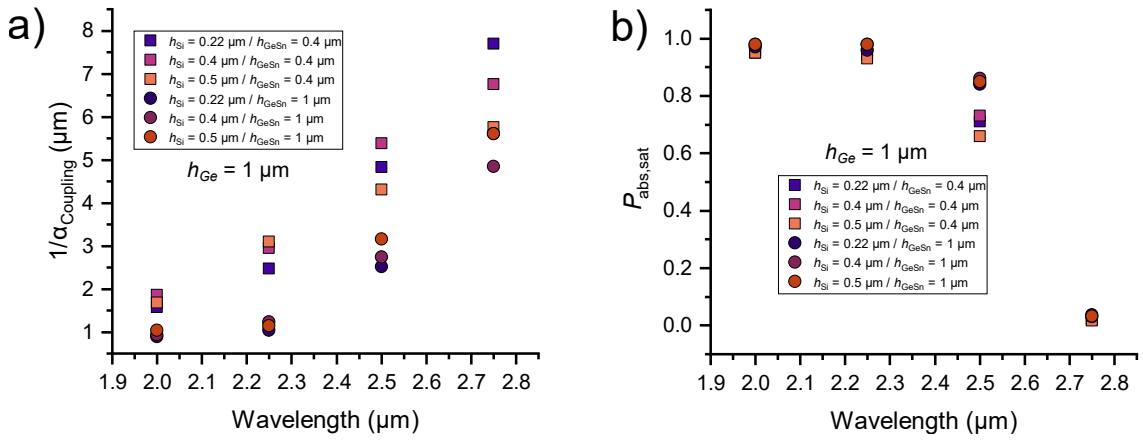


Figure 5.20 Wavelength dependence of coupling efficiency metrics in Scenario 1 by varying the waveguide height (h_{Si}) and the GeSn thickness (h_{GeSn}). (a) $1/\alpha_{Coupling}$. (b) $P_{abs,sat}$.

Scenario 2: Heterogeneous integration using the SOI platform

In scenario 2, the Ge buffer layer is replaced by a layer with a lower refractive index than the core and the active material. Due to the nature of evanescent coupling, light tends to be confined within higher-index materials, and the coupling efficiency depends on the separation gap. For a transferred membrane with relaxed compressive strain, the absorption coefficient is slightly higher for a given wavelength and the absorption cutoff wavelength is extended from about 2.8 to 3.1 μm.

Figure 5.21(a) shows the absorbed power as a function of the separation gap for different media used as the adhesive layer compared to air at a wavelength of 2 μm. SU-8 and BCB have refractive indices between 1.5 and 1.6, which leads to a longer evanescent tail of the optical mode and allows an efficient coupling across larger gaps. SU-8 is used as the passivation layer in subsequent modeling results and is also considered when computing the initial propagating mode. Figure 5.21(b) shows the wavelength dependence of the absorption from 1.5 to 3.5 μm for different separation gaps. By increasing the separation gap, the absorption efficiency decreases more rapidly for shorter wavelengths as the mode is less evanescent, while it also decreases near the cutoff of GeSn around 3 μm due to a weaker absorption coefficient.

Figure 5.22(a) shows the absorption as a function of GeSn thickness for different separation gaps. As the gap becomes larger, the absorption fraction becomes more efficient for specific GeSn thicknesses. While larger thicknesses are generally expected to enhance absorption, a minimal absorption is observed at certain thicknesses for a given gap value. However, this effect diminishes as the gap becomes smaller, where absorption efficiency remains relatively

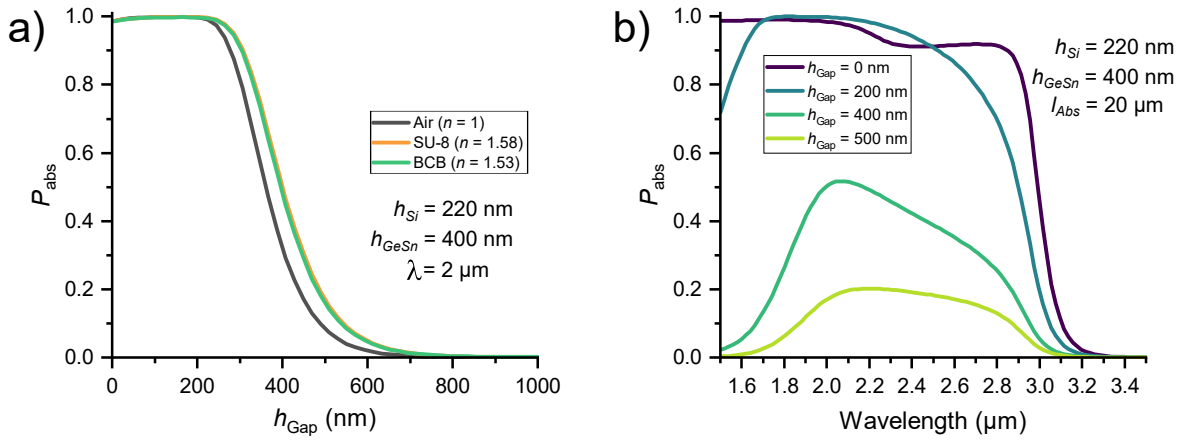


Figure 5.21 Impact of the properties of the gap on P_{abs}. (a) Dependence of the separation gap h_{Gap} using air, SU-8, and BCB as the medium for the gap. (b) Wavelength dependence for different separation gaps h_{Gap}.

consistent regardless of GeSn thickness. Figure 5.22(b) shows the absorbed power fraction as a function of GeSn thickness and the absorption length at a separation gap of 200 nm. Oscillations in P_{abs} are observed and highlight a less efficient coupling for some GeSn thicknesses, where a longer detector length would be required, compared to specific thicknesses where the fraction of absorbed power reaches a value of 0.9 for waveguide lengths of about 5 μm or less.

This beating effect is likely associated with a phase-matching condition between the modes of the waveguide and the active GeSn material, which behaves as a slab waveguide. Phase matching occurs when the effective refractive indices of the coupled modes in both structures are equal, enabling efficient energy transfer via evanescent coupling. The oscillation maxima observed in Fig. 5.22(a) and Fig. 5.22(b) then correspond to specific GeSn thicknesses where phase-matching is achieved. This phenomenon was also noted by J. Brouckaert in his thesis with simulations of a heterogeneously integrated InGaAs detector on an SOI waveguide [294].

This phase-matching condition can be verified by analyzing the evolution of the effective refractive index for each structure separately. Figure 5.23 shows the effective indices of the TE slab modes supported by the GeSn active region. The dashed horizontal line represents the effective index of the fundamental TE mode in the SOI waveguide ($n_{eff} \approx 2.62$) and intersects with the GeSn slab modes at thicknesses corresponding to the absorption maxima in Fig. 5.22(a) and Fig. 5.22(b), which are thicknesses of approximately 116 nm, 417 nm, and 711 nm. These thickness values are expected to change with variations in wavelength or waveguide dimensions. Maintaining a small separation gap then seems to be beneficial for

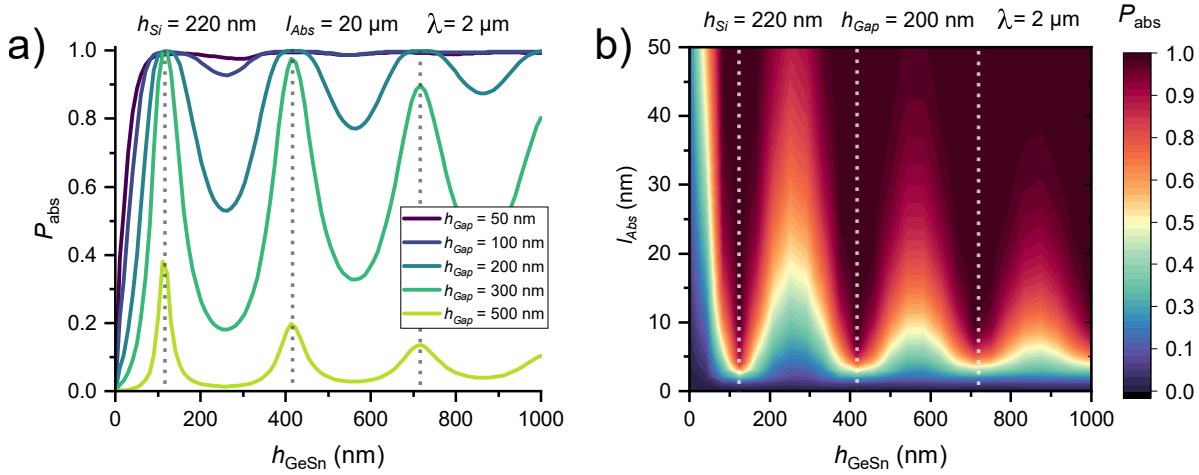


Figure 5.22 Influence of GeSn active region dimensions on the coupling efficiency. (a) Influence of the thickness of the GeSn layer for different gaps. (b) Influence of the thickness and the length of GeSn at a h_{Gap} of 200 nm.

stabilizing the absorbed power fraction, which would otherwise depend on several fluctuating parameters.

Figure 5.24 shows the absorbed power fraction as a function of separation gap for different waveguide heights using a TE polarization. The absorption efficiency quickly decreases as the waveguide height increases and is less tolerant to larger separation gaps filled with SU-8.

Figure 5.25 shows the wavelength dependence of the coupling rate (Fig. 5.25(a)) and $P_{abs,sat}$ (Fig. 5.25(b)) by varying the separation gap h_{Gap}. In this scenario, the cutoff wavelength extends beyond 3 μm due to the expected strain relaxation, resulting in a more efficient coupling and absorption at 2.75 μm compared to Scenario 1. The coupling rate decreases steadily as the separation gap increases across the studied wavelength range. Despite this, $P_{abs,sat}$ remains above 0.9 with values of $1/\alpha_{Coupling}$ below 8 μm for gap values up to 200 nm.

Performing a layer transfer of GeSn can provide an overall good absorption efficiency that is comparable to Scenario 1, provided that the separation gap between the two structures remains small (below 300 nm). Achieving phase-matching ensures efficient optical power transfer by aligning the propagation constants of the waveguide and GeSn layer. If phase-matching is not met, coupling efficiency drops significantly, leading to increased optical losses and longer required interaction lengths. The interfaces are expected to be largely defect-free, as most layer transfer methods involve partial surface etching. This would help in enhancing the quantum efficiency by minimizing defect-related losses.

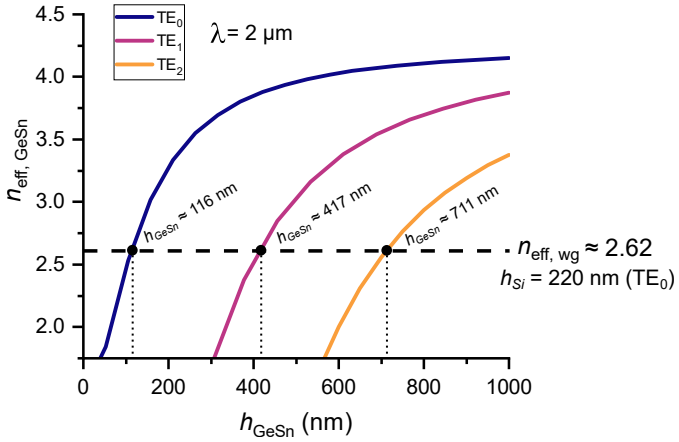


Figure 5.23 Effective index of the first three TE slab modes of the GeSn active region as a function of GeSn thickness. A phase-matching condition is met with the SOI slab waveguide at GeSn thicknesses corresponding to the oscillations where P_{abs} is maximal.

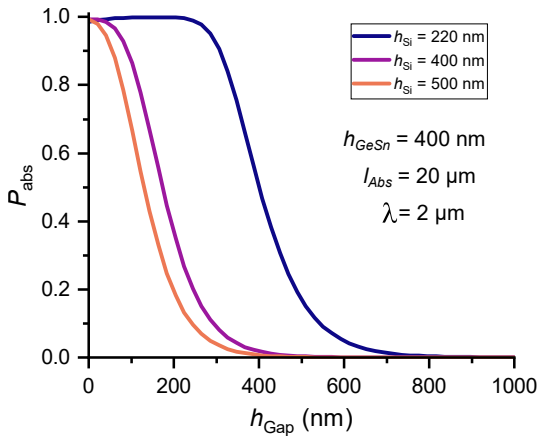


Figure 5.24 Absorbed power fraction as a function of separation gap for different waveguide heights h_{Si} and polarizations.

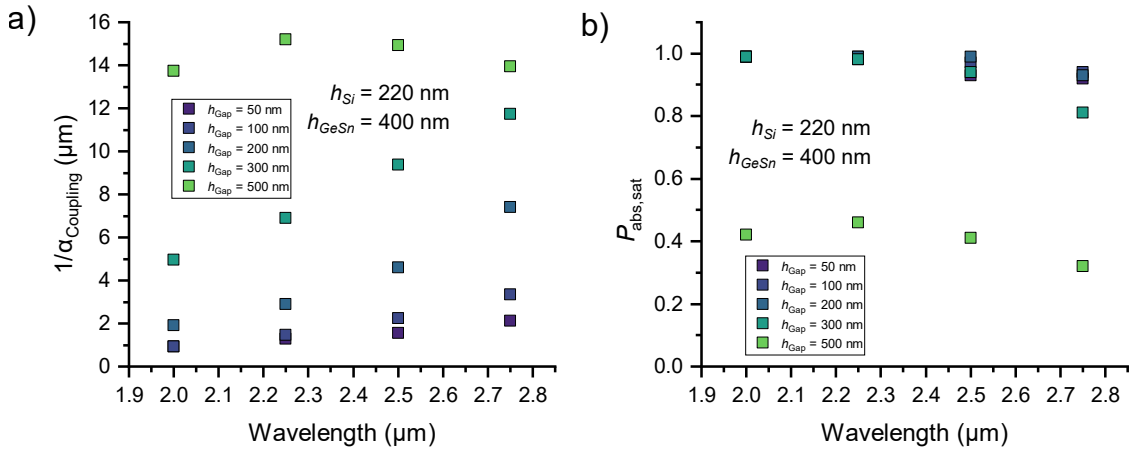


Figure 5.25 Wavelength dependence of coupling efficiency metrics in Scenario 2 by varying the gap (h_{Gap}). (a) $1/\alpha_{Coupling}$. (b) $P_{abs,sat}$.

Scenario 3: Monolithic integration using the GOS platform

In scenario 3, the Ge buffer layer functions as the waveguide layer, with GeSn monolithically integrated on top through growth combined with etching or SAE. Although defective interfaces are anticipated, this platform is primarily suited for operation in the mid-infrared range. Higher-quality GeSn layers with increased Sn content would enhance platform performance and extend its operational range. By default, the waveguide height is set to 1 μm, the GeSn layer thickness to 400 nm, and the wavelength to 2 μm. Figure 5.26(a) presents the absorbed power fraction as a function of length for both TE and TM polarizations. The results show similar efficiency for both polarizations, with approximately 90% of the power absorbed after a length of just 9 μm. Figure 5.26(b) the wavelength dependence of the absorbed power fraction for a waveguide length of 50 μm with the same dimensions. Most of the light is absorbed at wavelengths below 1.75 μm, with similar behavior observed for both TE and TM polarizations.

Figure 5.27(a) shows the effect of GeSn layer thickness on absorption efficiency using a fixed Ge waveguide height of 1 μm. The absorption efficiency increases steadily with thickness up to 400 nm for absorption lengths slightly above 10 μm, after which a small decrease in P_{abs} is observed for thicknesses of 600 and 1000 nm. This may be related to a mode beating phenomena, as observed in scenario 2, where the mismatch in the propagation constants can influence the coupling efficiency.

Figure 5.27(b) illustrates the influence of waveguide height for a fixed GeSn thickness of 400 nm. A smaller waveguide height of 500 nm results in a slightly faster coupling rate, where

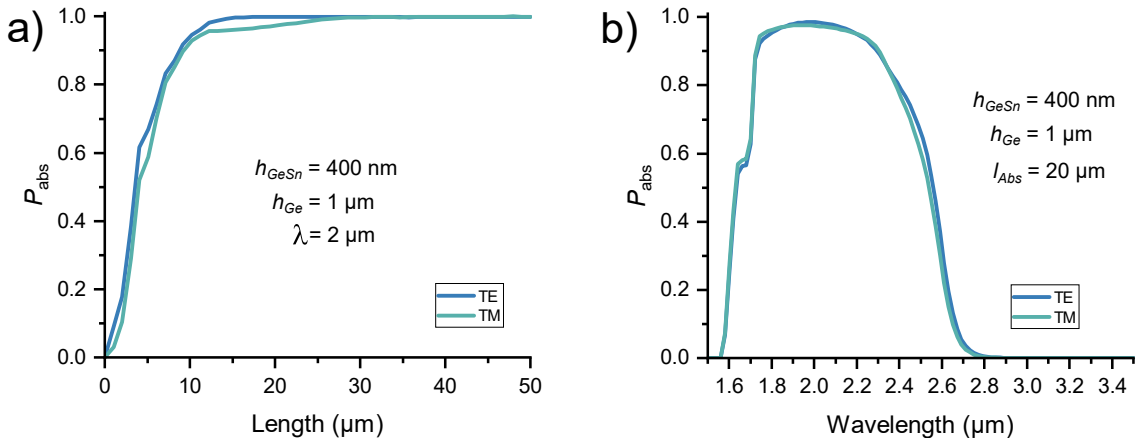


Figure 5.26 Impact of polarization on P_{abs}. (a) Absorbed power fraction as a function of length for TE and TM polarizations. (b) Wavelength dependence of the absorbed power fraction after propagating through 50 μm in the GOS waveguide.

shorter length of about 6 μm is required to effectively absorb 90% of the power, compared to 10 μm for a 1 μm height. While increasing the waveguide height can help design modes that avoid overlap with the defective zone, it significantly reduces the coupling rate. For instance, a length of approximately 45 μm is required to absorb 90% of the power at a height of 2 μm. When the waveguide height is 3 μm, only 60% of the power is absorbed after 50 μm. Tightly confined modes can lead to a lower coupling coefficient with other structures. To address this, incorporating tapered waveguides may improve the coupling efficiency by adiabatically varying the width, thereby reducing the required length of the active region [24].

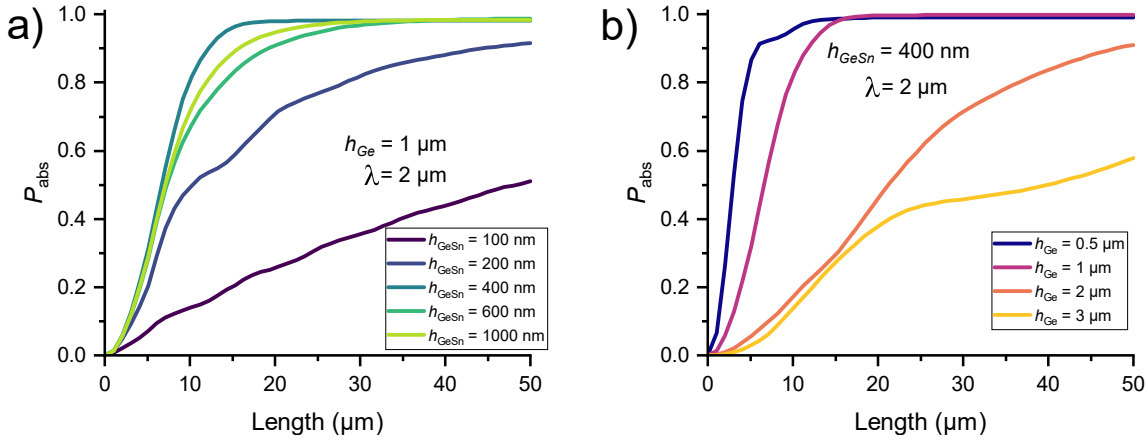


Figure 5.27 Impact of geometry on P_{abs}. (a) Absorbed power fraction as a function of length and GeSn material thickness. (b) Absorbed power fraction as a function of length and Ge waveguide height.

Figure 5.28 shows extracted values of $\alpha_{Coupling}$ (Fig. 5.28(a)) and $P_{abs,sat}$ (Fig. 5.28(b)) by varying the wavelength, the waveguide height h_{Ge} and the GeSn thickness h_{GeSn}. The behavior is similar to that observed in Scenario 1 but with significantly lower coupling rates. Consequently, the values of $1/\alpha_{Coupling}$ are nearly an order of magnitude higher than in scenarios 1 and 2. Moreover, the coupling rate tends to decrease as the waveguide height increases. Increasing the GeSn thickness seems to result in slower coupling for waveguide heights exceeding 1 μm. These trends highlight the importance of optimizing waveguide and GeSn layer dimensions to balance coupling efficiency with device constraints.

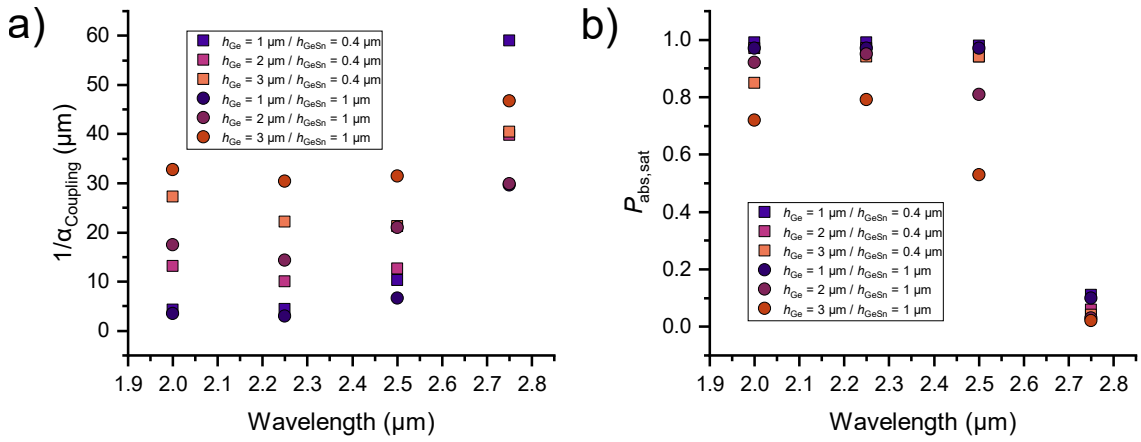


Figure 5.28 Wavelength dependence of coupling efficiency metrics in Scenario 3 by varying the waveguide height (h_{Ge}) and the GeSn thickness (h_{GeSn}). (a) $1/\alpha_{Coupling}$. (b) $P_{abs,sat}$.

The similar absorption efficiency for TE and TM modes in the GOS platform makes it highly suitable for integration with quantum cascade lasers (QCLs), which emit exclusively in TM polarization. This feature also enhances its potential for sensing applications, where strong TM evanescent fields improve analyte interaction. SOI waveguides can also be designed to favor a TM polarization for thicknesses of at least 400 nm. Additionally, defective regions near the GeSn/Ge and Ge/Si interfaces are anticipated as in Scenario 1.

5.5 Discussion on the impact of additional design considerations

These modeling scenarios demonstrate that effective coupling between SOI and GOS platforms and the GeSn active material is achievable via monolithic or heterogeneous integration, even for relatively short detector lengths. Further exploration of additional parameters could yield deeper insights, but we briefly discuss key considerations below:

- **Other coupling schemes**

  Evanescent coupling is particularly advantageous for integrated photodetectors as it enables efficient optical power transfer without direct material contact. This reduces fabrication complexity while preserving high coupling efficiency. While these scenarios focus on evanescent coupling, other coupling schemes are worth considering. A widely used alternative is vertical coupling, which utilizes a diffraction grating etched into the waveguide during heterogeneous integration. This approach increases tolerance to separation gaps but may introduce higher coupling losses, as light can also be diffracted downward toward the substrate. This scheme will be studied in Chapter 6 and compared to evanescent coupling. Van Thourhout *et al.* provide a comprehensive overview of coupling schemes for heterogeneous integration [284].

  Li *et al.* investigated GeSn designs through modeling utilizing the *butt-coupling* scheme on an SOI platform [25], where the waveguide facet directs light into the active region grown in a recessed area adjacent to the facet. This strategy, which is accessible through either heterogeneous or monolithic integration, has been employed by Remis *et al.* to enable the coupling between a GaSb-based diode laser and SiN waveguides [210]. Muthuganesan *et al.* also employed butt-coupling to couple SOI waveguides with InGaAs membrane photodetectors that were transfer-printed into the recessed area [295]. While offering potentially high efficiency through direct waveguide-to-active-region transfer, this approach is more sensitive to alignment and requires precise fabrication of recessed regions.

  Depending on the specific application requirements, each coupling scheme presents distinct advantages and trade-offs. For GeSn-based mid-infrared photodetectors integrated with silicon photonics, evanescent coupling remains a highly favorable choice given its demonstrated scalability and robust performance.

- **Waveguide width**

  The 2D FDTD simulations conducted earlier utilized slab waveguides to analyze coupling behavior along the longitudinal cross-section. Defining the waveguide and GeSn active region width requires 3D FDTD simulations, significantly increasing computational demands. As discussed in Section 5.3,defining the waveguide width affects the properties of the supported optical modes. Specifically, the effective refractive index (n_{eff}) and waveguide dispersion can be tuned, which strongly influences coupling behavior in all three scenarios, including the phase-matching condition observed in Scenario 2. Extending the simulations to 3D FDTD and studying the evolution of the

confinement factor of the different modes would provide a more accurate depiction of the coupling mechanisms.

The waveguide geometry and the refractive index contrast between the core and active materials are expected to influence the coupling rate [293]. To illustrate the impact of waveguide width on absorption efficiency, 3D FDTD simulations were performed using the Scenario 2 configuration based on heterogeneous integration, with the waveguide width defined and varied. The results are shown in Fig. 5.29 at an operating wavelength of 2 μm. In this case, the active region is modeled as a slab waveguide, and the waveguide thickness/height is 220 nm. A slight variation in the absorbed power fraction is observed for small separation gaps, such as a minor reduction in absorption for a waveguide width of 500 nm. However, the overall behavior closely aligns with the results from 2D FDTD simulations shown in Fig. 5.24.

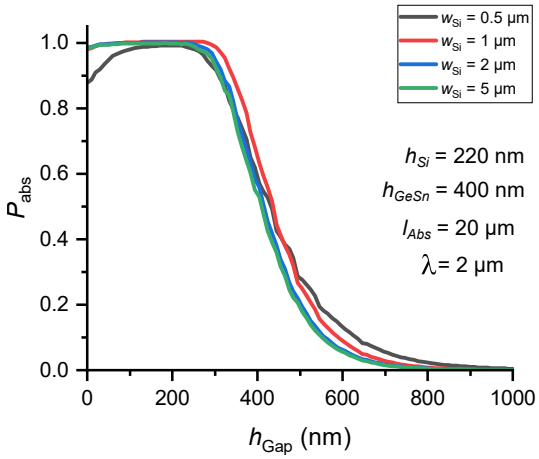


Figure 5.29 Absorbed power fraction as a function of separation gap for different waveguide widths w_{Si}.

- **GeSn layer properties**

  For these simulations, we used a content of 11 at.% Sn with two different strain values (-0.6% for scenarios 1 and 3, and 0% for scenario 2). Modifying the Sn content and strain significantly impacts the optical properties of the GeSn layer, particularly the magnitude and spectral range of absorption. Higher Sn content lowers the bandgap and extends the absorption cutoff, broadening the spectral bandwidth. However, higher Sn content introduces a greater lattice mismatch and reduced thermal stability, potentially increasing defect density. These defects contribute to additional absorption that does not generate electron-hole pairs. While maximizing spectral bandwidth can support

multiple applications, it is preferable to select an Sn content that achieves sufficient absorption without excessive defects.

Monolithic integration supports various Sn contents, though higher Sn levels may require GeSn buffer layers to enhance quality [121, 122]. Conversely, lower Sn contents result in a reduced absorption coefficient and a narrower operational range but are expected to produce fewer defects. The presence of dopants also affects the absorption magnitude as Ge and GeSn layers are grown using CVD typically exhibit p-type behavior with a carrier concentration around $1 \times 10^{17}\,\mathrm{cm}^{-3}$. This was accounted for in the calculation of the optical properties for determining the Fermi levels when using $k \cdot p$ theory.

- **Heat dissipation**

  Effective thermal management is important to prevent overheating, particularly given GeSn's limited thermal stability and the significant heat generated by active devices. Chrétien *et al.* demonstrated optically pumped lasing in GeSn microdisks at room temperature, attributing the success to enhanced heat dissipation provided by the AlN pedestal supporting the microdisk [65]. While adhesives like SU-8 and BCB are useful for prototyping, their poor thermal conductivity may limit thermal stability.

  Although the thermal properties of GeSn have been scarcely explored, Spirito *et al.* extracted the thermal conductivity of GeSn samples with Sn contents up to 14 at.% using Raman thermometry [133]. They observed a decrease in thermal conductivity from 18 to $4\,\mathrm{W/(m \cdot K)}$ for Sn contents ranging from 5 to 14 at.%. Direct bonding, which avoids adhesives, often requires a dielectric layer (such as SiO_2, SiN, or Al_2O_3) to improve bonding yield [22, 23, 296]. Alternatively, direct growth could enhance heat dissipation at the GeSn/waveguide interface.

  Table 5.1 summarizes the thermal conductivity of GeSn and other materials commonly used in various platforms and integration schemes at room temperature. Efficient heat dissipation is essential for GeSn-based photonic devices, as excessive heat can degrade performance and induce structural changes. Among passive platforms, the GOS platform offers superior heat dissipation compared to the SOI platform due to the significantly higher thermal conductivity of its cladding layer (Si) relative to the BOX (SiO_2) layer [297].

Table 5.1 Thermal conductivity of GeSn and other materials.

Material	**Thermal conductivity** ($\mathrm{W/(m \cdot K)}$)
GeSn (5 at.% Sn)	18 [133]
GeSn (14 at.% Sn)	4 [133]
Ge	56 [298]
Si	139 [298]
SiO_2	1.3 [298]
SiN	10–43 [298]
AlN	285 [298]
Al_2O_3	30 [298]
SU-8	0.2 [299]
BCB	0.293 [300]

- **Types of detectors**

  Two common types of photodetectors in integrated photonics are metal-semiconductor-metal (MSM) detectors and p-i-n junctions. MSM detectors generally have lower capacitance, enabling high-bandwidth operation, while p-i-n junctions, with an intrinsic layer between p- and n-doped regions, offer lower dark current densities and more stable operation. Our model has been simplified for compatibility with MSM detectors but can be adapted for more complex designs to study p-i-n detectors. In both configurations, a passivation layer such as SiO_2 is typically required atop the waveguide, with vias etched through the layer to connect metal contacts to the p- and n-doped regions. GeSn waveguide photodetectors can utilize a lateral p-i-n junction design by doping the sides of the waveguide [301]. In p-i-n detectors, the electric field is confined within the intrinsic layer between the p-doped and n-doped layers, meaning that photocarriers contributing to the photocurrent are generated primarily from the optical power absorbed in this region.

- **Impact of metal contacts**

  The modeling results presented are well-suited for MSM detector integration, which requires relatively simple fabrication involving the deposition of metal contacts. However, a significant overlap between the guided optical modes and the metal contacts can result in undesired absorption [218]. To address this, optimizing the contact design is necessary for improving photocarrier collection while minimizing optical losses, which can be achieved by performing electrical and optical simulations to estimate the optimal spacing between the electrodes. Additionally, a capping layer with a lower refractive index, such as lower Sn content GeSn or Ge, could be deposited above the active GeSn

layer to reduce the overlap between the evanescent field and the metal contacts.

5.6 Conclusion

The modeling results in this chapter demonstrate effective coupling of GeSn alloys with SOI and GOS platforms for both monolithic and heterogeneous integration. Heterogeneous integration via GeSn membrane transfer appears to be a viable approach for active component development, provided the separation gap remains small enough to minimize phase mismatch effects. For wavelengths beyond 4 μm, GOS is necessary for monolithic GeSn integration, whereas SOI remains suitable for shorter wavelengths. However, material growth challenges make heterogeneous integration the preferred approach for rapid prototyping. The simulation study aimed to provide a general understanding of the influence of geometrical parameters on coupling efficiency. Parameter ranges were selected to remain within realistic fabrication constraints, such as achievable membrane thicknesses and standard SOI and GOS waveguide dimensions. Future work could include a systematic optimization approach to further refine coupling performance. The next chapter will experimentally demonstrate GeSn membrane integration onto SOI waveguides to further explore this approach.

CHAPTER 6 TRANSFER-PRINTED GESN MEMBRANES FOR WAVEGUIDE-COUPLED MID-INFRARED DETECTORS

6.1 Introduction

As discussed earlier, while GeSn alloys have been widely proposed for Si photonics, their direct integration remains largely unexplored, with most studies limited to numerical simulations [25,26] and a few experimental efforts [20,21]. Previous demonstrations of GeSn waveguide photodetectors (WGPDs) have focused on monolithic integration via edge coupling, but without coupling to passive waveguides [90, 301]. This study bridges that gap by demonstrating the feasibility of heterogeneous GeSn membrane integration using transfer printing. Building on the numerical evaluations of integration schemes, demonstrating heterogeneous integration via transfer printing of GeSn membranes would be valuable. This approach not only circumvents monolithic integration challenges but also facilitates rapid prototyping and multi-material co-integration [221]. GeSn membranes, when heterogeneously integrated as active devices with SOI waveguides, hold significant potential for mid-infrared applications and group-IV integrated photonics.

This chapter investigates the feasibility of integrating $Ge_{0.89}Sn_{0.11}$ membranes onto SOI waveguides, as characterized in Chapter 4. The integration follows Scenario 2 from the previous chapter, where GeSn is heterogeneously integrated with an adhesion-enhancing interlayer. A single printing step successfully transferred multiple membranes, yielding devices with consistent properties and underscoring the approach's potential. Unlike in Chapter 4, where metal contacts were transfer-printed, this study employs direct evaporation onto the membranes. The following sections provide an in-depth description of the device concept, integration process, and characterization methods. Through this demonstration, we aim to establish transfer printing as a viable path for the heterogeneous integration of GeSn alloys, which could offer new possibilities for mid-infrared photonic systems.

6.2 Concept and modeling

The device concept is illustrated in Fig. 6.1(a), where a metal-semiconductor-metal (MSM) detector is realized by transfer-printing a GeSn membrane onto an SOI waveguide. Efficient evanescent coupling is achieved when the separation gap between the membrane and the waveguide is minimized, ensuring effective light transfer and absorption in the GeSn layer. Light from the laser is coupled into the waveguide through a surface grating coupler (SGC).

To enhance adhesion and provide electrical insulation for the metal contacts, an SU-8 layer is spin-coated onto the passive chip before membrane transfer. After transferring the GeSn membranes, a Ti/Au bilayer is evaporated to form electrical contacts, completing the MSM device fabrication.

Figure 6.1(b) presents a cross-sectional side view of the final device, highlighting the different material layers. Openings in the SU-8 layer are created around the SGCs to maintain air as the top cladding, ensuring the transmission properties are not affected by the SU-8 thickness. The $Ge_{0.89}Sn_{0.11}$ membranes, approximately 400 nm thick, are strain-relaxed and exhibit a photodetection cutoff at approximately 3.1 μm, effectively covering the 2–3 μm range of the mid-infrared spectrum. Characterization is conducted at 2.33 μm, chosen for its proximity to the 2 μm band and its strategic importance in sensing applications, including CO and CH_4 detection and glucose monitoring. MSM devices offer advantages such as lower capacitance compared to p-i-n devices and simplified fabrication processes. However, they typically exhibit higher dark current levels, which can impact overall device performance.

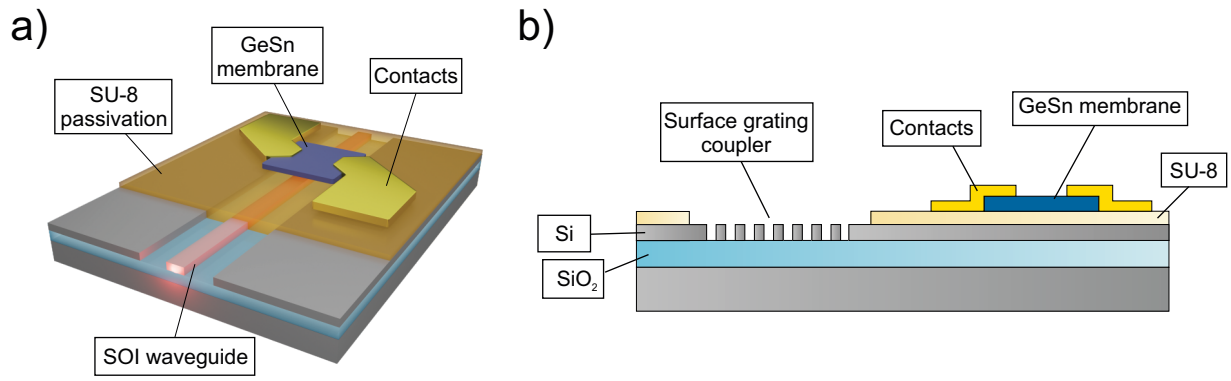


Figure 6.1 Device schematic of a waveguide-integrated GeSn photodetector. (a) Illustration of the concept. (b) Cross-section of the designed device. A GeSn membrane is transfer-printed on top of a waveguide using a thin SU-8 layer to enhance adhesion and passivate the circuit.

Several key design parameters must be defined to successfully fabricate the device. These include optimizing the layout configuration to maximize yield for simultaneous fabrication of multiple devices and determining the appropriate SU-8 thickness to ensure efficient coupling at the operating wavelength. The SGC design needs to be optimized to ensure an optimal performance at 2.33 μm.

6.2.1 Layout design

A layout that enables the simultaneous fabrication of multiple devices is preferable, as it facilitates yield evaluation, performance assessment, and ensures a sufficient number of devices for characterization. Optimizing the device density is crucial while adhering to technical constraints. The PDMS stamps used for membrane transfer are relatively large, with dimensions typically ranging from 1 mm × 1 mm to 2 mm × 2 mm, as they are manually cut using a scalpel. A 2D array configuration maximizes device density within the PDMS stamp area but requires the use of SGCs as interconnects, unlike a 1D array where edge couplers could be placed along the chip edge. SGCs are advantageous as they allow shorter waveguide lengths and provide easier optical access through out-of-plane coupling, reducing propagation losses compared to edge couplers. In contrast, edge couplers suffer from insertion loss variability due to uncontrolled cleaving or dicing quality, often requiring mechanical polishing to minimize losses.

Despite their advantages, SGCs have limitations. Their coupling efficiency is wavelength-dependent, as it relies on a diffraction grating inscribed in the waveguide. Additionally, their performance is sensitive to fabrication variations, such as changes in grating period and etch depth. Figure 6.2 presents the final device layout. The fabrication process includes four overlapping patterning layers: SOI waveguides and grating couplers (purple and green), GeSn membranes (cyan), SU-8 openings (dark blue), and evaporated metal contacts (yellow). Waveguides are 2 μm wide, defined by etching 5 μm trenches in Si. This width was chosen as a compromise to ensure fabrication reliability and efficient vertical coupling while minimizing the presence of high-order modes.

The waveguide structures, GeSn membranes, and metal contact pairs are arranged in a 2D array with a pitch of 400 μm × 200 μm. Two distinct waveguide designs with alternating positions are incorporated in the 2D array: a 300 μm long waveguide with a membrane transfer printed at its center, and a 125 μm long waveguide with the membrane positioned above an SGC. These units form a 7 × 11 array to ensure that the array is sufficiently large ($\sim$2.8 mm × 2.2 mm) to accommodate various sizes of PDMS stamps. These configurations enable the separate study of evanescent and grating-assisted coupling, which is important for understanding their individual contributions to the device performance. The contact pads have dimensions of 100 μm × 100 μm and taper toward each other with a 5 μm gap above the transferred GeSn membrane. Openings in the SU-8 layer around the SGCs ensure that their performance remains relatively unaffected by the SU-8 thickness.

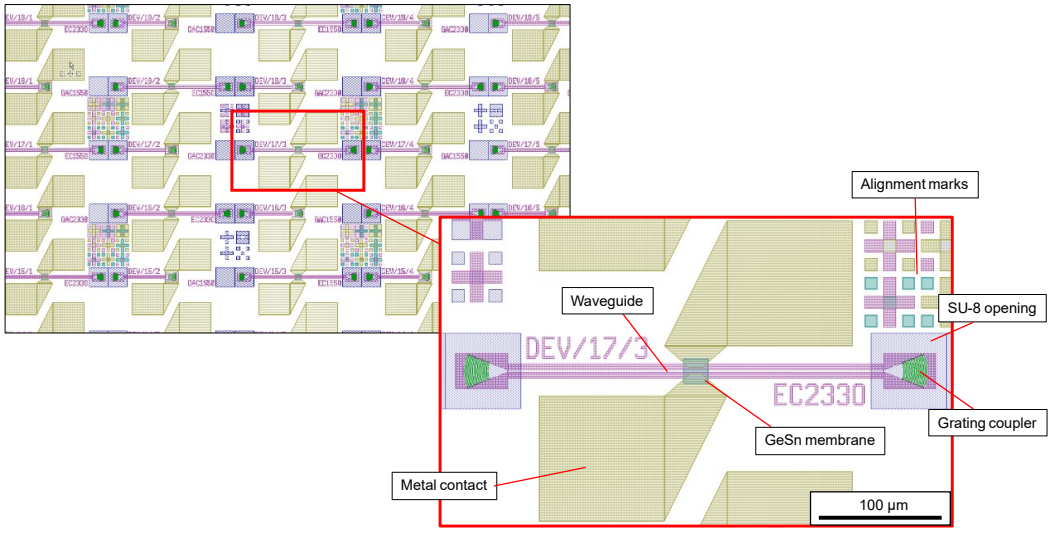


Figure 6.2 Layout of the 2D array of waveguide-coupled GeSn membranes. Inset: Close-up view of a single device with the identification of the different components.

6.2.2 Grating coupler design

In this design, the SGCs are optimized for operation around a wavelength of 2.33 μm at an injection (out-of-plane) angle of 10° and for a TE polarization. Figure 6.3 illustrates the key parameters defining the SGC. Light traveling through the waveguide is diffracted at an out-of-plane angle θ. The grating is defined by its period Λ, and the grating teeth are defined by a width w_g and depth h_g, which is determined using the Bragg condition for the first diffraction order of the grating [178]:

$$\Lambda = \frac{\lambda}{n^*_{eff} - \sin\theta} \tag{6.1}$$

where λ is the operation wavelength and n^*_{eff} is the weighted average of the effective refractive index in the grating region, defined as $n^*_{eff} = F n_{eff1} + (1-F) n_{eff2}$, with F being the ratio of the grating teeth width to the grating period ($F = w_g/\Lambda$) and n_{eff1} and n_{eff2} being the effective refractive indices of the grating teeth and slots, respectively. While the primary objective is to diffract light vertically upwards, a portion of it is also diffracted downward toward the substrate and backwards, potentially causing losses and internal reflections. To mitigate these effects, advanced SGC designs often incorporate a metallic layer beneath the bottom cladding to reflect downward-diffracted light and enhance coupling efficiency.

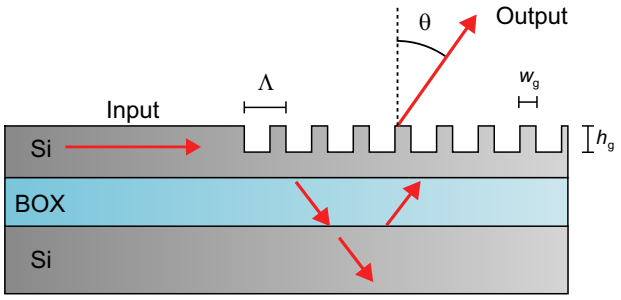


Figure 6.3 Concept of an SGC with the key design parameters.

However, Equation 6.1 does not provide insights into the grating's performance. To determine optimal design parameters and evaluate transmission efficiency, 2D FDTD simulations can be employed. These simulations allow for parameter sweeps or the application of optimization algorithms to identify the most effective configuration. Figure 6.4 presents a 2D map of the transmission efficiency in an SGC using a TE polarization as a function of the grating period Λ and the etch depth h_g for injection at 10° on an SOI platform (220 nm thick Si layer), with an F factor of 0.75 and air as the top cladding. The value of 0.75 for F is used as a starting point, but corresponds to a grating teeth width w_g of roughly 250–300 nm for an expected grating period of 1–1.2 μm when using Equation 6.1, which is near the minimum opening width that could be clearly obtained using EBL on an SOI sample and the subsequent fabrication steps. Optimal transmission occurs at a grating period of 1.22 μm and an etch depth of 220 nm, reaching a maximum of 0.39 (-4.09 dB). The abrupt transition in the map between etch depths of 200 and 210 nm could be related to numerical artifacts caused by the chosen mesh and step sizes in the parameter sweeps.

An optimization algorithm available in *Lumerical FDTD* is used to obtain a more precise set of design parameters, as the F ratio also needs to be optimized. The optimization yields a grating period of 1.224 μm, a fill factor F of 0.66, and an etch depth of 220 nm. This etch depth corresponds to a full etch through the Si layer, simplifying fabrication by allowing the SGCs and waveguides to be defined in a single dry etching step. Using the optimized parameters, 3D FDTD simulations were conducted to evaluate the wavelength dependence of the SGC transmission, as shown in Fig. 6.5. The results indicate a maximum transmission of about 0.44 or -3.57 dB at a wavelength of 2.34 μm, with a bandwidth spanning from 2.25 and 2.45 μm.

The final grating coupler design, inspired by literature, features a pie-shaped grating section that tapers to match the waveguide width. This design enhances coupling efficiency by

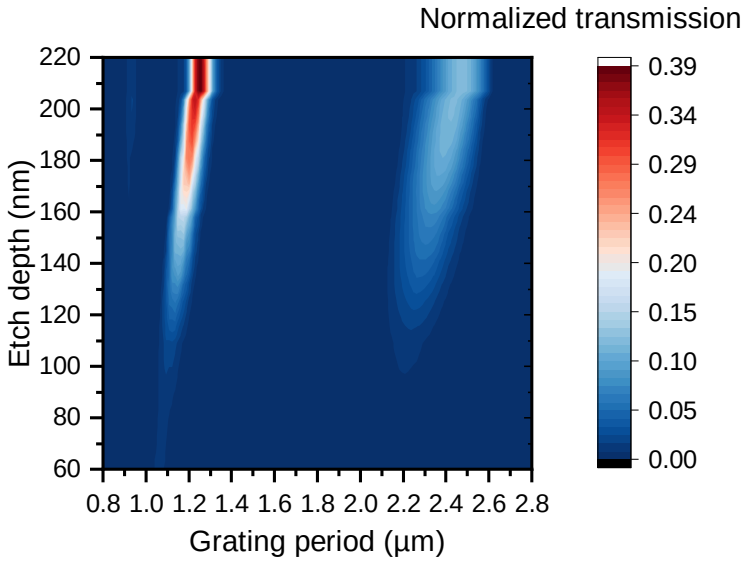


Figure 6.4 2D FDTD calculation of the transmission through an SGC as a function of grating period and etch depth of the teeth on a 220 nm thick SOI. The grating angle is 10°, the operation wavelength is 2.33 μm, and the F ratio is 0.75. The transmission is normalized to the input power.

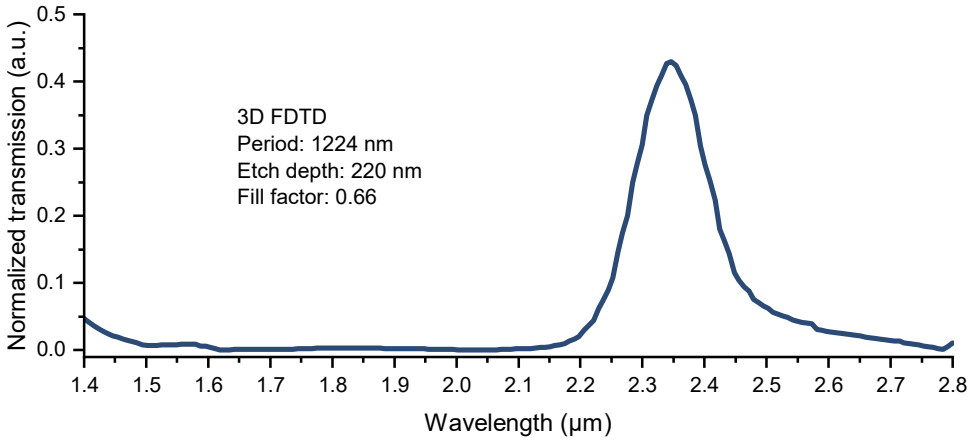


Figure 6.5 Wavelength dependence of the transmission of the SGC using the optimized parameters computed using 3D FDTD.

optimizing the overlap with the mode field diameter of a single-mode optical fiber, which is approximately 9 μm. Ensuring proper overlap minimizes coupling losses and maximizes power transfer between the fiber and the waveguide.

6.2.3 Extraction of the optical constants of GeSn using ellipsometry

The optical constants of the GeSn material used in the modeling were extracted via spectroscopic ellipsometry using an RCA2 ellipsometer from J.A. Woollam, which can provide data from 0.4 to 2.5 μm[1]. This technique measures changes in the polarization of an elliptically polarized light source upon reflection from the thin film, allowing interactions with different layers to be analyzed. For GeSn, a sum of oscillators was employed to model and extract the optical constants.

Since ellipsometry could not be performed on small-sized membranes, the optical constants from the as-grown sample were used as an approximation. While strain relaxation in membranes alters the alloy's band structure, which enhances absorption by extending the absorption cutoff, using the as-grown sample is expected to provide similar refractive index values. Based on previous observations in Chapter 4, the absorption cutoff is estimated to shift from approximately 2.8 μm to 3.1 μm in the membrane.

The extracted values, shown in Fig. 6.6, are compared with $k \cdot p$ calculations. Although the extracted values do not perfectly align with the $k \cdot p$ model, they are within the same order of magnitude. The discrepancies may stem from the robustness of the ellipsometry fitting model and assumptions made in the $k \cdot p$ model, such as uniformity of the strain in the layer and other absorption mechanisms. The optical constants of SU-8 and BCB shown earlier in Fig 5.5 in the previous chapter were obtained similarly, with a simple Cauchy model being used.

6.2.4 Coupling mechanisms

While the interaction between the optical waveguide and the GeSn membrane was discussed in the previous chapter, our focus here is to identify the optimal SU-8 thickness range for efficient operation at a wavelength of 2.33 μm. Figure 6.7 provides an overview of the modeling results for an SOI waveguide interacting with a GeSn membrane. Figure 6.7(a) presents the cross-section of an SOI waveguide with a 200 nm thick SU-8 layer, showing the electric field distribution $|E|$ of its fundamental TE mode (TE_{00}). The effective refractive

[1]Ellipsometry measurements were carried out at the Functional Coating and Surface Engineering Laboratory at Polytechnique Montréal with assistance from Anis Attiaoui and Nicolas Rotaru for the fitting model.

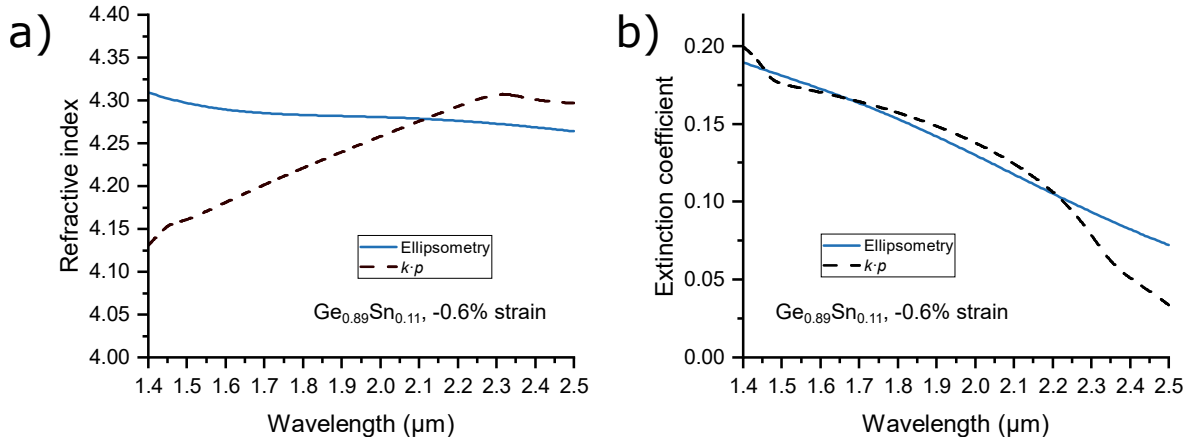


Figure 6.6 Optical constants of $Ge_{0.89}Sn_{0.11}$ with a compressive strain of -0.6%. The extracted ellipsometry values are compared to 8-band $k \cdot p$ calculations.

index n_{eff} of this fundamental mode at a wavelength of 2.33 μm is 2.4339 and has an effective area of 0.66 μm^2. While higher-order modes can propagate, their impact on device measurements is expected to be minimal.

As discussed in Chapter 5, the evanescent coupling (EC) efficiency decreases exponentially with increasing separation gap due to reduced field overlap between the supported modes. Efficient coupling typically requires a gap on the order of hundreds of nanometers, which can be controlled by adjusting the SU-8 thickness via spin coating speed and solids content. To enhance tolerance to larger gaps, an alternative approach involves incorporating a diffraction grating to redirect light vertically toward the active medium, a technique known as grating-assisted coupling (GAC). However, the efficiency of this mechanism is highly dependent on the grating's quality and design.

Figure 6.7(b) illustrates the two coupling mechanisms by showing the electric field distribution $|E|$ for each case with a 20 μm long membrane and a fixed 200 nm gap. The gap between the membrane and waveguide structures is fixed at 200 nm. The diffraction grating parameters are identical to those used in the SGCs, although the presence of an SU-8 top cladding instead of air may affect performance. In the evanescent coupling scenario, oscillations in the distribution profile indicate a small coupling length due to a propagation constant mismatch between the structures. Engineering the effective refractive indices can improve phase matching, increasing the coupling length and achieving full absorption over shorter distances.

For grating-assisted coupling, the light appears to be absorbed over a shorter distance, but oscillations in the waveguide suggest possible backward reflections and scattering toward the

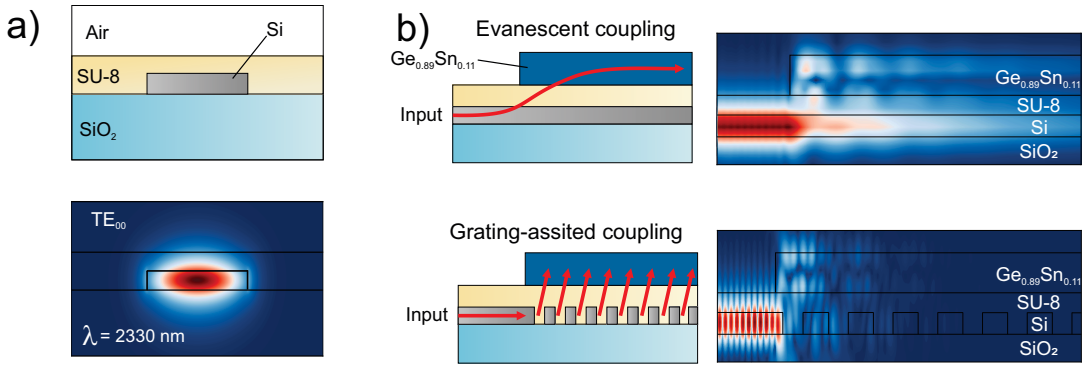


Figure 6.7 Modeling results of the evanescent and grating-assisted coupling between an SOI waveguide and a GeSn membrane. (a) Cross-section of the waveguide (top) with the normalized distribution of $|E|$ of TE_{00} at a wavelength of 2.33 μm (bottom). (b) Illustration of the principle of evanescent (top) and grating-assisted coupling (bottom) with the distribution of $|E|$ of the propagating mode in each case.

substrate, which can reduce overall coupling efficiency. Figure 6.8 shows the behavior of the absorbed power fraction P_{abs} for the evanescent and grating-assisted coupling schemes. Figure 6.8(a) shows P_{abs} as a function of the separation gap h_{Gap}. Evanescent coupling remains efficient at small gaps but decays rapidly, whereas grating-assisted coupling becomes advantageous for gaps exceeding 480 nm. This efficiency is expected to be improved with a set of parameters optimized for absorption [213]. However, evanescent coupling is expected to perform optimally for separation gaps, or SU-8 thicknesses, within the range of 100 to 200 nm.

Figure 6.8(b) shows the wavelength dependence of P_{abs} at a separation gap of 200 nm. Evanescent coupling excels in broadband light transfer with minimal reflection losses, making it ideal for integrated photodetectors. In contrast, grating-assisted coupling enhances vertical light redirection, accommodating larger separation gaps but introducing additional diffraction losses.

6.3 Device fabrication

Fabrication of these integrated photodetectors consists of two main steps involving transfer printing. The first step involves the fabrication of the donor and receiver chips, followed by transfer printing and metal deposition to form the contacts. Unlike the exfoliated contacts in Chapter 4, this study directly evaporates contacts onto the membranes instead of transferring them from another substrate. This approach was achieved by optimizing the SU-8 layer

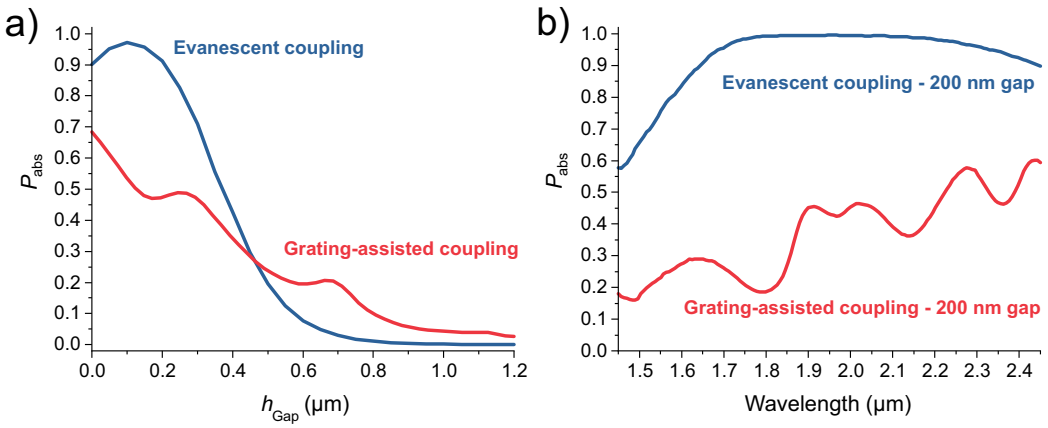


Figure 6.8 Evolution of the absorbed power fraction for the two coupling mechanisms as a function of (a) the separation gap and (b) the wavelength.

through post-deposition hardbaking and surface conditioning, detailed in this section. A comparison of the electrical performance between evaporated and exfoliated contacts will be presented in the next section.

6.3.1 Chip fabrication

Figure 6.9 provides an overview of the fabrication steps for the chips involved in the transfer printing process. This approach requires separate processing of the GeSn membranes (donor chip) and the passive SOI chip containing the waveguides (receiver chip). For this experiment, we use the same membranes with an Sn content of 11 at.% that were fully characterized in Chapter4 with dimensions of approximately 20 μm $\times$ 20 μm. Consequently, this section will focus on the fabrication details of the passive chip.

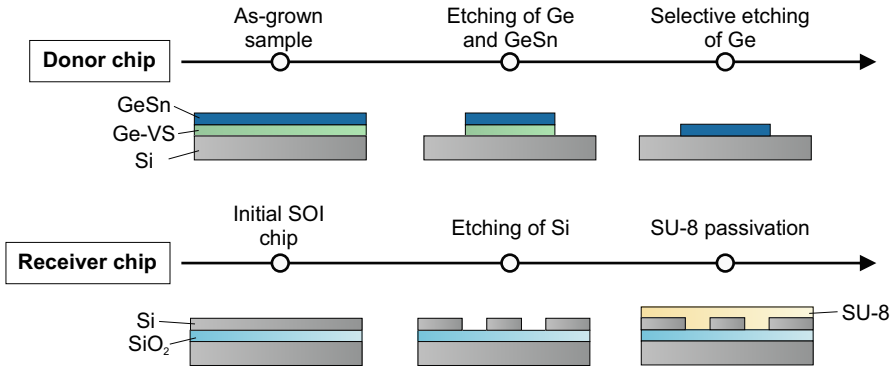


Figure 6.9 Overview of the fabrication steps for the GeSn membranes (donor chip) and the passive SOI chip (receiver chip).

The receiver chip is patterned on an SOI chip (B-doped, $8.5-11.5\,\Omega\cdot$cm) with a 220 nm device layer using EBL with a 20 kV acceleration voltage and PMMA 495k A6 as the resist for patterning and masking. The etching and patterning of the Si layer are performed by ICP-RIE using SF_6 and C_4F_8 gases, with the parameters shown in Table 6.1. The etch rate of Si using these parameters is approximately 297 nm/min.

Table 6.1 ICP-RIE parameters for the pseudo-Bosch etching of Si (Plasmalab 100 - Oxford Instruments at LMN).

Parameter	**Value**
SF_6 flow (sccm)	19
C_4F_8 flow (sccm)	30
RF (W)	50
ICP (W)	1500
T (°C)	15
P (mTorr)	5

Figure 6.10 shows images of the passive chip after EBL patterning and after the pseudo-Bosch dry etching and resist removal. Figure 6.11 provides SEM micrographs showing a waveguide unit and a close-up view of the etched grating coupler teeth. No stitching defects were observed in the 125 μm and 300 μm long waveguide structures.

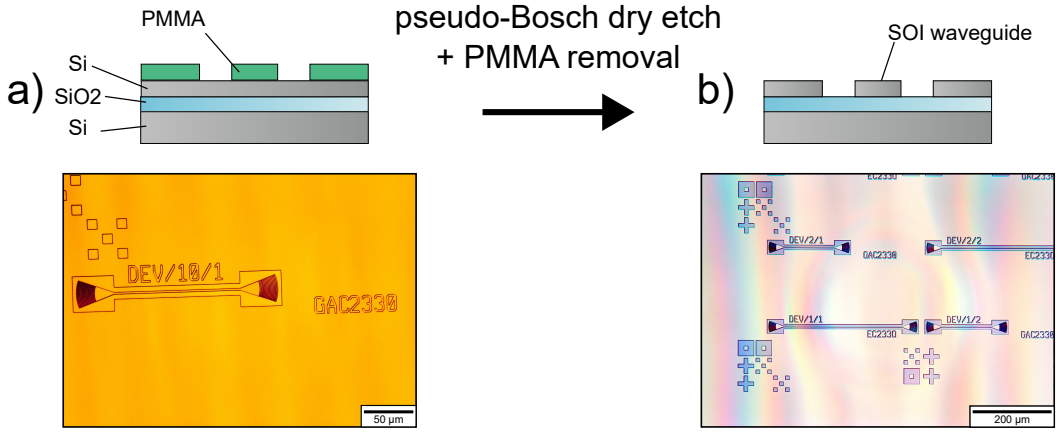


Figure 6.10 Microscope images of the PIC (a) after EBL patterning and (b) after dry etching and PMMA removal.

Waveguide transmission measurements were conducted using the setup in Section 3.4.6 to assess performance. De-embedding structures with varying waveguide lengths were patterned to determine propagation loss. However, due to the EBL tool's maximum writefield size of 200 μm $\times$ 200 μm, stitching defects appeared at the interfaces between writefields in

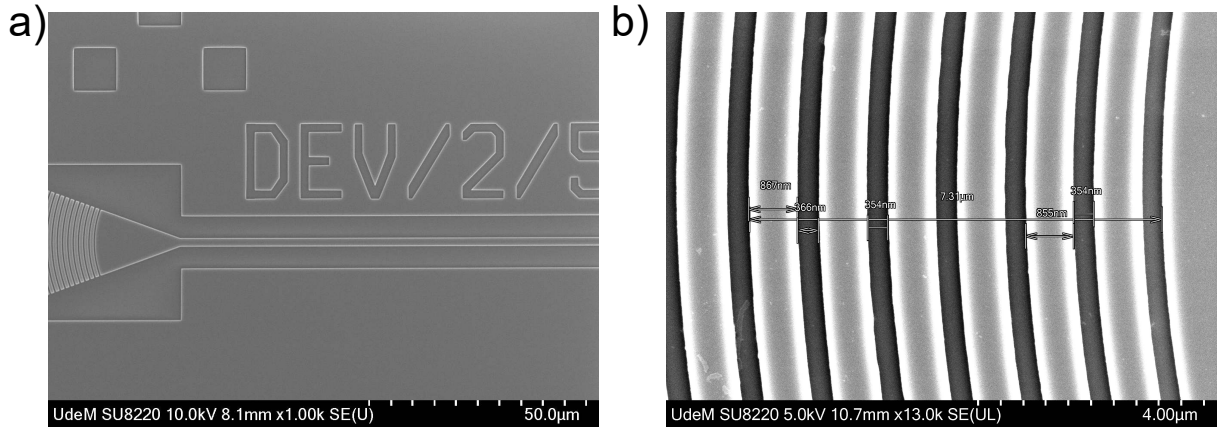


Figure 6.11 SEM micrographs of the structures on the PIC. (a) Waveguide unit. (b) Close-up view of the grating coupler.

larger structures, as shown in Fig. 6.12. These defects resulted in propagation losses of 26.6 dB/cm, appearing as abrupt offsets or gaps in the waveguide geometry. For comparison, SOI waveguides typically have a propagation loss within a few dB/cm (typically 2–3 dB/cm). Such defects introduce significant scattering loss due to mismatches in the optical mode positions at the interfaces. Fortunately, the short waveguide lengths in our structures limit the impact of propagation loss, with an estimated 0.8 dB loss for a 300 μm waveguide. The insertion loss of the fabricated SGCs is estimated to be approximately 12.9 dB at 2.33 μm per grating coupler, which includes the propagation loss of the 150 μm waveguide section. Since no significant defects were observed in the waveguide structures except these de-embedding structures, the propagation loss within the waveguide section is assumed to be negligible compared to the coupling loss associated with the SGCs. This assumption is factored into the computation of the error in estimating the optical power inside the waveguide, as detailed in Appendix B.

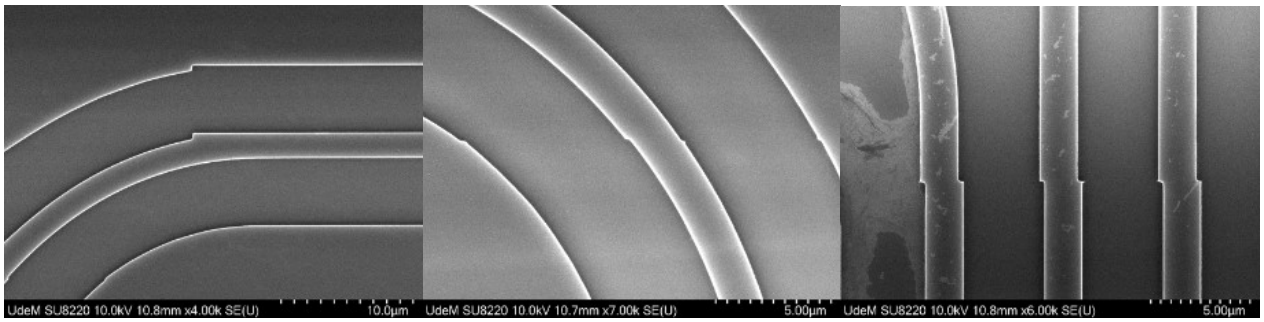


Figure 6.12 Stitching defects observed on the SOI chip caused by the EBL patterning step.

Following initial characterization, the chip was passivated with a 160 nm thick SU-8 layer, achieved by diluting SU-8 in cyclopentanone to obtain the desired thickness. Openings were patterned around the SGCs using UV exposure to preserve the air cladding for efficient coupling. The total transmission through the waveguide remained unchanged after SU-8 deposition.

6.3.2 Transfer printing

Once chip fabrication is complete, the process continues with the transfer printing of GeSn membranes followed by metal contact evaporation. These steps are illustrated in Fig. 6.13, with microscope images at different stages shown as insets. GeSn membranes are transferred onto the passive chip using a transfer printing setup (HQ Graphene) inside a nitrogen-filled glovebox. A ∼1.5 mm × 1.5 mm polydimethylsiloxane (PDMS) stamp, controlled by a multiaxis stage, is used to pick up multiple GeSn membranes by applying pressure to the donor chip. After pickup, the donor chip is replaced with the receiver chip, and the membranes are transferred by applying pressure and gradually retracting the stamp.

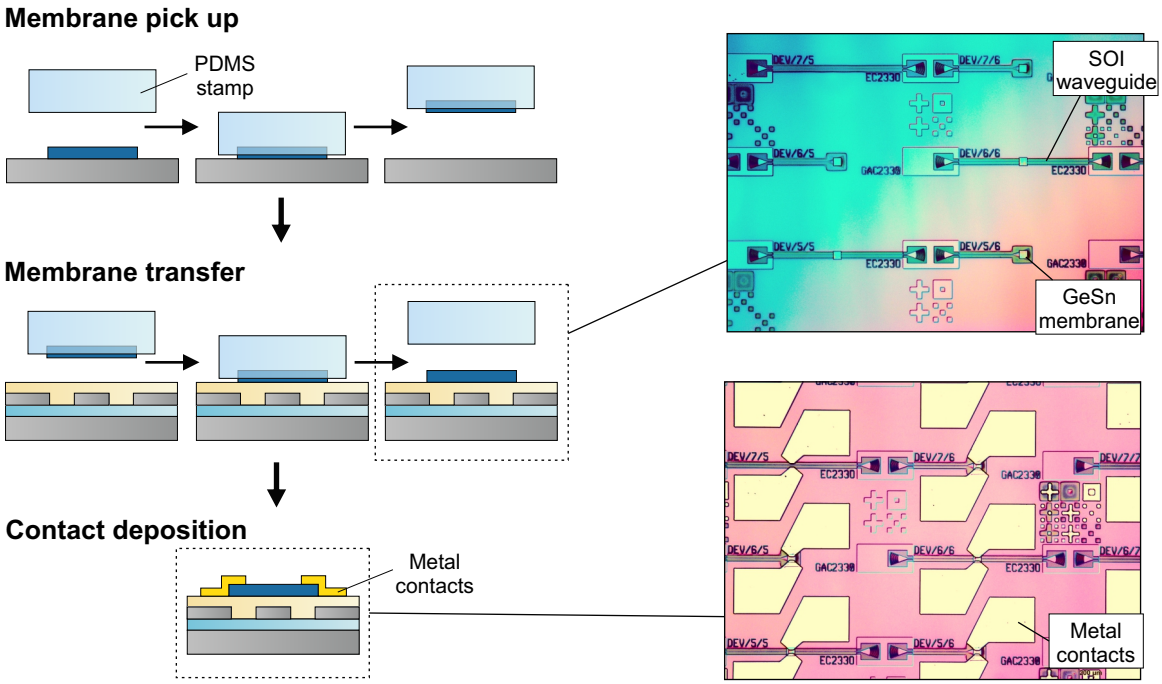


Figure 6.13 Transfer printing steps with the subsequent deposition of metal contacts on the transferred membranes. Insets: pictures taken from an optical microscope at different steps (The change in color is related to unintentional modifications in the camera settings of the microscope).

The membranes were successfully transferred without a polycarbonate film on the PDMS stamp, as the SU-8 layer ensured sufficient adhesion. After transfer, the chip undergoes thermal treatment at 250 °C for 30 min under a nitrogen atmosphere to hardbake the SU-8 and anneal the GeSn membranes. The hardbake enhances the density of crosslinks in the SU-8 polymer matrix, while annealing helps reduce lattice defects in the GeSn membranes. Hardbaking prevents SU-8 delamination during photoresist stripping with MICROPOSIT Remover 1165 (Dow Chemical Materials). This property was uncovered after the work has been carried out on the GeSn membranes with exfoliated contacts presented in Chapter 4.

Following transfer, the chip is dipped in a HF:HCl:H_2O solution for 15 s to remove residual byproducts from the underetching process, such as nonvolatile SnF_x species. Metal contacts are then deposited using a lift-off technique, consisting of a 20 nm Ti adhesion layer and a 120 nm Au layer. Before metal evaporation, a 30-s O_2 plasma treatment improves metal adhesion to SU-8. The final devices consist of photoconductive GeSn membranes coupled to waveguide structures. A contact gap of approximately 7 μm is achieved, which deviates by about 2 μm from the original design. The transfer printing step successfully positioned multiple GeSn membranes at their designated locations. The waveguide array consists of two configurations: Design EC, where a GeSn membrane is aligned atop a waveguide for evanescent coupling, and Design ECGAC, where the membrane is positioned over a grating coupler to facilitate both evanescent and grating-assisted coupling.

A key distinction of Design ECGAC is the inclusion of a tapered waveguide section, which is expected to enhance interaction with the GeSn active medium. Given the SU-8 thickness of 160 nm and the substantial overlap with the tapered waveguide, coupling in Design ECGAC is anticipated to occur through both evanescent and grating-assisted mechanisms. Although minor displacements from their original array positions were observed for a few membranes, a total of four devices based on Design EC and seven on Design ECGAC were successfully fabricated in a single transfer-printing step. Some membranes were missing from their intended positions, limiting the total yield to 11 fabricated devices instead of the 18 that could have been obtained based on the stamp area. Figure 6.14 presents optical and SEM images of these two designs, demonstrating good adhesion of the membranes and metal contacts to the underlying structures.

6.4 Characterization results

The characterization of the waveguide-coupled devices is carried out using the setup illustrated in Fig. 6.15, which includes a microscope image of a device coupled with an SMF-28 optical fiber and electrical probes. This setup enables light coupling into the devices via the

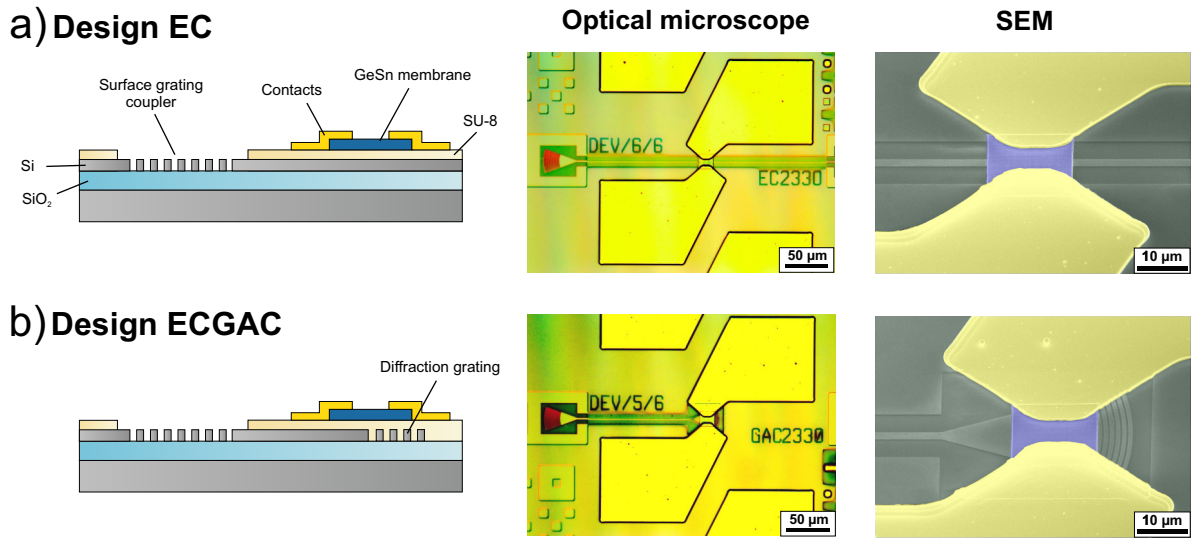


Figure 6.14 Images from optical microscopy and SEM for a device based on (a) Design EC and (b) Design ECGAC.

fiber to measure their responsivity. A multiaxis stage and microscope are used to precisely position the fiber above the SGC at the optimal injection angle.

A TE-polarized laser with a center wavelength of 2.33 μm (custom laser from Nanoplus) is collimated into the optical fiber using a FiberPort collimator (PAF2P-11E, Thorlabs). Despite significant propagation losses in the SMF-28 fiber at this wavelength, the optical power at the fiber output is used as a reference and measured with an extended-InGaAs biased photodetector (DET10D2, Thorlabs). Electrical probes are placed on the metal pads to collect the photocurrent, which is measured using a lock-in technique. The light source is modulated at 500 Hz using a mechanical chopper and the signal is analyzed with a lock-in amplifier (MFLI, Zurich Instruments). A current preamplifier (SR570, Stanford Research Systems) is used to amplify the signal and apply bias voltage to the MSM device. This technique eliminates dark current and minimizes noise components in the measured signal. The setup is calibrated using the extended-InGaAs biased photodetector. Considering the fiber-to-waveguide insertion losses of approximately 12.9 dB via the SGC, the estimated maximum optical power injected into the waveguide before reaching the membrane is around 92 μW.

The initial electrical and optical response of the devices is assessed using a semiconductor analyzer (Keithley 4200A-SCS). Figure 6.16(a) shows the current-voltage characteristics of a device (Design ECGAC) from -1 V to 1 V, both without and with laser illumination at different optical powers. The dark current (without illumination) is approximately 66 μA at

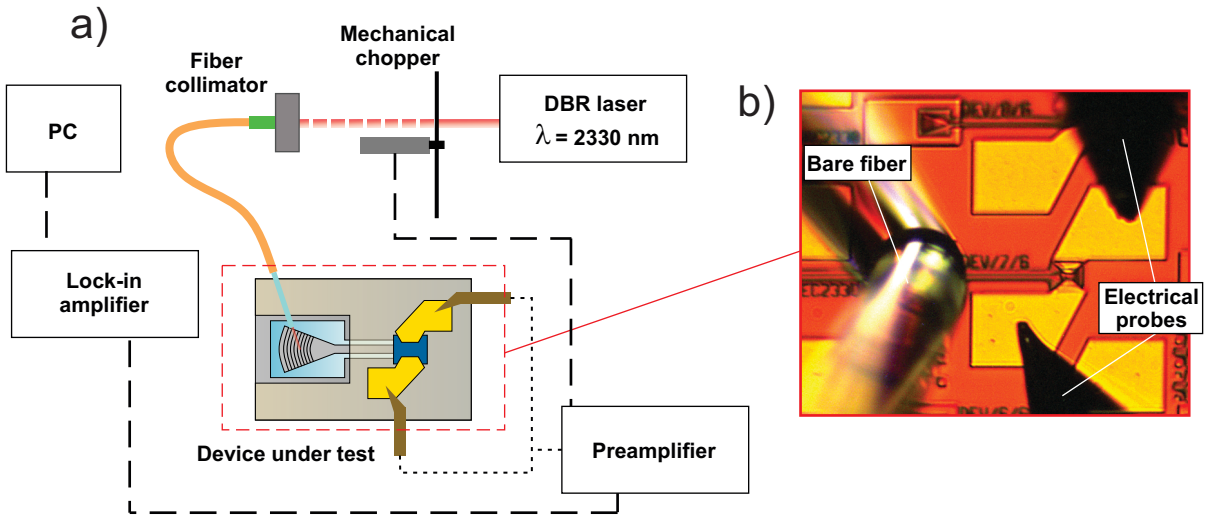


Figure 6.15 Characterization setup. (a) Schematic of the setup components to measure the responsivity while injecting light. (b) Microscope image of a coupled device with electrical probes.

1 V and exhibits a linear behavior indicative of ohmic-like contacts. Figure 6.16(b) shows the time-dependent response of a device biased at 0.1 V under varying optical powers. The device exhibits a fast response with a stable total current and returns to its original dark current value when illumination is removed, indicating rapid recovery times. Under illumination, the total current increases with both optical power and applied bias voltage, confirming photocurrent generation. Additionally, the responsivity tends to improve with higher bias voltages. However, at optical powers exceeding 58 μW, temporal variations in the total current can be observed under exposition. These variations could be attributed to different carrier dynamics, such as thermally induced carrier fluctuations from strong photon absorption or the activation of trap-assisted recombination centers.

The Ohmic-like behavior observed in Fig. 6.16(a) contrasts with the membrane devices fabricated in Chapter 4, where contacts were exfoliated and transfer printed instead of evaporated. Figure 6.17 compares the I–V curves obtained using these two techniques, showing that the evaporated contacts exhibit linear characteristics and enhanced conductivity. The electrical contact between a metal and a p-type semiconductor exhibits Ohmic behavior due to the Fermi level pinning to the charge neutrality level near the valence band. As mentioned in Chapter 4, the Schottky behavior observed with the p-type material could be related to passivation resulting from the underetching of Ge using the CF_4 plasma.

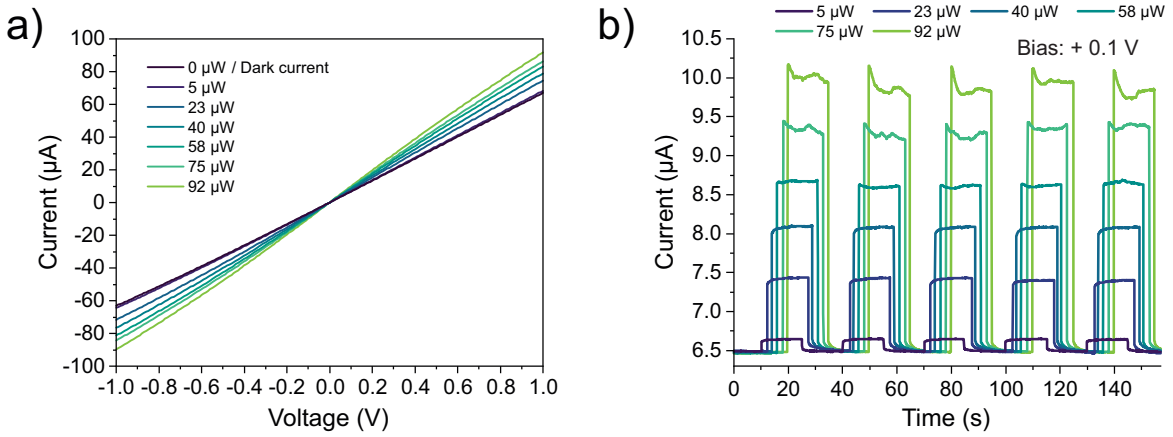


Figure 6.16 Electrical and optical characterization of the devices. (a) Current-voltage measurements of a device from -1 V to 1 V under illumination. (b) Transient photoresponse of a device under illumination at different optical powers.

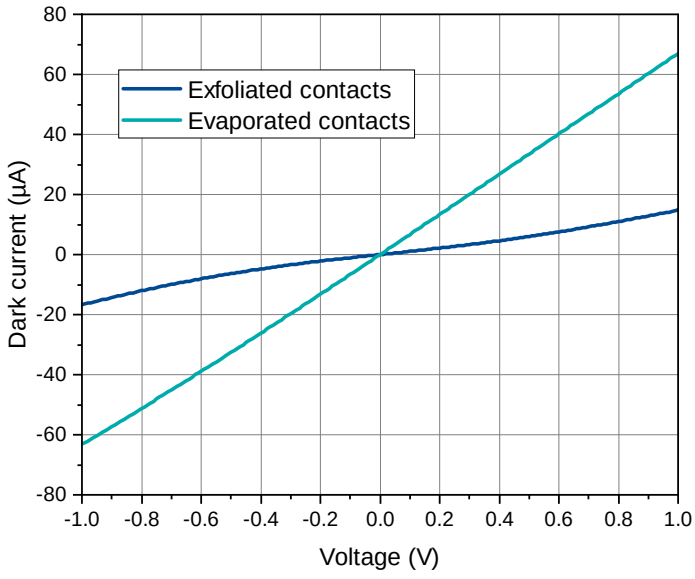


Figure 6.17 Current-voltage measurements of a device with evaporated contacts compared to exfoliated contacts.

Figure 6.18 shows the photocurrent as a function of optical power injected into the waveguide for applied biases from 0.1 V to 1 V for a device based on Design EC (Fig. 6.18(a)) and Design ECGAC (Fig. 6.18(b)). The increase in responsivity with higher bias voltages indicates photoconductive gain, where charge carriers circulate multiple times before recombination, effectively amplifying the photocurrent. The bias was limited to 1 V to avoid degradation of the devices. For Design EC, the photocurrent response exhibits a significant nonlinearity with increasing optical power, suggesting potential carrier recombination effects, whereas Design ECGAC demonstrates a more linear response. This nonlinearity may originate from an electric field screening effect induced by carrier trapping, as the response tends toward a more linear behavior with increasing bias [302]. The Design ECGAC device achieved a responsivity of 361 mA/W at a 1 V bias, compared to 159 mA/W for the Design EC device. The calculation of the error bars on the optical power inside the waveguide, which is roughly 10% of the computed value, is detailed in Appendix B. The photocurrent error bar reflects the maximum oscillation amplitude observed at the highest injected optical powers. It is conservatively estimated as three times this amplitude and then rounded to 1 μA.

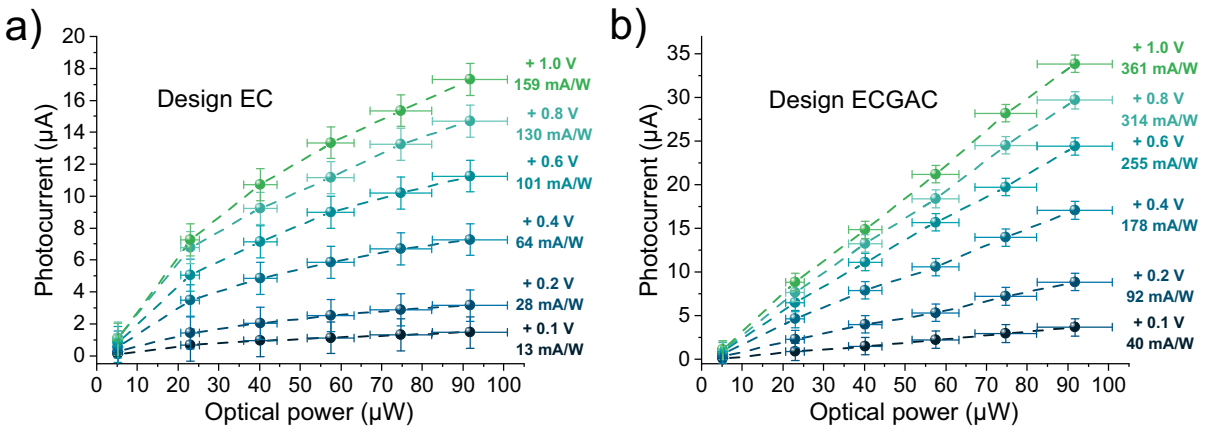


Figure 6.18 Photocurrent as a function of optical power in the waveguide for a device based on (a) Design EC and (b) Design ECGAC.

To evaluate performance consistency, the rest of the fabricated devices were characterized. Figure 6.19 shows the dark current measured from -1 V to 1 V for both designs. In each case, the devices exhibit linear behavior, with dark currents ranging between 50 and 90 μA at a 1 V bias. The photocurrent as a function of optical power was also measured, with the results presented in Fig. 6.20 for each design. Despite slight variations in responsivity, all devices exhibit similar photocurrent levels. Some devices based on Design ECGAC show a sublinear increase in photocurrent, similar to observations in Design EC. These variations may stem from differences in contact resistance, potentially caused by a slight misalignment

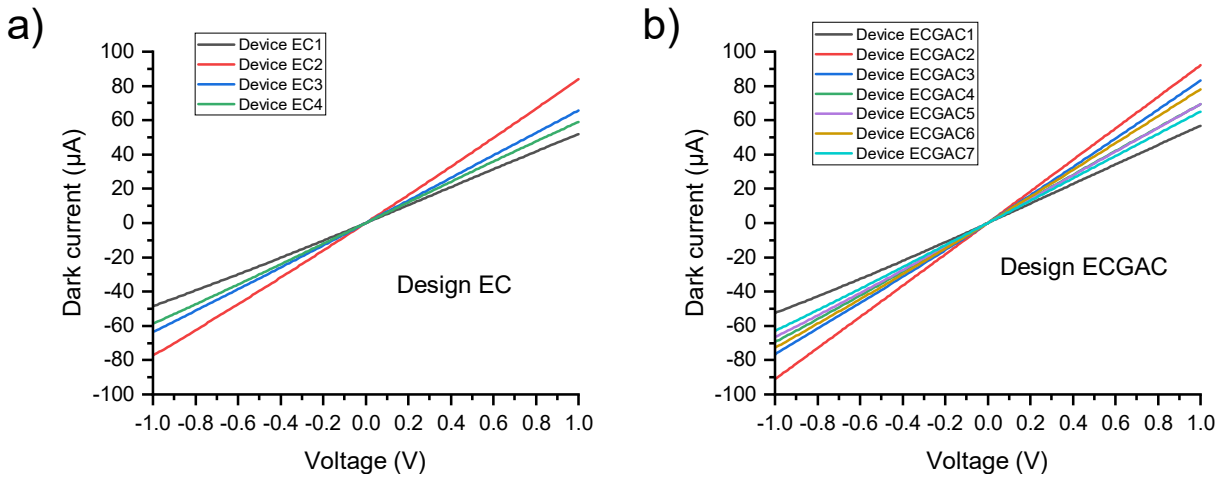


Figure 6.19 Dark current as a function of bias for all fabricated devices based on (a) Design EC and (b) Design ECGAC.

of the membranes during transfer, which could alter the contacted metal-GeSn membrane area.

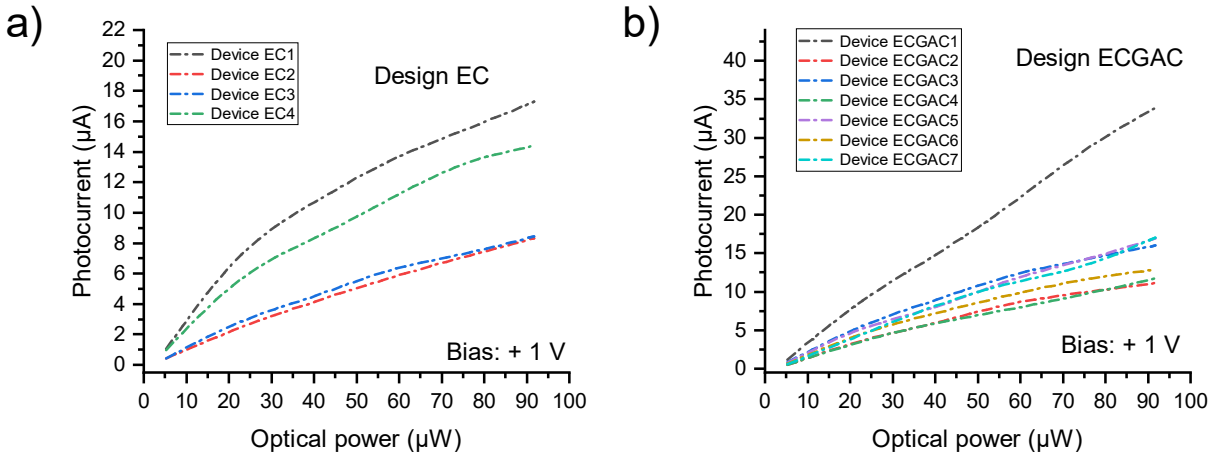


Figure 6.20 Photocurrent as a function of optical power for all fabricated devices based on (a) Design EC and (b) Design ECGAC under a bias of 1 V.

To better understand the observed discrepancies between the two designs, key parameters influencing responsivity can be analyzed. One notable factor is the significant increase in responsivity with higher bias voltages, which suggests an increase in photoconductive gain (G), where Equation 5.4 can be rewritten as:

$$R = G\eta\frac{e\lambda}{hc} \tag{6.2}$$

This photoconductive gain can be represented as the ratio between the carrier lifetime τ and the transit time of excess carriers within the device τ_t. When the transit time is significantly shorter than the carrier lifetime, multiple photogenerated carriers can contribute to the current, effectively amplifying the device's responsivity. This enables the following expression for G:

$$G = \frac{\tau}{\tau_t} \tag{6.3}$$

By considering the contributions from electrons and holes, this overall transit time can be described as [291]:

$$\frac{1}{\tau_t} = \frac{1}{\tau_{t,e}} + \frac{1}{\tau_{t,h}} = (\mu_e + \mu_h)\frac{V}{l^2} \tag{6.4}$$

where $\tau_{t,e}$ ($\tau_{t,h}$) and μ_e (μ_h) denote the transit time and mobility of electrons (holes), respectively. Here, l represents the spacing between the electrodes, and V is the applied voltage bias. The photoconductive gain G can be enhanced by either increasing V or reducing l to further improve the device responsivity. Physically, this gain corresponds to the number of times an electron circulates through the external circuit before recombining with a hole after the absorption of a single photon. As both Design EC and Design ECGAC share the same material and contact deposition method, their photoconductive gain contributions to responsivity should be comparable.

However, responsivity can also be influenced by the quantum efficiency η, as not all absorbed photons necessarily contribute to the generation of electron-hole pairs. To investigate whether absorption efficiency differs between the two designs, 3D FDTD simulations[2] were conducted to analyze the instantaneous 2D and cumulative generation rates as a function of distance, which serves as an analog to absorption efficiency. The results, shown in Fig. 6.21, provide insights into the spatial distribution of photocarrier generation.

In these simulations, the 2D generation rate represents the instantaneous photocarrier generation at a given position, while the cumulative generation rate accounts for the accumulated photocarrier production over the propagation distance. The generation rate (G_r) is computed using [178]:

[2]Using Lumerical. The mesh type is *auto non-uniform* with a mesh accuracy setting of 6 and a minimum mesh size of 50 nm. Perfectly matched layers are set at the boundaries of the simulation domain.

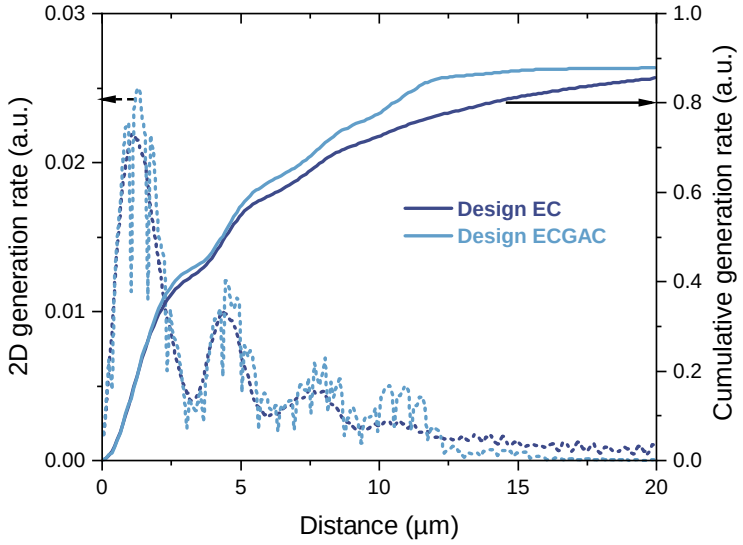


Figure 6.21 Computation of the 2D and cumulative generation rates for designs EC and ECGAC using 3D FDTD.

$$G_r = -ck|E|^2 n_r n_i \tag{6.5}$$

and is directly proportional to the absorbed power fraction P_{abs} after normalization in Equation 5.8.

Although slight variations are observed when light interacts with the grating, the final cumulative generation rate shows minimal difference between the two designs, reaching approximately 0.85 for Design EC and 0.88 for Design ECGAC. Since most potential factors influencing responsivity have been accounted for, this suggests that the observed variations in device performance may stem from fabrication-related inconsistencies, such as variations in SU-8 thickness, which could impact the coupling efficiency between the waveguide and the membrane. These waveguide-coupled detectors exhibit responsivity values comparable to other GeSn-based photodetectors, with the highest observed responsivity reaching 361 mA/W at 2.33 μm. By considering all of the 11 fabricated devices disregard their design, they exhibit an average dark current of 70 μA (standard deviation of 13 μA) and an average responsivity of 167 mA/W (standard deviation of 8 mA/W) under a bias of 1 V. Compared to other reported devices, most waveguide-integrated photodetectors operating above 2 μm are based on p-i-n structures, which necessitate additional fabrication steps to create separate contacts for the p- and n-doped layers.

Table 6.2 provides a comparison of various waveguide-coupled photodetectors operating in the 2–3 μm range. While III–V-based p-i-n devices generally outperform GeSn MSM detectors in terms of responsivity and dark current, the latter still holds promise for simpler fabrication and integration with silicon photonics and are generally associated with fast response times. However, achieving performance parity with III–V devices would require improvements in both responsivity and dark current. This performance enhancement could potentially be realized by transitioning from MSM to p-i-n GeSn membranes, which offer better carrier separation and collection efficiency as the electric field is confined within the p- and n-doped layers in a vertical heterostructure. A lower density of defects can be achieved in a vertical p-i-n epitaxial stack by first growing GeSn buffer layers, in which most of the defects will be confined and would contribute minimally to the device performance.

Table 6.2 Comparison of waveguide-coupled photodetectors operating in the 2–3 μm range.

Active material	PD type	Wavelength (μm)	Responsivity (mA/W)	Dark current (μA)	Reference
InGaAsSb	p-i-n	2.29	440 @ -0.1 V	1.13 @ -0.1 V	Hattasan *et al.* [212]
InGaAs/GaAsSb MQW	p-i-n	2.35	1600 @ -0.5 V	0.01 @ -0.5 V	Wang *et al.* [214]
InGaAsSb	p-i-n	2.3	1400 @ -1 V	1.8 @ -1 V	Gassenq *et al.* [213]
$Ge_{0.89}Sn_{0.11}$	**MSM**	**2.33**	**361 @ 1 V**	**66 @ 1 V**	**This work**

6.5 Estimation of the photoresponse bandwidth

These detectors were designed to maximize transfer printing yield, but their high-speed operation potential can be evaluated by estimating their photoresponse bandwidth. The 3-dB photoresponse bandwidth f_{3dB} is primarily constrained by the carrier transit time within the active material and the resistance-capacitance (RC) delay of the electrical circuit. These factors collectively define the overall response time of the device, given by:

$$f_{3dB} = \frac{1}{\sqrt{(f_T^{-2} + f_{RC}^{-2})}} \tag{6.6}$$

where f_T and f_{RC} are respectively the transit- and RC-limited frequencies. f_T can be estimated using:

$$f_T = \frac{0.45\nu_s}{t} \tag{6.7}$$

where ν_s is the saturation velocity of carriers in GeSn and t the separation between the electrodes. We can approximate ν_s of GeSn to that of Ge ($6 \times 10^6\,\mathrm{cm\,s^{-1}}$) and set t as the observed separation gap (7.5 μm), yielding a value of 3.6 GHz for f_T. f_{RC} can be estimated using:

$$f_{RC} = \frac{1}{2\pi R_{Tot} C_{Tot}} \tag{6.8}$$

where R_{Tot} and C_{Tot} are the total resistance and capacitance respectively. R_{Tot} includes the series resistance R_s of the device, which is influenced by the contact and bulk resistances, and the load resistance R_{Load}, which is set to 50 Ω during measurements. R_s can be determined from the current-voltage curve, corresponding to approximately 16.7 kΩ, as the value of R_s is much larger, R_{Load} is negligible. The total capacitance is composed of the junction capacitance (C_j) and parasitic capacitance (C_{par}) of the device. For MSM structures with coplanar electrodes, the capacitance can be expressed using the following relationship [303]:

$$C_j = \frac{K(k)}{K(k')} \epsilon_0 (1 + \epsilon_{r,GeSn})(N-1)L \tag{6.9}$$

where L is the detector's length (approximately 20 μm), N is the number of electrodes (here $N = 2$), ϵ_0 is the free-space dielectric constant and ϵ_r is the relative dielectic constant of GeSn ($\epsilon_r \sim 4.2^2 = 17.64$). $K(k)$ is the elliptical integral of the first kind, defined as:

$$K(k) = \int_0^{\pi/2} \frac{1}{\sqrt{(1 - k^2 \sin^2 \phi)}} d\phi \tag{6.10}$$

with k and k' defined as:

$$k = \tan^2 \frac{\pi f_w}{4(f_s + f_w)} \tag{6.11}$$

and

$$k' = \sqrt{1 - k^2} \tag{6.12}$$

with f_s and f_w which are respectively defined as the electrode spacing and width (approximated as 7.5 μm and 6.5 μm respectively). With these parameters, the junction capacitance C_j is estimated to be 1.45 fF. However, the large contact pads, separated by just 160 nm of SU-8, introduce significant parasitic capacitance, substantially increasing the total capaci-

tance. The parasitic capacitance C_{par} can be approximated by modeling the contact pads as two parallel plates in series, separated by the SU-8 layer, yielding the following expression:

$$C_{par} = \frac{1}{2}\frac{\epsilon_0 \epsilon_{r,SU-8} A}{d} \tag{6.13}$$

where $\epsilon_{r,SU-8}$ is the relative dielectic constant of SU-8 ($\epsilon_{r,SU-8} \sim 1.58^2 = 2.5$), A is the contact area (100 μm $\times$ 100 μm), and d is the separation formed by the SU-8 layer (here 160 nm). Using these parameters, the parasitic capacitance C_{par} is calculated to be 0.691 pF, which is significantly larger than the estimated MSM contact terminal capacitance. Substituting these values into Equation 6.8 results in a value of 13.8 MHz for the RC-limited frequency, which will limit the overall photoresponse bandwidth f_{3dB} to a similar value. Consequently, the corresponding device response time, estimated using $\tau_r = 0.35/f_{3dB}$ is approximately 25.4 ns.

The estimated bandwidth is relatively low for high-speed data communication. To achieve GHz-level performance and compete with state-of-the-art devices, further optimization of the photodetector and contact pad design is necessary to significantly improve f_{3dB} by reducing the parasitic capacitance and the series resistance. Reducing the electrode spacing can improve carrier transit time but may also increase optical losses due to greater mode overlap with the metal contacts. Additionally, transitioning to p-i-n structures could provide enhanced bandwidth by defining the transit time through the thickness of the intrinsic layer, enabling better control over carrier dynamics. However, the junction capacitance is expected to be significantly higher than in an MSM device as the depletion width is set by the thickness of the intrinsic region and thus smaller.

6.6 Conclusion

In this work, we successfully transferred $Ge_{0.89}Sn_{0.11}$ membranes onto SOI waveguides to fabricate MSM detectors operating in the mid-infrared range. Multiple functional waveguide-integrated photodetectors were fabricated in a single transfer-printing step, demonstrating the scalability and practicality of the process. By evaluating two different photonic structures, we found that tapered waveguides with diffraction gratings exhibited higher responsivity compared to direct evanescent coupling with 2 μm-wide waveguides. While minimal variation was expected between these designs, further characterization could help pinpoint the specific factors contributing to the observed performance differences. A key advantage of these GeSn-based detectors is their ability to operate at room temperature, unlike many other mid-infrared materials that require cryogenic cooling. This makes them particularly

attractive for applications such as portable spectroscopic systems and mid-infrared intra-chip communication. Moreover, the compatibility of GeSn with silicon substrates offers a cost-effective and scalable solution for mid-infrared photonic integration.

This demonstration establishes transfer printing as a viable and efficient method for integrating GeSn alloys into mid-infrared photonic platforms, paving the way for further advancements in group-IV optoelectronics. The approach also enables the parallel integration of multiple devices from different material systems, enhancing versatility and scalability for heterogeneous integration in photonic circuits, particularly in cases where direct epitaxial growth is impractical or direct bonding yields are limited. Although the estimated operational bandwidth of the current devices is relatively low compared to state-of-the-art detectors, prior advancements in monolithic GeSn devices have demonstrated the feasibility of achieving high-speed operation, with bandwidths exceeding 10 GHz in all-GeSn p-i-n heterostructures [15, 94]. Future work could explore strategies to enhance bandwidth through optimized device geometry, reduced parasitic capacitance, and the implementation of p-i-n heterostructures for improved carrier dynamics.

CHAPTER 7 GENERAL DISCUSSION

In this thesis, we explored the potential of GeSn membranes as a platform for the heterogeneous integration of the material onto silicon photonic chips. The first objective was achieved by improving the fabrication process of these membranes, enabling their reliable transfer printing onto various platforms, as detailed in Chapter 4. Subsequently, in Chapter 6, their integration onto an SOI platform was demonstrated, resulting in multiple waveguide-coupled detectors operating at a wavelength of 2.33 μm, thereby fulfilling the third objective. To the best of my knowledge, this work represents one of the few demonstrations of GeSn integration onto a PIC and the first utilizing transfer printing. This approach presents a promising pathway for heterogeneous integration, offering greater flexibility for co-integration with other active materials compared to wafer bonding or flip-chip techniques.

For the second objective, Chapter 5 presents an analysis of different integration approaches for GeSn onto mid-infrared platforms, providing insights into the coupling efficiency. The modeling results contribute to the design of future devices by identifying optimal parameters and potential constraints for specific applications and operational wavelength ranges. Unlike previous studies, which primarily focus on wavelengths up to 2 μm, our study extends the operational range to approximately 3 μm, addressing broader application possibilities. The methodology outlined in Chapter 5 can be extended to other mid-infrared platforms and GeSn compositions, as well as more complex device architectures such as p-i-n-based structures. The following sections provide a comprehensive discussion of the various aspects of this research project.

7.1 GeSn membranes as a transferable active platform

In the early stages of this thesis, GeSn membranes were fabricated in collaboration with Dr. Mahmoud R. M. Atalla, demonstrating promising properties after successful transfer printing and achieving the longest observed cutoff wavelength in GeSn structures at approximately 4.6 μm [14]. However, to enhance the yield and reliability of their transfer printing, new strategies were required to address challenges such as inconsistent adhesion. Chapter 4 addresses these issues by introducing solutions, including the use of relaxed GeSn layers and an adhesive layer to improve transfer printing reliability. A novel approach was also implemented for contact formation, involving the simultaneous transfer of exfoliated metal contacts with membrane pick-up. The transferred membranes exhibited minimal bowing and could be arranged in an array, although slight movement was observed after release.

This movement poses a significant challenge, as misalignment can impact overall fabrication reliability, potentially reducing coupling efficiency and device performance consistency. Precise membrane placement is essential for optimal coupling and device uniformity, minimizing losses and ensuring repeatable performance. While the initial detectors exhibited relatively low responsivity, they demonstrated an extended photodetection cutoff wavelength from 2.8 to 3.1 μm, opening new possibilities for diverse integration schemes and mid-infrared applications. According to Table 4.1, the measured absolute responsivity at 1.55 μm is at a similar scale to that of the first device reported in by our group [14] and also to that of a membrane detector fabricated using a flip-chip approach [268]. Other devices using the latter approach reported higher responsivities, which could be related to differences in the contact resistance.

The transfer of mechanically exfoliated contacts was initially explored to prevent potential membrane displacement after transfer. This approach also aimed to enable rapid contact placement post-transfer printing, ensuring compatibility with various substrates, including flexible materials unsuitable for conventional metal evaporation. However, the electrical performance of these contacts was found to be suboptimal, likely due to the presence of residual SnF_x or SnO_x species on the membrane surface, which can introduce a Schottky barrier. Applying a chemical treatment to the membrane surface prior to contact deposition, possible when membranes are transferred separately, has shown to improve contact quality by effectively removing these residues. Additionally, post-transfer annealing further enhanced contact performance, resulting in a current-voltage response that closely resembles ohmic behavior. Later, in the work presented in Chapter 6, the direct evaporation of contacts onto SU-8 was achieved, yielding improved electrical performance. This was enabled by developing an SU-8 conditioning process that involved a hardbake followed by a short O_2 plasma exposure, ensuring the polymer film could withstand a lift-off process and that an evaporated metal film could adhere well.

Our findings indicate that GeSn membranes with a predominantly relaxed structure and slight residual compressive strain are easier to transfer compared to the highly compressively strained layers used in earlier studies. Additionally, incorporating an adhesive layer significantly improved fabrication yield by enhancing adhesion during transfer. The size and shape of the membranes were also found to influence structural integrity. While not extensively studied in this project, disk-shaped membranes exhibited minimal structural bowing compared to square or rectangular ones. As there are only a few reports available on this subject and fabrication methods may vary, further investigation into processing techniques could provide valuable insights for optimizing membrane integration. Lastly, the underetching selectivity, as mentioned in Appendix A, varies with Sn content. While we primarily investigated Sn contents for which the etching selectivity is expected to be high, it has been

observed that Sn contents lower than 7 at.% could be partially etched using CF_4. Lower Sn content membranes remain unexplored but could clarify this approach's compatibility and limitations. If such membranes were to be heavily damaged due to the lower selectivity, they could serve as reference samples for the optimization of underetching recipe. Alternating etching and passivation steps, similar to the Bosch process, could enhance the etching selectivity.

To enhance the performance of integrated optoelectronic devices, GeSn membranes based on p-i-n heterostructures could offer significant advantages. These structures confine the electric field within the intrinsic layer, sandwiched between n- and p-type GeSn layers, enhancing carrier separation and reducing noise. Additionally, defects from the underlying layers are expected to have minimal impact on the dark current, further improving device performance. Such devices could benefit from the removal of the underlying Ge buffer and Si layers in addition to being transferable. However, their fabrication requires additional processing steps compared to MSM devices. A mesa structure must first be formed to facilitate the placement of electrical contacts on the separately doped regions before membrane release. Figure 7.1 illustrates the concept of a transfer-printed p-i-n membrane onto an SOI waveguide. In addition to enabling the rapid prototyping of active systems based on PICs with transfer-printed components, these structures could facilitate the tracking of the improvement in performance of post-fabrication treatments after being transfer-printed on different substrates, either for photodetection or light emission, by applying a reverse bias.

Figure 7.2 presents a schematic of the proposed fabrication process for realizing p-i-n GeSn membranes via transfer printing, inspired by previous studies [223]. To prevent unintended displacement during transfer, tether structures made of photoresist could be patterned over the membranes before release to keep the membranes attached to the substrate once the underetching is complete. These anchors are designed to break upon pick-up using a PDMS

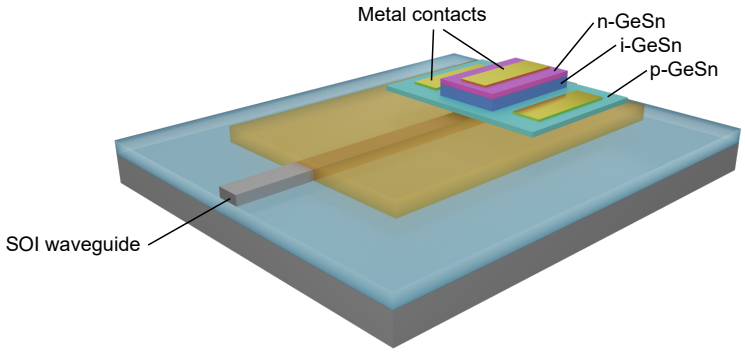


Figure 7.1 Illustration of a transfer-printed GeSn p-i-n membrane onto an SOI waveguide.

stamp, ensuring precise membrane placement.

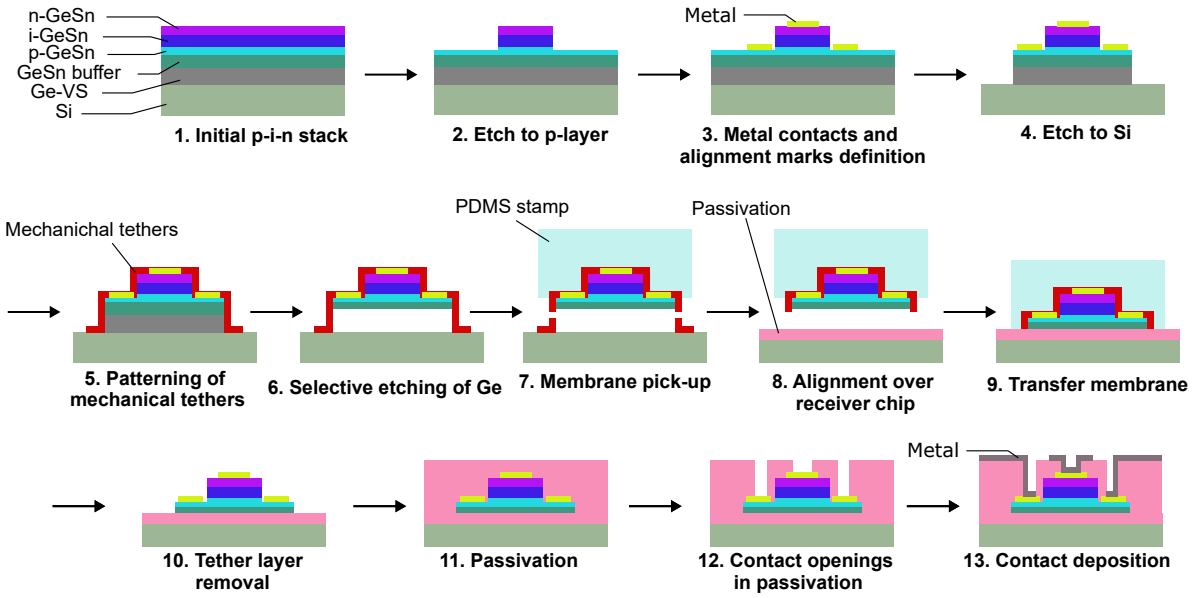


Figure 7.2 Proposed processing flow for the fabrication of GeSn p-i-n membranes assisted by transfer printing.

7.2 Monolithic integration compared to heterogeneous integration

The successful co-integration of photonics and electronics requires the monolithic integration of active materials like GeSn for light emitters and photodetectors. However, GeSn's significant lattice mismatch with Si or Ge buffer layers results in high defect densities. While monolithic integration is preferred for scalability, addressing these defects is critical for both photonics and microelectronics applications.

Heterogeneous integration of GeSn, through wafer bonding or transfer printing, offers a practical alternative to overcome growth challenges while providing flexibility in selecting the target platform in addition to effectively removing defects at the former Ge/GeSn interface. Although potentially scalable, its success heavily depends on transfer yield. This approach has enabled room-temperature lasing via optical pumping by improving thermal management [65]. Although transfer printing is a relatively novel technique differing from monolithic integration, it reduces material waste and enables co-integration of diverse materials onto photonic integrated circuits (PICs). Examples include InGaAs or GaSb for infrared and mid-infrared light emitters, respectively, and lithium niobate for high-speed modulators [47]. Additionally, transfer printing facilitates rapid prototyping of fully functional active PICs,

offering valuable insights into the performance limits of monolithic approaches. However, it presents challenges for back-end-of-line (BEOL) integration, especially due to the thermal budget imposed by the GeSn alloy and the compatibility of integrated materials with subsequent processing steps.

An all-monolithic approach using a Ge-on-Si (GOS) platform was initially considered, wherein components would be defined through subsequent etching steps. However, this approach encountered pit defects and Sn segregation in GeSn samples. Pit defects, originating from the Ge buffer layer growth due to unintentional contamination, exhibited spatial variation across the wafer. This primarily affected the patterning of passive components, which require a large footprint and defect-free regions to ensure low-loss waveguide propagation. elective area epitaxy (SAE) of GeSn through aspect ratio trapping in a BEOL process could enable active material growth in defined regions on defect-free SOI or GOS PICs without adhesives, improving heat dissipation. While effective for III–V compounds on Si [37], further research is needed for GeSn alloys [211].

Given the low growth temperature of GeSn, SAE could potentially be achieved on pre-processed PIC wafers in recessed areas to enable a butt-coupling configuration [210] or through direct growth on top of the waveguide for vertical coupling, provided that the waveguide material is compatible. Effective thermal management is crucial for these applications, as poor thermal conductivity of materials like silicon dioxide and adhesives limits the performance of transfer-printed devices. Alternative platforms, such as Si-on-SiN or aluminum-based structures, offer improved heat dissipation and have demonstrated room-temperature lasing [65, 72, 73].

Chapter 5 explored GeSn integration on photonic platforms, with numerical modeling results confirming the efficient evanescent coupling for Si- and Ge-based platforms. Si-based platforms benefit from high refractive index contrast and favorable waveguide geometries that enable small detector lengths in waveguide-coupled detectors, which is crucial to minimize the device dark current and capacitance. The methodology used can be extended to other platforms and GeSn compositions for further optimization, with 3D FDTD simulations offering higher accuracy at the expense of increased computation time. Monolithic integration remains an important objective, but the main challenge lies in designing the layer structure and improving the growth quality to enable SAE.

As transfer printing is becoming an emerging integration technique, advanced systems are being developed to enable accurate and automated transfer printing at a large scale[1].

[1]X-Celeprint is a company based at Tyndall National Institute (Cork, Ireland) specialized in micro-transfer printing solutions: https://x-celeprint.com/

7.3 GeSn for silicon photonics and mid-infrared applications

The integration approach developed for mass transfer of GeSn membranes was successfully applied to SOI waveguides for 2.33 μm photodetectors via transfer printing, as detailed in Chapter 6. While the transferred MSM devices exhibited high dark current, they achieved promising responsivities of up to 361 mA/W, demonstrating their potential for mid-infrared applications. The elevated dark current is likely due to bulk and surface defects. Future improvements could include enhanced surface passivation techniques, such as dielectric layers to reduce surface states, and optimized metal contact deposition to minimize interface defects in addition to an annealing step of the transferred membrane. This first demonstration of transfer-printed GeSn membranes coupled to photonic waveguides underscores transfer printing's growing role in silicon photonics. The membrane devices first presented in Chapter 4 could also serve as detectors that can be easily transferred on flexible platforms to unlock mid-infrared sensing.

Although room-temperature lasing via electrical injection remains challenging, GeSn holds immediate promise for silicon photonics, particularly in mid-infrared sensing and communication applications. These applications include photodetectors covering the telecom and 2 μm bands, as well as integrated light sources for spectroscopic sensing in the 2–4 μm range. Due to its relative cost-effectiveness, GeSn could serve as an ideal material for transferred detector arrays in demultiplexing circuits, where a single III–V laser would be sufficient. During early-stage device development, the co-integration of GeSn photodetectors alongside III–V light sources should thus be explored. GeSn-on-insulator (GeSnOI) is a promising platform that can leverage silicon nitride (SiN) to apply tensile strain and form waveguides [23].

While this study focused on photodetectors, other GeSn-based devices, such as electroabsorption modulators (EAMs), could also benefit from similar modeling and optimization efforts. EAMs offer higher speed and lower power consumption compared to thermo-optic modulators, making them critical for communication applications. The integration of light sources, particularly lasers, presents additional challenges due to the need to overcome optical losses within the laser cavity. Heterogeneous methods, such as direct or adhesive bonding, are commonly employed for mid-infrared lasers. Although III–V materials have demonstrated mid-infrared laser integration on Si, challenges persist due to thick buffer layer requirements and defective interfaces [153]. Promising results have been achieved through heterogeneous integration, with Spott *et al.* demonstrating mid-infrared lasers via direct bonding [304–306], and Jung *et al.* using transfer printing to integrate QCLs onto SOI waveguides [307]. Despite material quality challenges, GeSn-based light source integration continues to be actively explored. Marzban *et al.* proposed a monolithically integrated GeSn disk laser coupled to

a GOS waveguide [308], but high defect densities at the Ge/GeSn interface remain a concern, potentially limiting gain performance. GeSn microdisks that are directly released on Si, which are processed identically to membranes, could potentially be coupled to a PIC using transfer printing to transmit the emitted light [266]. Transferred GeSn membranes could also potentially be used as gain material when coupled to integrated optical resonators, with passive elements enabling the feedback to form integrated lasers [39].

7.4 GeSn material quality in its current state and limitations

GeSn's viability for commercial mid-infrared photonics is still under evaluation, as III–V compounds currently outperform it in responsivity, detectivity, and thermal stability. They however suffer from high fabrication costs, limited scalability, and complex integration requirements. In contrast, GeSn presents a silicon-compatible solution with potential cost reductions through CMOS integration. Key challenges such as material quality, defect density, and thermal stability still need to be addressed. Further optimization in growth techniques, strain engineering, and defect passivation will determine whether GeSn can achieve performance levels comparable to III–V solutions while leveraging its scalability advantages. Continued progress in these areas will be crucial for enabling GeSn-based photonics as a competitive alternative in mid-infrared applications.

While GeSn offers strategic advantages such as silicon compatibility and room-temperature operation, its competitiveness is currently limited to mid-infrared photodetector applications beyond 2.3 μm, where it achieves 3-dB bandwidths surpassing those of III–V-based detectors. Addressing key challenges in this binary system is imperative; while some limitations are intrinsic, others can be mitigated through process optimization and strain engineering. Further research on the alloy's properties, as well as its growth and processing, is necessary to enhance material quality, which would significantly benefit GeSn-based devices.

A major challenge is the persistent formation of defects at the interface due to the significant lattice mismatch between GeSn and Si or Ge substrates, which are not fully understood [119]. GeSn exhibits substantial lattice parameter variations, leading to defects that contribute to high dark currents and the inherent acceptor-like behavior. Although annealing mitigates these issues, it requires low temperatures to prevent Sn diffusion. Advanced annealing methods such as laser annealing could potentially help improve the properties of GeSn layers by reducing the density of bulk defects with minimal Sn segregation. Bulk defects can be mitigated using GeSn buffer layers that accommodate most of the defects before the growth of higher-quality top layers. Strategies such as layer transfer [65] or microstructuring [129] offer potential solutions by mechanically or chemically removing defects located near interfaces.

The latter can be applied to membranes and potentially help inhibit Sn diffusion mechanisms during annealing as dislocations at the origin of segregation can be isolated, thus enabling higher annealing temperatures. Post-growth annealing on transferred $Ge_{0.89}Sn_{0.11}$ membrane detectors has been explored in Chapter 4, where a reduction in the dark current was observed after annealing at a temperature of 320 °C while maintaining a similar collected photocurrent. However, responsivity dropped after annealing at 335 °C, suggesting potential contact degradation. It could be interesting to study the effect of post-growth annealing of transferred membranes by performing annealing prior the deposition of metal contacts.

While this study primarily focused on the binary alloy, exploring ternary SiGeSn compounds provides additional tunability, enabling simultaneous bandgap and strain engineering [52]. However, controlling the kinetics of these ternary systems introduces additional challenges. Ellis *et al.* suggested further investigation into group-IV alloys, such as SiGeSn and even dilute carbides, the latter of which could potentially exhibit a direct or quasi-direct bandgap, according to theoretical studies [74]. SiGeSn is particularly promising as a barrier material for quantum wells, offering higher band offsets compared to Ge or GeSn-based barriers [57]. However, the offset remains insufficient to ensure carrier confinement at room temperature. In the context of light emitters, the lack of a sufficiently high band offset in all-GeSn heterostructures makes room-temperature lasing challenging, necessitating effective defect management or band structure engineering.

CHAPTER 8 CONCLUSIONS AND PERSPECTIVES

In this thesis, we explored thin film processing techniques for GeSn and investigated various strategies for integrating GeSn as an active material into silicon photonics. A key achievement was fabricating strain-relaxed GeSn membranes for heterogeneous integration via transfer printing onto multiple substrates. This integration approach provides greater design flexibility by allowing the combination of different materials with optimized properties and facilitating the rapid prototyping of GeSn-based photonic integrated circuits (PICs).

The primary objective of this research was to explore the feasability of an integration approach for GeSn in silicon photonics based on GeSn membranes, while comparing this approach to other integration scenarios through numerical simulations. Early efforts focused on developing GeSn membranes in collaboration with research group members, leading to significant improvements in their integration via transfer printing. The numerical studies conducted throughout the project evaluated different integration scenarios, particularly on SOI and GOS platforms, to assess detector efficiency and identify optimal integration methods. The results demonstrated that SOI platforms provide superior coupling efficiency, whereas GOS platforms offer better thermal management and extended mid-infrared operation. While these findings provide valuable insights, numerous mid-infrared photonic platforms and integration configurations remain unexplored, warranting further investigation.

Although monolithic integration remains the preferred long-term solution due to its scalability, significant challenges related to material growth persist, particularly the formation of defects near the interface with the substrate. In the meantime, heterogeneous integration provides a viable pathway for the early adoption of GeSn-based devices in applications such as on-chip spectroscopic sensing and data communications. This work experimentally demonstrated, for the first time, the use of transfer printing to integrate GeSn membranes onto SOI waveguides for photodetection at 2.33 μm, achieving promising responsivities of up to 361 mA/W. These results establish GeSn membranes as promising building blocks for heterogeneously integrated mid-infrared PICs. Furthermore, the transfer printing technique allows for the co-integration of GeSn MSM detectors with other active materials, offering a comprehensive solution for developing a complete set of active components.

In light of these results, GeSn alloys have a considerable potential in key applications such as communications and spectroscopic sensing, though several challenges need to be addressed. The following research directions may contribute to the integration of GeSn into silicon photonics or further our understanding of its properties.

Look into selective area epitaxy and defect management

Selective area growth of GeSn in a back-end-of-line (BEOL) process could facilitate monolithic integration, seamlessly incorporating GeSn photodetectors into photonic foundry workflows. Leveraging platforms based on silicon nitride (SiN) waveguides could facilitate this integration, offering a broader transparency range and reducing the impact of defective interfaces either through evanescent coupling or butt-coupling. Future efforts should prioritize defect management through post-growth annealing to lower dislocation density and passivation to neutralize surface states.

Improve the fabrication and transfer printing of GeSn membranes

Further optimization of GeSn membrane fabrication and transfer printing is also critical to improving the adhesion and minimizing the thermal limitations associated with current adhesive materials. Future research should explore transferring membranes onto substrates with higher thermal conductivity to improve heat dissipation and device performance. Recent room-temperature lasing demonstrations with GeSn alloys highlight the need for layers with optimized thermal management to ensure stable operation. The performance of optoelectronic membrane-based devices could also benefit from the use of p-i-n heterostructures to reduce the dark current and noise to achieve an overall better detectivity.

Investigate the growth and properties of SiGeSn ternary alloys

The exploration of SiGeSn ternary alloys represents another promising research avenue, as it could enable independent tuning of bandgap energy and strain, offering greater flexibility in optimizing optical and electronic properties for specific applications. However, the complex kinetics of these ternary compounds present additional challenges that require careful control during growth. SiGeSn alloys have already shown promise as barrier materials in quantum wells, but achieving sufficient band offsets for effective carrier confinement at room temperature remains a challenge.

Explore designs for GeSn-based integrated light sources and modulators

While the focus of this thesis was put on photodetectors, future research should also investigate GeSn-based optoelectronic devices, such as electroabsorption modulators (EAMs) and light emitters integrated onto PICs. These components are critical for communication and sensing applications and could be integrated monolithically or heterogeneously with

enhanced defect management strategies. Leveraging platforms such as GeSn-on-insulator (GeSnOI) with tensile strain applied through SiN waveguides could further enhance emission properties and broaden the scope of GeSn applications. The transferred membranes could also be used in the development of light emitters by coupling them to passive optical cavities.

Develop prototypes for applications and co-integration demonstrations

Although monolithic integration of GeSn remains challenging due to inherent defects and substrate limitations, heterogeneous integration offers a practical and scalable solution for investigating potential applications and to realize fully functional PICs. Techniques such as wafer bonding and transfer printing can effectively remove defects at the Ge/GeSn interface and facilitate the integration of GeSn-based components alongside III–V materials. This approach could drive the development of cost-effective, high-performance photonic devices for mid-infrared applications, including chemical sensing, medical diagnostics, and 2 μm-band transceivers. Complete PIC prototypes that are designed for target applications could highlight the potential of GeSn-based components in concrete proof-of-concept experiments.

This thesis has laid the groundwork for GeSn integration into silicon photonics, demonstrating the feasibility of heterogeneous approaches and identifying key pathways for future advancements. Further developments in material quality, fabrication processes, and integration techniques will be crucial to realizing the full potential of GeSn-based devices in emerging photonic applications.

REFERENCES

[1] Cisco. (2020) Cisco Annual Internet Report (2018-2023). [Online]. Available: https://www.cisco.com/c/en/us/solutions/collateral/executive-perspectives/annual-internet-report/white-paper-c11-741490.html

[2] Research and Markets. (2024) Global Online Population Forecast 2023-28. [Online]. Available: https://www.researchandmarkets.com/reports/5986753/global-online-population-forecast-28

[3] Lorenzo Pavesi, David J. Lockwood, , and Editors, *Silicon Photonics III*, 1st ed., L. Pavesi and D. J. Lockwood, Eds. Berlin: Springer, 2016.

[4] D. Thomson, A. Zilkie, J. E. Bowers, T. Komljenovic, G. T. Reed *et al.*, "Roadmap on silicon photonics," *Journal of Optics*, vol. 18, no. 7, p. 073003, 2016.

[5] J. J. Ackert, D. J. Thomson, L. Shen, A. C. Peacock, P. E. Jessop *et al.*, "High-speed detection at two micrometres with monolithic silicon photodiodes," *Nature Photonics*, vol. 9, no. 6, pp. 393–396, 2015.

[6] T. Yin, R. Cohen, M. M. Morse, G. Sarid, Y. Chetrit *et al.*, "31 GHz Ge n-i-p waveguide photodetectors on Silicon-on-Insulator substrate," *Optics Express*, vol. 15, no. 21, p. 13965, 2007.

[7] S. Lischke, A. Peczek, J. S. Morgan, K. Sun, D. Steckler *et al.*, "Ultra-fast germanium photodiode with 3-dB bandwidth of 265 GHz," *Nature Photonics*, vol. 15, no. 12, pp. 925–931, 2021.

[8] J. Liu, X. Sun, D. Pan, X. Wang, L. C. Kimerling *et al.*, "Tensile-strained, n-type Ge as a gain medium for monolithic laser integration on Si," *Optics Express*, vol. 15, no. 18, p. 11272, 2007.

[9] B. Dutt, D. S. Sukhdeo, D. Nam, B. M. Vulovic, Z. Yuan *et al.*, "Roadmap to an efficient germanium-on-silicon laser: Strain vs. n-type doping," *IEEE Photonics Journal*, vol. 4, no. 5, pp. 2002–2009, 2012.

[10] O. Moutanabbir, S. Assali, X. Gong, E. O'Reilly, C. A. Broderick *et al.*, "Monolithic infrared silicon photonics: The rise of (Si)GeSn semiconductors," *Applied Physics Letters*, vol. 118, no. 11, p. 110502, 2021.

[11] S. Wirths, R. Geiger, N. von den Driesch, G. Mussler, T. Stoica *et al.*, "Lasing in direct-bandgap GeSn alloy grown on Si," *Nature Photonics*, vol. 9, no. 2, pp. 88–92, 2015.

[12] B.-J. Huang, C.-Y. Chang, Y.-D. Hsieh, R. A. Soref, G. Sun *et al.*, "Electrically Injected GeSn Vertical-Cavity Surface Emitters on Silicon-on-Insulator Platforms," *ACS Photonics*, vol. 6, no. 8, pp. 1931–1938, 2019.

[13] Y. Zhou, Y. Miao, S. Ojo, H. Tran, G. Abernathy *et al.*, "Electrically injected GeSn lasers on Si operating up to 100 K," *Optica*, vol. 7, no. 8, p. 924, 2020.

[14] M. R. M. Atalla, S. Assali, A. Attiaoui, C. Lemieux-Leduc, A. Kumar *et al.*, "All-Group IV Transferable Membrane Mid-Infrared Photodetectors," *Advanced Functional Materials*, vol. 31, no. 3, p. 2006329, 2021.

[15] M. R. M. Atalla, S. Assali, S. Koelling, A. Attiaoui, and O. Moutanabbir, "High-Bandwidth Extended-SWIR GeSn Photodetectors on Silicon Achieving Ultrafast Broadband Spectroscopic Response," *ACS Photonics*, vol. 9, no. 4, pp. 1425–1433, 2022.

[16] Y. Zhou, S. Ojo, C.-W. Wu, Y. Miao, H. Tran *et al.*, "Electrically injected GeSn lasers with peak wavelength up to 2.7 μm," *Photonics Research*, vol. 10, no. 1, p. 222, 2021.

[17] J. Margetis, A. Mosleh, S. Al-Kabi, S. Ghetmiri, W. Du *et al.*, "Study of low-defect and strain-relaxed GeSn growth via reduced pressure CVD in H_2 and N_2 carrier gas," *Journal of Crystal Growth*, vol. 463, pp. 128–133, 2017.

[18] D. Stange, S. Wirths, N. von den Driesch, G. Mussler, T. Stoica *et al.*, "Optical Transitions in Direct-Bandgap $Ge_{1-x}Sn_x$ Alloys," *ACS Photonics*, vol. 2, no. 11, pp. 1539–1545, 2015.

[19] R. Soref, "Enabling 2 μm communications," *Nature Photonics*, vol. 9, no. 6, pp. 358–359, 2015.

[20] H. Wang, Y. Chen, J. Zhang, G. Zhang, Y.-C. Huang *et al.*, "First Demonstration of Waveguide-Coupled $Ge_{0.92}Sn_{0.08}$/Ge Multiple-Quantum-Well Photodetector on the SOI Platform for 2-μm Wavelength Optoelectronic Integrated Circuit," in *2021 Symposium on VLSI Circuits*, vol. 28, no. Papers. IEEE, 2021, pp. 1–2.

[21] H. Wang, J. Zhang, G. Zhang, Y. Chen, K. Han *et al.*, "Monolithic Waveguide Group IV Multiple-Quantum-Well Photodetectors and Modulators on 300-mm Si Substrates for

2-μm Wavelength Optoelectronic Integrated Circuit," *IEEE Transactions on Electron Devices*, vol. 69, no. 12, pp. 7161–7166, 2022.

[22] D. Lei, K. H. Lee, S. Bao, W. Wang, B. Wang *et al.*, "GeSn-on-insulator substrate formed by direct wafer bonding," *Applied Physics Letters*, vol. 109, no. 2, p. 022106, 2016.

[23] B. Wang, E. Sakat, E. Herth, M. Gromovyi, A. Bjelajac *et al.*, "GeSnOI Mid-infrared Laser Technology," *Light: Science & Applications*, vol. 10, no. 1, p. 232, 2021.

[24] M. Akie, T. Fujisawa, T. Sato, M. Arai, and K. Saitoh, "GeSn/SiGeSn Multiple-Quantum-Well Electroabsorption Modulator With Taper Coupler for Mid-Infrared Ge-on-Si Platform," *IEEE Journal of Selected Topics in Quantum Electronics*, vol. 24, no. 6, pp. 1–8, 2018.

[25] X. Y. Li, J. Y. Wang, Y. F. Liu, J. J. Chen, Y. Du *et al.*, "Design of $Ge_{1-x}Sn_x$-on-Si waveguide photodetectors featuring high-speed high-sensitivity photodetection in the C- to U-bands," *Applied Optics*, vol. 59, no. 25, p. 7646, aug 2020.

[26] S. Ghosh, R. Bansal, G. Sun, R. A. Soref, H.-H. Cheng *et al.*, "Design and Optimization of GeSn Waveguide Photodetectors for 2-μm Band Silicon Photonics," *Sensors*, vol. 22, no. 11, p. 3978, 2022.

[27] S. Shekhar, W. Bogaerts, L. Chrostowski, J. E. Bowers, M. Hochberg *et al.*, "Roadmapping the next generation of silicon photonics," *Nature Communications*, vol. 15, no. 1, p. 751, 2024.

[28] S. E. Miller, "Integrated optics: An introduction," *Bell System Technical Journal*, vol. 48, no. 7, pp. 2059–2069, 1969.

[29] R. Soref and J. Lorenzo, "Single-crystal silicon: a new material for 1.3 and 1.6 μm integrated-optical components," *Electronics Letters*, vol. 21, no. 21, p. 953, 1985.

[30] Y. Li, S. Feng, Y. Zhang, and A. W. Poon, "Sub-bandgap linear-absorption-based photodetectors in avalanche mode in PN-diode-integrated silicon microring resonators," *Optics Letters*, vol. 38, no. 23, p. 5200, 2013.

[31] J.-B. You, H. Kwon, J. Kim, H.-H. Park, and K. Yu, "Photon-assisted tunneling for sub-bandgap light detection in silicon PN-doped waveguides," *Optics Express*, vol. 25, no. 4, p. 4284, 2017.

[32] Y. Peng, Y. Yuan, W. V. Sorin, S. Cheung, Z. Huang *et al.*, "An 8 × 160 Gb s^{-1} all-silicon avalanche photodiode chip," *Nature Photonics*, vol. 18, no. 9, pp. 928–934, 2024.

[33] R. E. Camacho-Aguilera, Y. Cai, N. Patel, J. T. Bessette, M. Romagnoli *et al.*, "An electrically pumped germanium laser," *Optics Express*, vol. 20, no. 10, p. 11316, 2012.

[34] N. Li, G. Chen, D. K. T. Ng, L. W. Lim, J. Xue *et al.*, "Integrated lasers on silicon at communication wavelength: A progress review," *Advanced Optical Materials*, vol. 10, no. 23, p. 2201008, 2022.

[35] M. Smit, X. Leijtens, H. Ambrosius, E. Bente, J. van der Tol *et al.*, "An introduction to InP-based generic integration technology," *Semiconductor Science and Technology*, vol. 29, no. 8, p. 083001, 2014.

[36] J. E. Bowers and A. Y. Liu, "A comparison of four approaches to photonic integration," in *Optical Fiber Communication Conference*, ser. OFC, no. viable. OSA, 2017, p. M2B.4.

[37] Y. Han and K. M. Lau, "III-V lasers selectively grown on (001) silicon," *Journal of Applied Physics*, vol. 128, no. 20, p. 200901, 2020.

[38] Y. Bian, K. Ramachandran, Z.-J. Wu, B. Hedrick, K. K. Dezfulian *et al.*, "3D Integrated Laser Attach Technology on a 300-mm Monolithic CMOS Silicon Photonics Platform," *IEEE Journal of Selected Topics in Quantum Electronics*, vol. 29, no. 3, pp. 1–19, 2023.

[39] S. Keyvaninia, S. Verstuyft, L. V. Landschoot, F. Lelarge, G.-H. Duan *et al.*, "Heterogeneously integrated III-V/silicon distributed feedback lasers," *Optics Letters*, vol. 38, no. 24, p. 5434, 2013.

[40] A. W. Fang, H. Park, O. Cohen, R. Jones, M. J. Paniccia *et al.*, "Electrically pumped hybrid AlGaInAs-silicon evanescent laser," *Optics Express*, vol. 14, no. 20, p. 9203, 2006.

[41] J. Sun, R. Kumar, M. Sakib, J. B. Driscoll, H. Jayatilleka *et al.*, "A 128 Gb/s PAM4 Silicon Microring Modulator With Integrated Thermo-Optic Resonance Tuning," *Journal of Lightwave Technology*, vol. 37, no. 1, pp. 110–115, 2019.

[42] M. He, M. Xu, Y. Ren, J. Jian, Z. Ruan *et al.*, "High-performance hybrid silicon and lithium niobate Mach-Zehnder modulators for 100 Gbit s^{-1} and beyond," *Nature Photonics*, vol. 13, no. 5, pp. 359–364, 2019.

[43] C. Zhang and J. E. Bowers, "Silicon photonic terabit/s network-on-chip for datacenter interconnection," *Optical Fiber Technology*, vol. 44, pp. 2–12, 2018.

[44] A. Netherton, M. Dumont, Z. Nelson, J. Koo, J. Jhonsa *et al.*, "High capacity, low power, short reach integrated silicon photonic interconnects," *Photonics Research*, vol. 12, no. 11, p. A69, 2024.

[45] C. Zhang, M. A. Tran, Z. Zhang, A. E. Dorche, Y. Shen *et al.*, "Integrated photonics beyond communications," *Applied Physics Letters*, vol. 123, p. 230501, 2023.

[46] L. Tombez, E. J. Zhang, J. S. Orcutt, S. Kamlapurkar, and W. M. J. Green, "Methane absorption spectroscopy on a silicon photonic chip," *Optica*, vol. 4, no. 11, p. 1322, 2017.

[47] Y. Zhang, X. Guo, X. Ji, J. Shen, A. He *et al.*, "What can be integrated on the silicon photonics platform and how?" *APL Photonics*, vol. 9, p. 090902, 2024.

[48] S. Y. Siew, B. Li, F. Gao, H. Y. Zheng, W. Zhang *et al.*, "Review of silicon photonics technology and platform development," *Journal of Lightwave Technology*, vol. 39, no. 13, pp. 4374–4389, 2021.

[49] C. Goodman, "Direct-gap group IV semiconductors based on tin," *IEE Proceedings I Solid State and Electron Devices*, vol. 129, no. 5, p. 189, 1982.

[50] P. R. Pukite, A. Harwit, and S. S. Iyer, "Molecular beam epitaxy of metastable, diamond structure Sn_xGe_{1-x} alloys," *Applied Physics Letters*, vol. 54, no. 21, pp. 2142–2144, 1989.

[51] J. Taraci, S. Zollner, M. R. McCartney, J. Menendez, M. A. Santana-Aranda *et al.*, "Synthesis of Silicon-Based Infrared Semiconductors in the Ge–Sn System Using Molecular Chemistry Methods," *Journal of the American Chemical Society*, vol. 123, no. 44, pp. 10 980–10 987, 2001.

[52] S. Wirths, D. Buca, and S. Mantl, "Si–Ge–Sn alloys: From growth to applications," *Progress in Crystal Growth and Characterization of Materials*, vol. 62, no. 1, pp. 1–39, 2016.

[53] P. Moontragoon, Z. Ikonić, and P. Harrison, "Band structure calculations of Si–Ge–Sn alloys: achieving direct band gap materials," *Semiconductor Science and Technology*, vol. 22, no. 7, pp. 742–748, 2007.

[54] S. Wirths, "Group IV Epitaxy for Advanced Nano- and Optoelectronic Applications," Ph.D. dissertation, Forschungszentrum Jülich, 2015.

[55] S. Gupta, B. Magyari-Köpe, Y. Nishi, and K. C. Saraswat, "Achieving direct band gap in germanium through integration of Sn alloying and external strain," *Journal of Applied Physics*, vol. 113, no. 7, p. 073707, 2013.

[56] A. Attiaoui and O. Moutanabbir, "Indirect-to-direct band gap transition in relaxed and strained $Ge_{1-x-y}Si_xSn_y$ ternary alloys," *Journal of Applied Physics*, vol. 116, no. 6, p. 063712, 2014.

[57] N. von den Driesch, D. Stange, S. Wirths, D. Rainko, I. Povstugar *et al.*, "SiGeSn ternaries for efficient group IV heterostructure light emitters," *Small*, vol. 13, no. 16, p. 1603321, 2017.

[58] V. Reboud, O. Concepción, W. Du, M. El Kurdi, J. Hartmann *et al.*, "Advances in GeSn alloys for MIR applications," *Photonics and Nanostructures - Fundamentals and Applications*, vol. 58, p. 101233, 2024.

[59] R. Soref, J. Kouvetakis, and J. Menendez, "Advances in SiGeSn/Ge Technology," *MRS Proceedings*, vol. 958, 2006.

[60] M. Oehme, J. Werner, M. Gollhofer, M. Schmid, M. Kaschel *et al.*, "Room-Temperature Electroluminescence From GeSn Light-Emitting Pin Diodes on Si," *IEEE Photonics Technology Letters*, vol. 23, no. 23, pp. 1751–1753, 2011.

[61] M. R. M. Atalla, S. Assali, G. Daligou, A. Attiaoui, S. Koelling *et al.*, "Continuous-Wave GeSn Light-Emitting Diodes on Silicon with 2.5 μm Room-Temperature Emission," *ACS Photonics*, vol. 11, no. 3, pp. 1335–1341, 2024.

[62] D. Stange, S. Wirths, R. Geiger, C. Schulte-Braucks, B. Marzban *et al.*, "Optically Pumped GeSn Microdisk Lasers on Si," *ACS Photonics*, vol. 3, no. 7, pp. 1279–1285, 2016.

[63] J. Chrétien, N. Pauc, F. Armand Pilon, M. Bertrand, Q.-M. Thai *et al.*, "GeSn Lasers Covering a Wide Wavelength Range Thanks to Uniaxial Tensile Strain," *ACS Photonics*, vol. 6, no. 10, pp. 2462–2469, 2019.

[64] A. Elbaz, D. Buca, N. von den Driesch, K. Pantzas, G. Patriarche *et al.*, "Ultra-low-threshold continuous-wave and pulsed lasing in tensile-strained GeSn alloys," *Nature Photonics*, vol. 14, no. 6, pp. 375–382, 2020.

[65] J. Chrétien, Q. M. Thai, M. Frauenrath, L. Casiez, A. Chelnokov *et al.*, "Room temperature optically pumped GeSn microdisk lasers," *Applied Physics Letters*, vol. 120, no. 5, p. 051107, 2022.

[66] S. Acharya, H. Stanchu, R. Kumar, S. Ojo, M. Alher *et al.*, "Electrically Injected Mid-Infrared GeSn Laser on Si Operating at 140 K," *IEEE Journal of Selected Topics in Quantum Electronics*, vol. 31, no. 1: SiGeSn Infrared Photon, pp. 1–7, 2025.

[67] L. Seidel, T. Liu, O. Concepción, B. Marzban, V. Kiyek *et al.*, "Continuous-wave electrically pumped multi-quantum-well laser based on group-IV semiconductors," *Nature Communications*, vol. 15, no. 1, p. 10502, 2024.

[68] L. Peng, X. Li, Z. Liu, X. Liu, J. Zheng *et al.*, "Horizontal GeSn/Ge multi-quantum-well ridge waveguide LEDs on silicon substrates," *Photonics Research*, vol. 8, no. 6, p. 899, 2020.

[69] D. Stange, N. von den Driesch, D. Rainko, C. Schulte-Braucks, S. Wirths *et al.*, "Study of GeSn based heterostructures: towards optimized group IV MQW LEDs," *Optics Express*, vol. 24, no. 2, p. 1358, 2016.

[70] D. Stange, N. von den Driesch, T. Zabel, F. Armand-Pilon, D. Rainko *et al.*, "GeSn/SiGeSn Heterostructure and Multi Quantum Well Lasers," *ACS Photonics*, vol. 5, no. 11, pp. 4628–4636, 2018.

[71] V. Reboud, A. Gassenq, N. Pauc, J. Aubin, L. Milord *et al.*, "Optically pumped GeSn micro-disks with 16% Sn lasing at 3.1 μm up to 180 K," *Applied Physics Letters*, vol. 111, no. 9, p. 092101, 2017.

[72] A. Bjelajac, M. Gromovyi, E. Sakat, B. Wang, G. Patriarche *et al.*, "Up to 300 K lasing with GeSn-On-Insulator microdisk resonators," *Optics Express*, vol. 30, no. 3, p. 3954, 2022.

[73] D. Buca, A. Bjelajac, D. Spirito, O. Concepción, M. Gromovyi *et al.*, "Room Temperature Lasing in GeSn Microdisks Enabled by Strain Engineering," *Advanced Optical Materials*, vol. 10, no. 22, p. 2201024, 2022.

[74] A. R. Ellis, D. A. Duffy, I. P. Marko, S. Acharya, W. Du *et al.*, "Challenges for room temperature operation of electrically pumped GeSn lasers," *Scientific Reports*, vol. 14, no. 1, p. 10318, 2024.

[75] B. Marzban, L. Seidel, T. Liu, K. Wu, V. Kiyek *et al.*, "Strain Engineered Electrically Pumped SiGeSn Microring Lasers on Si," *ACS Photonics*, vol. 10, no. 1, pp. 217–224, 2022.

[76] T. Liu, L. Seidel, O. Concepción, V. Reboud, A. Chelnokov *et al.*, "Electrically Pumped GeSn Micro-Ring Lasers," *IEEE Journal of Selected Topics in Quantum Electronics*, vol. 31, no. 1: SiGeSn Infrared Photon., pp. 1–7, 2025.

[77] D. Stange, N. von den Driesch, D. Rainko, S. Roesgaard, I. Povstugar *et al.*, "Short-wave infrared LEDs from GeSn/SiGeSn multiple quantum wells," *Optica*, vol. 4, no. 2, p. 185, 2017.

[78] L. Casiez, M. Bertrand, J. Chretien, A. Quintero, Q. M. Thai *et al.*, "GeSn heterostructures LEDs for gas detection," in *2020 IEEE Photonics Conference (IPC)*. IEEE, 2020.

[79] M. R. M. Atalla, Y. Kim, S. Assali, D. Burt, D. Nam *et al.*, "Extended-SWIR GeSn LEDs with Reduced Footprint and Efficient Operation Power," *ACS Photonics*, vol. 10, no. 5, pp. 1649–1653, 2023.

[80] J. Mathews, R. Roucka, J. Xie, S.-Q. Yu, J. Menéndez *et al.*, "Extended performance GeSn/Si(100) p-i-n photodetectors for full spectral range telecommunication applications," *Applied Physics Letters*, vol. 95, no. 13, 2009.

[81] Y. Dong, G. Liang, Y.-C. Yeo, W. Wang, X. Xu *et al.*, "Germanium-Tin on Si Avalanche Photodiode: Device Design and Technology Demonstration," *IEEE Transactions on Electron Devices*, vol. 62, no. 1, pp. 128–135, 2015.

[82] M. Wanitzek, M. Hack, D. Schwarz, J. Schulze, and M. Oehme, "Low-temperature performance of GeSn-on-Si avalanche photodiodes toward single-photon detection," *Materials Science in Semiconductor Processing*, vol. 176, p. 108303, 2024.

[83] C. Cardoux, L. Casiez, M. Frauenrath, N. Pauc, V. Calvo *et al.*, "Direct Band Gap $Ge_{0.85}Sn_{0.15}$ Photodiodes for Room Temperature Gas Sensing," in *2023 IEEE Silicon Photonics Conference (SiPhotonics)*. IEEE, 2023, pp. 1–2.

[84] M. Oehme, M. Schmid, M. Kaschel, M. Gollhofer, D. Widmann *et al.*, "GeSn p-i-n detectors integrated on Si with up to 4% Sn," *Applied Physics Letters*, vol. 101, no. 14, p. 141110, 2012.

[85] T. Pham, W. Du, H. Tran, J. Margetis, J. Tolle *et al.*, "Systematic study of Si-based GeSn photodiodes with 2.6 μm detector cutoff for short-wave infrared detection," *Optics Express*, vol. 24, no. 5, p. 4519, 2016.

[86] B.-J. Huang, J.-H. Lin, H. H. Cheng, and G.-E. Chang, "GeSn resonant-cavity-enhanced photodetectors on silicon-on-insulator platforms," *Optics Letters*, vol. 43, no. 6, p. 1215, 2018.

[87] H. Tran, T. Pham, J. Margetis, Y. Zhou, W. Dou *et al.*, "Si-Based GeSn Photodetectors toward Mid-Infrared Imaging Applications," *ACS Photonics*, vol. 6, no. 11, pp. 2807–2815, 2019.

[88] H. Zhou, S. Xu, S. Wu, Y.-C. Huang, P. Zhao *et al.*, "Photo detection and modulation from 1,550 to 2,000 nm realized by a GeSn/Ge multiple-quantum-well photodiode on a 300-mm Si substrate," *Optics Express*, vol. 28, no. 23, p. 34772, 2020.

[89] X. Li, L. Peng, Z. Liu, Z. Zhou, J. Zheng *et al.*, "30 GHz GeSn photodetector on SOI substrate for 2 μm wavelength application," *Photonics Research*, vol. 9, no. 4, p. 494, 2021.

[90] H. Wang, J. Zhang, G. Zhang, Y. Chen, Y.-C. Huang *et al.*, "High-speed and high-responsivity p-i-n waveguide photodetector at a 2 μm wavelength with a $Ge_{0.92}Sn_{0.08}$/Ge multiple-quantum-well active layer," *Optics Letters*, vol. 46, no. 9, p. 2099, 2021.

[91] E. Talamas Simola, V. Kiyek, A. Ballabio, V. Schlykow, J. Frigerio *et al.*, "CMOS-Compatible Bias-Tunable Dual-Band Detector Based on GeSn/Ge/Si Coupled Photodiodes," *ACS Photonics*, vol. 8, no. 7, pp. 2166–2173, 2021.

[92] J. Cui, J. Zheng, Y. Zhu, X. Liu, Q. Huang *et al.*, "Sn component gradient GeSn photodetector with 3 dB bandwidth over 50 GHz for extending L band telecommunication," *Optics Letters*, vol. 48, no. 23, p. 6148, 2023.

[93] J. Cui, J. Zheng, Y. Zhu, X. Liu, Y. Wu *et al.*, "High-speed GeSn resonance cavity enhanced photodetectors for a 50 Gbps Si-based 2 μm band communication system," *Photonics Research*, vol. 12, no. 4, p. 767, 2024.

[94] M. R. M. Atalla, C. Lemieux-Leduc, S. Assali, S. Koelling, P. Daoust *et al.*, "Extended short-wave infrared high-speed all-GeSn PIN photodetectors on silicon," *APL Photonics*, vol. 9, no. 5, p. 056103, 2024.

[95] M. R. M. Atalla, S. Assali, S. Koelling, A. Attiaoui, and O. Moutanabbir, "Dark current in monolithic extended-SWIR GeSn PIN photodetectors," *Applied Physics Letters*, vol. 122, no. 3, p. 031103, 2023.

[96] B. Chen, Y. Chen, and Z. Deng, "Recent Advances in High Speed Photodetectors for eSWIR/MWIR/LWIR Applications," *Photonics*, vol. 8, no. 1, p. 14, 2021.

[97] J. Cui, R. Fang, X. Liu, Y. Wu, Q. Huang *et al.*, "Comprehensive Investigation of GeSn Metasurface Photodetector for Short-Wave Infrared Application," *ACS Photonics*, vol. 11, pp. 4126–4133, 2024.

[98] H. Zhao, S. Park, G. Lin, Y. Zhang, T. Zhama *et al.*, "Transferable GeSn ribbon photodetectors for high-speed short-wave infrared photonic applications," *Journal of Vacuum Science & Technology B*, vol. 42, no. 4, p. 042205, 2024.

[99] P.-C. Wang, P.-R. Huang, S. Ghosh, R. Bansal, Y.-T. Jheng *et al.*, "CMOS-compatible Self-powered Short-wave Infrared Imagers Based on GeSn Photodetector Arrays," *ACS Photonics*, vol. 11, no. 7, pp. 2659–2666, 2024.

[100] C. Chang, H. Li, C.-T. Ku, S.-G. Yang, H. H. Cheng *et al.*, "$Ge_{0.975}Sn_{0.025}$ 320 × 256 imager chip for 1.6-1.9 μm infrared vision," *Applied Optics*, vol. 55, no. 36, p. 10170, 2016.

[101] G. Xu, H. Cong, Y. Li, Z. Wu, F. Fu *et al.*, "GeSn 320 × 256 Focal Plane Array for Silicon-Based Short-wave Infrared Imaging," 2024. [Online]. Available: https://arxiv.org/abs/2409.12814

[102] R. Ponce, S. S. Azadeh, D. Stange, F. Merget, B. Marzban *et al.*, "Design of a high-speed germanium-tin absorption modulator at mid-infrared wavelengths," in *2017 IEEE 14th International Conference on Group IV Photonics (GFP)*. IEEE, 2017, pp. 19–20.

[103] G. Sun, R. A. Soref, and H. H. Cheng, "Design of an electrically pumped SiGeSn/GeSn/SiGeSn double-heterostructure midinfrared laser," *Journal of Applied Physics*, vol. 108, no. 3, p. 033107, 2010.

[104] G. Sun and R. A. Soref and H. H. Cheng, "Design of a Si-based lattice-matched room-temperature GeSn/GeSiSn multi-quantum-well mid-infrared laser diode," *Optics express*, vol. 18, no. 19, pp. 19 957–19 965, 2010.

[105] B. Marzban, D. Stange, D. Rainko, Z. Ikonic, D. Buca *et al.*, "Modeling of a SiGeSn Quantum Well Laser," *Photonics Research*, vol. 9, no. 7, p. 1234, 2021.

[106] Q. M. Thai, J. Chrétien, M. Bertrand, L. Casiez, A. Chelnokov *et al.*, "GeSn optical gain and lasing characteristics modelling," *Physical Review B*, vol. 102, no. 15, p. 155203, 2020.

[107] M. Adams, "Design eines optisch gepumpten and wellenleiter and gekoppelten Germanium-Zinn and Lasers und Aufbau and eines optischen Messplatzes für 2,5 μm Wellenlänge," Master's thesis, RWTH Aachen, 2016.

[108] Y.-D. Hsieh, J.-H. Lin, R. Soref, G. Sun, H.-H. Cheng *et al.*, "Electro-absorption modulation in GeSn alloys for wide-spectrum mid-infrared applications," *Communications Materials*, vol. 2, no. 1, p. 40, 2021.

[109] A. C. Meng, C. S. Fenrich, M. R. Braun, J. P. McVittie, A. F. Marshall *et al.*, "Core-Shell Germanium/Germanium–Tin Nanowires Exhibiting Room-Temperature Direct- and Indirect-Gap Photoluminescence," *Nano Letters*, vol. 16, no. 12, pp. 7521–7529, 2016.

[110] S. Assali, A. Dijkstra, A. Li, S. Koelling, M. A. Verheijen *et al.*, "Growth and Optical Properties of Direct Band Gap $Ge/Ge_{0.87}Sn_{0.13}$ Core/Shell Nanowire Arrays," *Nano Letters*, vol. 17, no. 3, pp. 1538–1544, 2017.

[111] S. Assali, M. Albani, R. Bergamaschini, M. A. Verheijen, A. Li *et al.*, "Strain engineering in Ge/GeSn core/shell nanowires," *Applied Physics Letters*, vol. 115, no. 11, p. 113102, 2019.

[112] L. Luo, S. Assali, M. R. M. Atalla, S. Koelling, A. Attiaoui *et al.*, "Extended-SWIR Photodetection in All-Group IV Core/Shell Nanowires," *ACS Photonics*, vol. 9, no. 3, pp. 914–921, 2022.

[113] L. Luo, M. R. M. Atalla, S. Assali, S. Koelling, G. Daligou *et al.*, "Mid-infrared Imaging Using Strain-Relaxed $Ge_{1-x}Sn_x$ Alloys Grown on 20 nm Ge Nanowires," *Nano Letters*, vol. 24, no. 16, pp. 4979–4986, 2024.

[114] Y. Kim, S. Assali, H.-J. Joo, S. Koelling, M. Chen *et al.*, "Short-wave infrared cavity resonances in a single GeSn nanowire," *Nature Communications*, vol. 14, no. 1, p. 4393, 2023.

[115] D. Lei, K. H. Lee, Y.-C. Huang, W. Wang, S. Masudy-Panah *et al.*, "Germanium-tin (GeSn) p-channel fin field-effect transistor fabricated on a novel GeSn-on-insulator substrate," *IEEE Transactions on Electron Devices*, vol. 65, no. 9, pp. 3754–3761, 2018.

[116] G. Han, S. Su, C. Zhan, Q. Zhou, Y. Yang *et al.*, "High-mobility germanium-tin (GeSn) P-channel MOSFETs featuring metallic source/drain and sub-370 °C process modules," in *2011 International Electron Devices Meeting*. IEEE, 2011, pp. 16.7.1–16.7.3.

[117] M. Liu, D. Yang, A. Shkurmanov, J. H. Bae, V. Schlykow *et al.*, "Epitaxial GeSn/Ge Vertical Nanowires for p-Type Field-Effect Transistors with Enhanced Performance," *ACS Applied Nano Materials*, vol. 4, no. 1, pp. 94–101, 2021.

[118] Y. Junk, O. Concepción, M. Frauenrath, J. Sun, J. H. Bae *et al.*, "Enhancing Device Performance with High Electron Mobility GeSn Materials," *Advanced Electronic Materials*, p. 2400561, 2024.

[119] A. Giunto and A. Fontcuberta i Morral, "Defects in Ge and GeSn and their impact on optoelectronic properties," *Applied Physics Reviews*, vol. 11, no. 4, p. 041333, 2024.

[120] E. Kasper, J. Werner, M. Oehme, S. Escoubas, N. Burle *et al.*, "Growth of silicon based germanium tin alloys," *Thin Solid Films*, vol. 520, no. 8, pp. 3195–3200, 2012.

[121] J. Aubin, J. M. Hartmann, A. Gassenq, J. L. Rouviere, E. Robin *et al.*, "Growth and structural properties of step-graded, high Sn content GeSn layers on Ge," *Semiconductor Science and Technology*, vol. 32, no. 9, p. 094006, 2017.

[122] S. Assali, J. Nicolas, S. Mukherjee, A. Dijkstra, and O. Moutanabbir, "Atomically uniform Sn-rich GeSn semiconductors with 3.0-3.5 μm room-temperature optical emission," *Applied Physics Letters*, vol. 112, no. 25, p. 251903, 2018.

[123] W. Takeuchi, T. Asano, Y. Inuzuka, M. Sakashita, O. Nakatsuka *et al.*, "Characterization of Shallow-and Deep-Level Defects in Undoped $Ge_{1-x}Sn_x$ Epitaxial Layers by Electrical Measurements," *ECS Journal of Solid State Science and Technology*, vol. 5, no. 4, pp. P3082–P3086, 2016.

[124] A. Elbaz, R. Arefin, E. Sakat, B. Wang, E. Herth *et al.*, "Reduced Lasing Thresholds in GeSn Microdisk Cavities with Defect Management of the Optically Active Region," *ACS Photonics*, vol. 7, no. 10, pp. 2713–2722, 2020.

[125] R. W. Olesinski and G. J. Abbaschian, "The Ge–Sn (Germanium-Tin) system," *Bulletin of Alloy Phase Diagrams*, vol. 5, no. 3, pp. 265–271, 1984.

[126] P. Zaumseil, Y. Hou, M. A. Schubert, N. von den Driesch, D. Stange *et al.*, "The thermal stability of epitaxial GeSn layers," *APL Materials*, vol. 6, no. 7, p. 076108, 2018.

[127] J. Nicolas, S. Assali, S. Mukherjee, A. Lotnyk, and O. Moutanabbir, "Dislocation Pipe Diffusion and Solute Segregation during the Growth of Metastable GeSn," *Crystal Growth & Design*, vol. 20, no. 5, pp. 3493–3498, 2020.

[128] S. Mukherjee, S. Assali, and O. Moutanabbir, "Atomic Pathways of Solute Segregation in the Vicinity of Nanoscale Defects," *Nano Letters*, vol. 21, no. 23, pp. 9882–9888, 2021.

[129] V. Bonino, N. Pauc, V. Calvo, M. Frauenrath, J.-M. Hartmann *et al.*, "Microstructuring to Improve the Thermal Stability of GeSn Layers," *ACS Applied Materials & Interfaces*, vol. 14, no. 19, pp. 22 270–22 277, 2022.

[130] S. Assali, M. Elsayed, J. Nicolas, M. O. Liedke, A. Wagner *et al.*, "Vacancy complexes in nonequilibrium germanium-tin semiconductors," *Applied Physics Letters*, vol. 114, no. 25, p. 251907, 2019.

[131] M. Morea, C. E. Brendel, K. Zang, J. Suh, C. S. Fenrich *et al.*, "Passivation of multiple-quantum-well $Ge_{0.97}Sn_{0.03}$/Ge p-i-n photodetectors," *Applied Physics Letters*, vol. 110, no. 9, p. 091109, 2017.

[132] Y. Dong, W. Wang, D. Lei, X. Gong, Q. Zhou *et al.*, "Suppression of dark current in germanium-tin on silicon p-i-n photodiode by a silicon surface passivation technique," *Optics Express*, vol. 23, no. 14, p. 18611, 2015.

[133] D. Spirito, N. von den Driesch, C. L. Manganelli, M. H. Zoellner, A. A. Corley-Wiciak *et al.*, "Thermoelectric Efficiency of Epitaxial GeSn Alloys for Integrated Si-Based Applications: Assessing the Lattice Thermal Conductivity by Raman Thermometry," *ACS Applied Energy Materials*, vol. 4, no. 7, pp. 7385–7392, 2021.

[134] S. Assali, A. Attiaoui, S. Koelling, M. R. M. Atalla, A. Kumar *et al.*, "Micrometer-thick, atomically random $Si_{0.06}Ge_{0.90}Sn_{0.04}$ for silicon-integrated infrared optoelectronics," *Journal of Applied Physics*, vol. 132, no. 19, p. 195305, 2022.

[135] C. Xu, D. Ringwala, D. Wang, L. Liu, C. D. Poweleit *et al.*, "Synthesis and Fundamental Studies of Si-Compatible (Si)GeSn and GeSn Mid-IR Systems with Ultrahigh Sn Contents," *Chemistry of Materials*, vol. 31, no. 23, pp. 9831–9842, 2019.

[136] M. A. Mircovich, C. Xu, D. A. Ringwala, C. D. Poweleit, J. Menéndez *et al.*, "Extended Compositional Range for the Synthesis of SWIR and LWIR $Ge{-}1-ySn_y$ Alloys and Device Structures via CVD of SnH_4 and Ge_3H_8," *ACS Applied Electronic Materials*, vol. 3, no. 8, pp. 3451–3460, 2021.

[137] M. Sieger and B. Mizaikoff, "Toward On-Chip Mid-Infrared Sensors," *Analytical Chemistry*, vol. 88, no. 11, pp. 5562–5573, 2016.

[138] M. Yu, Y. Okawachi, A. G. Griffith, N. Picqué, M. Lipson *et al.*, "Silicon-chip-based mid-infrared dual-comb spectroscopy," *Nature Communications*, vol. 9, no. 1, p. 1869, 2018.

[139] R. Wang, S. Sprengel, A. Vasiliev, G. Boehm, J. V. Campenhout *et al.*, "Widely tunable 2.3 μm III-V-on-silicon Vernier lasers for broadband spectroscopic sensing," *Photonics Research*, vol. 6, no. 9, p. 858, 2018.

[140] A. Lambrecht and K. Schmitt, *Mid-infrared gas-sensing systems and applications.* Elsevier, 2020, pp. 661–715.

[141] D. Caffey, M. B. Radunsky, V. Cook, M. Weida, P. R. Buerki *et al.*, "Recent results from broadly tunable external cavity quantum cascade lasers," in *Novel In-Plane Semiconductor Lasers X*, A. A. Belyanin and P. M. Smowton, Eds. SPIE, 2011.

[142] I. Gordon, L. Rothman, C. Hill, R. Kochanov, Y. Tan *et al.*, "The HITRAN2016 molecular spectroscopic database," *Journal of Quantitative Spectroscopy and Radiative Transfer*, vol. 203, pp. 3–69, 2017.

[143] J. Hodgkinson and R. P. Tatam, "Optical gas sensing: a review," *Measurement Science and Technology*, vol. 24, no. 1, p. 012004, 2013.

[144] L. Flannigan, L. Yoell, and C.-Q. Xu, "Mid-wave and long-wave infrared transmitters and detectors for optical satellite communications–a review," *Journal of Optics*, vol. 24, no. 4, p. 043002, 2022.

[145] P. Loubere, "The global climate system," *Nature Education Knowledge*, vol. 3, no. 10, p. 24, 2012.

[146] A. Rogalski, "Progress in focal plane array technologies," *Progress in Quantum Electronics*, vol. 36, no. 2–3, pp. 342–473, 2012.

[147] G. G. Taylor, D. Morozov, N. R. Gemmell, K. Erotokritou, S. Miki *et al.*, "Photon counting LIDAR at 2.3 μm wavelength with superconducting nanowires," *Optics Express*, vol. 27, no. 26, p. 38147, 2019.

[148] S. P. Mahulikar, H. R. Sonawane, and G. Arvind Rao, "Infrared signature studies of aerospace vehicles," *Progress in Aerospace Sciences*, vol. 43, no. 7–8, pp. 218–245, 2007.

[149] A. Godard, "Infrared (2–12 μm) solid-state laser sources: a review," *Comptes Rendus. Physique*, vol. 8, no. 10, pp. 1100–1128, 2007.

[150] A. Spott, "Heterogeneous integration and of mid-infrared and lasers on silicon," Ph.D. dissertation, University of California – Santa Barbara, 2018.

[151] D. Jung, S. Bank, M. L. Lee, and D. Wasserman, "Next-generation mid-infrared sources," *Journal of Optics*, vol. 19, no. 12, p. 123001, 2017.

[152] E. Tournié and A. N. Baranov, *Mid-Infrared Semiconductor Lasers*. Elsevier, 2012, pp. 183–226.

[153] E. Tournié, L. Monge Bartolome, M. Rio Calvo, Z. Loghmari, D. A. Díaz-Thomas *et al.*, "Mid-infrared III–V semiconductor lasers epitaxially grown on Si substrates," *Light: Science & Applications*, vol. 11, p. 165, 2022.

[154] Z. Yin and X. Tang, "A review of energy bandgap engineering in III–V semiconductor alloys for mid-infrared laser applications," *Solid-State Electronics*, vol. 51, no. 1, pp. 6–15, 2007.

[155] W. Lei and C. Jagadish, "Lasers and photodetectors for mid-infrared $2-3$ μm applications," *Journal of Applied Physics*, vol. 104, no. 9, p. 091101, Nov. 2008.

[156] K. Vizbaras and M.-C. Amann, "Room-temperature 3.73 μm GaSb-based type-I quantum-well lasers with quinternary barriers," *Semiconductor Science and Technology*, vol. 27, no. 3, p. 032001, 2012.

[157] J. T. Olesberg and M. E. Flatté, *Theory of Mid-wavelength Infrared Laser Active Regions: Intrinsic Properties and Design Strategies*. Springer London, 2006, pp. 3–92.

[158] M. Razeghi, N. Bandyopadhyay, Y. Bai, Q. Lu, and S. Slivken, "Recent advances in mid infrared (3–5 μm) Quantum Cascade Lasers," *Optical Materials Express*, vol. 3, no. 11, p. 1872, 2013.

[159] B. S. Williams, "Terahertz quantum-cascade lasers," *Nature Photonics*, vol. 1, no. 9, pp. 517–525, 2007.

[160] J. Faist, F. Capasso, D. L. Sivco, C. Sirtori, A. L. Hutchinson *et al.*, "Quantum Cascade Laser," *Science*, vol. 264, no. 5158, pp. 553–556, 1994.

[161] W. W. Bewley, C. L. Canedy, C. S. Kim, M. Kim, C. D. Merritt *et al.*, "Continuous-wave interband cascade lasers operating above room temperature at $\lambda = 4.7$–5.6 μm," *Optics Express*, vol. 20, no. 3, p. 3235, 2012.

[162] A. Krier, E. Repiso, F. Al-Saymari, P. Carrington, A. Marshall *et al.*, *Mid-infrared light-emitting diodes*. Elsevier, 2019, pp. 59–90.

[163] J. Meyer, W. Bewley, C. Canedy, C. Kim, M. Kim *et al.*, "The Interband Cascade Laser," *Photonics*, vol. 7, no. 3, p. 75, 2020.

[164] S. D. Jackson, "Towards high-power mid-infrared emission from a fibre laser," *Nature Photonics*, vol. 6, no. 7, pp. 423–431, 2012.

[165] F. Vanier, F. Côté, M. E. Amraoui, Y. Messaddeq, Y.-A. Peter *et al.*, "Low-threshold lasing at 1975 nm in thulium-doped tellurite glass microspheres," *Optics Letters*, vol. 40, no. 22, p. 5227, 2015.

[166] S. B. Mirov, I. S. Moskalev, S. Vasilyev, V. Smolski, V. V. Fedorov *et al.*, "Frontiers of Mid-IR Lasers Based on Transition Metal Doped Chalcogenides," *IEEE Journal of Selected Topics in Quantum Electronics*, vol. 24, no. 5, pp. 1–29, 2018.

[167] K. L. Vodopyanov, "Mid-infrared optical parametric generator with extra-wide (3–19-μm) tunability: applications for spectroscopy of two-dimensional electrons in quantum wells," *Journal of the Optical Society of America B*, vol. 16, no. 9, p. 1579, 1999.

[168] A. Lemière, R. Bizot, F. Désévédavy, G. Gadret, J.-C. Jules *et al.*, "1.7-18 μm mid-infrared supercontinuum generation in a dispersion-engineered step-index chalcogenide fiber," *Results in Physics*, vol. 26, p. 104397, 2021.

[169] N. Picqué and T. W. Hänsch, "Frequency comb spectroscopy," *Nature Photonics*, vol. 13, no. 3, pp. 146–157, 2019.

[170] H. Abramczyk, *Introduction to Laser Spectroscopy*. Elsevier, 2005, ch. Lasers, pp. 59–106.

[171] A. Rogalski, "Infrared detectors: status and trends," *Progress in Quantum Electronics*, vol. 27, no. 2–3, pp. 59–210, 2003.

[172] A. Rogalski, "History of infrared detectors," *Opto-Electronics Review*, vol. 20, no. 3, pp. 279–308, 2012.

[173] C. L. Tan and H. Mohseni, "Emerging technologies for high performance infrared detectors," *Nanophotonics*, vol. 7, no. 1, pp. 169–197, 2017.

[174] M. Razeghi and B.-M. Nguyen, "Advances in mid-infrared detection and imaging: a key issues review," *Reports on Progress in Physics*, vol. 77, no. 8, p. 082401, 2014.

[175] T. Hu, B. Dong, X. Luo, T.-Y. Liow, J. Song *et al.*, "Silicon photonic platforms for mid-infrared applications [Invited]," *Photonics Research*, vol. 5, no. 5, p. 417, 2017.

[176] Y. Zou, S. Chakravarty, C.-J. Chung, X. Xu, and R. T. Chen, "Mid-infrared silicon photonic waveguides and devices [Invited]," *Photonics Research*, vol. 6, no. 4, p. 254, 2018.

[177] H. Lin, Z. Luo, T. Gu, L. C. Kimerling, K. Wada *et al.*, "Mid-infrared integrated photonics on silicon: a perspective," *Nanophotonics*, vol. 7, no. 2, pp. 393–420, 2018.

[178] L. Chrostowski and M. Hochberg, *Silicon photonics design: from devices to systems*. Cambridge University Press, 2015.

[179] S. A. Miller, M. Yu, X. Ji, A. G. Griffith, J. Cardenas *et al.*, "Low-loss silicon platform for broadband mid-infrared photonics," *Optica*, vol. 4, no. 7, p. 707, 2017.

[180] F. Li, S. D. Jackson, C. Grillet, E. Magi, D. Hudson *et al.*, "Low propagation loss silicon-on-sapphire waveguides for the mid-infrared," *Optics Express*, vol. 19, no. 16, p. 15212, 2011.

[181] S. Khan, J. Chiles, J. Ma, and S. Fathpour, "Silicon-on-nitride waveguides for mid- and near-infrared integrated photonics," *Applied Physics Letters*, vol. 102, no. 12, p. 121104, 2013.

[182] J. Soler Penadés, A. Ortega-Moñux, M. Nedeljkovic, J. G. Wangüemert-Pérez, R. Halir *et al.*, "Suspended silicon mid-infrared waveguide devices with subwavelength grating metamaterial cladding," *Optics Express*, vol. 24, no. 20, p. 22908, 2016.

[183] G. Z. Mashanovich, M. M. Milošević, M. Nedeljkovic, N. Owens, B. Xiong *et al.*, "Low loss silicon waveguides for the mid-infrared," *Optics Express*, vol. 19, no. 8, p. 7112, 2011.

[184] K. Luke, Y. Okawachi, M. R. E. Lamont, A. L. Gaeta, and M. Lipson, "Broadband mid-infrared frequency comb generation in a Si_3N_4 microresonator," *Optics Letters*, vol. 40, no. 21, p. 4823, 2015.

[185] M. Nedeljkovic, J. S. Penades, C. J. Mitchell, A. Z. Khokhar, S. Stankovic *et al.*, "Surface-Grating-Coupled Low-Loss Ge-on-Si Rib Waveguides and Multimode Interferometers," *IEEE Photonics Technology Letters*, vol. 27, no. 10, pp. 1040–1043, 2015.

[186] W. Li, P. Anantha, S. Bao, K. H. Lee, X. Guo *et al.*, "Germanium-on-silicon nitride waveguides for mid-infrared integrated photonics," *Applied Physics Letters*, vol. 109, no. 24, p. 241101, 2016.

[187] M. Brun, P. Labeye, G. Grand, J.-M. Hartmann, F. Boulila *et al.*, "Low loss SiGe graded index waveguides for mid-IR applications," *Optics Express*, vol. 22, no. 1, p. 508, 2014.

[188] A. Sánchez-Postigo, A. Ortega-Moñux, J. S. Penadés, A. Osman, M. Nedeljkovic *et al.*, "Suspended germanium waveguides with subwavelength-grating metamaterial cladding for the mid-infrared band," *Optics Express*, vol. 29, no. 11, p. 16867, 2021.

[189] R. A. Soref, S. J. Emelett, and W. R. Buchwald, "Silicon waveguided components for the long-wave infrared region," *Journal of Optics A: Pure and Applied Optics*, vol. 8, no. 10, pp. 840–848, 2006.

[190] R. Soref, "Mid-infrared photonics in silicon and germanium," *Nature Photonics*, vol. 4, no. 8, pp. 495–497, 2010.

[191] T. Baehr-Jones, A. Spott, R. Ilic, A. Spott, B. Penkov *et al.*, "Silicon-on-sapphire integrated waveguides for the mid-infrared," *Optics Express*, vol. 18, no. 12, p. 12127, 2010.

[192] J. Soler Penadés, A. Sánchez-Postigo, M. Nedeljkovic, A. Ortega-Moñux, J. G. Wangüemert-Pérez *et al.*, "Suspended silicon waveguides for long-wave infrared wavelengths," *Optics Letters*, vol. 43, no. 4, p. 795, 2018.

[193] Y.-C. Chang, V. Paeder, L. Hvozdara, J.-M. Hartmann, and H. P. Herzig, "Low-loss germanium strip waveguides on silicon for the mid-infrared," *Optics Letters*, vol. 37, no. 14, p. 2883, 2012.

[194] A. Malik, M. Muneeb, S. Pathak, Y. Shimura, J. V. Campenhout *et al.*, "Germanium-on-Silicon Mid-Infrared Arrayed Waveguide Grating Multiplexers," *IEEE Photonics Technology Letters*, vol. 25, no. 18, pp. 1805–1808, 2013.

[195] M. Nedeljkovic, J. S. Penades, V. Mittal, G. S. Murugan, A. Z. Khokhar *et al.*, "Germanium-on-silicon waveguides operating at mid-infrared wavelengths up to 8.5 μm," *Optics Express*, vol. 25, no. 22, p. 27431, 2017.

[196] D. A. Kozak, N. F. Tyndall, M. W. Pruessner, W. S. Rabinovich, and T. H. Stievater, "Germanium-on-silicon waveguides for long-wave integrated photonics: ring resonance and thermo-optics," *Optics Express*, vol. 29, no. 10, p. 15443, 2021.

[197] A. Malik, M. Muneeb, S. Radosavljevic, M. Nedeljkovic, J. S. Penades *et al.*, "Silicon-based Photonic Integrated Circuits for the Mid-infrared," *Procedia Engineering*, vol. 140, pp. 144–151, 2016.

[198] K. Gallacher, R. Millar, U. Griškevičiūte, L. Baldassarre, M. Sorel *et al.*, "Low loss Ge-on-Si waveguides operating in the 8–14 μm atmospheric transmission window," *Optics Express*, vol. 26, no. 20, p. 25667, 2018.

[199] J. Kang, M. Takenaka, and S. Takagi, "Novel Ge waveguide platform on Ge-on-insulator wafer for mid-infrared photonic integrated circuits," *Optics Express*, vol. 24, no. 11, p. 11855, 2016.

[200] S. Kim, J.-H. Han, J.-P. Shim, H.-j. Kim, and W. J. Choi, "Verification of Ge-on-insulator structure for a mid-infrared photonics platform," *Optical Materials Express*, vol. 8, no. 2, p. 440, 2018.

[201] M. Sinobad, A. DellaTorre, R. Armand, B. Luther-Davies, P. Ma *et al.*, "Mid-infrared supercontinuum generation in silicon-germanium all-normal dispersion waveguides," *Optics Letters*, vol. 45, no. 18, p. 5008, 2020.

[202] M. Montesinos-Ballester, C. Lafforgue, J. Frigerio, A. Ballabio, V. Vakarin *et al.*, "On-Chip Mid-Infrared Supercontinuum Generation from 3 to 13 μm Wavelength," *ACS Photonics*, vol. 7, no. 12, pp. 3423–3429, 2020.

[203] A. Osman, M. Nedeljkovic, J. S. Penades, Y. Wu, Z. Qu *et al.*, "Suspended low-loss germanium waveguides for the longwave infrared," *Optics Letters*, vol. 43, no. 24, p. 5997, 2018.

[204] T. S. Karnik, K. P. Dao, Q. Du, L. Diehl, C. Pflügl *et al.*, "High-efficiency mid-infrared InGaAs/InP arrayed waveguide gratings," *Optics Express*, vol. 31, no. 3, p. 5056, 2023.

[205] P. Ma, D.-Y. Choi, Y. Yu, Z. Yang, K. Vu *et al.*, "High Q factor chalcogenide ring resonators for cavity-enhanced MIR spectroscopic sensing," *Optics Express*, vol. 23, no. 15, p. 19969, 2015.

[206] V. Mittal, N. P. Sessions, J. S. Wilkinson, and G. S. Murugan, "Optical quality ZnSe films and low loss waveguides on Si substrates for mid-infrared applications," *Optical Materials Express*, vol. 7, no. 3, p. 712, 2017.

[207] W. Shen, P. Zeng, Z. Yang, D. Xia, J. Du *et al.*, "Chalcogenide glass photonic integration for improved 2 μm optical interconnection," *Photonics Research*, vol. 8, no. 9, p. 1484, 2020.

[208] A. Yadav and A. M. Agarwal, "Integrated photonic materials for the mid-infrared," *International Journal of Applied Glass Science*, vol. 11, no. 3, pp. 491–510, 2020.

[209] S. Jung, D. Palaferri, K. Zhang, F. Xie, Y. Okuno *et al.*, "Homogeneous photonic integration of mid-infrared quantum cascade lasers with low-loss passive waveguides on an InP platform," *Optica*, vol. 6, no. 8, p. 1023, 2019.

[210] A. Remis, L. Monge-Bartolome, M. Paparella, A. Gilbert, G. Boissier *et al.*, "Unlocking the monolithic integration scenario: optical coupling between GaSb diode lasers epitaxially grown on patterned Si substrates and passive SiN waveguides," *Light: Science & Applications*, vol. 12, no. 1, p. 150, 2023.

[211] H. Stanchu, G. Abernathy, J. Grant, F. M. de Oliveira, Y. I. Mazur *et al.*, "Development of aspect ratio trapping growth of gesn on si for midwave infrared applications," *Journal of Vacuum Science & Technology B*, vol. 42, no. 4, p. 042802, 2024.

[212] N. Hattasan, A. Gassenq, L. Cerutti, J.-B. Rodriguez, E. Tournie *et al.*, "Heterogeneous Integration of GaInAsSb p-i-n Photodiodes on a Silicon-on-Insulator Waveguide Circuit," *IEEE Photonics Technology Letters*, vol. 23, no. 23, pp. 1760–1762, 2011.

[213] A. Gassenq, N. Hattasan, L. Cerutti, J. B. Rodriguez, E. Tournié *et al.*, "Study of evanescently-coupled and grating-assisted GaInAsSb photodiodes integrated on a silicon photonic chip," *Optics Express*, vol. 20, no. 11, p. 11665, 2012.

[214] R. Wang, M. Muneeb, S. Sprengel, G. Boehm, A. Malik *et al.*, "III-V-on-silicon 2-μm-wavelength-range wavelength demultiplexers with heterogeneously integrated InP-based type-II photodetectors," *Optics Express*, vol. 24, no. 8, p. 8480, 2016.

[215] A. Spott, E. J. Stanton, N. Volet, J. D. Peters, J. R. Meyer *et al.*, "Heterogeneous Integration for Mid-infrared Silicon Photonics," *IEEE Journal of Selected Topics in Quantum Electronics*, vol. 23, no. 6, pp. 1–10, 2017.

[216] R. Wang, B. Haq, S. Sprengel, A. Malik, A. Vasiliev *et al.*, "Widely Tunable III–V/Silicon Lasers for Spectroscopy in the Short-Wave Infrared," *IEEE Journal of Selected Topics in Quantum Electronics*, vol. 25, no. 6, pp. 1–12, 2019.

[217] N. Hattasan, A. Gassenq, L. Cerutti, J. B. Rodriguez, E. Tournié *et al.*, "GaSb-based integrated lasers and photodetectors on a Silicon-On-Insulator waveguide circuit for sensing applications in the shortwave infrared," in *2012 Photonics Global Conference (PGC)*. IEEE, 2012.

[218] J. Brouckaert, G. Roelkens, D. Van Thourhout, and R. Baets, "Thin-Film III–V Photodetectors Integrated on Silicon-on-Insulator Photonic ICs," *Journal of Lightwave Technology*, vol. 25, no. 4, pp. 1053–1060, 2007.

[219] M. L. Davenport, S. Liu, and J. E. Bowers, "Integrated heterogeneous silicon/III–V mode-locked lasers," *Photonics Research*, vol. 6, no. 5, p. 468, 2018.

[220] G. Roelkens, J. Zhang, L. Bogaert, M. Billet, D. Wang *et al.*, "Micro-Transfer Printing for Heterogeneous Si Photonic Integrated Circuits," *IEEE Journal of Selected Topics in Quantum Electronics*, vol. 29, no. 3: Photon. Elec. Co-Inte. and Ad, pp. 1–14, 2023.

[221] A. De Groote, P. Cardile, A. Z. Subramanian, A. M. Fecioru, C. Bower *et al.*, "Transfer-printing-based integration of single-mode waveguide-coupled III-V-on-silicon broadband light emitters," *Optics Express*, vol. 24, no. 13, p. 13754, 2016.

[222] J. Zhang, G. Muliuk, J. Juvert, S. Kumari, J. Goyvaerts *et al.*, "III-V-on-Si photonic integrated circuits realized using micro-transfer-printing," *APL Photonics*, vol. 4, no. 11, p. 110803, 2019.

[223] B. Haq, J. R. Vaskasi, J. Zhang, A. Gocalinska, E. Pelucchi *et al.*, "Micro-transfer-printed III-V-on-silicon C-band distributed feedback lasers," *Optics Express*, vol. 28, no. 22, p. 32793, 2020.

[224] M. Billet, L. Reis, Y. Léger, C. Cornet, F. Raineri *et al.*, "Gallium phosphide-on-insulator integrated photonic structures fabricated using micro-transfer printing," *Optical Materials Express*, vol. 12, no. 9, p. 3731, 2022.

[225] S. Xu, K. Han, Y.-C. Huang, K. H. Lee, Y. Kang *et al.*, "Integrating GeSn photodiode on a 200 mm Ge-on-insulator photonics platform with Ge CMOS devices for advanced OEIC operating at 2 μm band," *Optics Express*, vol. 27, no. 19, p. 26924, 2019.

[226] R. Wang, A. Vasiliev, M. Muneeb, A. Malik, S. Sprengel *et al.*, "III-V-on-Silicon Photonic Integrated Circuits for Spectroscopic Sensing in the 2–4 μm Wavelength Range," *Sensors*, vol. 17, no. 8, p. 1788, 2017.

[227] Y.-C. Chang, P. Wägli, V. Paeder, A. Homsy, L. Hvozdara *et al.*, "Cocaine detection by a mid-infrared waveguide integrated with a microfluidic chip," *Lab on a Chip*, vol. 12, no. 17, p. 3020, 2012.

[228] Z. Han, P. Lin, V. Singh, L. Kimerling, J. Hu *et al.*, "On-chip mid-infrared gas detection using chalcogenide glass waveguide," *Applied Physics Letters*, vol. 108, no. 14, p. 141106, 2016.

[229] H. D. Yallew, M. Vlk, A. Datta, S. Alberti, R. A. Zakoldaev *et al.*, "Sub-ppm Methane Detection with Mid-Infrared Slot Waveguides," *ACS Photonics*, vol. 10, no. 12, pp. 4282–4289, 2023.

[230] J. Lim, J. Shim, I. Kim, S. K. Kim, H. Lim *et al.*, "Ultrasensitive Mid-Infrared Optical Gas Sensor Based on Germanium-on-Insulator Photonic Circuits with Limit-of-Detection at Sub-ppm Level," *ACS Photonics*, vol. 11, pp. 4268–4278, 2024.

[231] M. Muneeb, X. Chen, P. Verheyen, G. Lepage, S. Pathak *et al.*, "Demonstration of Silicon-on-insulator mid-infrared spectrometers operating at 3.8 μm," *Optics Express*, vol. 21, no. 10, p. 11659, 2013.

[232] M. Muneeb, A. Vasiliev, A. Ruocco, A. Malik, H. Chen *et al.*, "III-V-on-silicon integrated micro - spectrometer for the 3 μm wavelength range," *Optics Express*, vol. 24, no. 9, p. 9465, 2016.

[233] A. Malik, M. Muneeb, Y. Shimura, J. V. Campenhout, R. Loo *et al.*, "Germanium-on-silicon planar concave grating wavelength (de)multiplexers in the mid-infrared," *Applied Physics Letters*, vol. 103, no. 16, p. 161119, 2013.

[234] C. J. Mitchell, T. Hu, S. Sun, C. J. Stirling, M. Nedeljkovic *et al.*, "Mid-infrared silicon photonics: From benchtop to real-world applications," *APL Photonics*, vol. 9, no. 8, p. 080901, 2024.

[235] W. Cao, D. Hagan, D. J. Thomson, M. Nedeljkovic, C. G. Littlejohns *et al.*, "High-speed silicon modulators for the 2 μm wavelength band," *Optica*, vol. 5, no. 9, p. 1055, 2018.

[236] J. Midkiff, K. M. Yoo, J.-D. Shin, H. Dalir, M. Teimourpour *et al.*, "Optical phased array beam steering in the mid-infrared on an InP-based platform," *Optica*, vol. 7, no. 11, p. 1544, 2020.

[237] J. Hartmann and T. Marion, "Impact of flows, temperature and pressure on the GeSn growth kinetics with a digermane and tin tetrachloride chemistry," *Materials Science in Semiconductor Processing*, vol. 169, p. 107893, 2024.

[238] É. Bouthillier, "Non-Equilibrium Germanium-Tin Microstructures for Silicon-compatible Mid-infrared Photonics," Master's thesis, Polytechnique Montréal, 2019.

[239] É. Bouthillier, S. Assali, J. Nicolas, and O. Moutanabbir, "Decoupling the effects of composition and strain on the vibrational modes of GeSn semiconductors," *Semiconductor Science and Technology*, vol. 35, no. 9, p. 095006, 2020.

[240] M. J. Madou, *Manufacturing Techniques for Microfabrication and Nanotechnology*. CRC Press, 2011, vol. 2.

[241] M. D. Henry, "ICP etching of silicon: for micro and nanoscale devices," Ph.D. dissertation, California Institute of Technology, 2010.

[242] M. A. Meitl, Z.-T. Zhu, V. Kumar, K. J. Lee, X. Feng *et al.*, "Transfer printing by kinetic control of adhesion to an elastomeric stamp," *Nature Materials*, vol. 5, no. 1, pp. 33–38, 2005.

[243] E. Menard, R. G. Nuzzo, and J. A. Rogers, "Bendable single crystal silicon thin film transistors formed by printing on plastic substrates," *Applied Physics Letters*, vol. 86, no. 9, p. 093507, 2005.

[244] J. A. Rogers, M. G. Lagally, and R. G. Nuzzo, "Synthesis, assembly and applications of semiconductor nanomembranes," *Nature*, vol. 477, no. 7362, pp. 45–53, 2011.

[245] J. Yoon, S. Lee, D. Kang, M. A. Meitl, C. A. Bower *et al.*, "Heterogeneously Integrated Optoelectronic Devices Enabled by Micro-Transfer Printing," *Advanced Optical Materials*, vol. 3, no. 10, pp. 1313–1335, 2015.

[246] C. Linghu, S. Zhang, C. Wang, and J. Song, "Transfer printing techniques for flexible and stretchable inorganic electronics," *npj Flexible Electronics*, vol. 2, no. 1, p. 26, 2018.

[247] X. Feng, M. A. Meitl, A. M. Bowen, Y. Huang, R. G. Nuzzo *et al.*, "Competing fracture in kinetically controlled transfer printing," *Langmuir*, vol. 23, no. 25, pp. 12 555–12 560, Nov. 2007.

[248] J. Justice, C. Bower, M. Meitl, M. B. Mooney, M. A. Gubbins *et al.*, "Wafer-scale integration of group III–V lasers on silicon using transfer printing of epitaxial layers," *Nature Photonics*, vol. 6, no. 9, pp. 610–614, 2012.

[249] J. Nicolas, "Ingénierie de contrainte et stabilité des hétérostructures de GeSn," Ph.D. dissertation, Polytechnique Montréal, 2022.

[250] J.-H. Fournier-Lupien, S. Mukherjee, S. Wirths, E. Pippel, N. Hayazawa *et al.*, "Strain and composition effects on Raman vibrational modes of silicon-germanium-tin ternary alloys," *Applied Physics Letters*, vol. 103, no. 26, p. 263103, 2013.

[251] nanoScience Instruments. (2024) What is scanning electron microscopy? [Online]. Available: https://www.nanoscience.com/techniques/scanning-electron-microscopy/

[252] T. B. Bahder, "Eight-band $k \cdot p$ model of strained zinc-blende crystals," *Physical Review B*, vol. 41, no. 17, pp. 11 992–12 001, 1990.

[253] G. Daligou, A. Attiaoui, S. Assali, P. Del Vecchio, and O. Moutanabbir, "Radiative carrier lifetime in $Ge_{1-x}Sn_x$ midinfrared emitters," *Physical Review Applied*, vol. 20, no. 6, p. 064001, 2023.

[254] P. Del Vecchio and O. Moutanabbir, "Light-hole spin confined in germanium," *Physical Review B*, vol. 110, no. 4, p. 045409, 2024.

[255] S. Assali, A. Dijkstra, A. Attiaoui, É. Bouthillier, J. Haverkort *et al.*, "Midinfrared Emission and Absorption in Strained and Relaxed Direct-Band-Gap $Ge_{1-x}Sn_x$ Semiconductors," *Physical Review Applied*, vol. 15, no. 2, p. 024031, 2021.

[256] D. Popa and F. Udrea, "Towards integrated mid-infrared gas sensors," *Sensors*, vol. 19, no. 9, p. 2076, 2019.

[257] Y. Alimi, V. Pusino, M. J. Steer, and D. R. S. Cumming, "InSb Avalanche Photodiodes on GaAs Substrates for Mid-Infrared Detection," *IEEE Transactions on Electron Devices*, vol. 67, no. 1, pp. 179–184, 2020.

[258] R. Müller, M. Haertelt, J. Niemasz, K. Schwarz, V. Daumer *et al.*, "Thermoelectrically-Cooled InAs/GaSb Type-II Superlattice Detectors as an Alternative to HgCdTe in a Real-Time Mid-Infrared Backscattering Spectroscopy System," *Micromachines*, vol. 11, no. 12, p. 1124, 2020.

[259] D. O. Alshahrani, M. Kesaria, E. A. Anyebe, V. Srivastava, and D. L. Huffaker, "Emerging Type-II Superlattices of InAs/InAsSb and InAs/GaSb for Mid-Wavelength Infrared Photodetectors," *Advanced Photonics Research*, vol. 3, no. 2, 2021.

[260] A. Rogalski, "7 - HgCdTe photodetectors," in *Mid-infrared Optoelectronics*, ser. Woodhead Publishing Series in Electronic and Optical Materials, E. Tournié and L. Cerutti, Eds. Woodhead Publishing, 2020, pp. 235–335.

[261] F. Li, J. Deng, J. Zhou, Z. Chu, Y. Yu *et al.*, "HgCdTe mid-Infrared photo response enhanced by monolithically integrated meta-lenses," *Scientific Reports*, vol. 10, no. 1, p. 6372, 2020.

[262] V. Pusino, C. Xie, A. Khalid, M. J. Steer, M. Sorel *et al.*, "InSb Photodiodes for Monolithic Active Focal Plane Arrays on GaAs Substrates," *IEEE Transactions on Electron Devices*, vol. 63, no. 8, pp. 3135–3142, 2016.

[263] W. Lei, J. Antoszewski, and L. Faraone, "Progress, challenges, and opportunities for HgCdTe infrared materials and detectors," *Applied Physics Reviews*, vol. 2, no. 4, p. 041303, 2015.

[264] X. Liu, J. Zheng, C. Niu, T. Liu, Q. Huang *et al.*, "Sn content gradient GeSn with strain controlled for high performance GeSn mid-infrared photodetectors," *Photonics Research*, vol. 10, no. 7, p. 1567, 2022.

[265] C.-Y. Chang, P.-L. Yeh, Y.-T. Jheng, L.-Y. Hsu, K.-C. Lee *et al.*, "Mid-infrared resonant light emission from GeSn resonant-cavity surface-emitting LEDs with a lateral p-i-n structure," *Photonics Research*, vol. 10, no. 10, p. 2278, 2022.

[266] Y. Kim, S. Assali, D. Burt, Y. Jung, H. Joo *et al.*, "Enhanced GeSn Microdisk Lasers Directly Released on Si," *Advanced Optical Materials*, vol. 10, no. 2, p. 2101213, 2022.

[267] S. Assali, J. Nicolas, and O. Moutanabbir, "Enhanced Sn incorporation in GeSn epitaxial semiconductors via strain relaxation," *Journal of Applied Physics*, vol. 125, no. 2, p. 025304, 2019.

[268] S. An, S. Wu, C. S. Tan, G.-E. Chang, X. Gong *et al.*, "Modulation of light absorption in flexible GeSn metal–semiconductor–metal photodetectors by mechanical bending," *Journal of Materials Chemistry C*, vol. 8, no. 39, pp. 13 557–13 562, 2020.

[269] S. An, Y. Liao, and M. Kim, "Flexible Titanium Nitride/Germanium-Tin Photodetectors Based on Sub-Bandgap Absorption," *ACS Applied Materials & Interfaces*, vol. 13, no. 51, pp. 61 396–61 403, 2021.

[270] Q. Chen, S. Wu, L. Zhang, H. Zhou, W. Fan *et al.*, "Transferable single-layer GeSn nanomembrane resonant-cavity-enhanced photodetectors for 2 μm band optical communication and multi-spectral short-wave infrared sensing," *Nanoscale*, vol. 14, no. 19, pp. 7341–7349, 2022.

[271] M. A. Nawwar, M. S. Abo Ghazala, L. M. Sharaf El-Deen, and A. E.-h. B. Kashyout, "Impact of strain engineering and Sn content on GeSn heterostructured nanomaterials for nanoelectronics and photonic devices," *RSC Advances*, vol. 12, no. 38, pp. 24 518–24 554, 2022.

[272] W. Dou, M. Benamara, A. Mosleh, J. Margetis, P. Grant *et al.*, "Investigation of GeSn Strain Relaxation and Spontaneous Composition Gradient for Low-Defect and High-Sn Alloy Growth," *Scientific Reports*, vol. 8, no. 1, p. 5640, 2018.

[273] S. An, H. Park, and M. Kim, "Recent advances in single crystal narrow band-gap semiconductor nanomembranes and their flexible optoelectronic device applications: Ge, GeSn, InGaAs, and 2D materials," *Journal of Materials Chemistry C*, vol. 11, no. 7, pp. 2430–2448, 2023.

[274] H.-C. Yuan, G. Wang, Z. Ma, M. M. Roberts, D. E. Savage *et al.*, "Flexible thin-film transistors on biaxial- and uniaxial-strained Si and SiGe membranes," *Semiconductor Science and Technology*, vol. 22, no. 1, pp. S72–S75, 2006.

[275] D. Nam, D. Sukhdeo, A. Roy, K. Balram, S.-L. Cheng *et al.*, "Strained germanium thin film membrane on silicon substrate for optoelectronics," *Optics Express*, vol. 19, no. 27, p. 25866, 2011.

[276] S.-C. Liu, D. Zhao, Y. Liu, H. Yang, Y. Sun *et al.*, "Photonic crystal bandedge membrane lasers on silicon," *Applied Optics*, vol. 56, no. 31, p. H67, 2017.

[277] M. Zamiri, F. Anwar, B. A. Klein, A. Rasoulof, N. M. Dawson *et al.*, "Antimonide-based membranes synthesis integration and strain engineering," *Proceedings of the National Academy of Sciences*, vol. 114, no. 1, pp. E1–E8, 2016.

[278] W. Pan, Z. Zhang, R. Gu, S. Ma, L. Faraone *et al.*, "Van der Waals Epitaxy of HgCdTe Thin Films for Flexible Infrared Optoelectronics," *Advanced Materials Interfaces*, vol. 10, no. 4, p. 2201932, 2022.

[279] Y.-C. Tai, P.-L. Yeh, S. An, H.-H. Cheng, M. Kim *et al.*, "Strain-free GeSn nanomembranes enabled by transfer-printing techniques for advanced optoelectronic applications," *Nanotechnology*, vol. 31, no. 44, p. 445301, 2020.

[280] Y. Liu, J. Guo, E. Zhu, L. Liao, S.-J. Lee *et al.*, "Approaching the Schottky–Mott limit in van der Waals metal–semiconductor junctions," *Nature*, vol. 557, no. 7707, pp. 696–700, 2018.

[281] S. Gupta, R. Chen, Y.-C. Huang, Y. Kim, E. Sanchez *et al.*, "Highly Selective Dry Etching of Germanium over Germanium–Tin ($Ge_{1-x}Sn_x$): A Novel Route for $Ge_{1-x}Sn_x$ Nanostructure Fabrication," *Nano Letters*, vol. 13, no. 8, pp. 3783–3790, 2013.

[282] J.-R. Wu, Y.-H. Wu, C.-Y. Hou, M.-L. Wu, C.-C. Lin *et al.*, "Impact of fluorine treatment on Fermi level depinning for metal/germanium Schottky junctions," *Applied Physics Letters*, vol. 99, no. 25, p. 253504, 2011.

[283] H. Keum, H.-J. Chung, and S. Kim, "Electrical Contact at the Interface between Silicon and Transfer-Printed Gold Films by Eutectic Joining," *ACS Applied Materials & Interfaces*, vol. 5, no. 13, pp. 6061–6065, 2013.

[284] D. Van Thourhout, G. Roelkens, R. Baets, W. Bogaerts, J. Brouckaert *et al.*, "Coupling mechanisms for a heterogeneous silicon nanowire platform," *Semiconductor Science and Technology*, vol. 23, no. 6, p. 064004, 2008.

[285] H. Tran, W. Du, S. A. Ghetmiri, A. Mosleh, G. Sun *et al.*, "Systematic study of $Ge_{1-x}Sn_x$ absorption coefficient and refractive index for the device applications of Si-based optoelectronics," *Journal of Applied Physics*, vol. 119, no. 10, p. 103106, 2016.

[286] E. D. Palik, *Handbook of Optical Constants of Solids*. Academic Press, 1985.

[287] R. Kitamura, L. Pilon, and M. Jonasz, "Optical constants of silica glass from extreme ultraviolet to far infrared at near room temperature," *Applied Optics*, vol. 46, no. 33, p. 8118, 2007.

[288] J. Lacey and F. Payne, "Radiation loss from planar waveguides with random wall imperfections," *IEE Proceedings J Optoelectronics*, vol. 137, no. 4, p. 282, 1990.

[289] S. Pogossian, L. Vescan, and A. Vonsovici, "The single-mode condition for semiconductor rib waveguides with large cross section," *Journal of Lightwave Technology*, vol. 16, no. 10, pp. 1851–1853, 1998.

[290] B. E. A. Saleh and M. C. Teich, *Fundamentals of Photonics*. John Wiley & Sons, 2019.

[291] S. L. Chuang, *Physics of photonic devices*. John Wiley & Sons, 2009.

[292] A. W. Snyder and J. Love, *Optical Waveguide Theory*. Springer, 1983.

[293] D. Ahn, L. C. Kimerling, and J. Michel, "Evanescent Coupling Device Design for Waveguide-Integrated Group IV Photodetectors," *Journal of Lightwave Technology*, vol. 28, no. 23, pp. 3387–3394, 2010.

[294] J. Brouckaert, "Integration of Photodetectors on Silicon Photonic Integrated Circuits (PICs) for Spectroscopic Applications," Ph.D. dissertation, Universiteit Gent, 2010.

[295] H. Muthuganesan, E. Mura, S. Chugh, C. Antony, E. Pelucchi *et al.*, "100 Gbps PAM4 ultra-thin photodetectors integrated on SOI platform by micro transfer printing," *Optics Express*, vol. 31, no. 22, p. 36273, 2023.

[296] D. Burt, H.-J. Joo, Y. Jung, Y. Kim, M. Chen *et al.*, "Strain-relaxed GeSn-on-insulator (GeSnOI) microdisks," *Optics Express*, vol. 29, no. 18, p. 28959, 2021.

[297] A. Malik, A. Spott, E. J. Stanton, J. D. Peters, J. D. Kirch *et al.*, "Integration of Mid-Infrared Light Sources on Silicon-Based Waveguide Platforms in 3.5–4.7 μm Wavelength Range," *IEEE Journal of Selected Topics in Quantum Electronics*, vol. 25, no. 6, p. 1502809, 2019.

[298] W. M. Haynes, *CRC Handbook of Chemistry and Physics*, W. M. Haynes, Ed. CRC Press, 2016.

[299] L. Guerin, M. Bossel, M. Demierre, S. Calmes, and P. Renaud, "Simple and low cost fabrication of embedded micro-channels by using a new thick-film photoplastic," in *Proceedings of International Solid State Sensors and Actuators Conference (Transducers '97)*, ser. SENSOR-97, vol. 2. IEEE, 1997, pp. 1419–1422.

[300] C. Wang, "8 - Laser-assisted polymer joining methods for photonic devices," in *Laser Growth and Processing of Photonic Devices*, W. Publishing, Ed. Woodhead Publishing, 2012, ch. 8 – Laser-assisted polymer joining methods for photonic devices, pp. 269–284.

[301] C.-H. Tsai, K.-C. Lin, C.-Y. Cheng, K.-C. Lee, H. H. Cheng *et al.*, "GeSn lateral p-i-n waveguide photodetectors for mid-infrared integrated photonics," *Optics Letters*, vol. 46, no. 4, p. 864, 2021.

[302] R. Mao, C. Li, Y. Zuo, B. Cheng, X. Teng *et al.*, "Fabrication of 1.55-μm Si-Based Resonant Cavity Enhanced Photodetectors Using Sol-Gel Bonding," *IEEE Photonics Technology Letters*, vol. 16, no. 8, pp. 1930–1932, 2004.

[303] J. Soole and H. Schumacher, "InGaAs metal-semiconductor-metal photodetectors for long wavelength optical communications," *IEEE Journal of Quantum Electronics*, vol. 27, no. 3, pp. 737–752, 1991.

[304] A. Spott, M. Davenport, J. Peters, J. Bovington, M. J. R. Heck *et al.*, "Heterogeneously integrated 2.0 μm CW hybrid silicon lasers at room temperature," *Optics Letters*, vol. 40, no. 7, p. 1480, 2015.

[305] A. Spott, J. Peters, M. L. Davenport, E. J. Stanton, C. D. Merritt *et al.*, "Quantum cascade laser on silicon," *Optica*, vol. 3, no. 5, p. 545, 2016.

[306] A. Spott, E. J. Stanton, A. Torres, M. L. Davenport, C. L. Canedy *et al.*, "Interband cascade laser on silicon," *Optica*, vol. 5, no. 8, p. 996, 2018.

[307] S. Jung, J. Kirch, J. H. Kim, L. J. Mawst, D. Botez *et al.*, "Quantum cascade lasers transfer-printed on silicon-on-sapphire," *Applied Physics Letters*, vol. 111, no. 21, p. 211102, 2017.

[308] B. Marzban, J. Nojic, D. Stange, D. Buca, and J. Witzens, "Design of a waveguide-coupled GeSn disk laser," in *2020 IEEE Photonics Society Summer Topicals Meeting Series (SUM)*. IEEE, 2020, pp. 1–2.

APPENDIX A THIN FILM PROCESSING TECHNIQUES ADAPTED FOR GERMANIUM-TIN

Introduction

Etching GeSn thin films requires chemistries that ensure uniform etch depths and reproducible sidewall angles for reliable device fabrication. Etching requirements vary by structure type and include factors like surface roughness, etch rate, selectivity, and sidewall profile. For photonic structures, achieving very low surface roughness and vertical sidewall profiles is essential to minimize scattering losses and ensure effective light confinement, which are critical for maintaining high efficiency and signal integrity. A slow and predictable etch rate is also preferable for achieving precise etch depths, which is particularly important for optoelectronic devices. While etching chemistries for Ge are well-established and often serve as a starting point for initial etching experiments, the inclusion of Sn in GeSn compounds introduces complexities. Specifically, the inclusion of Sn modifies etching selectivity by introducing non-volatile byproducts that alter surface chemistry, complicating process optimization. Although some studies have investigated GeSn etching, the existing literature provides limited insights into the general trends and underlying mechanisms.

This appendix provides a comprehensive analysis of dry and wet etching techniques for GeSn, detailing their mechanisms, observed etch rates, and selectivity across different compounds. It also presents fabrication results from this research, offering insights into optimizing GeSn processing. All fabrication experiments were conducted at the Laboratoire de Microfabrication (LMF) at Polytechnique Montréal and the Laboratoire de Micro et Nanofabrication (LMN) at the Institut National de la Recherche Scientifique (INRS).

Dry etching

ICP-RIE is preferred for dry etching because it allows independent optimization of plasma density and ion acceleration, providing greater process flexibility. Independent control of plasma density enables precise adjustment of chemical etching rates, while control over ion acceleration allows for fine-tuning of physical etching effects, such as sidewall profiles and anisotropy. This enables high-quality etching in complex structures. High anisotropy and low surface roughness can be achieved through careful optimization of plasma etching parameters, including RF power, gas flow rates, chamber pressure, and bias voltage. Smooth etching profiles are essential for minimizing scattering losses, while precise verticality control directly

impacts the effective refractive indices and dispersion in waveguides. Additionally, minimizing surface roughness and defects is critical to preventing degradation in electrical performance, as such defects can act as non-radiative recombination centers or increase surface state density, leading to elevated dark current. This section reviews the primary chemistries used in the dry etching of GeSn, focusing on the etching mechanisms and corresponding fabrication results. Fluorine- and chlorine-based plasma etching recipes were evaluated to identify optimal parameters. ICP-RIE (Plasmalab 100, Oxford Instruments) was utilized at both the LMF and LMN facilities, with chlorine-based etching specifically performed at LMN. Several of these dry etching recipes were successfully adapted for the fabrication of various GeSn-based devices, including transferable membranes [A1], LEDs [A2], and photodetectors [A3, A4].

Several dry etching recipes reported in the literature were evaluated in this work, as summarized in Table A.1, along with their respective etch rates. The recipes primarily originated from CEA-Leti, Forschungszentrum Jülich (FZJ), and the University of Delaware (UDel). É. Bouthillier, a former master's student in the group, initially investigated GeSn processing, and his data served as a foundation for further optimization [A5]. For the etching tests performed in this work, Ge and GeSn samples were patterned with waveguide designs. After photoresist stripping, the samples were cleaved, and their cross-sections were examined using SEM to evaluate the quality of the etched features. Most initial tests were conducted on Ge to refine the etching parameters before applying the process to GeSn thin films, which were limited in supply and share similar etching characteristics with Ge. In the literature, Ge is typically etched using fluorine- or chlorine-based chemistries, which rely on both chemical and physical etching mechanisms. Conventional chemistries were thus initially tested for GeSn etching by various research groups. However, with fluoride-based chemistries such as SF_6 and CF_4, significant differences in etch rates were observed due to the formation of non-volatile tin fluoride species, such as SnF_2 and SnF_4. These species form a non-volatile passivation layer that affects etching selectivity between Ge and GeSn [A6]. For instance, RIE using SF_6 or CF_4 results in rough surfaces and variable etch rates depending on the Sn content [A7]. In tests conducted using recipe **F2**, Ge etched at an approximate rate of 473 nm/min, whereas GeSn (with 10 at.% Sn) exhibited a significantly lower etch rate of 74 nm/min due to the accumulation of these non-volatile species. Etching through the passivation layer is still possible due to the ion bombardment component of the process, especially with the addition of Ar in the plasma. By reducing ion acceleration, selective isotropic etching of Ge relative to GeSn using CF_4 becomes achievable for specific Sn contents, enabling the fabrication of underetched structures, such as microdisks and membranes.

Table A.1 Dry etching recipes with reported etch rates and selectivities using chlorine- and fluorine-based chemistries. Various Sn contents were used for the GeSn samples (PL 100: Plasmalab 100 from Oxford Instruments).

	Recipe name	Instrument	Parameters					Etch rate (nm/min)		Ge/GeSn selectivity	Reference
			Gas : Gas flow (sccm)	P (mTorr)	T (°C)	RF (W)	ICP (W)	Ge	GeSn		
Chlorine-based	**C1**	PL 100 (CEA-Leti)	$Cl_2/N_2/O_2$: 100/25/10	10	-	100	200	340[a]	340[a]	-	[A8]
	C2	PL 100 (LMN)	$Cl_2/N_2/O_2$: 40/10/4	10	30	100	200*	200*	200	-	[A5] (adapted from [A8])
	C3	PL 100 (CEA-Leti)	$Cl_2/N_2/O_2$: 18/13/5	10	-	50	50	90 - 204[b]	90 - 204[b]	-	[A9] (adapted from [A8])
	C4	PL 100 (LMN)	$Cl_2/N_2/O_2$: 20/12/2	10	20	75	125	205	170 - 224[c]	0.91 - 1.08	This work
	C5	PL 100 (FZJ)	Cl_2/Ar : 8/20	4	-	100	1000	1044	960 - 1026[d]	1.02 - 1.09	[A10]
	C6	PL 100 (LMN)	Cl_2/Ar : 8/20	4	20	100	1000	382	408[e]	0.94	This work (adapted from [A10])
	C7	PL 100 (LMN)	Cl_2/Ar : 8/20	10	20	100	200	126	228	0.55	This work (adapted from [A10])
	C8	Plasma-Therm Apex SLR (UDel)	$Cl_2/Ar/O_2$: 100/25/10	10	-	100	200	67.5[f]	67.5[f]	-	[A11]
Fluorine-based	**F1**	PL 100 (LMF)	SF_6 : 100	30	20	0	500	>2400	-	-	This work
	F2	PL 100 (LMF)	SF_6/Ar : 4/40	10	20	50	200	473	74[g]	6.4	This work
	F3	PL 100 (FZJ)	SF_6/Ar : 100/8	15	-	100	0	1932	102 - 408[h]	4.7 - 18.9	[A10]
	F4	Tepla Gigabatch (LMF)	CF_4 : 200	600	-	-	200	2000	-	-	This work
	F5	Plasmalab 100 (LMF)	CF_4 : 50	50	20	0	300	1000	-	-	This work
	F6	Tepla Gigabatch (FZJ)	CF_4 : 40	100	-	0	35	156	0.4 - 40[i]	3.9 - 390	[A10]
	F7	Plasma-Therm Apex SLR (UDel)	CF_4 : 100	100	-	0	500	151	-	-	[A11]

[a] The reported etch rate includes GeSn and Ge. The selectivity cannot be assessed. The Sn content in the GeSn layer is 10 at.% Sn.
[b] Etch rates were reported for GeSn 6 at.% Sn (204 nm/min) and 10% (90 nm/min), but they included the etch depth of Ge. The selectivity cannot be assessed.
[c] Multiple GeSn samples were etched with contents up to 13 at.% Sn, with some heavily doped samples would provide an etch rate within this range.
[d] GeSn 5.5 at.% Sn: 1026 nm/min, GeSn 8.5 at.% Sn: 1026 nm/min, GeSn 12.5 at.% Sn: 960 nm/min.
[e] GeSn content: $\sim$ 10 at.% Sn.
[f] The reported etch rate includes GeSn and Ge. The selectivity cannot be assessed. The Sn content in the GeSn layer is 12.5 at.% Sn.
[g] GeSn content: $\sim$ 9 at.% Sn.
[h] GeSn 5.5 at.% Sn: 408 nm/min, GeSn 8. at.% Sn: 246 nm/min, GeSn 12.5 at.% Sn: 102 nm/min.
[i] GeSn 5.5 at.% Sn: 40 nm/min, GeSn 8.5 at.% Sn: 20 nm/min, GeSn 12.5 at.% Sn: 0.4 nm/min.

Cl_2-based plasmas, by contrast, typically provide non-selective etching of both Ge and GeSn, regardless of the Sn content in the GeSn alloy. These chemistries have been extensively studied for GeSn etching due to their ability to form volatile species with both Ge and Sn [A8, A9, A11]. Milord *et al.* developed a recipe based on $Cl_2/O_2/N_2$ (Recipe **C1**) to achieve smooth and vertical sidewalls during the etching of Ge and GeSn. The inclusion of O_2 was found to enhance the aspect ratio by passivating the sidewalls. However, the addition of O_2 also increases the etch rate of organic masking layers, such as photoresists, thereby reducing selectivity with Ge and GeSn. Cl_2/Ar-based chemistries are another option commonly employed for Ge and GeSn etching. C. Schulte-Braucks, for instance, used a Cl_2/Ar recipe to fabricate devices, achieving an etch rate of approximately 1 μm/min for both Ge and GeSn. This was accomplished by applying a high RF power (100 W) combined with a high plasma density (ICP power = 1000 W) (Recipe **C5**) [A10].

Figures A.1(a), A.1(b), and A.1(c) present SEM micrographs of cross-sections of etched Ge and GeSn structures using chlorine-based recipes **C4**, **C6** and **C7** respectively, highlighting the variation in the sidewall etching profiles. Recipe **C6**, an adaptation of Recipe **C5**, exhibited a significantly lower etch rate compared to that reported by C. Schulte-Braucks in his thesis (approximately 400 nm/min versus 1000 nm/min) [A10]. This discrepancy underscores that optimal etching parameters can vary between tools, as experimental results are not always directly reproducible. Such variations may arise from factors including plasma chamber conditioning, surface preparation, and the quality of the Ge/GeSn samples.

While a few studies discuss the influence of dry etching parameters on structure quality [A8, A11], clear optimization strategies are not well-documented. An efficient dry etching process depends on the volatility of the formed species and the effectiveness of physical etching in generating neutral species that react with the plasma. Physical etching plays a critical role in breaking atomic bonds at the surface, requiring ions with sufficient kinetic energy to do so. The dissociation energies of Ge–Ge, Ge–Sn, and Sn–Sn bonds are 264.4, 230.1, and 187.1 kJ/mol, respectively [A12]. In contrast, oxide bonds, such as Ge–O and Sn–O, have significantly higher dissociation energies of 657.5 and 528 kJ/mol, respectively, which suggests that oxidized surfaces are more resistant to etching. Introducing chemically reactive gases can facilitate etching by forming subspecies with lower boiling points when they react with the species generated through physical etching. This process not only enhances the removal of material but also contributes to smoother etching profiles.

Dry etching, while enabling high aspect ratios, can introduce defects such as sidewall roughness, notching, and grass-like features on the etched structures. These defects create surface trap states, which increase leakage current and degrade photonic device efficiency by enhanc-

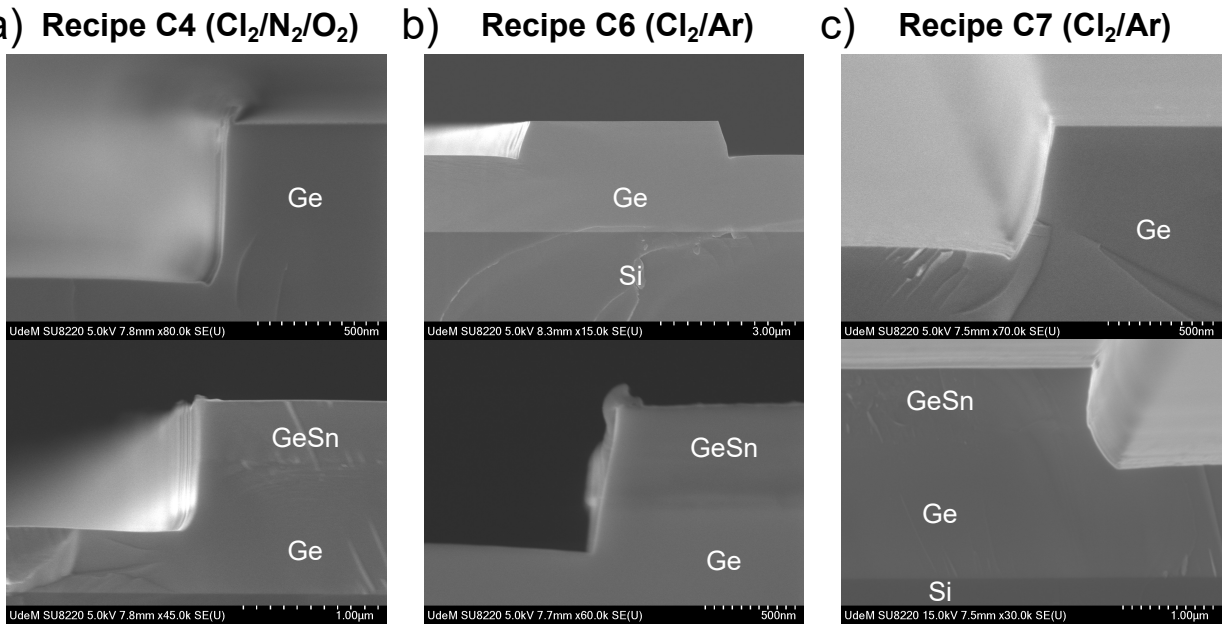


Figure A.1 SEM micrographs of the cross-sections of etched structures using Cl_2-based chemistries at LMN, with recipes (a) **C4**, (b) **C6**, and (c) **C7**. Line defects in the facets were introduced during the cleaving of the samples.

ing scattering. To mitigate these issues, it is essential to optimize plasma chamber parameters and implement appropriate surface preparation techniques. The primary objectives include minimizing surface roughness, eliminating grass-like defects caused by improper etching conditions, reducing lateral etching beneath the mask to preserve dimensional accuracy, and achieving smooth sidewalls. Smooth sidewalls are particularly critical for waveguides and light-emitting devices, such as laser cavities, as they help reduce scattering and improve quality factors. Additionally, surface passivation plays a significant role in conditioning surface states.

Optimizing plasma parameters, such as chamber pressure, temperature, gas flow rates, and CCP (or RF) and ICP generator powers, often requires multiple iterations. However, some parameters have a more pronounced impact than others. For instance, using Recipe **C2** for etching Ge or GeSn samples, which was adapted from Recipe **C1**, frequently resulted in the formation of grass-like defects. These defects, characterized as small, pillar-like features remaining after etching due to incomplete material removal, are undesirable as they increase surface roughness, degrade device performance, and contribute to scattering losses in photonic devices. Initially, the formation of these defects was attributed to micromasking, a phenomenon where sputtered material redeposits onto the surface, creating localized regions resistant to etching. In this case, sputtered photoresist caused by a high physical etching

rate was identified as a contributing factor. As shown in Figure A.2, reducing the RF and ICP generator powers mitigated these defects by softening the etch process and enhancing sidewall passivation.

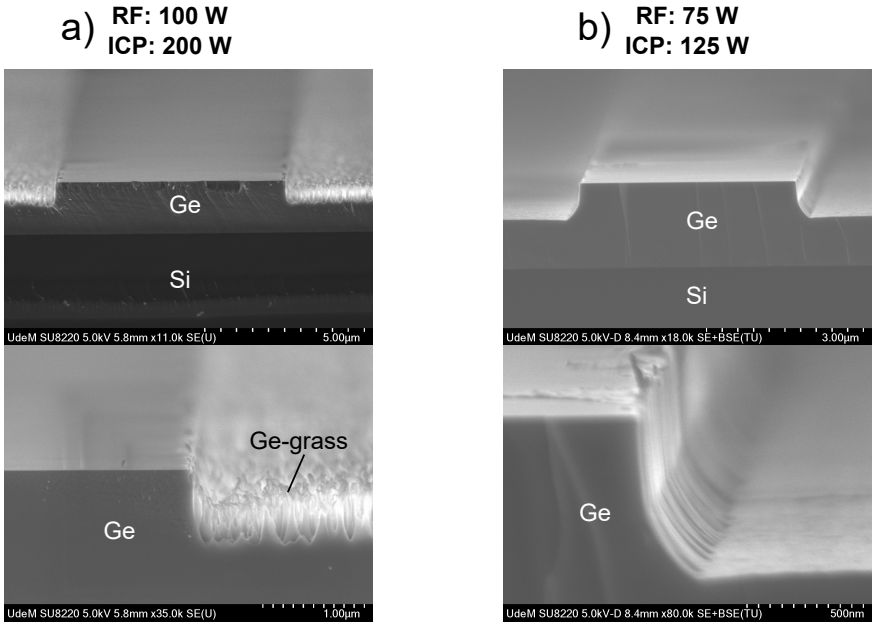


Figure A.2 SEM micrographs of the etching profile of Ge using Recipe **C2** with (a) its initial parameters (RF = 100 W, ICP = 200 W) compared to (b) lower generator powers (RF = 75 W, ICP = 125 W).

E. Eustache *et al.* proposed that grass-like defects may originate from Sn oxides forming on the GeSn surface, potentially contributing to micromasking [A9]. They observed that removing O_2 from the plasma reduced micromasking but compromised verticality. Similarly, Lin *et al.* demonstrated the role of surface oxidation in micromasking by testing an O_2 plasma treatment to remove photoresist residues before dry etching [A11]. This approach resulted in very rough and non-uniform etching with grass-like defects caused by the oxidation of the GeSn surface. However, these defects were eliminated when the sample was pre-treated with a diluted HCl solution prior to etching with a $Cl_2/Ar/O_2$ plasma (Recipe **C8**). To achieve high-quality etching, a compromise must be struck between maintaining the verticality enabled by O_2 in the plasma and minimizing defect formation. This balance can be achieved by carefully adjusting the ratio of Cl_2 and O_2 gas flows. Cl_2 primarily drives the chemical etching rate, while O_2 contributes to sidewall passivation. Excessive passivation or the redeposition of non-volatile byproducts can lead to micromasking, making precise control of the gas mixture critical.

As shown in the SEM micrographs in Fig. A.3, the Cl_2/O_2 ratio has a significant impact on

etch profiles. A Cl_2/O_2 ratio of 0.25 produces relatively straight sidewalls but introduces a trench at the top of the etched structure due to rapid lateral photoresist etching. Conversely, a ratio of 0.05 results in curved sidewalls and damage to the top surface due to insufficient passivation. A ratio of 0.15 appears to strike a balance, providing an optimal compromise between sidewall quality and overall etch performance. Increasing the chamber pressure can further improve etch quality by reducing physical ion bombardment. This occurs because higher pressures shorten the mean free path of reactive species, decreasing their kinetic energy. Guilloy *et al.* investigated the effects of introducing O_2 into the plasma and adjusting chamber pressure on the verticality and smoothness of Ge nanowires using Recipe **C1**. They found that a chamber pressure of 10 mTorr yielded optimal tapering of the nanowires [A13]. Waveguides patterned using standard photolithography often exhibit sidewall roughness caused by light diffraction. Although techniques such as electron beam lithography (EBL), UV stepper lithography, or direct laser writing can achieve lower roughness, these methods were not explored in this work.

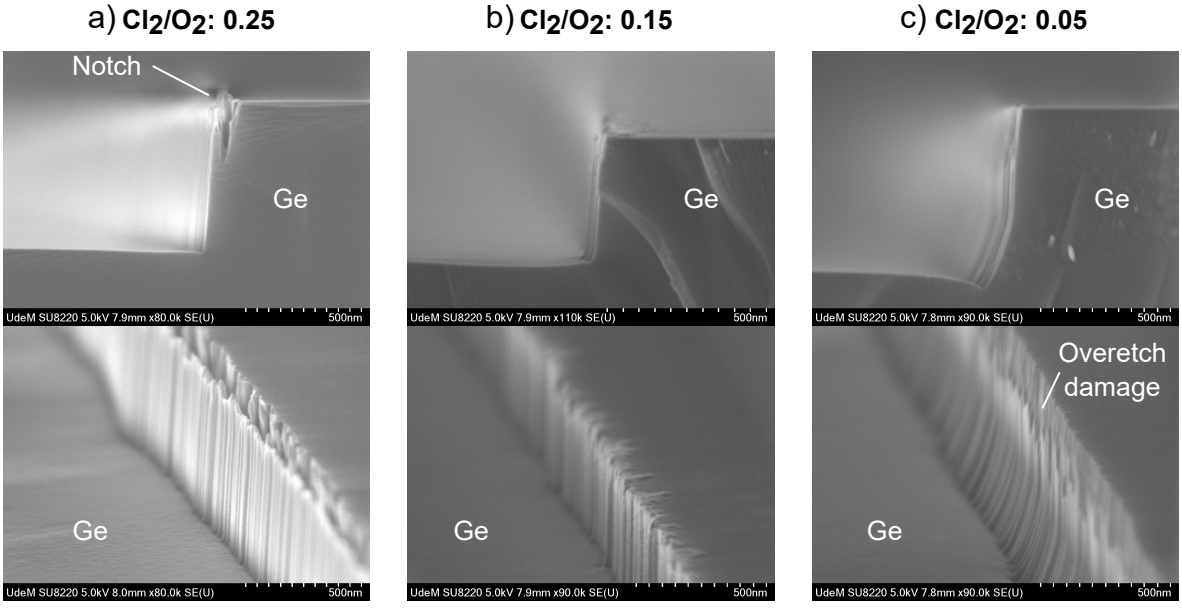


Figure A.3 SEM micrographs showing the impact of the Cl_2/O_2 ratio on the sidewall profile of Ge structures for values of (a) 0.25, (b) 0.15, and (c) 0.05 using Recipe **C4**. Top: View of the cross-section. Bottom: Tilted view of the sidewall profile.

Surface characterization techniques can be utilized to quantify improvements in surface quality. X-ray photoelectron spectroscopy (XPS) provides valuable insights into the species present on the surface after etching, aiding in understanding the accumulation of non-volatile byproducts [A6]. However, these measurements must be performed promptly to avoid sam-

ple oxidation. Effective control of plasma parameters is critical for managing these species, as their accumulation can significantly impact the etch rate and uniformity. Surface roughness can be evaluated qualitatively using SEM, while atomic force microscopy (AFM) offers a quantitative assessment of roughness improvements post-etching. However, AFM measurements were not extensively employed in this work due to the significant variability in roughness observed across the Ge and GeSn samples.

Wet etching

Wet etching is widely employed in large-scale integrated circuit fabrication due to its cost-effectiveness, stemming from lower equipment costs and simpler process requirements. Although wet etching is effective for patterning larger structures, its lower resolution and inconsistent etch rates limit its use compared to dry etching, especially for high-precision applications. In this work, wet etching of Ge and GeSn was explored as a contingency solution during periods when dry etching tools were unavailable due to extended maintenance. However, wet etching has several limitations, including lower precision, difficulty in achieving anisotropic profiles, and a tendency for undercutting. These factors can adversely affect the quality of etched features, rendering wet etching less suitable for high-resolution or complex structures compared to dry etching.

Wet etching of semiconductors typically involves three main components: an oxidizer, a solvent for the oxide, and a diluent. Table A.2 summarizes the reported etch rates of Ge and GeSn from the literature using various solutions. Cheng *et al.* were the first to investigate the etching of GeSn using an ammonia-peroxide mixture (APM) with recipe **W1**, consisting of hydrogen peroxide (H_2O_2), water, and ammonium hydroxide (NH_4OH) [A14]. They found that the etch rate of GeSn—and thus its etching selectivity relative to Ge—decreased as the Sn content in the alloy increased. In this process, H_2O_2 oxidizes Ge to form GeO_x and SnO_x, with GeO_2 being soluble in water, while SnO_x agglomerates, creating a protective layer that inhibits further etching of GeSn. This mechanism, as further reported by Dong *et al.*, results in a slower etch rate and a saturation of etch depth as Sn content increases (recipe **W2**), providing some degree of etch selectivity between Ge and GeSn [A15]. A similar trend was observed by C. Schulte-Braucks, who found that the etch rate of GeSn decreased with increasing Sn content when using a simpler solution of H_2O_2 and water (recipe **W6**) [A10]. In a comparative study of wet and dry etching techniques, Han *et al.* investigated mixtures with various APM ratios (recipes **W3** to **W5**) [A16]. They observed that increasing the volume of H_2O_2 significantly raised the surface roughness when etching GeSn thin films with a Sn content of 7.2 at.%. This observation suggests that H_2O_2 and Ge atoms primarily drive

the etching reaction. Additionally, they found that NH_4OH does not directly contribute to the etching of Ge or GeSn but instead reacts with the oxides formed during the reaction with H_2O_2, thereby increasing the etch rate. However, increasing the NH_4OH volume also led to higher surface roughness, primarily due to non-uniformities caused by the accumulation of Sn oxides.

A non-selective etching process independent of Sn content is desirable to achieve a uniform etch profile with minimal roughness. Such a process requires a compound capable of effectively removing Sn oxides, which hinder the wet etching of GeSn thin films. Adding hydrochloric acid (HCl) to the H_2O_2 solution has been found to dissolve Sn oxides and promote a linear etch rate, similar to the Standard Clean 2 (SC-2) solutions commonly used in the semiconductor industry to remove metallic contaminants. A research group at the University of Arkansas working on GeSn devices primarily employs an $HCl/H_2O_2/H_2O$ solution with a ratio of 1:1:20 (recipe **W7**), which provides an etch rate roughly independent of Sn content when used at 0 °C [A17]. This same solution was tested in-house (recipe **W8**) at room temperature, yielding a stable etch rate of approximately 80 nm/min for Ge and slightly lower rates—ranging from roughly 65 to 75 nm/min—for different GeSn samples. While the Sn content may influence the etch rate, the density of defects in the material is also likely to play a significant role.

Other wet etching solutions designed for specific materials were also found to effectively etch Ge and GeSn. For example, a solution commonly used for the wet etching of chromium (Chromium Etchant 1020, Transene), which is based on ceric ammonium nitrate ($(NH_4)_2[Ce(NO_3)_6]$) and nitric acid (HNO_3), was found to etch Ge and GeSn at rates ranging from 150 to 300 nm/min (recipe **W9**).

However, the etch rate does not appear to remain linear over time, likely due to the formation of redeposited species on the surface or variations in defect density, both of which can influence the etching dynamics. Redeposited species may create localized barriers that inhibit further etching, leading to slower and less uniform etching over time. Additionally, variations in defect density can impact the etch rate, as regions with higher defect concentrations may etch faster or slower depending on how these defects interact with the etchant. A high etch rate for Ge was reported for a similar chromium etchant by Williams *et al.* in a comparative study [A18]. Furthermore, line defects were observed on the sample surface after using this solution, which may correspond to findings by Souriau *et al.*, who demonstrated that ceric ammonium nitrate can be used to reveal threading dislocations in Ge [A19]. This etchant was utilized in the fabrication of GeSn membranes presented in Chapter 4, while its etching properties were concurrently investigated. These results underscore the potential

Table A.2 Etch rates of wet etching recipes. The wet etching is carried out at room temperature.

Recipe name	Compound	Etch rate (nm/min)		Ge:GeSn selectivity	Reference
		Ge	GeSn		
W1	H_2O_2:NH_4OH:H_2O (2:1:160)	370	<100	3.7–8.1[a]	[A14]
W2	H_2O_2:NH_4OH:H_2O (2:1:160)	228	<66[b]	>3.5	[A15]
W3	H_2O_2:NH_4OH:H_2O (2:1:160)	136	20[c]	6.9	[A16]
W4	H_2O_2:NH_4OH:H_2O (1:2:160)	98	23[c]	4.3	[A16]
W5	H_2O_2:NH_4OH:H_2O (16:1:160)	222	18[c]	12.1	[A16]
W6	H_2O_2:H_2O (1:10)	74	<19[a]	>3.9	[A10]
W7	HCl:H_2O_2:H_2O (1:1:20) at 0 °C	20	20	1[d]	[A17]
W8	HCl:H_2O_2:H_2O (1:1:20) at 20 °C	80	65–75	1.06–1.23	This work
W9	$(NH_4)_2[Ce(NO_3)_6]$:HNO_3:H_2O (4:1:15)	150 - 300	150 - 300	∼1[e]	This work

[a] The etch rate of GeSn decreases with Sn content.
[b] The etch rate decreases over time and with increasing Sn content.
[c] The GeSn sample had an Sn content of 7.2 at.%. A higher roughness is observed when increasing H_2O_2 in the volume ratio.
[d] The etch rate was found to be roughly independent of the Sn content.
[e] The etch rate was found to vary between samples and also along the etch time. The selectivity could not be assessed, but the etch rate was not observed to vary significantly with the Sn content.

incompatibility of GeSn with other commonly used etching compounds in microfabrication processes, highlighting the need for further study. Nevertheless, such compounds could serve as alternative wet etching solutions for processing GeSn thin films.

While wet etching is cost-effective, its inability to achieve high aspect ratios and its sensitivity to surface defects limit its reliability compared to dry etching. Variations in defect density and composition can result in inconsistent etch profiles and rates. Nevertheless, wet etching remains valuable in specific applications, such as the digital etching of GeSn. This technique involves using wet etching to periodically remove oxide passivation formed during plasma processing, allowing for precise diameter reduction of fine structures while maintaining a smooth surface [A20]. Digital etching has shown promise in the fabrication of nanowires, FET devices, and other fin structures [A21].

Selective etching of Ge for the fabrication of GeSn membranes and underetched structures

While fluoride reactions with Sn usually form an undesirable non-volatile passivation layer, they can be leveraged to achieve selective etching between Ge and GeSn. This selectiv-

ity is particularly useful for fabricating underetched structures such as microresonators and membranes. Gupta *et al.* demonstrated that CF_4 plasma can achieve high selectivity when etching Ge over GeSn [A6]. XPS analysis revealed that this high selectivity results from the formation of a solid SnF_y passivation layer, which effectively inhibits the etching of GeSn. C. Schulte-Braucks reported an impressive selectivity of 270 for Ge over GeSn with a Sn content of 12.5 at.% using a CF_4 plasma [A10]. This property has since been widely applied in the fabrication of various devices, including disk resonators, nanobridges, and membranes. However, as noted by Schulte-Braucks, the etch rate and depth of GeSn depend on the Sn content, with etch depth saturation occurring over time, in contrast to the more linear etching behavior observed in Ge [A10]. Similarly, Han *et al.* observed that etching selectivity increases dramatically when the Sn content exceeds 6 at.% [A16].

Figure A.4 illustrates the fabrication steps for partially underetched GeSn structures (microdisks). The process begins with directional etching through the GeSn and Ge layers (Fig.A.4(a)), followed by the selective etching of Ge (Fig.A.4(b)). The GeSn sample comprises layers with varying Sn content, ranging from 6 to approximately 9 at.%. A slight lateral overetch of the disk structure is observed at the bottom compared to the top, suggesting a possible variation in etching selectivity across the layers. In contrast, another structure fabricated with a GeSn content of approximately 11 at.% Sn did not exhibit this lateral overetch variation. A recipe was developed using the GIGAbatch 310 (PVA Tepla) at LMF, achieving etch rates between 1–2 μm/min (recipe **F4**). However, due to maintenance on this equipment, an alternative recipe was developed using the Plasmalab 100, which was temporarily connected to CF_4 (recipe **F5**). This alternative recipe produced a lower etch rate.

The fabrication of membranes involves etching through the GeSn and Ge layers, followed by a complete selective etching of the underlying Ge layer to release the GeSn film. Structural bowing was observed in high-aspect-ratio membranes, likely due to initial compressive strain or minor surface etching [A1]. Despite this, these structures hold significant promise, as they can be heterogeneously transferred to various substrates using transfer printing, enabling the development of transferable optoelectronic devices. Figure A.5 presents fully underetched membranes fabricated from different GeSn thin film samples.

The complete underetching of microdisks enabled photoluminescence and absorption studies on strain-relaxed structures, demonstrating that the underetching step did not introduce additional defects that could lead to trap-assisted recombination [A22]. Since the strain accumulated in GeSn layers during growth appears to influence the structural bowing of the resulting membranes, strain-relaxed samples are expected to exhibit reduced bowing. This improvement would enhance adhesion to new substrates during transfer printing. In Chapter 4, a

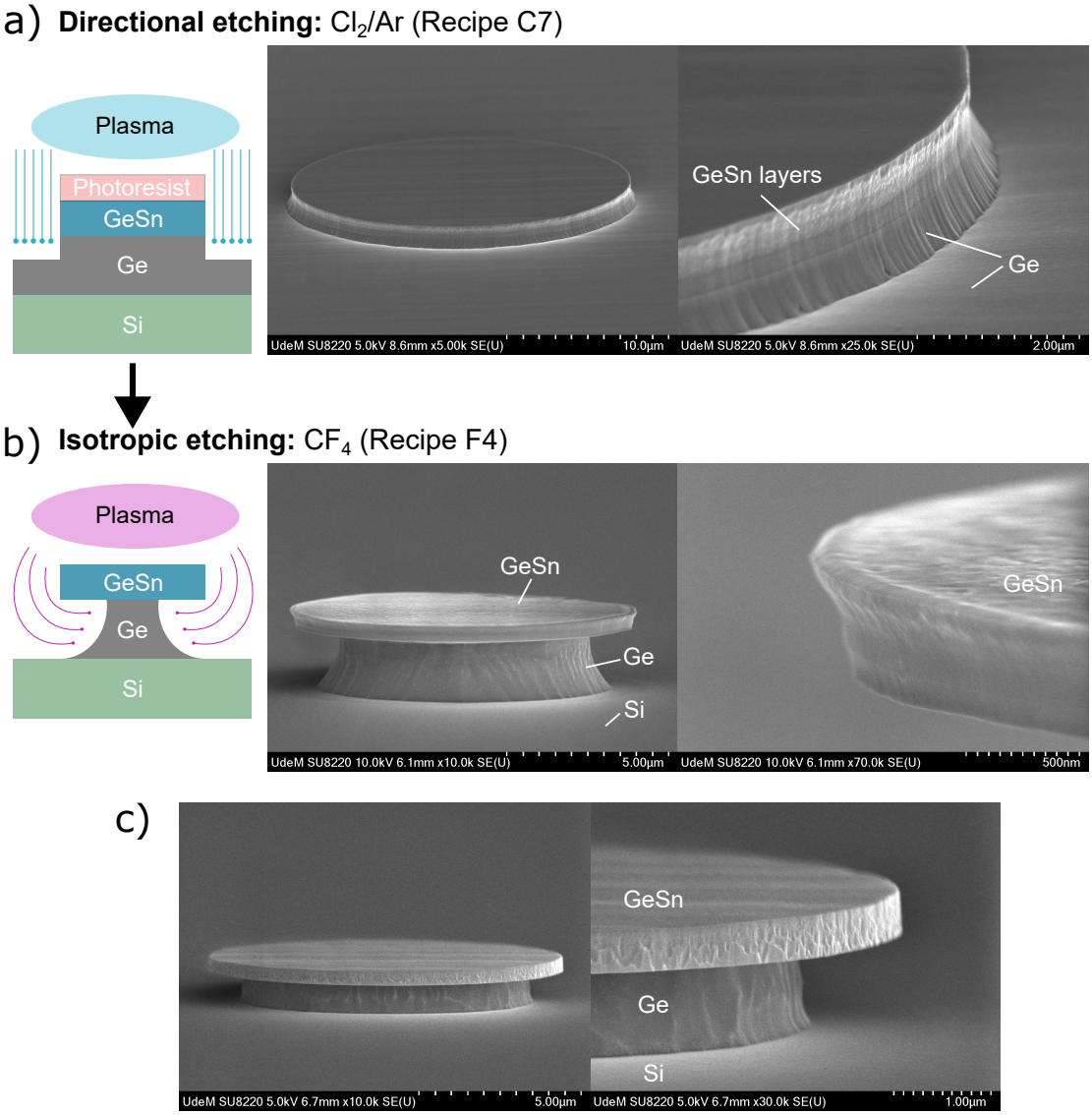


Figure A.4 Fabrication steps of partially underetched structures with a GeSn film sample composed of multiple layers with contents ranging from 6 to approximately 9 at.% Sn. (a) Resulting mesa after directional etching through the GeSn layers using a Cl_2/Ar plasma (recipe **C7**). (b) Resulting structure after selective and isotropic etching of Ge using a CF_4 plasma (recipe **F4**). (c) Disk structure from a different sample made of a single content around 11 at.% Sn.

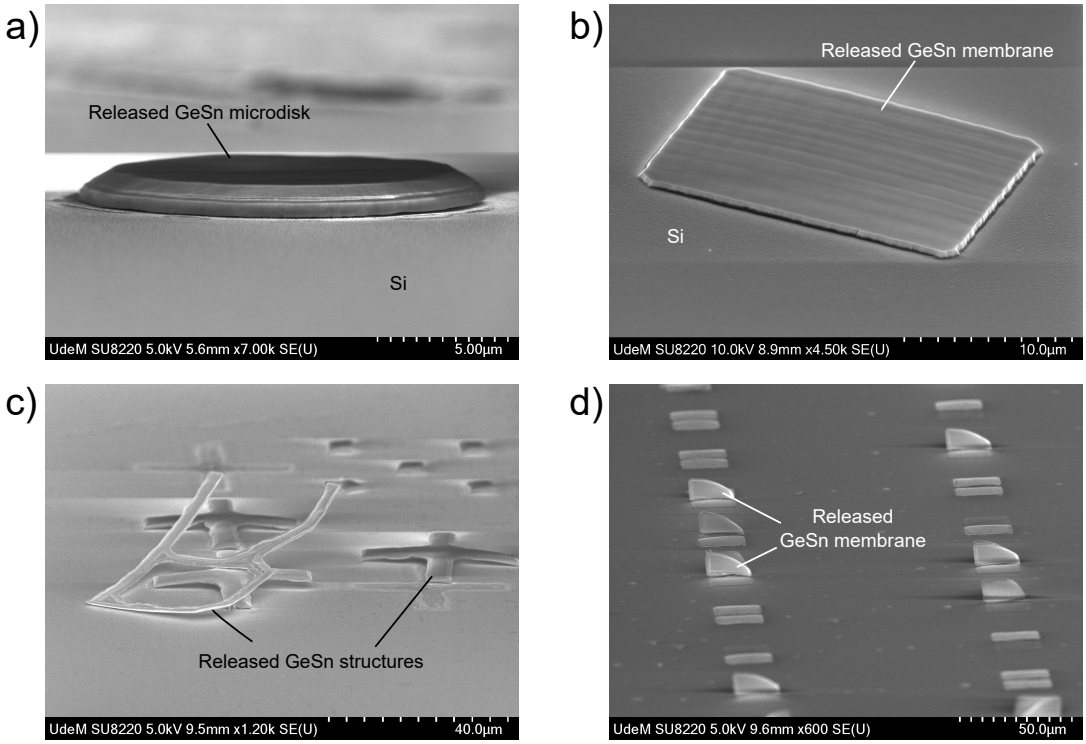


Figure A.5 Overview of GeSn membrane structures. (a) Released GeSn microdisk patterned using wet etching. (b) Released membrane on Si. (c) Larger structures that exhibit structural bowing. (d) Released thin membranes, with some exhibiting significant structural bowing.

sample with relatively low compressive strain of -0.6% was used to fabricate membranes that exhibited minimal bowing. The membrane dimensions were fixed at 20 μm $\times$ 20 μm, though larger dimensions are expected to be achievable. However, the underetch rate of GeSn structures using Recipe **F4** was observed to decrease significantly with extended etching times. Larger structures may require longer etching durations to fully release, as plasma species must reach the underlying Ge layer. Patterning strategic holes in the membranes could facilitate the etching process and mitigate this limitation.

Surface cleaning and passivation

Etch byproducts and surface oxides can modify Ge and GeSn properties, increasing dark current by creating dangling bonds before contact deposition. Consequently, effective surface passivation is crucial for the performance and stability of optoelectronic devices, particularly those utilizing Ge and GeSn. Prior to etching, surface cleaning is essential to remove contaminants and oxides. Standard cleaning solutions, such as Piranha solution (H_2O_2:H_2SO_4), are unsuitable for Ge and GeSn because H_2O_2 can etch these materials. Instead, cleaning solutions based on HCl and HF are typically employed, as they efficiently remove Ge oxides [A23]. HCl is also expected to effectively remove Sn oxides, as supported by several studies using XPS measurements [A6, A9]. To ensure comprehensive cleaning, solvent-based solutions are required in conjunction with HCl and HF, as these alone do not effectively remove organic contaminants [A10]. Additionally, in-situ cleaning during etching may help minimize residue buildup and reduce the need for extensive post-etch treatments.

Surface passivation is equally critical for stabilizing surface states and reducing surface trap densities, which otherwise contribute to non-radiative recombination and leakage currents, degrading device performance. The high reactivity of GeSn with air underscores the necessity of durable passivation techniques. Sulfur passivation has emerged as a promising approach [A24, A25]. Groell *et al.* reported that sulfur- and iodine-based passivation methods significantly reduce the reoxidation rate of Ge and $Ge_{0.9}Sn_{0.1}$ surfaces [A26].

Summary

An overview of various etching techniques commonly employed in the processing of devices based on GeSn thin films has been provided, along with a description of their underlying mechanisms. Observations from the literature and experiments conducted in the laboratory have been included to guide future recipe development and optimization for GeSn, serving as a prototype for a *troubleshooting* guide. The shared use of tools in academic cleanrooms

can affect chamber conditions, leading to contamination and variability in results. Table A.3 summarizes the observed etch rates for various chemistries used in etching selected materials, offering an overview of their selectivity and compatibility. A similar notation was employed by Williams *et al.* in a comparative study [A18]. These recipes were primarily investigated to optimize processing capabilities for GeSn and to minimize surface roughness on etched structures, enabling the fabrication of high-quality devices. The ultimate goal is to integrate these devices with silicon photonics. Further investigation into the selectivity between Ge and GeSn is required, particularly concerning the effects of Sn content, doping type and concentration, and defect density in GeSn thin films.

Table A.3 Summary of the etch rate of the different materials using different compounds ('W': etch rate not measured, but expected to work. 'S': etch rate not measured, but expected to be slow or near zero).

	Etchant	**Target material**	**Etch rate (nm/min)**							
			Ge	**GeSn**	**Si**	**SiO_2**	**Au**	**Cr**	**Al**	**Photoresist**
Dry etching	**$Cl_2/N_2/O_2$**	**Ge, GeSn**	100 - 200	100 - 200	S	S	W	W	W	50
	Cl2/Ar	**Ge, GeSn**	100 - 200	100 - 200	W	W	W	W	W	W
	SF_6/Ar	**Ge**	400	50	400	S	W	W	W	100
	CF_4	**Ge**	>1000	W	R	0	W	W	W	S
Wet etching	**Buffered HF (1:6)**	**SiO_2**	0	0	0	80	S	S	S	0
	HCl:H_2O_2:H_2O	**Ge, GeSn**	80	W	S	S	W	-	-	S
	Chromium etchant (Transene 1020)	**Cr**	100 - 300	100 - 300	0	S	S	W	W	0
	APM	**Ge, GeSn**	100 - 400	20 - 100	S	-	-	-	-	-

References

[A1] M. R. M. Atalla, S. Assali, A. Attiaoui, C. Lemieux-Leduc, A. Kumar, S. Abdi, and O. Moutanabbir, "All-Group IV Transferable Membrane Mid-Infrared Photodetectors," *Advanced Functional Materials*, vol. 31, no. 3, p. 2006329, 2021.

[A2] M. R. M. Atalla, S. Assali, G. Daligou, A. Attiaoui, S. Koelling, P. Daoust, and O. Moutanabbir, "Continuous-Wave GeSn Light-Emitting Diodes on Silicon with 2.5 μm Room-Temperature Emission," *ACS Photonics*, vol. 11, no. 3, pp. 1335–1341, 2024.

[A3] M. R. M. Atalla, S. Assali, S. Koelling, A. Attiaoui, and O. Moutanabbir, "High-Bandwidth Extended-SWIR GeSn Photodetectors on Silicon Achieving Ultrafast Broadband

Spectroscopic Response," *ACS Photonics*, vol. 9, no. 4, pp. 1425–1433, 2022.

[A4] M. R. M. Atalla, C. Lemieux-Leduc, S. Assali, S. Koelling, P. Daoust, and O. Moutanabbir, "Extended short-wave infrared high-speed all-GeSn PIN photodetectors on silicon," *APL Photonics*, vol. 9, no. 5, 2024.

[A5] É. Bouthillier, "Non-Equilibrium Germanium-Tin Microstructures for Silicon-compatible Mid-infrared Photonics," Master's thesis, Polytechnique Montréal, 2019.

[A6] S. Gupta, R. Chen, Y.-C. Huang, Y. Kim, E. Sanchez, J. S. Harris, and K. C. Saraswat, "Highly Selective Dry Etching of Germanium over Germanium-Tin ($Ge_{1-x}Sn_x$): A Novel Route for $Ge_{1-x}Sn_x$ Nanostructure Fabrication," *Nano Letters*, vol. 13, no. 8, pp. 3783–3790, 2013

[A7] Y. Dong, D. Lei, X. Xu, W. Wang, and Y.-C. Yeo, "Chlorine- and Fluorine-based dry etching of Germanium-Tin," in *2014 7th International Silicon-Germanium Technology and Device Meeting (ISTDM)*. IEEE, 2014, pp. 99–100.

[A8] L. Milord, J. Aubin, A. Gassenq, S. Tardif, K. Guilloy, N. Pauc, J. Rothman, A. Chelnokov et al., "Inductively coupled plasma etching of germanium tin for the fabrication of photonic components," in *Silicon Photonics XII*, G. T. Reed and A. P. Knights, Eds. SPIE, 2017.

[A9] E. Eustache, M. A. Mahjoub, Y. Guerfi, S. Labau, J. Aubin, J. M. Hartmann, F. Bassani, S. David et al., "Smooth plasma etching of GeSn nanowires for gate-all-around field effect transistors," *Semiconductor Science and Technology*, vol. 36, no. 6, p. 065018, 2021.

[A10] C. Schulte-Braucks, "Investigation of GeSn as Novel Group IV Semiconductor for Electronic Applications," Ph.D. dissertation, Forschungszentrum Jülich, 2017.

[A11] G. Lin, P. Cui, T. Wang, R. Hickey, J. Zhang, H. Zhao, J. Kolodzey, and Y. Zeng, "Fabrication of Germanium Tin Microstructures Through Inductively Coupled Plasma Dry Etching," *IEEE Transactions on Nanotechnology*, vol. 20, pp. 846–851, 2021.

[A12] W. M. Haynes, *CRC Handbook of Chemistry and Physics*, W. M. Haynes, Ed. CRC Press, 2016.

[A13] K. Guilloy, N. Pauc, A. Gassenq, and V. Calvo, "High aspect ratio germanium nanowires obtained by dry etching," *MRS Advances*, vol. 1, no. 13, pp. 875–880, 2016.

[A14] R. Cheng, W. Wang, X. Gong, L. Sun, P. Guo, H. Hu, Z. Shen, G. Han et al., "Relaxed and Strained Patterned Germanium-Tin Structures: A Raman Scattering Study," *ECS Journal of Solid State Science and Technology*, vol. 2, no. 4, pp. P138–P145, 2013.

[A15] Y. Dong, B. L. Ong, W. Wang, Z. Zhang, J. Pan, X. Gong, E.-S. Tok, G. Liang et al., "Etching of germanium-tin using ammonia peroxide mixture," *Journal of Applied Physics*, vol. 118, no. 24, p. 245303, 2015.

[A16] Y. Han, Y. Li, Y. Song, C. Chi, Z. Zhang, J. Liu, Z. Zhu, and S. Wang, "A comparative study of selective dry and wet etching of germanium-tin ($Ge_{1-x}Sn_x$) on germanium," *Semiconductor Science and Technology*, vol. 33, no. 8, p. 085011, 2018.

[A17] H. Tran, C. G. Littlejohns, D. J. Thomson, T. Pham, A. Ghetmiri, A. Mosleh, J. Margetis, J. Tolle et al., "Study of GeSn Mid-infrared Photodetectors for High Frequency Applications," *Frontiers in Materials*, vol. 6, no. 278, pp. 1–7, 2019.

[A18] K. Williams, K. Gupta, and M. Wasilik, "Etch rates for micromachining processing–Part II," *Journal of Microelectromechanical Systems*, vol. 12, no. 6, pp. 761–778, 2003.

[A19] L. Souriau, T. Atanasova, V. Terzieva, A. Moussa, M. Caymax, R. Loo, M. Meuris, and W. Vandervorst, "Characterization of Threading Dislocations in Thin Germanium Layers by Defect Etching: Toward Chromium and HF-Free Solution," *Journal of The Electrochemical Society*, vol. 155, no. 9, p. H677, 2008.

[A20] W. Wang, D. Lei, Y. Dong, X. Gong, E. S. Tok, and Y.-C. Yeo, "Digital Etch Technique for Forming Ultra-Scaled Germanium-Tin ($Ge_{1-x}Sn_x$) Fin Structure," *Scientific Reports*, vol. 7, no. 1835, 2017.

[A21] M. Liu, D. Yang, A. Shkurmanov, J. H. Bae, V. Schlykow, J.-M. Hartmann, Z. Ikonic, F. Baerwolf et al., "Epitaxial GeSn/Ge Vertical Nanowires for p-Type Field-Effect Transistors with Enhanced Performance," *ACS Applied Nano Materials*, vol. 4, no. 1, pp. 94–101, 2021.

[A22] S. Assali, A. Dijkstra, A. Attiaoui, É. Bouthillier, J. Haverkort, and O. Moutanabbir, "Midinfrared Emission and Absorption in Strained and Relaxed Direct-Band-Gap $Ge_{1-x}Sn_x$ Semiconductors," *Physical Review Applied*, vol. 15, no. 2, p. 024031, 2021.

[A23] P. Ponath, A. B. Posadas, and A. A. Demkov, "Ge(001) surface cleaning methods for device integration," *Applied Physics Reviews*, vol. 4, no. 2, p. 021308, 2017.

[A24] D. Lei, "Advanced germanium-tin p-channel metal-oxide-semiconductor field-effect transistors," Ph.D. dissertation, National University of Singapore, 2017.

[A25] P. Raynal, A. Quintero, V. Loup, P. Rodriguez, L. Vallier, J. Aubin, J. Hartmann, N. Chevalier et al., "GeSn surface preparation by wet cleaning and in-situ plasma treatments prior to metallization," *Microelectronic Engineering*, vol. 203–204, no. 38–39, pp. 38–43, 2019.

[A26] L. Groell, A. Attiaoui, S. Assali, and O. Moutanabbir, "Combined Iodine- and Sulfur-Based Treatments for an Effective Passivation of GeSn Surface," *The Journal of Physical Chemistry C*, vol. 125, no. 17, pp. 9516–9525, 2021.

APPENDIX B UNCERTAINTY CALCULATION ON THE OPTICAL POWER AND PHOTOCURRENT MEASUREMENTS

Optical power in the waveguide

In Chapter 6, device responsivity depends on accurate measurements of photocurrent (I_{ph}) and optical power in the waveguide (P_{wg}). The power inside the waveguide was estimated by correcting the measured fiber facet power (P_{Fiber}) for the insertion loss (IL) of a single SGC. Therefore, it is crucial to quantify the uncertainty associated with this conversion. First, P_{wg} was determined using the following equation:

$$P_{wg} = P_{Fiber} 10^{IL/10} \tag{B.1}$$

The uncertainty in P_{wg}, denoted as ΔP_{wg}, is estimated using partial derivatives:

$$\Delta P_{wg} = \left| \frac{\partial P_{wg}}{\partial P_{Fiber}} \right| \Delta P_{Fiber} + \left| \frac{\partial P_{wg}}{\partial IL} \right| \Delta IL \tag{B.2}$$

which results in the following equation:

$$\Delta P_{wg} = 10^{IL/10} \left(\Delta P_{Fiber} + \frac{\ln(10)}{10} P_{Fiber} \Delta IL \right) \tag{B.3}$$

The insertion loss (IL) and its uncertainty were determined through transmission measurements of a 300 μm waveguide with two SGCs acting as interconnects for light injection and collection. The optical power at the fiber facet used for the injection of light ($P_{Fiber,1}$) and the fiber used for collection ($P_{Fiber,2}$) were used to estimate IL using:

$$2 \times IL = 10 \log_{10} \left(\frac{P_{Fiber,2}}{P_{Fiber,1}} \right) \tag{B.4}$$

where the total loss is associated with the insertion of two SGCs. Because accurately estimating propagation loss in the waveguides was challenging, it was instead incorporated into the computed insertion loss of an SGC. Thus, IL represents both the coupling loss and propagation loss over a $\sim$150 μm waveguide section. From equation B.4, the error in IL (ΔIL) can be estimated using:

$$\Delta IL = \frac{1}{2}\frac{10}{\ln(10)}\left(\frac{\Delta P_{Fiber,1}}{P_{Fiber,1}} + \frac{\Delta P_{Fiber,2}}{P_{Fiber,2}}\right) \tag{B.5}$$

Values of $P_{Fiber,1}$ and $P_{Fiber,2}$ were measured using a photodetector (DET10D2, Thorlabs) connected to a photodiode amplifier to measure the current value (PDA200C, Thorlabs). An error of 5% is set on the measured values of this photodetector. The responsivity of the photodetector at 2.33 μm is 1.304 A/W. Here, values of 4968 μW and 12.9 μW were used for $P_{Fiber,1}$ and $P_{Fiber,2}$, respectively, yielding a value of -12.9 dB for IL using equation B.4. With a 5% relative error in power readings, equation B.5 gives an uncertainty of $\Delta IL = 0.22$ dB. Consequently, the uncertainty in P_{wg} is approximately 10% (i.e. 0.53 μW on a power of 5.219 μW and 11.08 μW on a power of 110.15 μW).

Photocurrent

The setup detailed in Chapter 6 does not directly measure the photocurrent I_{ph}. Instead, it provides a relative measurement due to the use of a lock-in amplifier and a preamplifier. The relative photocurrent measurement ($I_{ph,rel}$) is converted to an absolute value (I_{ph}) using:

$$I_{ph} = CI_{ph,rel} \tag{B.6}$$

where C is a constant determined by calibrating the setup and depends on various settings, which was carried out using an extended-InGaAs photodetector. For the given measurement settings, the calibration factor was determined to be $C = 0.2959$. The calibration factor ensures accurate conversion of relative photocurrent readings to absolute values, providing reliable data for device characterization.